CUKUROVA UNIVERSITY
INSTITUTE OF NATURAL AND APPLIED SCIENCE

PhD THESIS

Veysi GÜÇKAN

SYNTHESIS OF DOPED FLUOROPEROVSKITES AND OXIDE CERAMICS AS PHOSPHORS AND THEIR DOSIMETRIC CHARACTERIZATION

DEPARTMENT OF PHYSICS

ADANA-2021

To my family…

ABSTRACT

PhD THESIS

SYNTHESIS OF DOPED FLUOROPEROVSKITES AND OXIDE CERAMICS AS PHOSPHORS AND THEIR DOSIMETRIC CHARACTERIZATION

Veysi GÜÇKAN

CUKUROVA UNIVERSITY
INSTITUTE OF NATURAL AND APPLIED SCIENCES
DEPARTMENT OF PHYSICS

Supervisor : Prof. Dr. Zehra YEĞİNGİL
Year: 2021; Page: 261
Jury : Prof. Dr. Zehra YEĞİNGİL
: Prof. Dr. Kasım KURT
: Prof. Dr. Tunç TÜKEN
: Prof. Dr. Necmettin YAZICI
: Assoc. Prof. Dr. Ahmet EKİCİBİL

The aim of this study is to synthesize oxide-based MgO and ZnO, and fluoride-based perovskite $KMgF_3$ materials to be used as personal dosimeter, medical dosimeter or emergency dosimeter using thermoluminescence (TL) and optically stimulated luminescence (OSL) methods and to develop their dosimetric properties. These samples were synthesized using precipitation, sol-gel, or solution combustion synthesis methods. The crystallography of the newly synthesized samples was investigated by X-ray diffractometry analysis. The morphology and particle size analysis of the synthesized materials were carried out by Scanning Electron Microscopy. On the other hand, FT-IR Spectrophotometer was used to observe the vibrational modes of the samples. TL and OSL curves were compared with commercial dosimeters after optimization of variable parameters during calcination process in the production process of the samples to improve TL or OSL signals. Spectroscopic properties were examined with radioluminescence and photoluminescence analyzes to define the emission range of the samples. Basic dosimetric properties of the samples such as reusability, dose-response, minimum detectable dose and fading were reported. Kinetic parameters such as activation energies and frequency factors were calculated using different methods such as CGCD, VHR, FGT, T_m-T_{stop}, isothermal annealing and compared with each other.

Keywords: Radiation dosimetry, oxides, perovskites, MgO, ZnO, $KMgF_3$, thermoluminescence, optically stimulated luminescence, radioluminescence, photoluminescence, kinetic parameters.

ÖZ

DOKTORA TEZİ

SYNTHESIS OF DOPED FLUOROPEROVSKITES AND OXIDE CERAMICS AS PHOSPHORS AND THEIR DOSIMETRIC CHARACTERIZATION

Veysi GÜÇKAN

ÇUKUROVA ÜNİVERSİTESİ
FEN BİLİMLERİ ENSTİTÜSÜ
FİZİK ANABİLİM DALI

Danışman : Prof. Dr. Zehra YEĞİNGİL
Yıl: 2021; Sayfa: 261
Jüri : Prof. Dr. Zehra YEĞİNGİL
: Prof. Dr. Kasım KURT
: Prof. Dr. Tunç TÜKEN
: Prof. Dr. Necmettin YAZICI
: Doç. Dr. Ahmet EKİCİBİL

Bu çalışmanın amacı, Termolüminesans (TL) ve Optiksel Uyarmalı Lüminesans (OSL) yöntemlerini kullanarak kişisel dozimetre, medikal dozimetre veya acil durum dozimetre olarak kullanılacak oksit tabanlı MgO ve ZnO, ve florür tabanlı perovskit bir malzeme olan $KMgF_3$ malzemelerinin sentezlenmesi ve dozimetrik özelliklerinin geliştirilmesidir. Hedeflenen örnekler çöktürme, sol-gel veya çözelti yanma sentez yöntemleri kullanılarak sentezlendi. Üretilen malzemelerin kristalografisi X-ışını difraktometresi analizi ile incelenmiştir. Sentezlenen malzemelerin morfolojisi taramalı elektron mikroskopu ile gerçekleştirilmiştir. Diğer yandan örneklerin titreşim modlarını gözlemleyebilmek için FT-IR spektrofotometre kullanılmıştır. TL veya OSL sinyallerini iyileştirmek için örneklerin üretim sürecindeki kalsinasyon sıcaklık ve zaman parametreleri optimizasyonu yapıldıktan sonra TL ve OSL eğrileri ticari dozimetrelerle karşılaştırılmıştır. Spektroskopik özellikler Radyoluminesans ve Fotolüminesans analizleri ile incelenerek örneklerin emisyon bölgeleri tanımlandı. Örneklerin tekrar kullanılabilirlik, doz-yanıt, belirlenebilen minimum doz ve sinyal sönüm gibi temel dozimetrik özellikleri rapor edildi. Bütün örneklerin aktivasyon enerjileri ve frekans faktörleri gibi kinetik parametreleri CGCD, VHR, FGT, T_m-T_{stop}, izotermal sönüm gibi yöntemlerle bulundu ve birbirleri ile karşılaştırıldı.

Anahtar Kelimeler: Radyasyon dozimetrisi, oksitler, perovskitler, MgO, ZnO, $KMgF_3$, termolüminesans, optik olarak uyarılmış lüminesans, radyolüminesans, fotolüminesans, kinetik parametreler.

EXTENDED ABSTRACT

The aim of this thesis is to synthesize and analyze the dosimetric properties of magnesium oxide (MgO), zinc oxide (ZnO) and parascandolaite ($KMgF_3$) host materials, which can be used as high-sensitivity thermoluminescence and optically excited luminescence dosimeters, with various additive ions. The main goal is to create crystal defects (electron traps) to be formed in the materials to be obtained by doping the host materials to be synthesized with different dopants and co-dopants, and to achieve high beta dose sensitivity. This thesis will shed light on future studies of TL and OSL dosimeters, as well as the use of domestic dosimeters that will reduce foreign dependency, by bringing the analysis results of the researched materials to the literature.

In this thesis, after MgO samples were synthesized by solution combustion synthesis method (SCS) and added with different dopants, many characterizations and dosimetric analyzes were carried out, they were shown as both TL and OSL dosimeter candidates depending on the results.

To develop a dosimeter material with the required OSL dosimetry properties, sodium (Na) and lithium (Li) doped magnesium oxide (MgO:Na,Li) polycrystals were synthesized using the SCS technique. Dosimetric and luminescence properties of MgO:Na,Li ceramic prepared in pellet form were investigated. Phase identification and morphology of the samples were performed using x-ray diffraction (XRD) and scanning electron microscopy (SEM) analysis. The radioluminescence (RL) emission of the obtained $MgO:Na_{5\%},Li_{5\%}$ was reported as a promising OSL material with favorable dosimetric properties, sensitive to ionizing radiation. pellet samples showed two distinct emission bands, dominant at ~730 nm and weak and broad emission between 300 and 590 nm. The samples were characterized by a TL glow curve with dominant TL peaks at approximately 80, 155 and 315°C at a heating rate of 5 °C. We performed a step annealing procedure to investigate the depth of capture centers associated with the

OSL signal. The thermally affected OSL traps mostly appear to originate from a single TL peak between 170 and 250 °C with intensity comparable to Al_2O_3:C when using the Hoya U-340 filter. The stability of the OSL signal was tested for short-term and long-term fading in the dark. It was determined that the total OSL area decreased by approximately 15% after 5 weeks. The kinetic parameters of MgO:$Na_{5\%}$,$Li_{5\%}$ were evaluated using computer-assisted peak decomposition (CGCD), Tm-Tstop method, extended first rise method (IRM) for TL traps, and isothermal annealing for OSL traps. MgO:$Na_{5\%}$,$Li_{5\%}$ was reported as a promising OSL material with favorable dosimetric properties, sensitive to ionizing radiation.

MgO phosphors activated by copper (Cu), lithium (Li) and potassium (K); MgO:$_{Cu0.001\%}$,$Li_{10\%}$,$K_{10\%}$, another dosimetric material developed using the SCS method in this study, are also promising as TL dosimeters. TL sensitivity, dose dependence, spectral distribution of RL emission, glow curve properties and storage stability were found suitable for dosimetric purposes. Structural characterization and phase composition were checked using XRD and SEM. MgO:Cu,Li,K microcrystals with an average size of ~450 nm were obtained by sintering the material at 1200 °C for 4 hours. RL studies have shown that the energy traps in the samples are closely correlated with two emission bands located at ~750 nm (dominant) and between 320 and 500 nm. TL dose response curve from stable traps showed a near linear behavior between 0.1 Gy and 0.5 kGy. In addition, the minimum detectable dose value of MgO:$_{Cu0.001\%}$,$Li_{10\%}$,$K_{10\%}$ sample was found to be ~5.9 μGy. TL intensity was observed to decrease by approximately 3% and 3.3% for the peaks at 214 and 285 °C, respectively, within 48 hours. Then, the same signal fading was determined as 5.1% and 6.2% at the end of four weeks. The kinetic parameters were determined by CGCD and IRM methods and the activation energy of the main dosimetric peak, located around 214 °C, is E ~ 1.40 eV. The frequency factor s for this peak is 10^{14} s^{-1}. With these results, the luminescence properties of MgO:Cu,Li,K deserve further attention as a possible dosimeter in the field of radiation dosimetry.

The temperature dependence of infrared excited luminescence, an OSL technique, of terbium (Tb), gadalonium (Gd) and lithium (Li) doped MgO was investigated and basic dosimetric properties for radiation dosimetry were investigated. MgO:Tb,Gd,Li phosphorus was synthesized using solution combustion synthesis method and characterization of the material was done by XRD and SEM techniques. The effects of dopants were investigated by determining the RL, TL and OSL curves of MgO:Tb,Gd,Li phosphorus. The decay curves of the light flash against time showed that the MgO:Tb,Gd,Li ceramics were discharged most rapidly by infrared excitation. The temperature dependence of the IRSL samples was examined between 50 and 230 °C. The optimized read temperature was set at 120 °C, which provides the maximum IRSL density. For the studied MgO:Tb,Gd,Li samples, traps have been shown to be responsible for TL peaks below 200 °C, which can be suggested as the source of the IRSL signals. The high temperature TL peaks at about 400 °C were unaffected by infrared excitation and did not contribute to the IRSL signals obtained. Dosimetric properties such as reusability, multi-readability, dose-response and fading were examined for their applicability to radiation dosimetry. The thermal stability of the sample was investigated using isothermal annealing technique and the activation energy and frequency factor of the traps responsible for the IRSL signal were calculated as 0.62 eV and 10^6 Hz, respectively. The IRSL signals of the Tb, Gd and Li doped MgO sample reported in this study showed that it could be investigated and studied as a radiation dosimeter.

Another MgO-based phosphorus investigated in this study, cerium (Ce) and lithium (Li) doped MgO was synthesized by solid state synthesis reaction method (SSR) and its luminescence properties were investigated. XRD diffraction patterns and SEM images were used for structure analysis. The luminescence properties were investigated using TL, photoluminescence (PL) and RL techniques. The samples were characterized by TL peaks at 223 and 308 °C. The dose-response of phosphorus as a function of exposure to β-rays showed linear behavior for

exposures below 10 Gy. At higher radiation exposures, its dose-response behavior showed saturation. After the first day in the fading experiment, the TL intensity of Peak III decreased by ~13%, while Peak IV showed a slight increase of ~4 in the same period. Step annealing experiment was performed to determine the preheating temperature. Kinetic parameters such as activation energy, frequency factors and MgO:Ce,Li kinetic order were found using CGCD, different heating rates (VHR) methods and T_m-T_{stop} method assisted by IR method. The T_m-T_{stop} method revealed five regions responsible for TL peaks. Using these activation centers emitted between ~0.6 and ~1.5 eV, it was determined that the main contributions for radiation storage were from these energy levels. Experimental results of TL, PL and RL analyzes may contribute to a better understanding of the luminescence mechanism in Ce^{3+} and Li^{+} activated MgO for potential use of phosphor design as a dosimeter or optical ceramic material.

In order to develop a new TL or OSL dosimeter, zinc oxide (ZnO), different production methods and the variables in these production methods were investigated and optimized for TL and OSL sensitivities. In this study, it was aimed to optimize the preferred calcination conditions for maximum TL and OSL emissions of europium doped zinc oxide (ZnO:Eu) phosphors at micro/nano scale after exposure to β-particles when synthesized using precipitation method and sol-gel method. In the production of ZnO:Eu pellets, calcination temperature range of 800-1200 °C and calcination times between 2 hours and 24 hours were applied. The phase composition and morphology of the samples were investigated by XRD and SEM. Transmittance measurements were performed with Fourier transformed infrared (FT-IR) spectroscopy to understand the vibrational properties of ZnO:Eu nanocrystals. The formation of the hexagonal wurtzite phase of ZnO was observed in the XRD and SEM models. It was observed that the samples exhibited a weak green emission when the excitation wavelength was 350 nm. In addition, ZnO:Eu pellets exhibited two sharp peaks at 579 and 615 nm in relation to Eu transitions. PL densities decreased with increasing calcination temperatures. TL peaks set at

130 and 300 °C with a heating rate of 5 $^{o}Cs^{-1}$ were found to be similar when the pellets were calcined using different temperatures and times. The linearity of β-dose was observed from 1 Gy to 0.2 kGy for all samples studied. This comprehensive study of precipitation and sol-gel methods and the structural nature of the synthesized materials are of great importance in understanding the further development of new ZnO-based dosimetric materials and functional materials.

Europium (Eu), ytterbium (Yb) and lithium (Li) doped $KMgF_3$ ($KMgF_3$:Eu,Yb,Li) was synthesized using the sol-gel method. Structural and luminescence properties of $KMgF_3$:Eu,Yb,Li were investigated by TL, OSL and RL methods. Different contents of alkali metal Li co-additive were investigated regarding its effect on the structure and luminescence properties. The structures of the samples were specified using the XRD method. Cubic-$KMgF_3$ and tetragonal-MgF_2 phases were observed by XRD diffraction patterns and Rietveld analysis analyzes for all samples produced, and Eu, Yb doping and Li co-doping caused the formation of hexagonal-Li_2O_2 and cubic-MgO phases while reducing the MgF2 phase confirmed by x in KMgF3 dispersions. Also, the lattice parameters of $KMgF_3$ were evaluated as a=b=c=3.9907 and 3.9891 Å for the undoped sample. SEM images revealed better crystal formations with increasing Li concentration. FT-IR spectroscopy showed a reduction in Mg-F bands for all samples due to Eu, Yb doping and Li co-doping and Mg^{+2} ion substitutions. It was observed that the intensity of the TL peaks in the TL glow curves changed as the Li concentration changed, but the temperature of the peak maximums remained constant. The decaying time of OSL curves of $KMgF_3$:Eu,Yb,Li was slower with increasing Li concentration. The luminescence brightness reached its maximum with 15 mol% Li content. With the results obtained, it can be easily said that the investigated Eu and Yb doped and Li doped $KMgF_3$ exhibit promising luminescence properties and can be considered as suitable candidates for various technological applications including radiation dosimetry.

ACKNOWLEDGEMENTS

I am deeply grateful to my PhD supervisor Professor Zehra YEĞİNGİL for giving me the opportunity to pursue a PhD, for their incredible friendly support, guidance, encouragement and patience during my PhD. Her critical inputs have helped me constantly during my PhD, both in producing results and writing up this thesis. I could not have hoped for better support and would like to thank her for her incredible implication in this project.

I would like to thank The Scientific and Technological Research Council of Turkey (TUBITAK) for supporting me during the PhD under project number 2211-C. Also, I want to thank a lot the Council of Higher Education (YÖK) for the financial support under the 100/2000 YÖK PhD Scholarship project. I want to thank a lot to the Research Funding Projects Unit and its members at the Çukurova University for their support of this PhD thesis under the project numbers FDK-2018-10599. I am also grateful to all staff of the Institute of Natural and Applied Sciences for their valuable friendship and their support. I would like to thank North Atlantic Treaty Organization (NATO) in the frame of the NATO Science for Peace and Security (SPS) Program under the project number SfP 1984649 and SPS MYP G5647.

I would like to thank my co-workers Assoc. Prof. Dr. Adnan ÖZDEMIR and Res. Assist. Volkan ALTUNAL in TL/OSL Luminescence Dosimetry and Medical Physics Group for their incredible friendly support. My friends, who always keep their doors open to discussions and practical applications, have always supported me whenever I faced a problem and/or needed direction.

I would like to extend my sincerest thanks to Prof. Dr. Kasım KURT from Physics Department of Mersin University, Assoc. Prof. Dr. Ahmet EKICIBIL and Prof. Dr. Faruk KARADAĞ from Physics Department of Cukurova University, Assoc. Prof. Dr. Mustafa AKYOL from Department of Materials Science and Engineering of Alparslan Türkeş Science and Technology University, Assist. Prof. Dr. Doğan KAYA from the Department of Electronics and Automation of Cukurova University Vocational School of Adana for sparing time for me and helping to shape my thesis with their valuable comments and guidance.

I would like to thank Dr. Halil EŞGİN, Assoc. Prof. Dr. Selda KILIÇ ÇETİN and Res. Assist. Dr. Gönül AKÇA for their support and guidance at every stage of my thesis, especially during the material synthesis process and characterization analysis. I would like to thank the staff of Cukurova University Central Research Laboratory for their attention to analysis and their kind approach to me. I would also like to thank MSc. Tayfun ÇAVDAR from the Physics Department of Mersin University for his help in radioluminescence measurements, his patience, and his kind behavior towards me.

I would like to thank Professor Yaroslav ZHYDACHEVSKYY from the Institute of Physics of Polish Academy of Sciences, who opened the doors of his laboratory to me, both within the scope of the project work and the ERASMUS+ program. I am also grateful to the ERASMUS+ program and the Çukurova University Erasmus+ International Office for giving me this opportunity

Last but not least, I feel honored to express my feeling of indebtedness to my father Rayıf GÜÇKAN, my mother İnci GÜÇKAN, my brother Turan GÜÇKAN for their endless patience, financial and spiritual support at every stage of my life, and I would like to express my apologies for not spending as much time with them during the period of this study. Finally, I would like to thank my dear wife Tuğçe BOĞA GÜÇKAN for the patience she has shown me and for her kind behavior and support at every stage of this process, and I want her to know that I am grateful to her.

TABLE OF CONTENTS **PAGE**

LIST OF TABLES **PAGE**

LIST OF FIGURES **PAGE**

LIST OF ABREVIATIONS

TL : Thermoluminescence; TSL: Thermally stimulated luminescence
OSL : Optically stimulated luminescence
CW-OSL : Continuous-wave OSL
IRSL : Infrared stimulated OSL
LM-OSL : Linearly-modulated OSL
POSL : Pulsed-OSL
XRD : X-ray diffraction
SEM : Scanning electron microscope
FT-IR : Fourier-transform infrared
EDS : Energy dispersive spectroscopy
RL : Radioluminescence
PL : Photoluminescence
UV : Ultraviolet
VIS : Visible
IR : Infrared
SCS : Solution combustion synthesis
RTL : Residual TL
SSR : Solid state reaction
PM : Photomultiplier tube
β : Heating rate ($^{\circ}C.s^{-1}$ or $K.s^{-1}$)
τ : Lifetime (s)
T : Temperature ($^{\circ}C$)
I_0 : Initial density at time t=0
eV : Electron volt
LC : Luminescent centers
R : Recombination centers
E : Activation energy (eV)

E_f : Fermi energy level

b : Kinetic order

s : Frequency factor

Gy : Gray

k : Boltzmann constant, $k = 8.6173303(50) \times 10^5$ eV.K^{-1}

^{90}Sr : Strontium-90

^{90}Y : Yttrium-90

a.u. : Arbitrary unit

TLD : Thermoluminescence dosimeter

TLD-100 : LiF:Mg,Ti (magnesium and titanium doped lithium fluoride)

Φ : Optical stimulation density

σ : Photo-ionization cross section

E_0 : Stimulation threshold

λ : Wavelength

α : Absorption coefficient

I : Light intensity

p : Probability

FWHM : Full width at half maximum

T_m : The temperature corresponding to the peak temperature of the TL curve

FGT : Fraction glow technique

μ : Micro (10^{-6} m length unit)

MIR : Multiple initial rise method

MDD : Minimum detectable dose

VHR : Various heating rate

CGCD : Computerized glow curve deconvolution

1. INTRODUCTION

1.1. Definition of Luminescence

1.1.1. Electronic bands and traps

The electronic band structures defined by solid-state physics indicate the energy levels in which electrons can settle in solids, i.e., the energy range that electrons will have, and these intervals are defined as allowable bands or simply bands. Also, energy levels in which electrons cannot be found are called forbidden energy gaps, band gaps, or forbidden bands. This electrical behavior is largely related to the unique electronic band structure of each solid and varies (Calabrese et al., 1978). The very different electrical properties observed in different solids are due to differences in the band structure, and these energy levels they describe may differ or split into the continuum of levels called groups that are almost continuous. All of these are related to the width of the forbidden bandgap called the energy difference between the conduction and valence band.

The energies of the individual levels located very closely together appear like a continuous energy band. At the lowest level, the crystals of the inner electrons of the atoms have a fully filled band and are tightly bonded. They do not participate in the bond between the constituent atoms of this band layer. The outermost electrons of the atom, called valence electrons, establish chemical bonds and provide electrical conductivity. Electrons at higher energy levels than these interact in pairs to form localized bonds between the atoms of the solid. Electrons in single atoms or molecules that have been elevated to an excited state retain energy nearly equivalent to that of conduction band electrons. These electrons have very high freedom of movement in solids. In Figure 1.1, where the forbidden energy ranges are shown, graphical representative electronic bands of conductors, semiconductors, and insulators are given.

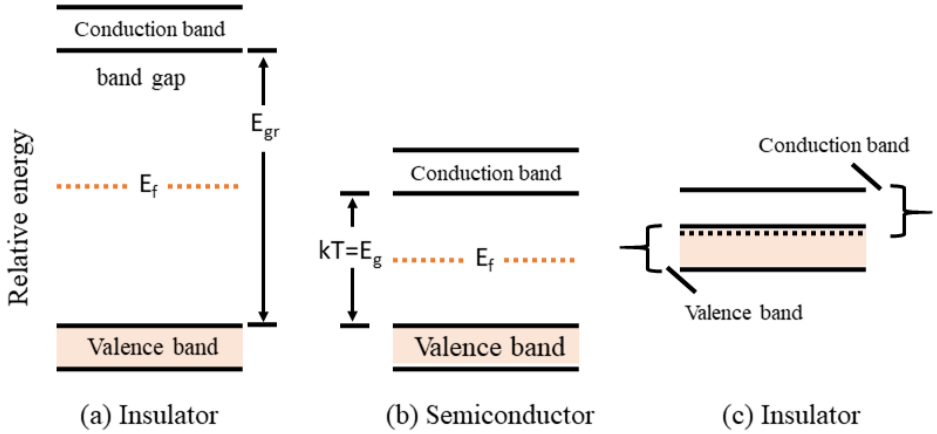

Figure 1.1. Representation of electronic bands in solids. Thermal excitation energy and Fermi energy are defined by kT and E_f, respectively (redrawn in http://www-opto.e-technik.uni-ulm.de/lehre/cs/).

In insulators where valence electrons are tightly bound to the nucleus, there are no free electrons, meaning the conduction bands are almost empty. However, the valence bands are full. The forbidden energy range for these materials can be up to 14-15 eV. However, if enough energy can be applied, they can become weak conductors because some of the electrons jump into the conduction band. Materials such as diamond and quartz are well-known insulators. Semiconductors have an electron loosely attached to the nucleus, and less energy is required to separate that electron from the nucleus. Their bandgap is usually up to 2 eV. On the other hand, there is no energy band gap in conductors where the valence band overlaps with the conduction band. Conductors have free or conductive electrons (even at room temperature). Since these electrons are free to move, they participate in conduction (Holcomb, 1967).

Crystals have some metastable energy levels localized in the forbidden energy range of the host material due to some impurities. This metastable state that exists at low excitation temperature (low energies) can have a very long lifetime. Their proximity to the conduction band causes an electron to be caught at these levels as it passes into the conduction band. Since electrons and holes are produced

in pairs, electrons are captured at one level and holes in the other. Usually, those close to the conduction band captured the electrons and the distant ones captured the holes because this depends on the energy of the trapped carriers and is related to defects in the forbidden space of the given crystal. The trapped electron needs extra energy to escape from the trapping centers. As a result, the hole trapping state is defined as luminescence centers and the electron trapping state as a trap.

With different excitation methods, different wavelengths of radiation can be observed in solids. Many types of luminescence and related stimulation methods and applications are summarized in Table 1.1 below by (Bos, 2006).

Table 1.1. Excitation methods of luminescence types and their efficiency in application fields (Bos, 2006).

Luminescence Types	**Excitation**	**Application Field**	**Efficiency**
Electroluminescence	Electric field	LEDs	0.1-50%
Photoluminescence	Optical photons (UV, VIS and IR lights)	Fluorescent lamp	20%
Chemiluminescence	Energy chemical	-	-
Cathodoluminescence	Electrons	Screens	10%
Black body radiation	Heat	Filament lamp	5%
Thermoluminescence	Ionizing radiation, Photon counts	Dating and Radiation dosimetry	0.01-1%
Radioluminescence	Ionizing radiation	-	-

1.1.2. Phosphorescence

Generally, phosphorescence lifetime is 10^{-8}-10^{-5} s and is slower than fluorescence (Chen et al., 1997). The temperature dependence of phosphorescence is given by Equation (1.1.

$$p = \left[s\,.\ \exp\left(-\frac{E}{kT}\right)\right] \tag{1.1}$$

The lifetime of a metastable energy level can take any value under any condition where the temperature "T" is relatively low and the activation energy "E" is high enough to slow the rate of thermal emission, p is the probability per unit time for thermal excitation. The value of "T" is storage time. The "s" is called the frequency factor and refers to the characteristic behavior of the trap that is proportional to the lattice vibration and the collision frequency of the electron. E is the energy difference between localized energy levels and trap depth (delocalized energy bands). k is the Boltzmann constant.

With its simplest and generalized definition, the luminescence intensity resulting from excited electrons in the ground state is expressed in the following Equation (1.2.

$$I(t) = I_0\,.\exp(-tp) \tag{1.2}$$

I_0 indicates the initial density at time $t = 0$. Under these conditions, the decay of phosphorescence is defined as a simple exponential time function at a constant temperature. In the case of $E >> kT$, the electron stays in a semi-steady state extends and can remain there indefinitely unless it receives excitation energy that can exceed the trap depth. If the stimulation is performed using heat, the resulting luminescence light is called Thermoluminescence (TL), if it is performed using light, it is called Optically Stimulated Luminescence (OSL).

1.1.3. History and overview of luminescence

Luminescence is called the emission of light above that expected for a black body, and all materials exhibiting this behavior are called phosphors. This emission is the release of energy stored in the solid, ie trapped electrons, by pre-

excitation of the solid electronic system. This can be induced by ultraviolet (UV), infrared (IR) or visible (VIS) light, or even ionizing radiation. It should be noted and emphasized that the emitted light has a longer wavelength than the incident radiation.

Each phosphor has a light-emitting at a different wavelength, and this is its characteristic behavior. This situation is given different names, taking into account the delay between excitation and light emission. The luminescence that occurs during excitation is called *Fluorescence*. If there is a delay of more than 10^{-8} s between excitation and light emission, this luminescence is called *Phosphorescence*. Figure 1.2 gives the different luminescence emissions in solids as a function of the delay between excitation and emission (McKeever, 1988). Moreover, Phosphorescence occurs in two parts as short period ($\leq 10^{-4}$ s) and long-period ($\geq 10^{-4}$ s) emissions. This process is called "thermoluminescence" or "optically stimulated luminescence" in minutes and longer periods. Short- and long-term luminescence can also differ between themselves as fluorescence is defined as a direct process in which absorption and emission occur only between a ground state and an excited state, but phosphorescence requires an extra transition state through an inter-system transition. As the return of phosphorescence to its ground state is prohibited, it occurs on a slow time scale. Figure 1.3 gives an example of a Jablonski diagram showing the different luminescence transitions within an anthracene molecule (Fox, 2002).

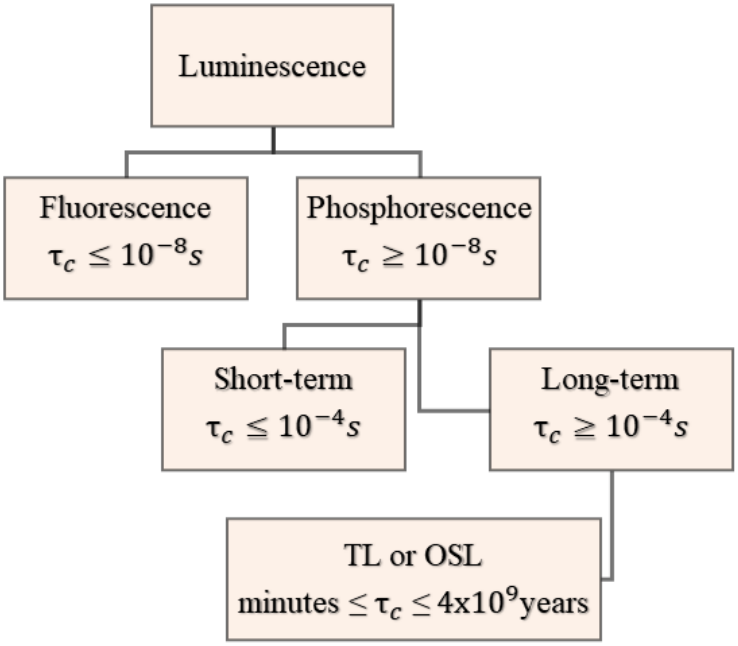

Figure 1.2. Luminescence phenomenon and related subtitles. The delay between excitation and emission "T" was defined for the luminescence subtitles. The prefixes indicate the mode of excitation (McKeever, 1988).

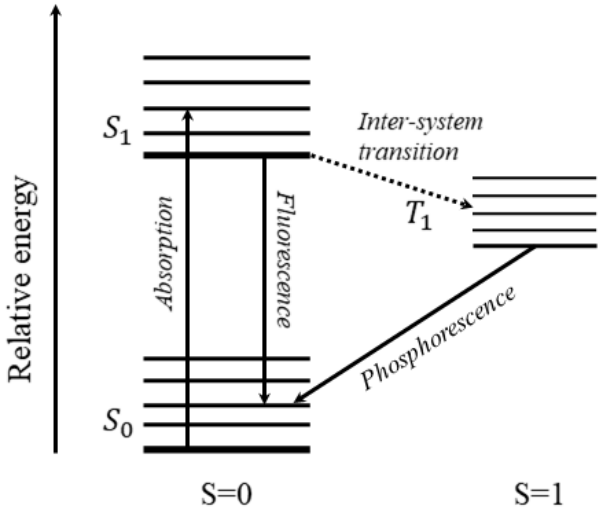

Figure 1.3. The representation of the Jablonski diagram for absorption, fluorescence, and phosphorescence emissions (Fox, 2002).

As can be seen in Figure 1.2, stimulated luminescence is accepted as a sub-state of phosphorescence thanks to the similarity of its mechanisms. In stimulated luminescence, electrons are excited from the valence band to the conduction band, from where they are trapped in the metastable states at different energy levels created by imperfections in the crystals. These energy levels arise due to impurities, lattice defects, dislocations, or other perturbations. Impurity atoms and larger complexes cause luminescence centers, while smaller perturbations generate electron trapping levels just below the conduction band (above the Fermi level). Electrons trapped at these levels remain there until external energy is delivered to the system by heating it (thermoluminescence) or by exposing it to light (optically stimulated luminescence). Electrons move within the conduction band with sufficient activation energy provided using thermally or optically stimulation and reach a recombination center containing a bonded hole where they emit light and can occur in the valence band or an intermediate state. Figure 1.4 shows the band diagram in which phosphorescence and fluorescence are explained.

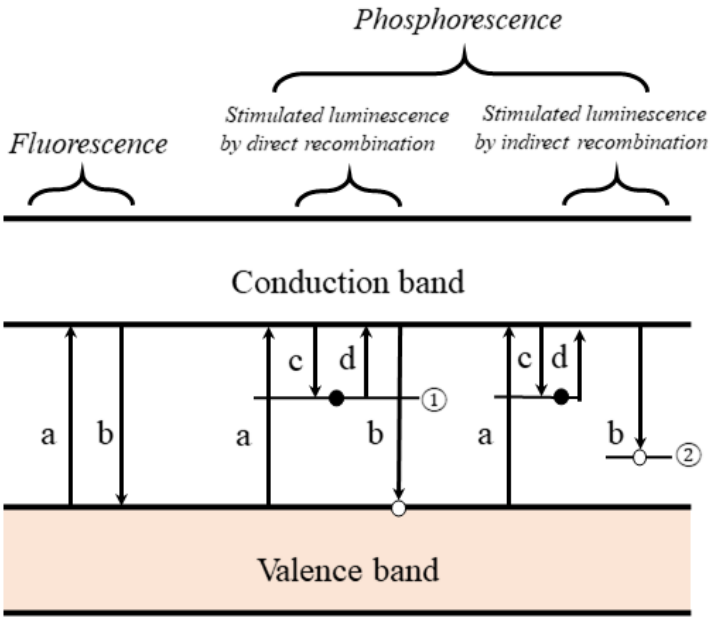

Figure 1.4. Schematic bandgap diagram for semiconductors or insulators with allowed transitions thanks to fluorescence and phosphorescence / stimulated luminescence emission. (1) Electron trap and (2) Recombination center indicated as lines. Luminescence occurs as a result of (a) Ionization, (b) recombination, (c) electron trapping, and (d) electron release, respectively.

1.2. Concepts and Basic Procedures of Thermo- and Optically- Stimulated Luminescence (TL and OSL)

For many years, several theories have been proposed regarding how luminescence occurs and its explanation, and these can be expressed in many equations that try to fit empirical data. Visualizing it may be the best way to better understand the luminescence process. In this process, the aforementioned lattice and lattice structural defects are associated with the presence of impurities. These are based on the fact that within the band gap there are no permitted energy levels in crystals. Multiple discrete energy states arise in the forbidden energy range due to structural defects. These energy levels are defined in Figure 1.5: If the case (I) for electrons is greater than the case (II), they are expressed as the trap (T). In the

opposite case, energy levels are described as recombination centers (R) where recombination takes place. If the recombination process is radiative in recombination centers where radiative or non-radiative transitions take place, luminescence occurs in the recombination centers. These are defined as luminescent centers (LC). Conversely, a decrease in luminescence intensity is observed since no luminescence can be observed during non-radiative recombination.

If the amount of energy absorbed by the valence electrons is greater than the forbidden energy range, the electrons are excited into the conduction band (case I). Electrons are known to move freely in the crystal here. As free-moving electrons move, they can transfer their excess energy to lattice vibrations and distribute them without radiation. If the crystal structure contains radiative recombination centers, the recombination centers can capture electrons and emit their excess energy as light. Possible transitions for all cases are given in Figure 1.5. The transition (I) is described as “band to band direct transition” for electrons and holes. “Band to trap transition” and “trap to band transition” are illustrated as a transition (II) and (III), respectively. Band to recombination center transition is presented in the case of (IV). The transition of the recombination center to the band is defined as (V) and the transition of the conduction band to the recombination center as (VI). Finally, the transition of holes from the valence band to the recombination center is specified as (VII).

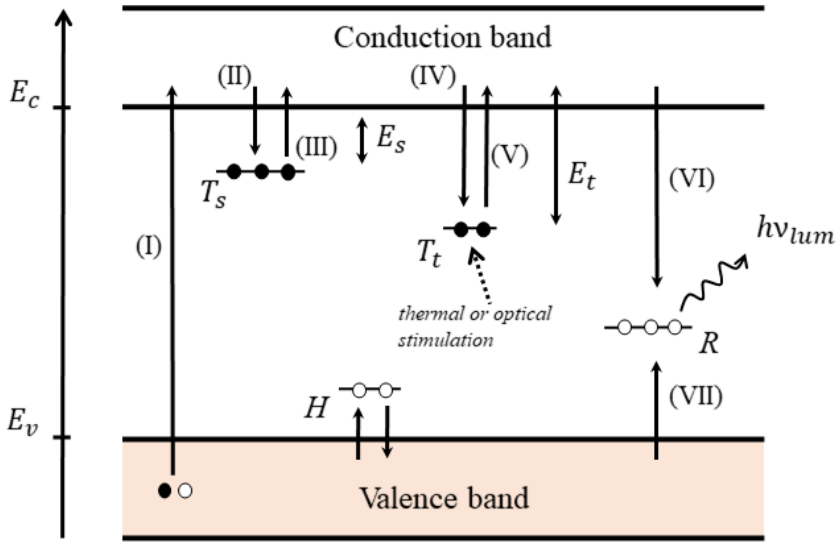

Figure 1.5. Basic schematic view of the irradiation process with possible electronic transitions in semiconductors or insulators. Possible transitions are indicated by arrows.

1.2.1. Thermoluminescence

During the TL readout, the emitted photons are recorded by the photomultiplier tube and a bandpass filter in front of it as the temperature rises to a predetermined maximum temperature with a certain rate of heating rate (optional, °C per second). Photons recorded as a result of luminescent light are plotted as a function of temperature across a temperature range. This graph, called the TL glow curve, reveals an indirect visual representation of traps that gradually run out as temperature increases. The TL glow curve including the TL peaks at different temperature values is given in Figure 1.6.

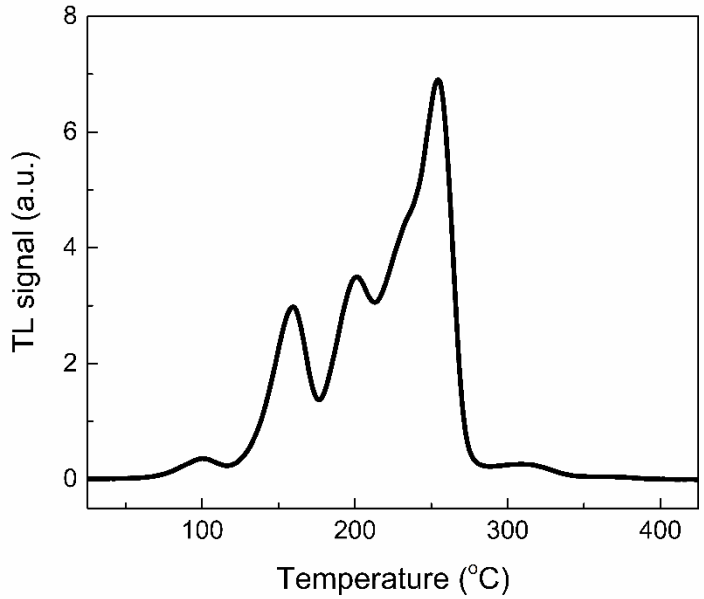

Figure 1.6. TL glow curve of LiF:Mg,Ti (TLD-100) chip as a function of temperature following 1 Gy beta dose exposure. TL signals were recorded using Schott BG-39 detection filter at 5 $^{o}Cs^{-1}$ heating rate.

Randall and Wilkins (1945) suggested that the rate of thermal excitation of electrons transferred from the trap to the conduction band, represented by the "d" transition in Figure 1.4, can be mathematically explained by the following Equation (1.3.

$$-\frac{dn}{dt} = np = ns\ exp\left(-\frac{E}{kT}\right) \tag{1.3}$$

where n is the concentration of filled electron traps per cm^3, p is the probability per unit time during excitation, s is the frequency factor per second. Activation energy is given with $E\ (eV)$. k_B is the Boltzmann constant. T is the temperature. The trap loses charge when the thermal stimulation is exposed and this is given by the negative sign of Equation (1.3 (Randall et al., 1945).

Luminescence intensity is proportional to the decay rate, considering that there is no re-trapping to the same energy level (Chen and McKeever, 1997) and therefore;

$$I(t) = -\eta \frac{dn}{dt} = \eta n p = \alpha n \tag{1.4}$$

where I is the luminescence intensity, η a constant, and $\alpha = \eta p$.

1.2.2. Optically Stimulated Luminescence

When it uses optical stimulation instead of heat to release trapped charges, the probability p of excitation for optical stimulation is written as follows (Bøtter-Jensen et al., 2003).

$$p(E_0) = \Phi \sigma(E_0) \tag{1.5}$$

where optical simulation density and photo-ionization cross-section are given as Φ and σ respectively. E_0 is defined as the stimulation energy threshold that will enable a charge to gain energy and move, i.e., release it. The absorption of light by the material is given by Beer-Lambert law as follows:

$$I(\lambda, x) = I_0(\lambda) \exp(-\alpha(\lambda) x) \tag{1.6}$$

where λ is the wavelength, $\alpha(\lambda)$ the absorption coefficient as a function of wavelength and $I(\lambda, x)$ is the light intensity as a function of depth x.
In this manner, the emitted luminescence intensity from irradiated material during the stimulation will be similar to TL and can be written as follows:

$$I(t) = -\eta \frac{dn}{dt} = \eta n \Phi \sigma(E_0) = \eta n p \tag{1.7}$$

The main difference between TL and OSL is known as the expression of stimulation probability p, and an Arrhenius law defines the probability of electron escape from the traps with Equation (1.8 and (1.9 for thermal stimulation (TL) and optical simulation (OSL), respectively.

$$p(t) = s \exp\left(-\frac{E}{kT}\right), (under\ thermal\ stimulation) \quad (1.8)$$

$$p(t) = Ct, (under\ optical\ stimulation) \quad (1.9)$$

where C is the decay constant.

A bandpass optical filter is placed between the photomultiplier tube (detection unit) and the sample in order to distinguish it from blackbody radiation caused by excessive heat in the case of TL or from the stimulation light used to stimulate the sample in the case of OSL. Two wavelengths are generally used in commercial OSL readers as blue LEDs (470 nm) or infrared diodes (850 nm) (Yukihara et al., 2011). The method using infrared stimulation is called Infrared-stimulated luminescence (IRSL). There are three different methods of application of Optically Stimulated Luminescence (OSL), such as Continuous-wave OSL (CW-OSL) where the stimulation light intensity is kept constant, Linearly-modulated OSL (LM-OSL) where the stimulation light intensity is increased linearly, and Pulsed-OSL (POSL) in which the OSL signal is recorded by short optical pulses.

1.2.2.1. Continuous-wave OSL (CW-OSL)

In this method, stimulation light intensity and wavelength keep constant throughout the measurement (Akselrod et al., 2006; Bøtter-Jensen et al., 2003; Yukihara and McKeever, 2011). Separation of stimulation and emission light is provided using the appropriate combination of optical excitation and bandpass

detection filters. Thus, OSL traps with specific energies can be searched and emission can be observed in a certain wavelength range in this stimulation mode. The stimulation for CW-OSL as a function of time and the typical decay curve at the end of CW-OSL are illustrated in Figure 1.7a and Figure 1.7b, respectively.

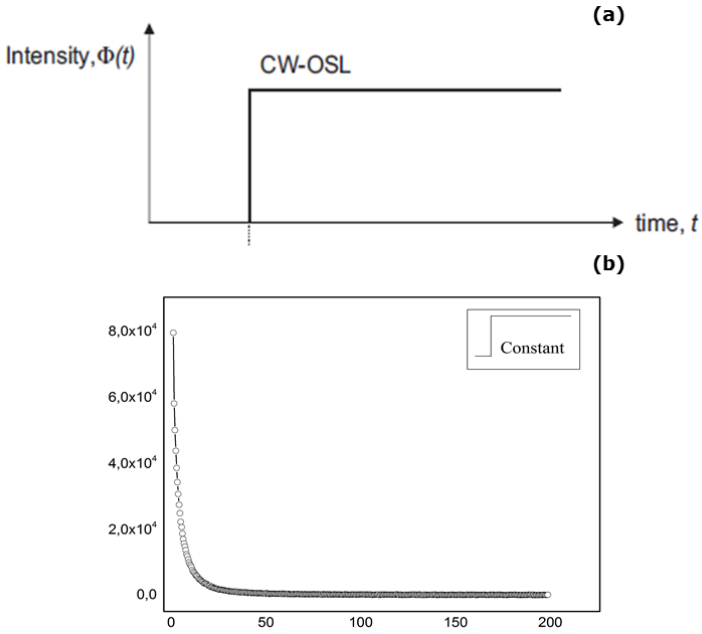

Figure 1.7. (a) OSL intensity was obtained using CW-OSL stimulation as a function of time and (b) A typical decay curve of the OSL signal when the CW-OSL stimulation method was used (Bøtter-Jensen et al., 2003).

1.2.2.2. Linear-modulated OSL (LM-OSL)

In this method, stimulation light intensity is increased linearly to observe the OSL signal and followed by a decrease due to depletion (Bulur, 1996). Consequently, the OSL signal is seen as a series of peaks that indicate the optical release of charge from different trap types. The stimulation as a function of time and the resulting typical decay curve of the LM-OSL are illustrated in Figure 1.8a. and Figure 1.8b, respectively.

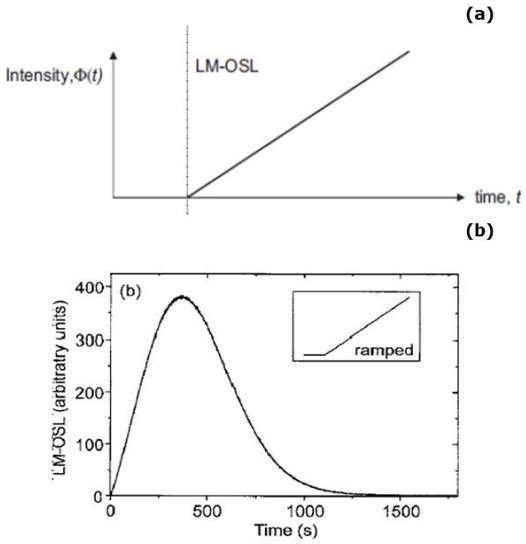

Figure 1.8. (a) OSL intensity obtained using LM-OSL stimulation as a function of time and (b) A typical OSL signal when the LM-OSL stimulation method was used (Bøtter-Jensen et al., 2003).

1.2.2.3. Pulsed OSL (POSL)

Pulsed OSL (POSL), another modification of the OSL technique, has a stimulation source that can make short pulses, and the OSL signal is obtained only after each short pulse. Because less optical filtering is required, emission light can be observed over a wider wavelength range. With this technique, recombination centers with different lifetimes can be distinguished. Moreover, the short excitation pulses delivered to the sample offer the possibility of fast OSL measurement in very short periods, and multiple readings of a sample are also possible, as the signal is not consumed in a single reading (Akselrod et al., 2006; Bøtter-Jensen et al., 2003; Yukihara and McKeever, 2011). Figure 1.9a. and Figure 1.9b. presents the OSL stimulation mode of POSL and a typical POSL signal, respectively.

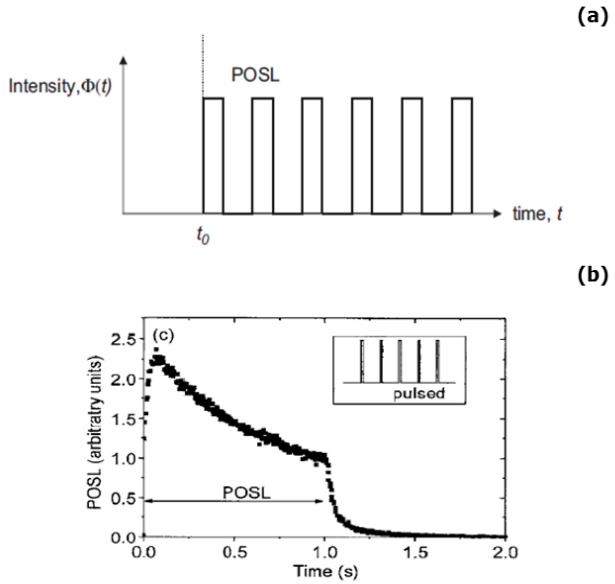

Figure 1.9. (a) OSL intensity obtained using POSL stimulation as a function of time and (b) a typical decay curve of the OSL signal when the POSL stimulation method used (Bøtter-Jensen et al., 2003).

2. LITERATURE REVIEW

Radiation emitted from natural and anthropogenic sources can be used in the treatment of diseases such as cancer where small doses of radiation may cause some harm. Human response to radiation from different sources causes intense discussions with great scientific uncertainty. Many factors play a role in determining the effects of radiation exposure such as the ability of radiation to damage and the amount of energy transferred to the tissue. For all these reasons, there is a need to measure the radiation from very small doses caused by natural radiation in the environment to very high doses at accident moments such as radiation leakage in isotopic laboratories. Thermoluminescence dosimetry is known as one of the most important techniques used to measure the absorbed dose in addition to other techniques based on solid-state dosimetry. There are many oxides, fluoride, and sulfate-based phosphors in the form of TLD badges used for different radiation monitoring applications. However, due to the not all of these dosimeters are suitable for all low or high radiation zones, all researchers in the world working in this field are struggling to discover efficient TLD materials on a wide variety of radiation doses or to improve the existing one.

The Thermoluminescence (TL) phenomenon usually termed Thermally Stimulated Luminescence (TSL) was first described in the 1950s (Daniels et al., 1953). They presented Lithium Fluoride (LiF) as a thermoluminescence phosphor. Following the commercial availability of reliable and highly sensitive photomultiplier (PM) tubes, this TL material was patented as TLD-100 (Harshaw Chemical Company) to measure nuclear radiation doses. TL was then applied in archaeological dating in the early 1960s (Aitken et al., 1964; Aitken et al., 1968; Mejdahl, 1969) and in the field of geological dating in the early 1980s (Wintle et al., 1980). Thermoluminescence dating is reviewed in detail by Aitken (Aitken, 1985b). Since the 1950s, many new dosimetric phosphors that provide different efficiency according to different radiation types and dose ranges have been

presented in the areas of personal (Gai et al., 2015), accidental (Veronese et al., 2010), medical (Efstathopoulos et al., 2003; Kron, 1999), retrospective (Kazakis et al., 2016; Mesterházy et al., 2012), thermal neutron dosimetry (Bhadane et al., 2016), solid-state lighting (Dalal et al., 2016; Naik et al., 2016) and 2D optical stimulated luminescence (OSL) mapping (Oliveira et al., 2016). The most widely used commercial dosimeters that are seen as standard in radiation dosimetry are LiF:Mg,Ti (TLD-100) as health and medical dosimeter, CaF_2:Dy (TLD-200) as an environmental dosimeter, CaF_2:Tm (TLD-300) as fast neutron dosimeter, CaF_2:Mn (TLD-400) as high dose dosimeter, Al_2O_3 (TLD- 500) as an environmental dosimeter, ^{6}LiF:Mg,Ti (TLD-600) as neutron dosimeter, ^{7}LiF:Mg,Ti (TLD-700) as gamma dosimeter, ^{7}LiF:Mg,Cu, P (TLD - 700H) as environmental dosimeter, $Li_2B_4O_7$:Mn (TLD-800) as neutron and high dose dosimeter and $CaSO_4$:Dy (TLD - 900) as an environmental dosimeter.

The application of OSL was first reported by Huntley et al. (1985), who used green light from an argon laser (514 nm) to induce luminescence from quartz in obtaining age determination of deposits for dating purposes (Huntley et al., 1985). The use of this technique as a tool for dating and dosimeter field has led to further study/investigation of the OSL properties of quartz (Aitken et al., 1988; Godfrey-Smith et al., 1988; Smith et al., 1990). In the same years, it was first reported by Hütt et al. that Infrared light can be used for the stimulation of luminescence in feldspars (Hütt et al., 1988). Stimulation units built by some researchers consisting of small IR light-emitting diodes (LEDs) (Bailiff et al., 1989; Bøtter-Jensen et al., 1991; Spooner et al., 1990), as well as broadband emitters such as incandescent or arc lamps, were used with appropriate filters to produce both infrared and visible-light-induced luminescence from feldspar and quartz samples (Bøtter-Jensen et al., 1992; Hutt, 1989; Pierson et al., 1994; Spooner et al., 1989). Similar luminescence techniques used in dating in the last few decades have filled a very important gap in retrospective dose assessment, for example, to reconstruct radiation doses received by the general population after

nuclear accidents, and have been adopted as a guide for humanity in this field. In the simplest terms, radiation doses can be determined using radiation measurements performed on various samples, such as quartz and feldspar, extracted from bricks, tiles or porcelain items collected from areas of radiation leakage/accident such as Hiroshima and Chernobyl (Bailiff, 1995; Bøtter-Jensen et al., 1996; Haskell, 1993a) (Bailiff, 1995; Bøtter-Jensen et al., 1996; Haskell, 1993a, 1993b).

This thesis, which includes studies on many materials, it is aimed to develop novel dosimeters with superior features. Various oxide-based structures or fluoroperovskite-based structures were selected as hosts and produced by doping various ions to develop radiation dosimetry, characterization and morphology studies, structural analyzes and dosimetric characterization analyzes were performed. The selection of suitable hosts for radiation dosimetry is very important. Both the structural and dosimetric properties of the hosts discussed in this thesis have been tested by many researchers for their suitability for radiation dosimetry and presented to the literature. The studies carried out with these hosts so far are given below.

2.1. Overview of Magnesium Oxide (MgO)

Polycrystalline MgO powder was studied to investigate its dosimetric features using TL, IRSL and OSL techniques. MgO, an insulator in a cubic structure, is a very attractive material in many different applications, such as paint (Bhargava et al., 1998), toxic waste remediation (Jeevanandam et al., 2002; Kakkar et al., 2004), an additive in heavy fuel oil (Davini et al., 1985), bactericides (Huang et al., 2005; Sawai et al., 2000), crucibles and refractory materials (Faghihi-Sani et al., 2002; Green, 1983), removing fluoride from drinking water (Copp, 1995; Maliyekkal et al., 2010) and insulators in industrial cables. This oxide material has also been doped with transition metals to study the defect formation for their function in optical and electrical properties (Dunphy et al., 1990; Hirsch et al.,

1991; Timmer et al., 1991). The MgO phosphors as a TL dosimeter was first proposed by Thomas and Houston in 1964 (Thomas et al., 1964). Las and Stoebe presented a review study for the lattice defect structure and TL mechanism of the MgO in 1984 (Las et al., 1984). This interest in MgO is due to its potential as a UV dosimeter (Kortov et al., 1993) and use in neutron dosimetry (Dolgov et al., 2002). In these applications, Al, Fe, Ti, Cr, Mn, Ni and V transition metals were used as dopants and they played important roles in the luminescence mechanisms. In contrast to the extensive utility of MgO in the industry, it was not widely used for dosimetric applications due to its inconsistent TL properties, and radiation and thermal treatment histories (McKeever et al., 1995).

MgO has been suggested as a promising dosimetric material by researchers because of its superior OSL properties in the literature (Gugliotti et al., 2018; Oliveira et al., 2013a; Oliveira et al., 2019). In recent years, the reason for attention on MgO as a radiation dosimeter is the research of the Tb^{3+} doped MgO (MgO:Tb) by Bos et al. (Bos et al., 2006). They showed that it is possible to synthesize MgO phosphorus with Tb^{3+} dopant creating new luminescence centers. Then, it was understood that this material has encouraging properties for applications in personal and medical dosimetry. The OSL intensity of the MgO was noted by the authors as potentially comparable to commercial Al_2O_3:C. But they reported that 43% of the OSL signal was faded during the first 36 h storage. However, they also emphasized that most of the Tb^{3+} emissions (380-650 nm) are blocked by the optical filters required for OSL measurements. Therefore, the authors noted that the Tb^{3+} additive is not an ideal dopant for OSL emission when stimulation is used in the VIS region (Bos et al., 2006). Sathyamoorthy and Luthra reported the TL emission spectra of MgO doped with transition metals (Mn, Cr, Ni, Fe, Co, Cu) (Sathyamoorthy et al., 1978). They showed that the new emission bands can be created with only Mn^{2+} (600 nm) and Ni^{2+} (490 nm). In addition, there are several luminescence studies of MgO doped with rare earth elements, such as Dy , Eu , Ce (Bapat et al., 1985a; Bapat et al., 1985b), Tb , Sm, Tm and Yb (Oliveira et al.,

2019). Some authors stated that undoped MgO is an excellent electrical insulator with the $<10^{-20}$ $(\Omega\ cm)^{-1}$ electrical conductivity, however, when Li-ion is doped, the conductivity in MgO crystals increases as a result of the formation of hole-trapped centers of the system after oxidation at high temperatures (Chen et al., 1980; Tardío et al., 2002). This can be attributed to an increase in TL signal, as it can be seen in some recent studies in the literature (Oliveira et al., 2013a; Oliveira et al., 2013b; Oliveira et al., 2016). They also stated that the oxidation at temperatures higher than ~800 °C produced a wide optical absorption band centered at ~700 nm due to the Li centers in MgO crystals.

There are many studies related to photoluminescence features of the MgO doped with lanthanides and alkali metal Li-ions representing that lanthanides create charge compensation effects due to the substitution of Mg^{+2} and Li^{+1} within the MgO crystal structure (Bapat and Sivaraman, 1985a; Gu et al., 2008). According to Dolgov et al., isoelectronic impurities were present when MgO was doped with Be, Ca, and Sr (Dolgov et al., 2004). Lacis et al. suggested that the luminescence signal in MgO occurs when the holes recombine with the trapped electrons via Be ions (Lacis et al., 1979). Mn and Ni dopants have shown emission bands at 600 and 490 nm respectively whereas the pure MgO has shown emission bands at 400 and 750 nm. Also, MgO doped with Cr ion showed a single emission at 700 nm (Sathyamoorthy and Luthra, 1978). Pure MgO crystal has $<10^{-20}$ $(\Omega cm)^{-1}$ electrical conductivity, making it an excellent electrical insulator (Chen et al., 1980; Tardıo et al., 2002). After oxidation at high temperatures with Li-ion dopant, it is known that the conductivity increases as a result of the formation of hole-trap centers in MgO crystal. It is emphasized that the reason for the increase in the TL signal of MgO is related to this situation. Researchers also determined that the oxidation process higher than 800 °C for the MgO crystal cultured a dominant and large emission band located at ~700 nm related to Li centers. Therefore, the importance of the production technique is understood for the creation of luminescent centers.

Recently, based on all of the mentioned results above, the research groups presented a systematic investigation of MgO ceramic samples doped with lanthanides, metals, or their binary systems to develop new materials for TL or OSL dosimetry (Kawano et al., 2017a; Oliveira et al., 2013a; Oliveira et al., 2013b; Orante-Barrón et al., 2011; Yukihara et al., 2013a). Oliveira et al. investigated the undoped and doped MgO with different concentrations of Li and Gd singly- and binary, as TL and OSL dosimeters. It was stated that the Li co-doping to MgO shows several orders of magnitude higher OSL signal than pure and single Gd doping. The authors also stated that the fading of the OSL signal could be reduced by the elimination of shallow traps. If not applied, they emphasized that the OSL signal would show fading between 20% and 30% during the 1 week storage period, since shallow trapping centers would discharge at room temperature (Oliveira et al., 2013a). Kawano et al. reported that the MgO has a strong OSL emission (λ_{ex}: 590 nm) originating from Tb^{3+} at about 385-550 nm after X-ray exposure. In addition, the TL and OSL dose-response behaviors of Tb doped MgO were linear from 0.1 to 1000 mGy (Kawano et al., 2017a). In another study by Oliveira et al., in which almost all lanthanides were added to MgO and their emissions were examined. MgO was extensively examined both as TL and OSL dosimeters and it was reported that Li-ion increased the RL, TL, and OSL intensity in MgO when used together with lanthanides as co-dopants (Oliveira et al., 2019).

This study presents the dosimetric properties of newly developed Na and Li doped MgO (MgO:Na,Li); Cu, Li and K doped MgO (MgO:Cu,Li,K); Tb, Gd and Li doped MgO (MgO:Tb,Gd,Li); and Ce and Li doped MgO (MgO:Ce,Li) phosphors as both TL and OSL dosimeters and their kinetic parameters. All MgO samples studied were newly produced in the laboratory by solution combustion synthesis (SCS) method or solid-state reaction (SSR) method. Their phases composition, structural characterization and morphology were characterized using XRD, SEM-EDS, and FT-IR techniques. The emission spectra of the doped MgO

samples were recorded using the radioluminescence (RL) technique. TL and Continuous-wave Optically Stimulated Luminescence (CW-OSL) technique stimulated with infrared (IRSL) or blue-light (OSL) were used to examine the dosimetric properties. The correlation between TL and OSL or IRSL traps was studied using Residual TL (RTL). The effects of dopant concentrations on the OSL intensities and shape of the TL glow curves and intensities were studied. To investigate the employment within the field of radiation dosimetry, dosimetric properties i.e., the annealing process, determination of the luminescence centers, reusability, dose-response, multi-readability, and short and long-term fading, and kinetic parameters i.e., the activation energies of the peaks, E_a, frequency factors, s, and order of kinetics, b of doped MgO phosphors were carried out. These parameters related to the determined TL peaks were evaluated via different techniques and compared with each other. The commercial TL and OSL dosimeters LiF:Mg,Ti chip (TLD-100, ThermoFisher Scientific Inc., USA) and Al_2O_3:C disc (TLD-500, Harshaw Saint Gobain, Cleveland-USA) were used for comparison with the same results.

2.2. Overview of Zinc Oxide (ZnO)

ZnO is a very important semiconductor with a wide band gap of 3.3 eV at room temperature (300 K) and a large exciton binding energy of ~60 meV, and these properties make it a material with high potential for use in technological applications (Berrezoug et al., 2015; Özgür et al., 2005; Silva et al., 2016). Therefore, it has received much attention in the past years, and the chemical and physical nature of ZnO has made it one of the most important inorganic functional materials for the electronics industry. In particular, its wide bandgap, high transparency, piezoelectricity, room-temperature ferromagnetism, enormous magneto-optical and chemical sensor properties make it a very useful and interesting semiconductor (Berrezoug et al., 2015; Nakate et al., 2016; Silva et al., 2016; Tereshchenko et al., 2016). It is known from the literature that well defined

structures and sizes of ZnO as new advanced material are important in material science for the behavior of the matter at smaller length scales. The fascinating electronic, optical, and magnetic properties of ZnO ranging from micro to nanoscale, along with chemical reactivity derived from small size effect, have contributed widely to various fields of applications, especially for optoelectronics, catalysis, chemical sensing, separations, medical diagnostics and dosimetry. The size reduction to the nanometer level leads to quantization of density of states, which alters the intrinsic properties of crystal materials (Wu et al., 2011). The key properties of ZnO depend on such intrinsic factors as structure and composition and also on its defect chemistry. Thus, understanding the structure and controlling the defect location in ZnO nano/micro-scaled crystals are a challenge and a realistic goal to tune the functional properties, including its dosimetric characteristics. ZnO has been also widely used in many applications, such as disinfectant (antimicrobial) materials for the prevention of increasing microorganisms in buildings (Dyshlyuk et al., 2020), absorber materials for thin film solar cells (Hu et al., 2019; Sengar et al., 2018), plasmons in thin-films in the wide spectral range etc. (Garg et al., 2018).

ZnO has potential as a dosimetric material (Kołodziejczak-Radzimska et al., 2014) and exhibits applications in luminescent materials. Its effective atomic number is Z_{eff} = ~27.7 (Avilés-Monreal et al., 2018; Borbón-Nuñez et al., 2014). Studies of TL and OSL of undoped ZnO (Cruz-Vázquez et al., 2005; Reddy et al., 2015; Secu et al., 2009) and doped ZnO (Tb, Mg, Ce) (Husain et al., 2014; Mazhdi et al., 2013; Pal et al., 2013a; Panda et al., 2013; Pushpa et al., 2016; Reddy et al., 2012) in micro and nanoscale can be found in the literature. It has been concerned as a dosimetric material at high doses. Unlike most of the TL phosphors, it exhibits dose linearity in dose response over high level of radiation doses under different kinds of exposures (up to 10 kGy) (Borbón-Nuñez et al., 2014; Cruz-Vázquez et al., 2005; Pushpa et al., 2017a; Pushpa et al., 2016; Reddy et al., 2011; Reddy et al., 2014; Soares et al., 2017a).

It is known that the luminescence curve shapes and their peak intensities obtained as the radiation response depends on the production method, the thermal processes (calcination or sintering) during synthesis, types of dopant ions, or types of ionizing radiation (beta particles, gamma rays etc.) to which the samples exposed. The defects and vacancies which play an important role in luminescence properties depend on these parameters. The TL and OSL responses of micro/nanoscaled ZnO, as well as the bulk ZnO, are highly dependent on the calcination and sintering conditions they affect the compositions and structures of the materials. Although ZnO-related studies on this subject do not appear quite frequently in the literature, several examples can be found. The effects of continuous and pulsed mode sonification on the TL glow curve were presented by Sahu et al. and they compared the results. The TL glow curve peaks of ZnO phosphors were found at 118, 164, 210, 266 and 326 °C for pulsed mode and 126, 166, 230, and 288 °C for continuous mode preparations. The thermal annealing during the preparation of ZnO samples was used by Cruz-Vázquez et al. (2005) and they obtained a broad TL glow curve nearly between 50 to 350 °C (Cruz-Vázquez et al., 2005). Some researchers studied the effects of both annealing temperature and pH impact on morphology, structures and photoluminescence of ZnO nanoparticles (Uthirakumar et al., 2009a). They claimed that the crystal quality of ZnO samples was significantly evolved with the increasing of annealing temperature. Remarkably lower full width at half maximum (FWHM) value was determined for annealing of 300 °C when compared to that of the samples annealed at lower temperatures.

A lot of PL studies about ZnO show that the photo-generated hole with an electron occupying the oxygen vacancy is responsible for the luminescence in green emission band at about ~520 nm (Pal et al., 2013c; Peng et al., 2010; Qiu et al., 2007; Raoufi, 2013; Sahu et al., 2010; Shinde et al., 2014a; Taunk et al., 2015). Uthirakumar et al. (2009), who studied the PL spectrum of ZnO samples annealed at different temperatures, observed that ZnO samples have a strong UV band

emission. Also, they observed the deep level emission but it was negligible in intensity. As the annealing temperature increased, they could hardly observe any UV-band-emission but observed a good predominant deep level emission. Therefore, they showed that the density of the deep level band is increased while the intensity of the UV band-edge emission is completely suppressed as the annealing temperature increases (Uthirakumar and Hong, 2009a).

An overview of some recent ZnO studies summarized that there are numerous methods for synthesis of ZnO micro/nanoparticles, such as; solution combustion (Ahmed et al., 2012; Orante-Barrón et al., 2015), precipitation (Atuchin et al., 2011; Chen et al., 2008; He et al., 2013; Soares et al., 2017a), sputtering (Kang et al., 2013), sol-gel methods (Ashraf et al., 2015; Hasnidawani et al., 2016; Ton-That et al., 2012) and solid-state precipitation (Atuchin et al., 2011). These methods need to be operated under strict conditions like stabilization of ambient conditions and impurity control. The objective of this study is the analysis of the TL, OSL and PL emissions of ZnO:Eu in the form of pellets synthesized via sol-gel and precipitation methods. The samples evaluated in this study were first calcined at 800, 900, 1000, 1100 and 1200 °C for 4h and then calcined for 2, 4, 6, 8, 10 and 24 h at the constant temperatures of 800 and 900 °C for the sol-gel and precipitation methods, respectively. The effects of calcination on structural and luminescence properties, such as TL, OSL and PL emissions, were investigated. To determine the dose-response characteristics for both methods we investigated the dose response behaviors of the TL curves of samples.

2.3. Overview of Parascandolaite ($KMgF_3$ - perovskite-type fluoride)

Researchers' efforts have shown that fluoroperovskites are potential phosphors highly sensitive to TL/OSL (Dotzler et al., 2007; Ramirez-Romero et al., 2018; Reddy et al., 2017; Schuyt et al., 2019). These crystals with a large bandgap energy (>5 eV) are suitable structures for investigating the optical properties of rare-earth (RE) metal impurity ions. Besides their low hygroscopicity,

they have high thermal and mechanical strength. With all these structural and physical properties, fluoroperovskites doped with RE elements are known to be efficient luminescent materials and are used in many applications including bio-imaging. Recently, their use with various activators ($LiBaF_3$:Ce, $RbMgF_3$:Mn, $NaMgF_3$:Pr, and $KMgF_3$:Eu) has attracted all the attention in terms of their possible use in radiation dosimetry (Gektin, 2000; Gektin et al., 1998; Kitis et al., 1999b; Pathak et al., 2020).

$KMgF_3$-based phosphors especially doped with RE elements and various other activators exhibit a variety of luminescence phenomena (Kück et al., 2006; Sokólska et al., 2001). $KMgF_3$ can be found in nature as Parascandolaite and it provides a cubic structure with a space group of $Pm\bar{3}m$ (Riley et al., 1970). $KMgF_3$ belongs to the fluoroperovskite family and has a crystal structure in which the monovalent K^+ ion is at the center of an F_6 octahedron and the Mg^{2+} divalent ion is located at the corners of a cube with a 12-fold peripheral region (Wood et al., 2002). $KMgF_3$ exhibits unique physical properties, such as high melting point and moderately effective atomic number (Z_{eff} = ~12.8) (Furetta et al., 2001). $KMgF_3$ was reported as a TL dosimeter (Furetta et al., 2001; Gektin et al., 1997; Kitis et al., 1999b; Marcazzó et al., 2010) due to its high sensitivity, stable traps responsible for TL peaks at high temperatures (Gektin et al., 1995), and consequently low fading (Furetta et al., 2001). Therefore, $KMgF_3$ has been extensively studied with many dopants and their combinations (Bacci et al., 1993; Furetta et al., 1994; Kitis et al., 1999a). Particularly, Eu- and Yb-doped $KMgF_3$ is much more efficient compared to commercial TL dosimeters. OSL was observed in $KMgF_3$ activated by several RE elements and their combinations. Among these, the OSL properties of Ce-doped $KMgF_3$ were potentially comparable to Al_2O_3:C (JM Le Masson et al., 2002). Camargo et al. (Camargo Jimenez et al., 2018) studied the effect of $KMgF_3$:Tm for a new OSL dosimeter. But their comparative study showed that the $KMgF_3$:Tm is less sensitive than Al_2O_3:C. Le Masson et al. also reported that the $KMgF_3$:Ce, which they prepared with the Czochralski method,

provided higher OSL intensity than Al_2O_3:C (JM Le Masson et al., 2002). The relation between TL and OSL traps in $KMgF_3$:Ce was also studied by Dallas et al (Dallas et al., 2010) and they presented that the bleaching of each individual glow-peak takes place in three different rates as a fast, medium, and slow rate. Recently, Daniel et al. investigated the OSL properties of the Eu- and Ce-single and co-doped $KMgF_3$ system (Daniel et al., 2016). They showed by thermal bleaching experiments that the OSL signals originate from traps that are stable around 200 °C. This result proves the suitability of the signals for dosimetric purposes. There are currently few studies on OSL properties of perovskites, and an in-depth understanding of the luminescence mechanism requires an examination of the relation between electron traps and recombination centers that contribute to OSL and TL signals.

Recent reports on the alkali metal ions, such as Na^+, Li^+, and K^+, have proven their action in different hosts, as co-activators and charge compensators (Balakrishnaiah et al., 2011; Dhananjaya et al., 2012; Joseph et al., 2009; Li et al., 2010; Lorbeer et al., 2014). These studies showed that the luminescence intensities of the phosphors were greatly increased with Li^+ co-doping which resulted in the upconversion emission in different hosts (Bae et al., 2005; Guckan et al., 2021b; Joseph et al., 2009). This result indicates that the improvement in the upconversion intensity arises from the breaking of the local crystal field symmetry around the RE ions by the Li^+ doping. Since Li^+ ion is smaller than others in terms of ionic radius, it easily enters the main lattice by occupying not only the substitution sites but also the intermediate regions (Dhannia et al., 2010). Both the substituent ions and the occupation of the intermediate regions are thought to break the symmetry of the crystalline field around the RE ions and result in an increase in luminescence intensity (Dhananjaya et al., 2011). The doping of Li+ ions cannot only improve the luminescence efficiency but also control the morphology and grain size of the luminescent. Since Li^+ ions often play an important role in enhancing the luminescence efficiency of phosphors as co-dopants, alkali metal ions such as Na^+,

Li^+, and K^+ have often been used to alter the local field symmetry of RE elements such as Eu^{3+}, Yb^{3+}, Gd^{3+}, and Dy^{3+} due to their different ionic radii (Altunal et al., 2020b; Altunal et al., 2020c; Guckan et al., 2021a, 2021b; Li et al., 2010; Lorbeer et al., 2014; Saha et al., 2013).

In this work, $KMg_{1-x}F_3:Eu_{0.5\%},Yb_{0.1\%},Li_{x\%}$ phosphors were prepared via the sol-gel synthesis method for dosimetric purposes. This study aims to examine the structural and morphological effects of alkali metal Li co-doping on the RE metals Eu and Yb doped $KMgF_3$ perovskite. We also determined the effects of Li co-doping on its RL, TL, and OSL intensities. The synthesized samples were characterized by techniques including XRD, SEM, EDX spectroscopy, and FT-IR. To the best of our knowledge, the systematic studies of the effects of Li^+ co-doping on the structural characterization and luminescence studies of $KMgF_3$ perovskites have not been published yet.

3. MATERIALS AND METHODS

3.1. Materials

3.1.1. Magnesium Oxide; MgO

Magnesium oxide (MgO), or magnesia, has been known as a white hygroscopic solid mineral that occurs naturally as periclase and is a source of magnesium (Lide, 2004). MgO has an empirical formula and consists of a lattice of Mg^{2+} ions and O^{2-} ions held together by ionic bonding. MgO is an interesting phosphor for radiation dosimetry. Because of its low effective atomic number of Z_{eff} = 10.8, simple cubic lattice structure (Pacchioni, 2001), and many defects that have been investigated by optical absorption, electron paramagnetic resonance, and TL (Las and Stoebe, 1984), it is very useful material. Due to its high chemical stability, such as melting point of ~2800 °C (Lide, 2004; Tamboli et al., 2009), and wide band gap of ~7.8 eV (Taurian et al., 1985), it is possible to engineer a large variety of stable trapping and color centers (Oliveira et al., 2013c).

3.1.2. Zinc Oxide; ZnO

Zinc oxide, which is abbreviated as ZnO, is an inorganic compound. ZnO is a white powder and is insoluble in water. It is used as an additive in many areas including rubbers, cosmetics, food supplements, ceramics, glass, plastics, lubricants, paints, pigments, foods, batteries, ferrites, fire retardants, and first-aid tapes. Although it occurs naturally as the mineral zincite, most zinc oxide is produced synthetically. ZnO has potential as a dosimetric material due to its being one of the technically important semiconductors. Its effective atomic number is Z_{eff}=27.7 and its melting point is 1975 °C. ZnO also exhibits high mechanical strength, thermal, chemical, and ambient stability. It is non-toxic and insoluble in water (Avilés-Monreal et al., 2018; Kołodziejczak-Radzimska and Jesionowski, 2014; Schmidt-Mende et al., 2007). ZnO has been used in many applications as luminescent materials as mentioned previous section.

3.1.3. Parascandolaite; $KMgF_3$

Crystals with perovskite structure represent the general chemical formula ABX3, where A, B, and X represent an alkali metal, an alkaline earth metal and a halide ion, respectively. Parascandolaite, abbreviated as $KMgF_3$, a new perovskite-type fluoride, represents a distinct class of multifunctional materials due to their simple structure, different electronic, and dielectric properties which are suitable for specific purposes. This material provides a wide range of applications in the advanced technologies, such as optoelectronics (Dawber et al., 2005; Scott, 2007), semiconductor devices (Lines et al., 2001; Pathak et al., 2020; Scott, 2007), solid-state lasers (Ellens et al., 1994; Garcia M et al., 1988), lighting phosphors (Ellens et al., 1994), scintillators (Gektin, 2000; Seo et al., 2004), upconverters (Wu et al., 2016b), radiation dosimeters (Daniel et al., 2015; Daniel et al., 2016; Schuyt et al., 2018), etc. (Cohen, 1992; Dawber et al., 2005; Gektin et al., 1997; Lines and Glass, 2001; Pathak et al., 2020; Scott, 2007; Sharma et al., 2013).

3.2. Methods

3.2.1. Synthesis Methods

The different chemical methods used for the synthesis of various dosimetric materials and their investigations, such as Solution Combustion Synthesis method (SCS), sol-gel, precipitation, etc., have been examined by several research groups (Blair et al., 2009; Correcher et al., 2006; Kawano et al., 2017b; Ntwaeaborwa et al., 2017; Ozdemir et al., 2018; Pushpa et al., 2017b; Yukihara et al., 2014a). In this study, many different samples were obtained using chemical production methods with many different dopant ions, and luminescence studies were carried out. All chemical production methods specified in Section 437, where the detailed explanation of the production steps of each sample is given, are as follows.

3.2.1.1. Solution Combustion Synthesis

The specific features of SCS contribute to the unique properties of the synthesized products. The reaction media being initially in the liquid state (e.g., aqueous solution) allows mixing the reactants on the molecular level, thus permitting precise and uniform formulation of the desired composition on the nanoscale (Dinka et al., 2006). The metal nitrate and fuel solution are usually dried (~ 200 °C) and then burned in a furnace or hot plate at < 500 °C (Kingsley et al., 1990). This high reaction temperature process ensures high product purity and crystallinity in one preparation step. In addition, it is known that short processing time and gas formation in this process prevents the growth of particle size and supports the synthesis of nano-sized powders with a high specific surface area. Usually, the dopants added as metal nitrate to the solution allow to control of the luminescence properties of the ceramic materials. The SCS method provides a more convenient synthesis route in metal oxides, as it also provides a doping process that takes place in shorter times than traditional solid-state or crystal growth methods. Thus, it facilitates the investigation of the effects of the luminescence properties of different additives on certain hosts (Barros et al., 2010; Blair et al., 2009; Blair et al., 2010). In this study, the production processes of ZnO and MgO samples obtained by SCS method are detailed in Section 4.1, Section 4.2, Section 4.3, and Section **Hata! Başvuru kaynağı bulunamadı.**, which follows the study.

3.2.1.2. Precipitation Technique

Since the precipitation technique is a simple and inexpensive method in material production, it is a frequently preferred method. It can be examined in three steps. First, a solution to which the precursors are added is mixed with the acid solution, and the intended compound precipitates to the bottom of the solution within seconds. Second, the precipitated material is separated from the solution with the aid of filter paper or centrifuge and washed several times. The precipitate

separated from the solution is dried with the aid of an oven and then cooled to room temperature. Finally, the dried material is calcined in a high-temperature oven and the desired compound is achieved. When a certain temperature is reached, it is kept at this temperature for a certain period and then cooled down to room temperature, i.e., the sample gradually moves towards a lower temperature crystallization zone (Azorin, 2014). Various samples have been produced for dosimetric purposes with this method preferred by many researchers. Some of these are metallic oxides (Azorín-Vega et al., 2007; Guckan et al., 2020a; Kumar et al., 1994; Soares et al., 2017b), lithium fluoride (Ha et al., 2007), calcium sulfate (Patil et al., 2007; Rivera et al., 2010; Roman et al., 2009), alkaline earths sulfides (Rao, 1986) etc. In this study, this technique was used to prepare the ZnO:Eu phosphors, which are described in detail in Section 4.1.

3.2.1.3. Sol-Gel Synthesis Method

Although obtaining different product forms in the Sol-Gel technique requires some special considerations, in techniques involving such colloidal dispersions, powder samples with low particle size, fibrous, thin-film, and monoliths can be easily prepared. The basic and general approaches in these colloidal dispersions are the same. The Sol-gel method, which offers many advantages such as low reaction temperature and homogeneity at the molecular level, is considered a very suitable method for obtaining many materials such as metal oxides and temperature-sensitive organic-inorganic hybrid materials (Huang, 2008). In this method, which is generally based on hydrolysis and condensation, precursors are selected as metal alkoxides or inorganic and organic salts. While organic or aqueous solvents can be used as solvents, catalysts are usually added to promote hydrolysis. The synthesis processes and detailed explanation of the ZnO and $KMgF_3$ samples are given in Section 4.1 and Section 4.6, respectively.

3.2.2. Structural Characterization Techniques

3.2.2.1. X-Ray Diffraction

In this study, all the X-ray Diffraction (XRD) patterns were obtained using a PANalytical EMPYREAN XRD diffractometer equipped with a copper and cobalt X-ray tube using Cu-Kα radiation (λ=0.1541 nm). The generator voltage and current were set at 60 kV and 40 mA, respectively, to investigate the crystalline structure and phase composition. The measurements were performed by scanning the 2θ in 0.01 degrees step size and 0.5 s scan step time. All phase identifications were performed using the Inorganic Crystal Structure Database (ICSD).

3.2.2.2. Scanning Electron Microscope

The surface morphology of all luminescent materials investigated in this study were analyzed from the SEM images obtained using a FEI Quanta 650 SEM instrument, field-emission with 30–100 kV accelerating voltage and 100 nA probe current.

3.2.3. Luminescence characterization

3.2.3.1. Radioluminescence

The Radioluminescence (RL) measurements were carried out using a custom-build equipment composed of two main parts which are an Ocean Optics QE Pro-model spectrometer and X-ray source with a silver target. In this spectrometer, the lead-glazed sample chamber was used and the electronics of both x-ray power supply and RL system, and the computer control interface unit were designed on purpose. This custom-build equipment are provided the scanning between 200 nm and 1100 nm. All samples were exposed to X-rays during the measurements. The X-ray voltage was ~20 kV. The X-ray tube current of this spectrometer is 188 μA. There is no filtration in this device. RL signals were detected by a back-thinned CCD detector. The spectrometer has been set up to record the x-ray luminescence of the synthesized phosphors. The spectrometer slits are changeable for improving sensitivity for low signals. This equipment was

established in the frame of a NATO project SfP984649 (2015-2018) consisting with the implementations of the project.

3.2.3.2. Photoluminescence

The photoluminescence emission (PL) and photoluminescence excitation (PLE) spectra were measured using a Horiba/Jobin-Yvon Fluorolog-3 spectrofluorometer equipped a continuous xenon lamp (450 W) as an excitation source. Hamamatsu R928P photomultiplier tube was used as a detector in photon counting mode. All PL and PLE spectra were recorded at room temperature. The measured PLE spectra were corrected by the xenon lamp emission spectrum.

3.2.3.3. Thermoluminescence

All TL readouts were performed using a Risø TL/OSL DA-20 model measurement system with a 1.48 GBq $^{90}Sr/^{90}Y$ beta source (maximum energy of 2.27 MeV, the dose rate of 6.67 Gy min^{-1}). The sample holder was heated from room temperature to 550 °C. During the heating process, a continuous flow of nitrogen gas was provided into the environment. The resulting light was sensed by the bialkali 235QB model PM tube (max efficiency between 200 and 400 nm) in the reader. TL readouts of the samples were performed using a Schoot BG-39 filter in VIS region.

3.2.3.4. Optically Stimulated Luminescence

OSL measurements were performed using a Risø TL/OSL DA-20 reader equipped with an optical stimulation unit owing blue (λ_{blue}= 470 nm) or infrared (λ_{IR}= 870 nm) light-emitting diodes (LEDs). OSL signals were recorded during 50 or 100 s continuous-wave stimulation with ~70 $mWcm^{-2}$ power density. A Hoya U-340 bandpass filter (between 290 and 390 nm transmittance; max 340 nm, Hoya Corp., Japan) was used in front of the photomultiplier tube to avoid the mixing of stimulation light and luminescence emission lights. All the OSL measurements of the samples were carried out after waiting for 30 min at RT to stabilization of traps after the sintering process.

4. RESULTS AND DISCUSSIONS

4.1. Study of the Eu-doped ZnO

4.1.1. Material Synthetization

In this study, the effect of the calcination process on pellet-shaped ZnO:Eu samples prepared using sol-gel and precipitation methods. All chemicals used for sample synthesis were Sigma-Aldrich branded. In order to create defects in the ZnO bandgap, the Eu ion was used as dopant at 0.1% molar concentration. For both methods, the calcination temperatures and times are 800, 900, 1000, 1100 and 1200 °C for 2, 4, 6, 8, 10 and 24 h. In this process, the material was first produced with the specified methods and both were divided into 5 equal parts. Then these parts were calcined at the given temperatures successively with 5 °Cmin-1 heating rate, keeping the calcinating time constant for 4 h, in both methods. To have more settled TL, OSL and PL signals and easy handling, the ZnO:Eu phosphors were studied in pellet-shaped form. Pelletization of the ZnO phosphors was performed with 25 mg calcined powders into a disc mold with a 6 mm diameter and 0.6 mm thickness. The PL, TL and OSL measurements were performed with the samples as prepared in pellets form and sintered at 1200 °C for 4 h. The curves of luminescence output as a function of calcination temperatures and times given above were used as a precursor to determine optimal calcination conditions.

The preparation process of ZnO phosphors by Precipitation method is as follows; zinc sulfate ($Zn(NO_3)_2.6H_2O$, Sigma Aldrich, ≥99.0%) was used as the precursor. The polyethyleneimine (50% (w/v) in H_2O, analytical standard) solution was used for the polymerization. NH_4OH (Ammonium hydroxide solution, 28.0–30.0% NH_3 basis) was used as an initiator of the precipitate. $Eu(NO_3)_3.5H_2O$ (Europium (III) nitrate pentahydrate, Sigma Aldrich, 99.9% trace metals basis) was used as the dopant material. Firstly, certain amounts of zinc sulfate and europium nitrate were dissolved in distilled water using a magnetic stirrer. Also, the polyethyleneimine solution was dissolved in a different beaker. When solutions

become homogeneous, the polyethyleneimine was added to the zinc sulfate solution. For the pH controlling, a certain amount of ammonia was added and the precipitate was observed at the bottom of the solution. After filtering the white bulk sample, the heat treatment was applied until the sample was completely dry. The dried sample was calcined in a furnace using specified temperatures.

Synthetization of the Eu doped ZnO phosphors using the sol-gel method is as follows; $Zn(NO_3)_2.6H_2O$ (Zinc nitrate, Sigma Aldrich, ≥99.0%) and $C_6H_8O_7$ (Citric acid, Sigma Aldrich, >99.5%) were used as reactants. The solution was prepared by mixing stoichiometric amounts of $Zn(NO_3)_2.6H_2O$ and $C_6H_8O_7$ solutions at a constant temperature (at 100 °C for 30 min). $C_6H_8O_7$ was used as a chelating agent for the mixing of cations at the molecular level. $C_2H_6O_2$ (Ethylene glycol, Sigma Aldrich, >99.8%) which was used as a solvent, was dribbled into the solution for the gel-forming. $Eu(NO_3)_3.5H_2O$ (Europium nitrate, Sigma Aldrich, 99.9% trace metals basis) was used as the dopant material. The heater temperature was increased to 200 °C until the translucent gel was obtained and the solution color darkened in about 2 hours. The dark brown gel was gradually heated in an oven to 300 °C and burned for 1 hour. The flow chart of the two synthesis methods mentioned above is given in Figure 4.1.

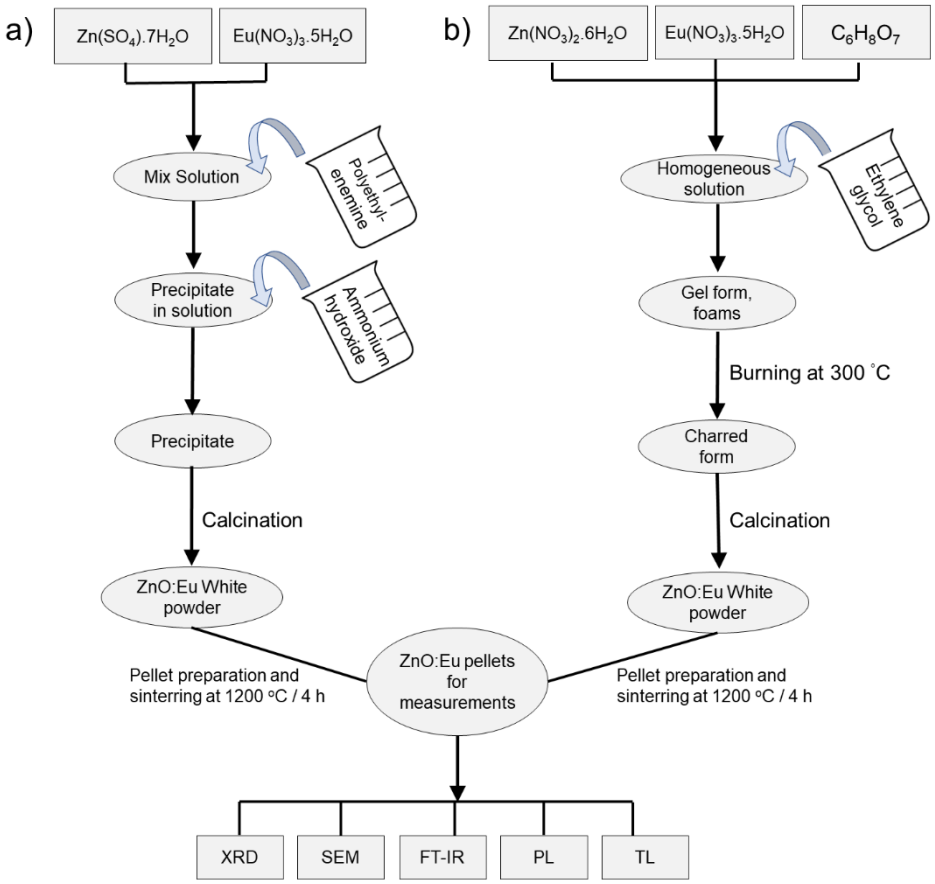

Figure 4.1. Flowchart of the ZnO:Eu synthesis processes. (a) The process of the precipitation method was presented on the left side and (b) the process of the sol-gel method on the right side of the flowchart.

4.1.2. Effect of Calcination Process on ZnO:Eu

To determine the effect of the calcination process on the crystal structure and grain size, the XRD analysis was carried out. The X-ray diffraction patterns of ZnO:Eu samples calcined at different temperatures are given in Figure 4.2. The XRD lines of all samples identified by the Miller indices match that from ICSD card 98-019-5803 (P 63 mc space group, hexagonal phase with wurtzite structure). The magnified XRD lines (100), (002), (101), (102), (110) and (103) are shown in

Figure 4.3a, Figure 4.3b, Figure 4.4a and Figure 4.4b with the locations at 2theta = 31.8°, 34.5°, 36.3°, 47.6°, 56.6°, and 62.9°, respectively. The diffraction lines of the samples are broad. This leads to the idea that the samples have nano-sized particles.

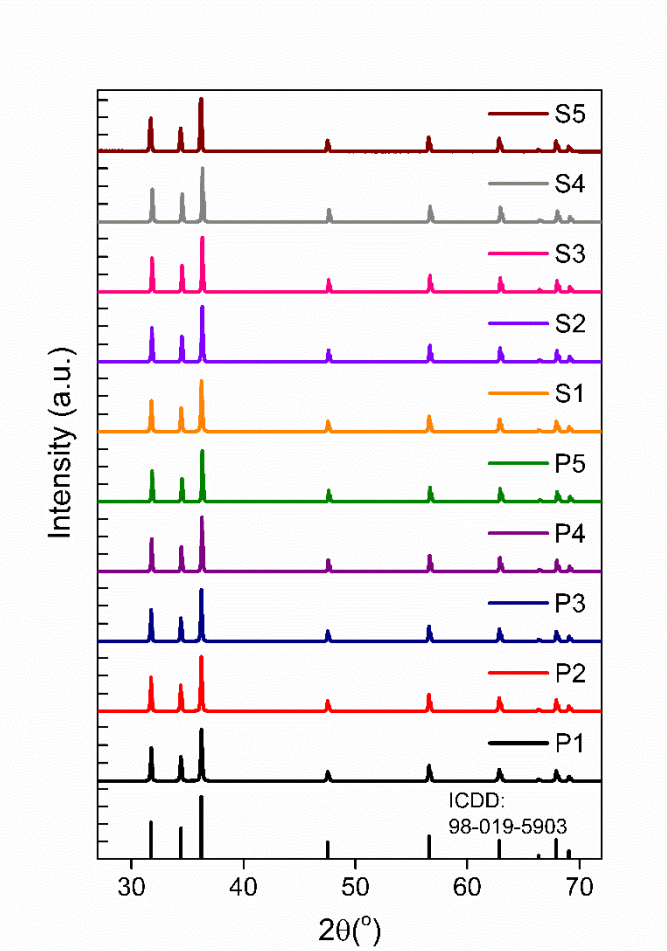

Figure 4.2. X-ray diffraction patterns of ZnO:Eu phosphors synthesized using the precipitation method described as P1-5 and sol-gel methods as S1-5.

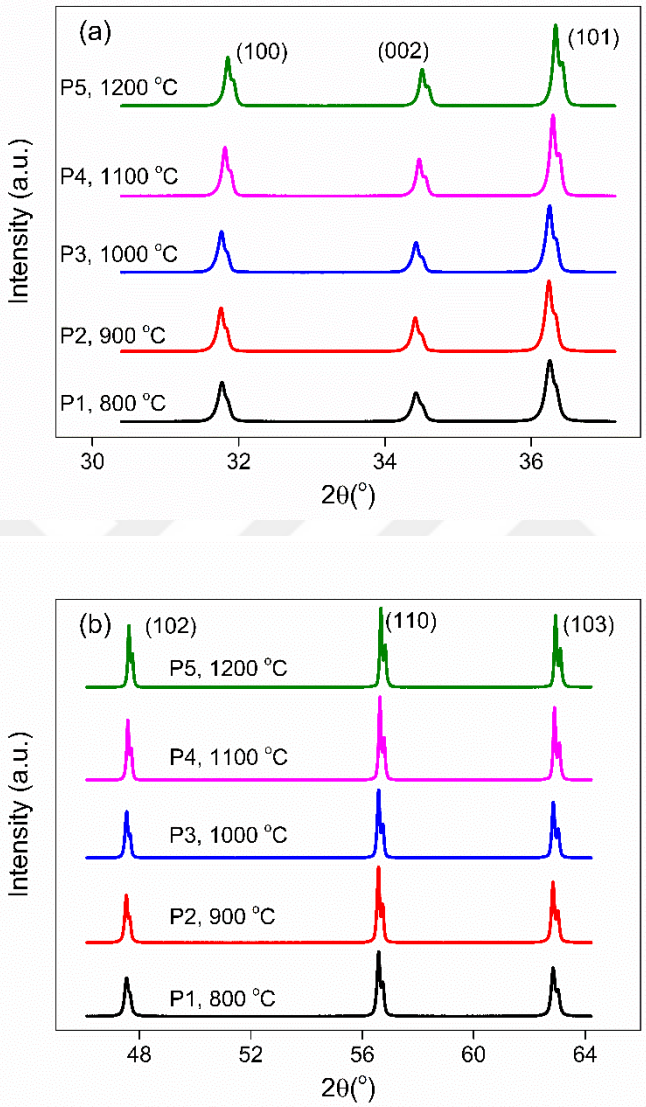

Figure 4.3. Magnified diffraction lines in the range of (a) 30-37 ^{o} and (b) 45-65 ^{o} for XRD spectra of ZnO:Eu samples obtained using precipitation method. (The shoulders are caused by the doublets of unfiltered $CuK\alpha_1$ and $CuK\alpha_2$ lines and they are developed for the most intensive lines.)

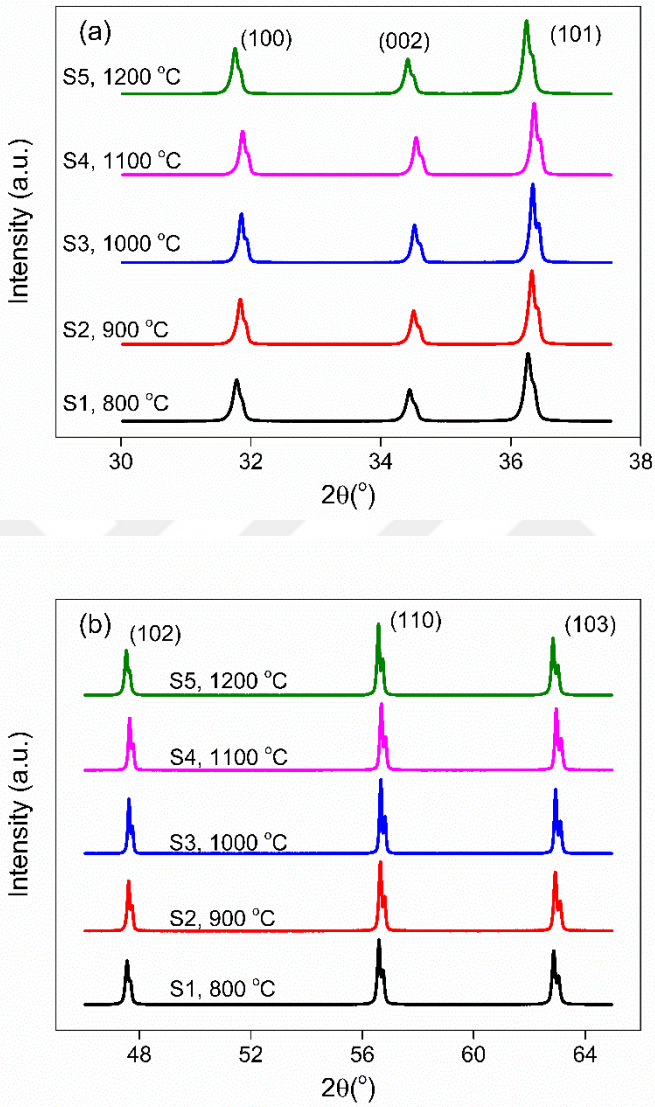

Figure 4.4. Magnified diffraction lines in the range of (a) 30-37° and (b) 45-65° for XRD spectra of ZnO:Eu samples obtained using the sol-gel method. (The shoulders are caused by the doublets of unfiltered CuKα1 and CuKα2 lines and they are developed for the most intensive lines.)

The XRD patterns of samples calcined at high temperatures exhibit narrower peak widths and increased peak densities (Vorokh, 2018). Vibrations mean that grain sizes are affected by varying calcination temperatures or times. For the ZnO samples whose mean crystallite size (D) were calculated, the Scherrer equation was used as follows (Kroon, 2013);

$$D = \frac{K\lambda}{\beta cos\theta} \tag{4.1}$$

where $K, \lambda, \beta \; and \; \theta$ are described as Sherrer constant (0.89), X-ray wavelength (1.5418 Å), peak width at half-maximum and the Bragg diffraction angle, respectively. The variation of D and Full width at half maximum (FWHM) with the calcination temperature is given in Figure 4.5a. and Figure 4.5b. As seen in the figures, it was observed that the ZnO diffraction peak intensities increased with increasing crystallite sizes due to increasing calcination temperatures in samples obtained using precipitation and sol-gel methods.

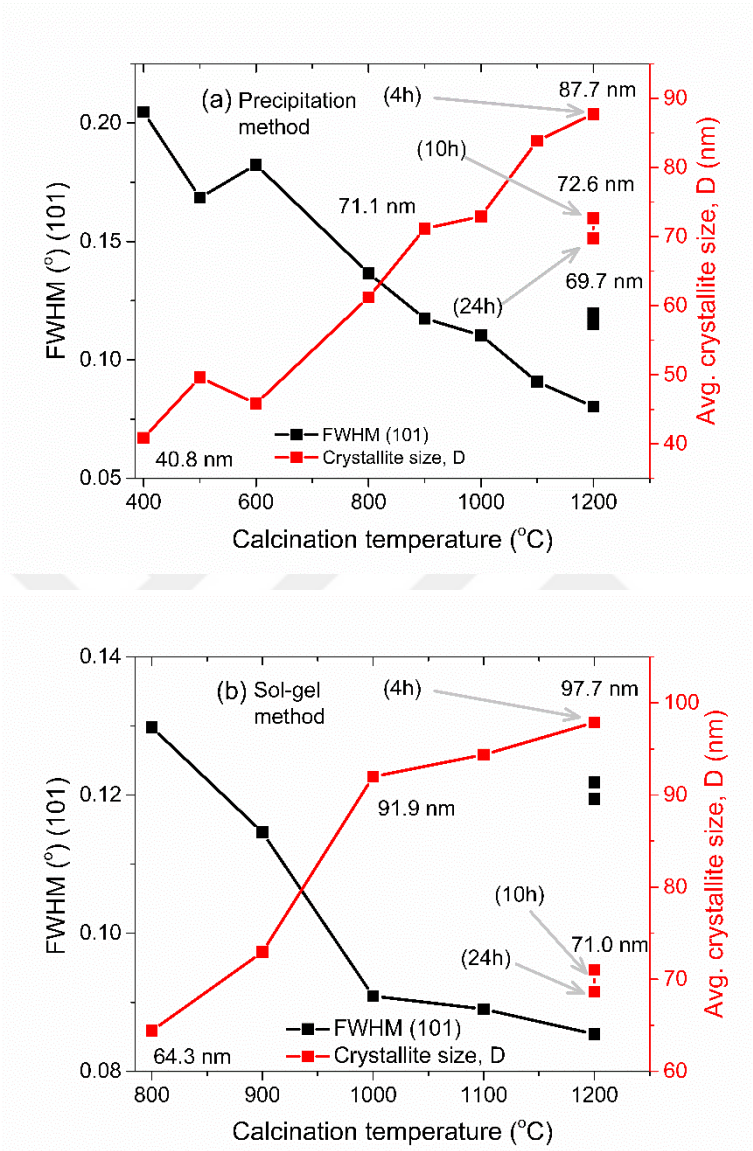

Figure 4.5. FWHM versus crystallite size for the diffraction peak described with Miller indices as (101) for ZnO:Eu nanoparticles prepared using (a) precipitation and (b) sol-gel methods with different calcination temperatures. All data points were calculated from calcined samples in powder form without sintering). The crystallinity sizes increased with increasing calcination temperatures for all of the studied samples. We observed a decrease in crystalline sizes for P5 samples with increasing calcination times of 4 h, 10 h, and 24 h, at 1200 °C.

In Figure 4.6a. and Figure 4.6b., the characteristic infrared spectra (FT-IR) of both types of Eu^{3+} doped ZnO pellets recorded at room temperature in the range of 450 and 4000 cm^{-1} are shown. The IR spectra of all samples are in good agreement with each other, as seen in Figure 4.6a. and Figure 4.6b. As a result, the characteristic infrared (IR) spectra of both types of ZnO: Eu phosphors recorded at room temperature between 450 and 4000 cm^{-1} are in good agreement with each other. Two strong absorption bands around 455 and 550 cm^{-1} are attributed to Zn-O vibrations for the pure ZnO spectrum in the literature. In this study, we obtained Zn-O absorption bands shifted to 505 and 650 cm^{-1}. This shifting is due to the distortion of the Zn-O-Zn network by the presence of Eu in the host matrix (Sharma et al., 2009). The broadband of about 460 cm can be assigned to the Eu-O stretching mode. This means that Eu^{3+} ions settle at Zn^{2+} sites. Therefore, it can be said that Eu ions occupy the Zn positions in the host matrix for both types of ZnO:Eu samples. The small peak around 2350 cm^{-1} has been assigned to the O-H group and the CO_2 stretch mode (Ravichandrika et al., 2012; Udayakumar et al., 2012). It can be said that zinc sulfate or zinc nitrate residues used in the preparation of ZnO phosphors are associated with asymmetric and symmetrical stress vibrations (Ntwaeaborwa et al., 2017).

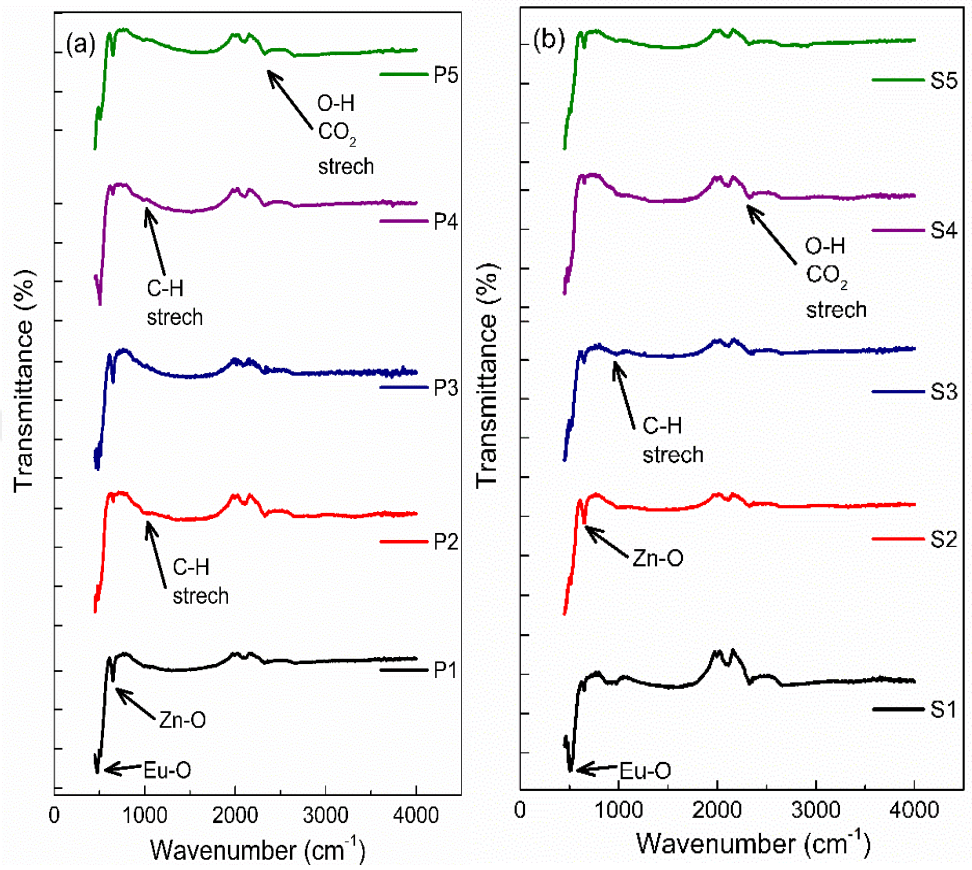

Figure 4.6. FTIR spectra of the ZnO:Eu pellets prepared using (a) precipitation and (b) sol-gel methods.

The effect of sintering on the material and the surface of the material is known as the reduction of the porous structure in the surface area by heat transfer to the material and the formation of necks between the particles in contact with each other. For this reason, the contact of the particles causes the deformation of the particles and pores, and thus the pore volume changes (Altunal et al., 2019; Atuchin et al., 2008; Atuchin et al., 2018; Lim et al., 2015). The surface morphology of the ZnO pellets obtained at different calcination temperatures was investigated by SEM. The SEM images shown in Figure 4.7 showed that varying calcination temperatures produced different surface morphologies in the samples.

The images showed that the particle shapes and sizes are clearly distinguishable at 800 °C calcination temperature. As the calcination temperature increased, the particle boundaries became more uncertain and the particle shapes became more irregular. It is also seen that the structures forming the local neck are dispersed. In the samples calcined at 1200 °C, the porous structure was completely covered and neck formation became apparent. Interlocking particles were observed. The interpretation of SEM images' relationship with TL and OSL is given in the section of luminescence studies.

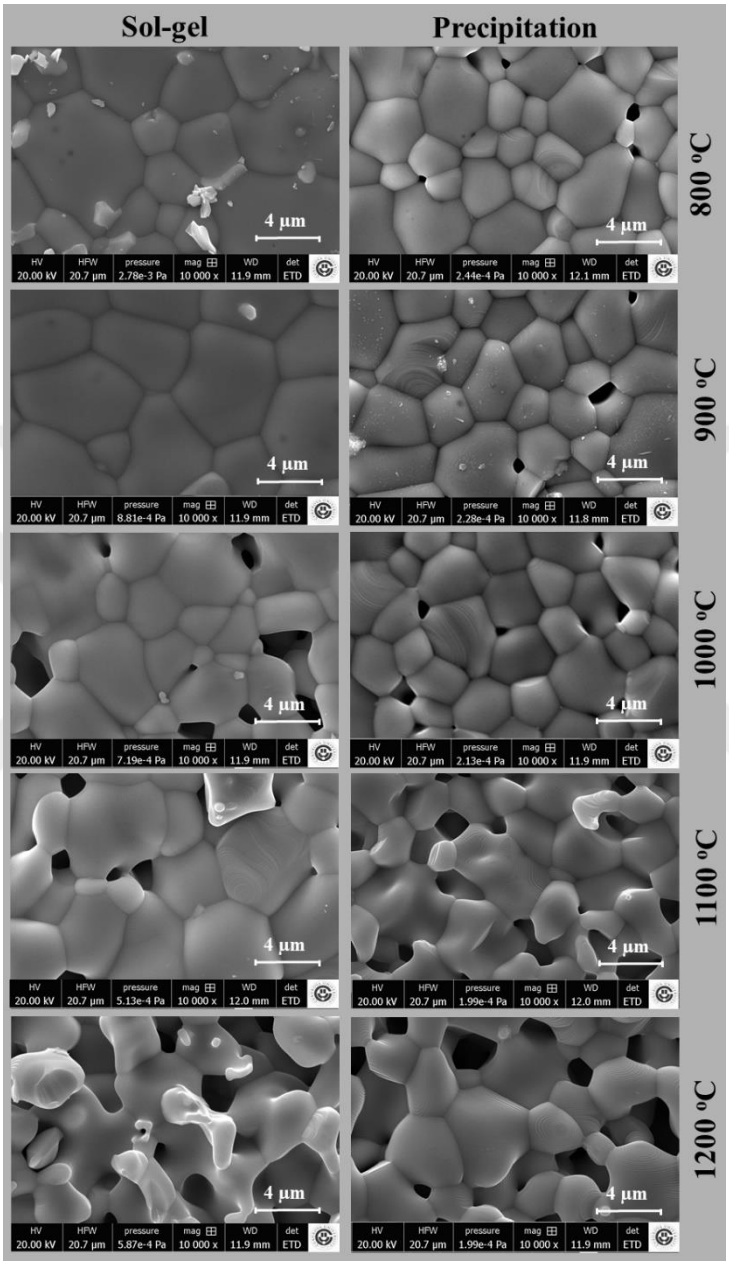

Figure 4.7. Typical SEM images of the ZnO:Eu structures with x10,000 magnification. The images obtained from pellet samples are given comparatively according to the production methods and calcination temperatures (All the SEM images were taken from the ZnO:Eu pellets sintered at 1200 ^{o}C for 4h after the calcination processes).

4.1.3. Photoluminescence

The optical features and the information on the purity of the samples were investigated by photoluminescence (PL) spectroscopy. All the PL measurement were carried out at room temperature. Figure 4.8 and Figure 4.9 are presented the emission and excitation spectra of ZnO:Eu pellets. The emission spectra of the ZnO:Eu pellets calcined at different temperatures were recorded with the excitations of $\lambda_{ex} = 350\,nm$ and $\lambda_{ex} = 464.5\,nm$. Depending on the calcination temperature, the emission spectra of ZnO: Eu show a difference in PL density related to defect formation. The PL emission spectra of ZnO:Eu shows a variation in PL intensity related to the defect formation dependent on the calcination temperature. During the excitation at the wavelength of 350 nm using the 450 W xenon lamp, only defects related to VIS emission at ~580 nm were observed. This broad emission band (green) is generally attributed to the radiative recombination of a photo-generated hole with an electron occupying the oxygen vacancy (Shinde et al., 2014b). A dominant deep level emission was observed in almost all calcined samples and no UV band-edge emission was observed. The intensity of deep level emission decreased as the calcination temperature increased.

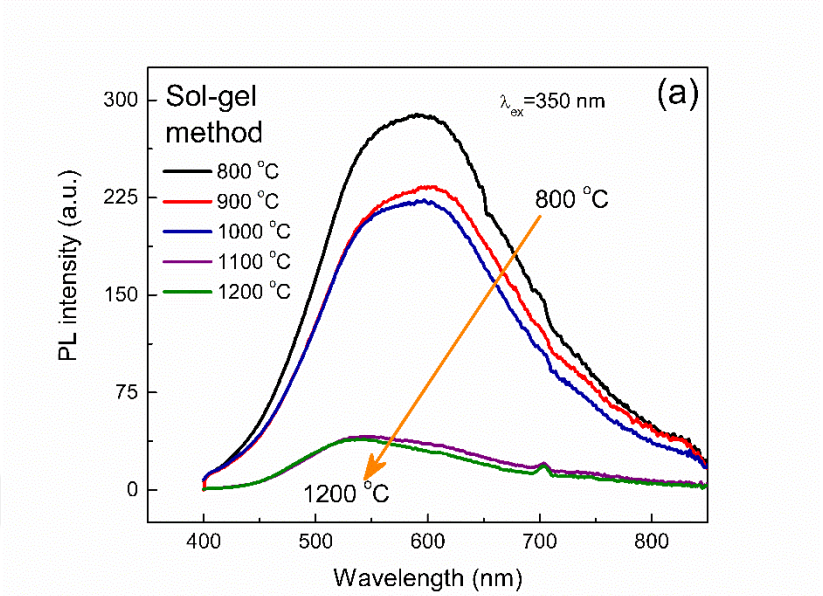
Sol-gel
method
(a)
λex=350 nm
800 °C
900 °C
1000 °C
1100 °C
1200 °C
800 °C
1200 °C
PL intensity (a.u.)
Wavelength (nm)
300
225
150
75
0
400
500
600
700
800

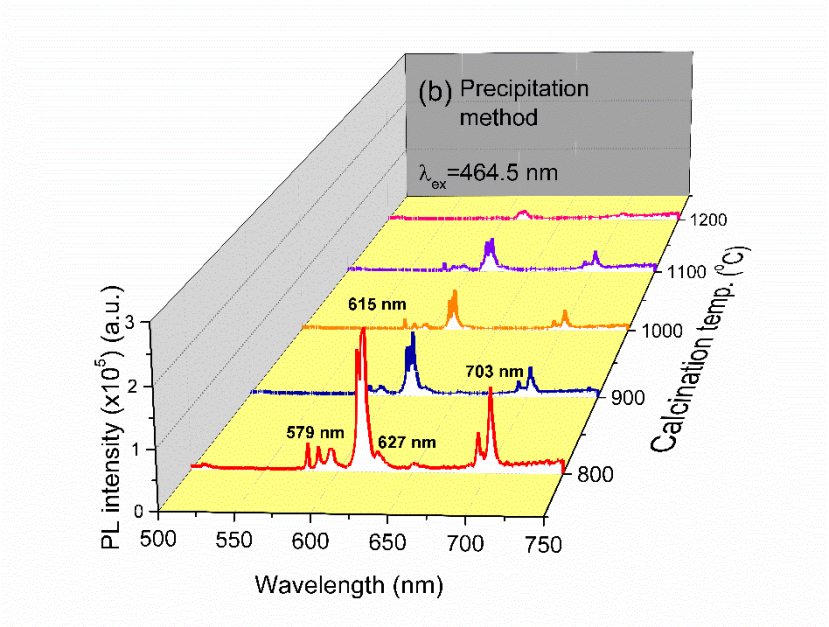
(b) Precipitation
method
λex=464.5 nm
615 nm
703 nm
579 nm
627 nm
1200
1100
1000
900
800
Calcination temp. (°C)
PL intensity (x10^5) (a.u.)
Wavelength (nm)
0
1
2
3
500
550
600
650
700
750

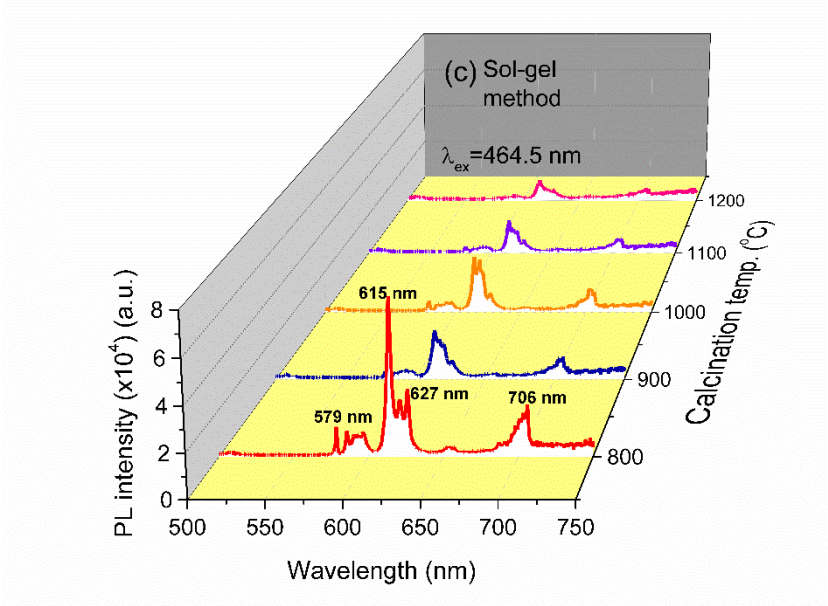

Figure 4.8. The emission spectra of the ZnO:Eu pellets excited at (a) 350 nm and (b-c) 464.5 nm. All the PL measurements were performed at room temperature.

We observed two sharp peaks at 579 and 615 nm, and two relatively fewer sensitive peaks at 650 and 700 nm with the excitation at 464.5 nm. The $^5D_0 \rightarrow {}^7F_1$, $^5D_0 \rightarrow {}^7F_2$, $^5D_0 \rightarrow {}^7F_3$ *and* $^5D_0 \rightarrow {}^7F_4$ transitions of the Eu^{3+} ions lead to the emergence of these peaks, respectively (Atuchin et al., 2014; Denisenko et al., 2018; Fang et al., 2009; Nassar et al., 2010; Pal et al., 2013b). It is stated in the literature that the intensity of the emission lines of $^5D_0 \rightarrow {}^7F_1$ associated with magnetic dipole transitions consisting of two peaks or three peaks for the sol-gel and precipitation methods, respectively, varies significantly with the local environment of Eu^{3+} ions(Xu et al., 2011; Yang et al., 2014). The most intense lines in the emission spectra of the samples are related to the $^5D_0 \rightarrow {}^7F_2$ electric dipole transitions and show two peaks in precipitation and three peaks in the sol-gel method. The peak at 615 nm was found in all Eu doped samples. It has already been reported that Eu^{3+} ions are mainly included at the center of inversion

antisymmetry (Pal and Manam, 2013b). As can be observed from Figure 4.8b. and Figure 4.8c., it can be said that the concentration of specific point defects responsible for emission due to defects in the green-yellow range decreases with increasing calcination temperature. Decreasing its intensity without changing the structure of the emission spectrum can only mean that the concentration of Eu^{3+} ions is reduced. It can be thought of as the chemical reduction of $Eu^{3+} \rightarrow Eu^{2+}$ as a mechanism of concentration change. It is known that Eu^{2+} has a completely different emission which emits in the green range when excited in UV. This is another reason why it is of interest to analyze the structural changes of the yellow-green emission with calcination in detail. There will likely be some disproportion in the nature of this complex emission, such as a decrease in emission associated with defects in yellow and possibly some increase in green emission related to Eu^{2+}. Disappearing of point defects required for charge compensation of $Eu^{3+}(Zn^{2+})$ ions looks reasonable with the creation of Eu^{2+} with the chemical reduction instead of Eu^{3+} with increasing calcination temperature. Considering the intrinsic emission in yellow is caused by zinc vacancies or oxygen interstitials, puzzles are put together. As the calcination temperature increases, the concentration of Eu^{3+} ions decreases with decreasing concentration of zinc vacancies/oxygen interstitials because they are no longer required for charge compensation. It physically means that diffusion out of the excess oxygen atoms from the material.

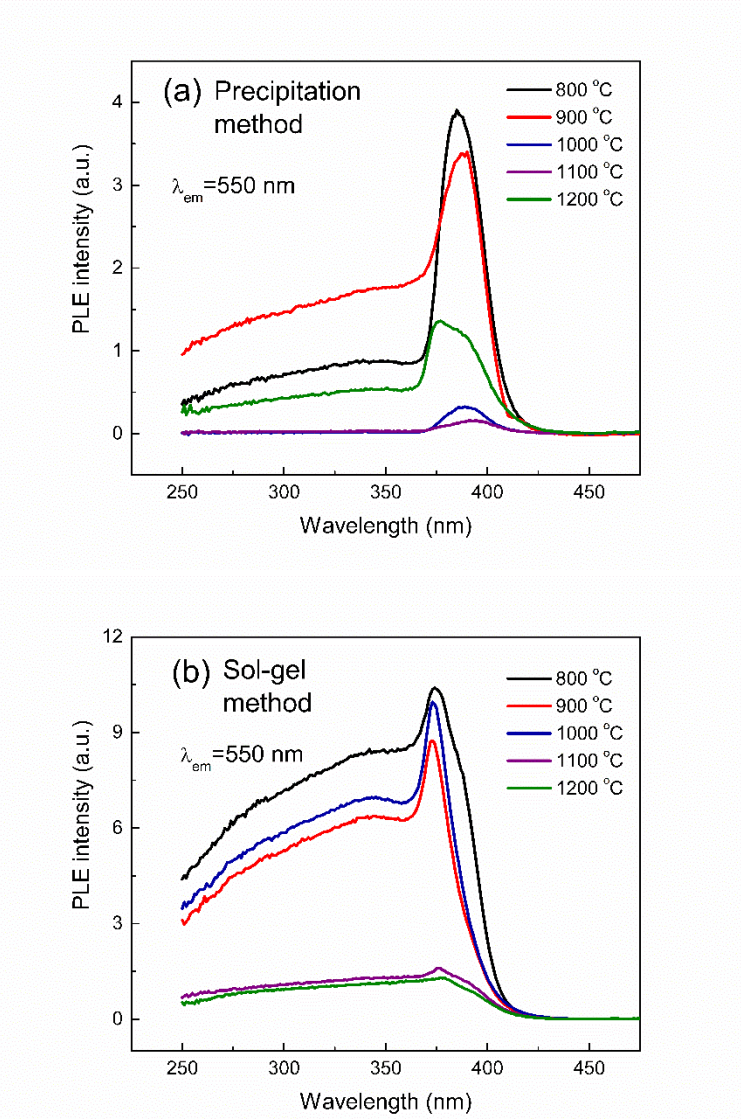

Figure 4.9. The excitation spectra of the ZnO:Eu pellets were synthesized using precipitation and sol-gel methods (λ_{em}= 550 nm). All PLE measurements were carried out at room temperatures.

The excitation spectra were measured with $\lambda_{em} = 550\,nm$ as is seen in Figure 4.9a and Figure 4.9b The spectrum of the ZnO:Eu showed a broad peak at 385 nm (related with 4f → 4f transitions of Eu^{3+} in the ZnO host matrix).

4.1.4. Thermoluminescence

The TL glow curves were recorded from ZnO pellets irradiated with a 20 Gy beta test dose. To determine the dopant effect, TL glow curves of undoped and Eu doped ZnO are given together in Figure 4.10 It is seen that there exists an increase in TL intensities due to dopant. Following our Eu^{3+} chemical reduction assumption, the higher TL intensity of the Eu doped samples compared to the undoped and the increase in the TL intensity for the doped samples can be explained by the increase in the calcination temperature. The sensitivity range of the photomultiplier tube contains the green emission-related with Eu^{3+} ions, whereas the yellow emission – not. The emission in the visible region resulting from the increase in defects is closely related to the Eu contribution. On the other hand, ZnO:Eu pellets calcined at 5 different temperatures and times and sintered at 1200 °C for 4 hours were examined under ionizing radiation. The figure presents the TL glow curves of ZnO:Eu pellets. It is seen that the ZnO samples have clearly defined TL peaks after exposure to a 2 Gy beta test dose following the calcination process at different temperatures and times. To study the defects in materials, the variation of the calcination/sintering process is a widely used method. During the annealing process, the structural alignment and stoichiometry of the material will vary due to dislocations and other defects produced in the material. Thermal conductivity improves thanks to the growth of sample beads, better binding of particles in the material, better crystallization of the material, and a non-porous structure in sintered samples (Altunal et al., 2019; Uthirakumar et al., 2009b; Wang et al., 2011b). Therefore, we did not receive a TL signal from the non-sintered powder samples after the calcination process. It was observed that TL curves consisted of multiple overlapping TL peaks in both synthesis methods (see Figure

4.11). Calcination temperature of 800 °C for the sol-gel method and 900 °C for precipitation were determined as ideal calcination temperatures for TL sensitivity and signal intensities, and these temperatures were kept constant for 2, 4, 6, 8, 10 and 24 h calcination times. At the end of the time experiment, it was observed that the efficiency of TL did not increase significantly between 2 and 24 hours. The calcination process at 900 °C for 4 hours and at 800 °C for 10 hours, respectively, for the precipitation and sol-gel methods were determined as optimum conditions for TL signal efficiency.

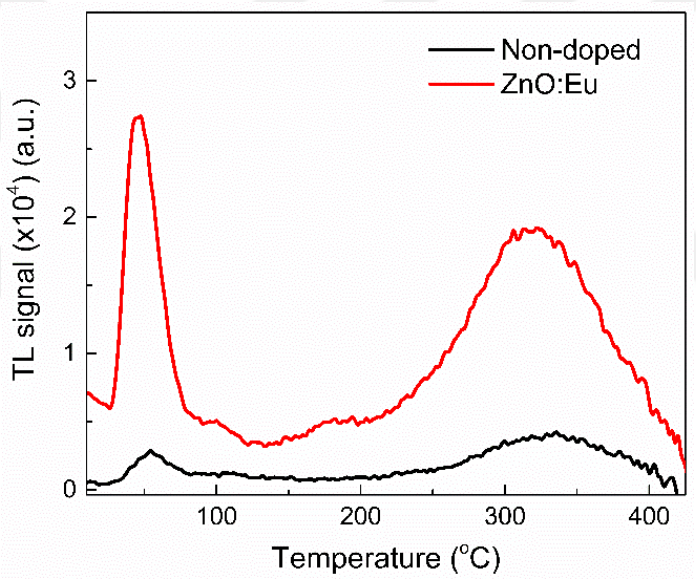

Figure 4.10. TL glow curves of undoped and Eu doped ZnO pellets following 20 Gy beta dose.

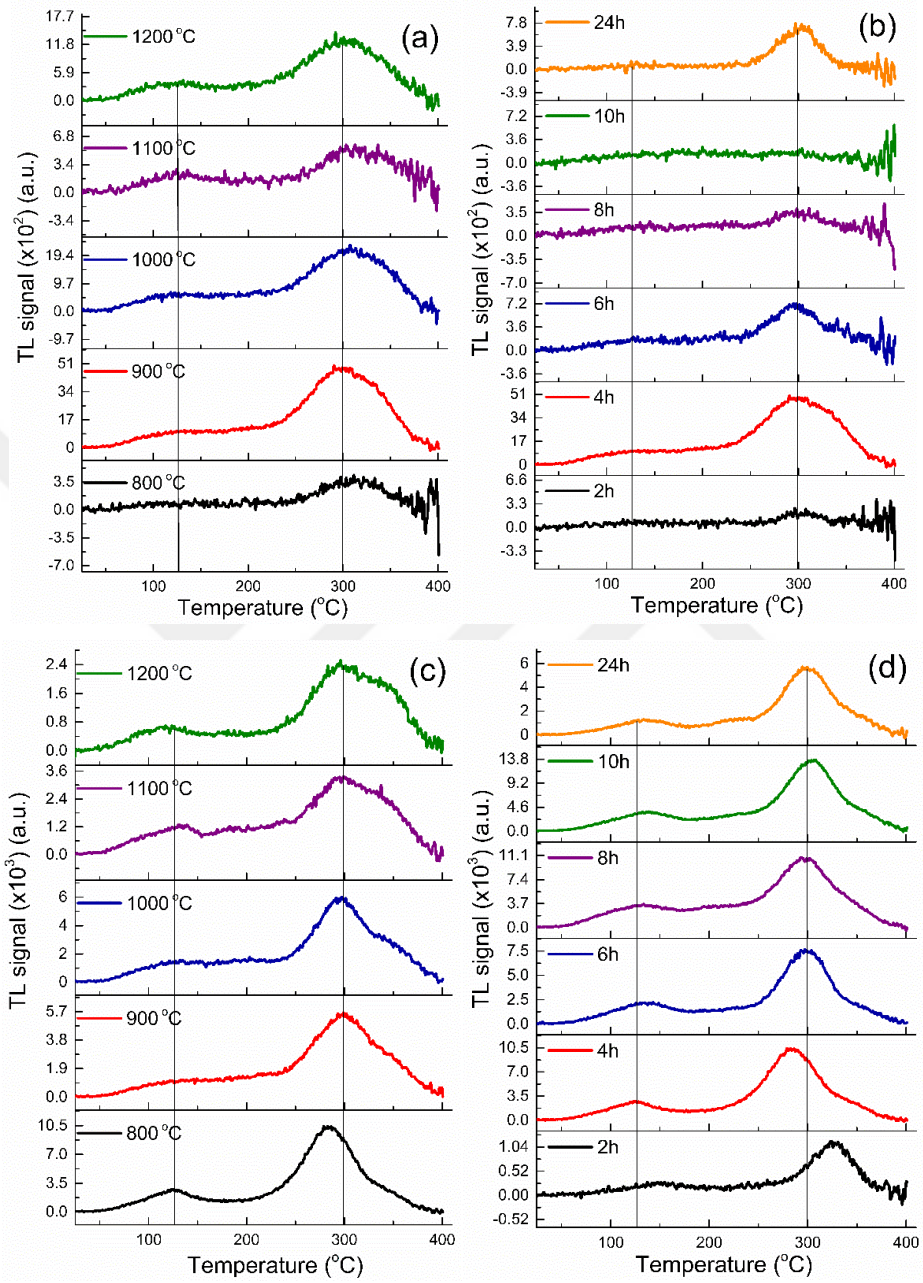

Figure 4.11. TL glow curves obtained from ZnO pellets prepared using (a, b) precipitation and (c, d) sol-gel methods with different calcination temperatures and times. All the TL measurements were recorded after 2 Gy of beta exposure.

Dose-response behavior of ZnO:Eu pellets was studied between 1 Gy and 5 kGy. Total TL intensity of the samples prepared by precipitation and sol-gel methods are given in Figure 4.12a and Figure 4.13a, respectively, as a function of dose values. Dose-response data (solid squares) were obtained as the average of three pellets per cycle, and error bars were obtained from the standard deviations of these data. Dose-response values are indicated in log-log scales. The superlinearity indices where linear dose-response data varied between 1 Gy and 0.2 kGy for samples produced by both methods are given as the lower part of the graphs. For both samples, two TL peaks at ~ 130 and 300 °C were recorded along the entire glow curve of the irradiated samples. The superlinearity index g(D) of the dose-response behavior was calculated using the following Equation (4.2;

$$g(D) = DS''(D)/\, S'(D) + 1 \tag{4.2}$$

where $S''(D)$ and $S'(D)$ are the first and second derivatives of dose-response D from irradiated samples. The $g(D)$ distributions are given in the lower parts of Figure 4.12b and Figure 4.13b For the Precipitation method, the TL dose-response behavior of the samples was calculated to be linear ($g(D) = \sim 1.04$) from 1 Gy to 0.2 kGy using Equation (4.2. The dose-response behavior of the samples showed linear behavior between 1 Gy and 0.2 kGy for the sol-gel method using. The $g(D)$ was calculated about 1.04 and it was determined that both samples exhibited a saturation tendency after 0.2 kGy beta exposure.

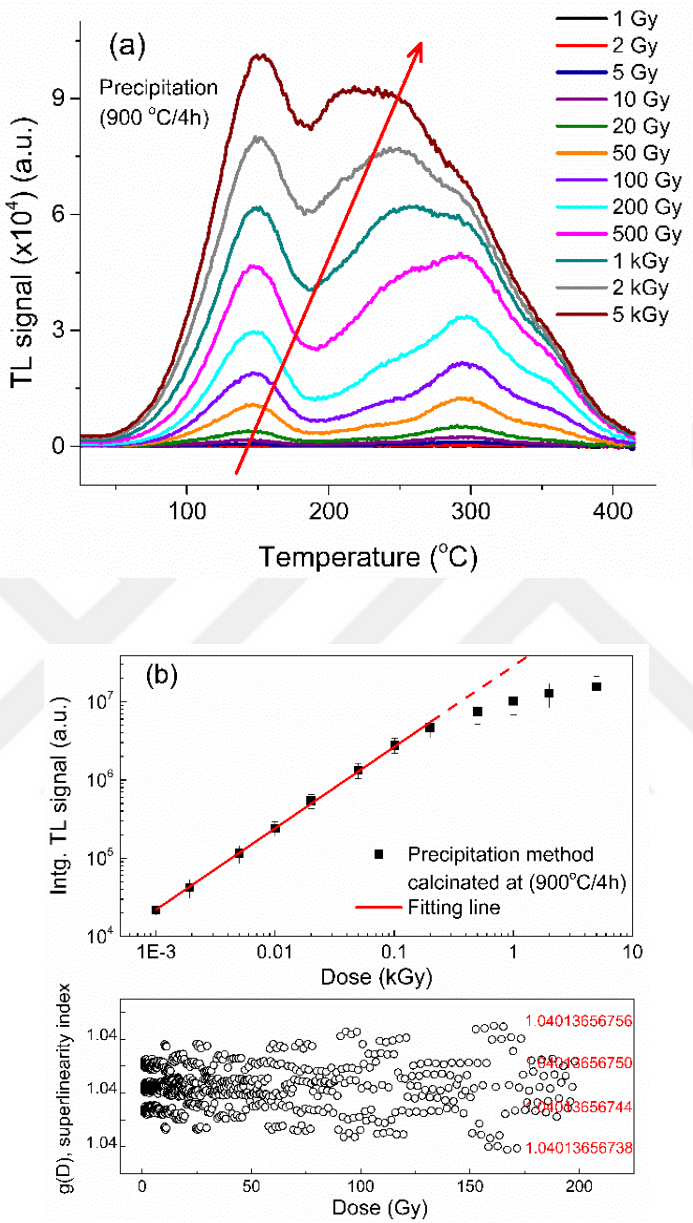

Figure 4.12. (a) TL glow curve of ZnO:Eu at the different doses of beta exposure. (b) The variation of TL intensities at different dose rates for ZnO:Eu pellets synthesized using the precipitation method. The lower part of the (b): The change in the superlinearity index between 1 Gy and 0.2 kGy.

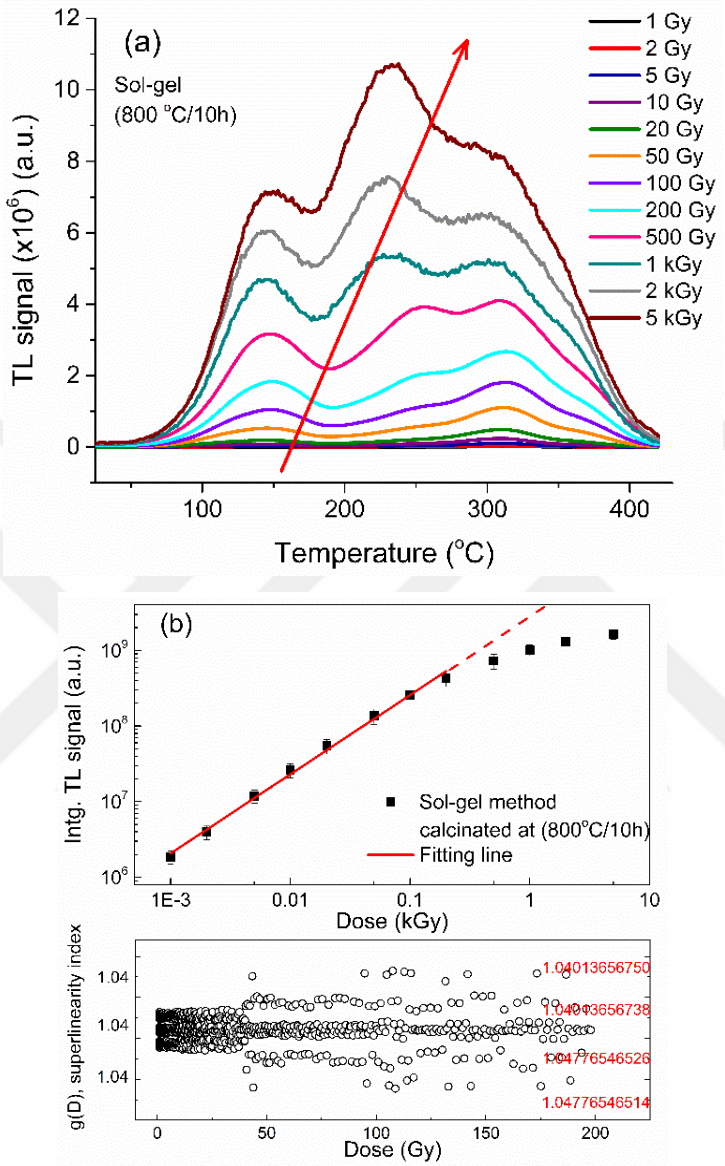

Figure 4.13. (a) TL glow curve of ZnO:Eu at the different doses of beta exposure. (b) The variation of TL intensities at different dose rates for ZnO:Eu pellets synthesized using the sol-gel method. The lower part of the (b): The change in the superlinearity index between 1 Gy and 0.2 kGy.

Continuous-wave optically stimulated luminescence (CW-OSL) measurements were performed for undoped and Eu doped ZnO pellets. These

measurements were carried out by stimulating the sample for 100 s with blue LEDs ($\lambda_{blue} = 470\,nm$) using a power density of ~70mWcm^{-2}. The dose-response behaviors of ZnO pellets from 1 Gy to 0.1 kGy are given in Figure 4.15a and Figure 4.15b with the CW-OSL decay curves as a function of stimulation time. OSL signal intensities were observed to increase with increasing doses as expected. It was observed in the previous section that the sample calcined at 900 ° C exhibited a crystal structure consisting of well-shaped and clearly defined hexagonal grains. Changes in grain shape were observed up to 1200 ° C calcination condition and this change may be related to the deterioration of the wurtzite structure, which has a negative effect on TL and OSL responses. The same behavior was observed in sol-gel samples sintered at 800 °C. CW-OSL readouts were performed under the same conditions for all samples. The calcination condition of 900 °C - 4 h for the precipitation method and 800 °C - 10 h for the sol-gel method provided meaningful OSL responses.

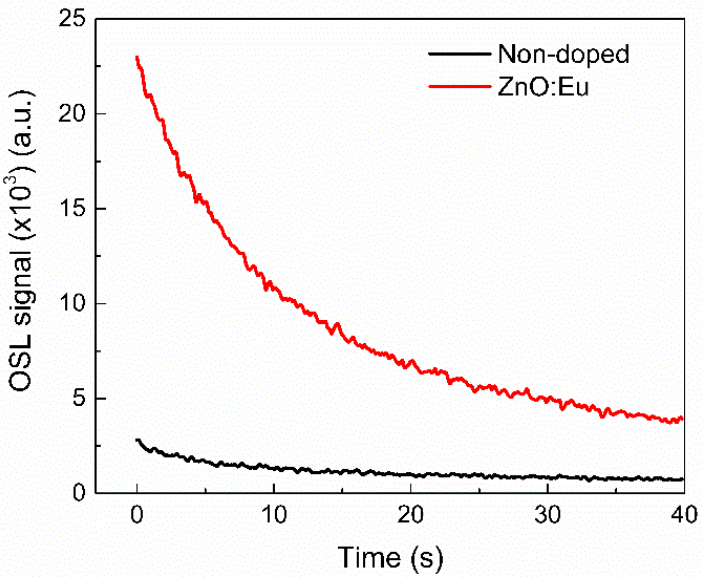

Figure 4.14. The OSL decay curves of undoped and Eu doped ZnO pellets following 20 Gy beta dose using 100 s blue light (λ_{blue}: 470 nm) stimulation. The power density of the light was ~70mWcm^{-2}.

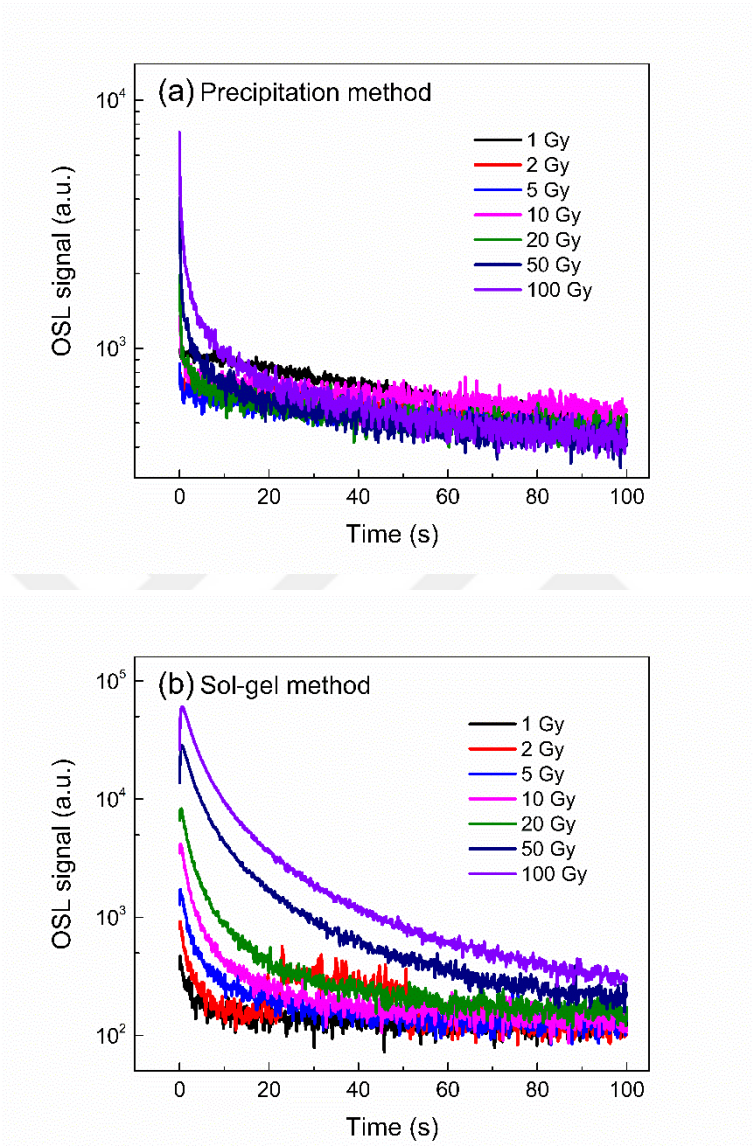

Figure 4.15. The OSL decay curves of the samples calcined (a) at 900 °C for 4 h for the precipitation method and (b) at 800 °C for 10 h for the sol-gel method after exposure of different doses between 1 Gy and 0.1 kGy.

4.1.5. Conclusion

In this study, the effects of precipitation and sol-gel methods and different calcination conditions on the basic PL, TL and OSL curves and the intensities of the relevant signals were investigated. ZnO phosphors were successfully produced by both methods and the calcination conditions were applied afterward. The effects of the production methods and calcination conditions of the samples on TL, OSL and PL properties were reported comparatively. XRD results with single-phase pure hexagonal wurtzite structure and SEM images with well-defined grains are presented. Besides, it was observed from SEM images that porous structures became apparent after 1000 °C with increasing calcination temperatures in both samples. The defect-related green emissions were observed from the PL spectra with $\lambda_{ex} = 350\,nm$. With the excitation of 464 nm, the sharp emission peaks, which are located at 579, 615, 650 and 700 nm, due to $^5D_0 \rightarrow {}^7F_1$, $^5D_0 \rightarrow {}^7F_2$, $^5D_0 \rightarrow {}^7F_3$ and $^5D_0 \rightarrow {}^7F_4$ transitions were clearly seen in the spectra. Two TL peaks located at 130 and 300 °C were determined from ZnO:Eu pellets irradiated with 20 Gy beta doses and these peaks were well separated and simple. Further, these TL peak locations or curve shapes did not change and not shifted with changing the calcination conditions. In the sol-gel and precipitation methods, calcined samples at 800 °C - 10h and 900 ^{o}C - 4h, respectively, showed relatively higher intensities for TL, OSL and PL measurements. Linear dose-response behavior of the samples was determined in the range from 1 Gy to 0.2kGy for both types of samples.

4.2. Study of the Na- and Li-doped MgO

4.2.1. Synthesis Procedure

In the process of preparing MgO phosphors, the solution combustion synthesis method was used by using nitrate-based components and fuel. Firstly, magnesium nitrate hexahydrate and urea were mixed in 100 ml of distilled water.

Stirring was carried out on a hot plate with the help of a magnetic bar in the beaker, and this process took place in a fume hood. The magnetic bar was in the solution until the solution was completely homogeneous. The solution was then heated to 250 °C for 2 hours, then the temperature was raised to 370 °C to dry completely. When the color of the dried material turned into a burnt brown, the heater was turned off. The bulk material cooled to room temperature was taken to the ceramic crucible and the samples were heat-treated at 800 °C for 4 h using a furnace for calcination. The dopants (i.e., lithium and/or sodium nitrate solutions) were used in the first section of the process into the initial solution. The white powder MgO phosphors were collected and ground for the pellet-shaped MgO. Each molding was obtained from 25 mg powder of MgO phosphors. The pellets were prepared for luminescence measurements by sintering at the temperature of 1200 °C for 4 h.

4.2.2. Structural characterization

XRD analyses were carried out to confirm the structural characterization of MgO phosphors (powder) annealed at 800 °C for 4 h. Figure 4.16 shows the diffraction peaks identified by the Miller indices of the Na and Li doped MgO. No different phase due to Na and Li dopant ions was observed. It was determined that the lines of the diffraction pattern of Na and Li doped MgO phosphors matched well with the ICCD: 98-010-4845 reference model reported with a cubic structure for the Fm-3m space group with the unit cell parameters of a=b=c=4.2030 Å. Since no significant change was observed in the XRD patterns of the doped MgO samples, it can be said that the Li and Na doped samples crystallized in the same phase.

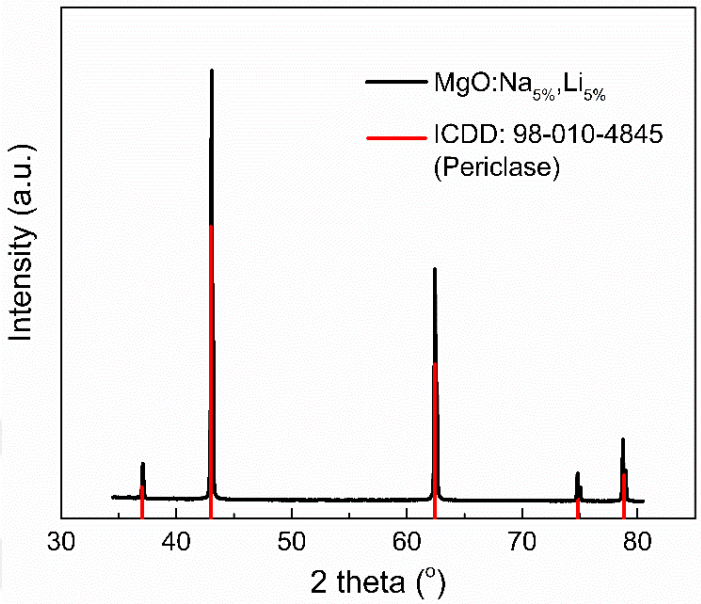

Figure 4.16. The XRD pattern of the MgO:$Na_{5\%}$,$Li_{5\%}$ phosphors synthesized using SCS. Na and Li doped MgO powder were calcined at 800 °C for 4h with an increment of 5 °C per minute.

Figure 4.17 presents SEM images of MgO at different magnifications of 5000, 10000, and 20000 times. SEM images show that the sample calcined at 800 °C has isolated pores, with evident boundaries between its particles of average 300 nm size. It was observed that the particles that were quite evident and homogeneously distributed on the material surface had spherical shapes.

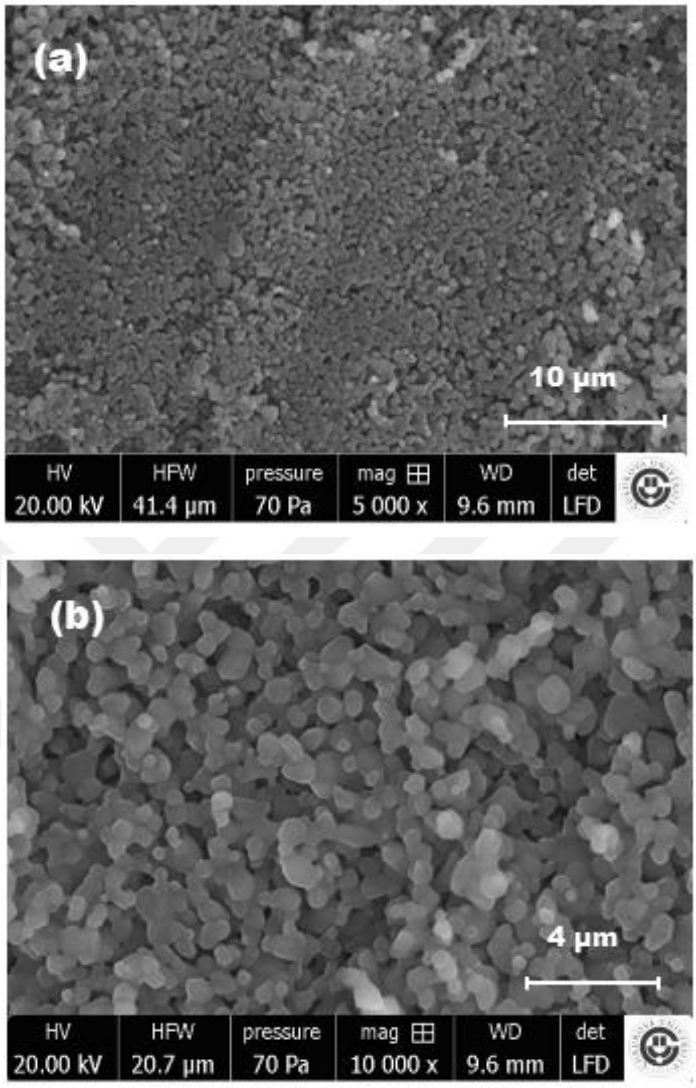
(a)
10 µm
HV
20.00 kV
HFW
41.4 µm
pressure
70 Pa
mag
5 000 x
WD
9.6 mm
det
LFD
(b)
4 µm
HV
20.00 kV
HFW
20.7 µm
pressure
70 Pa
mag
10 000 x
WD
9.6 mm
det
LFD

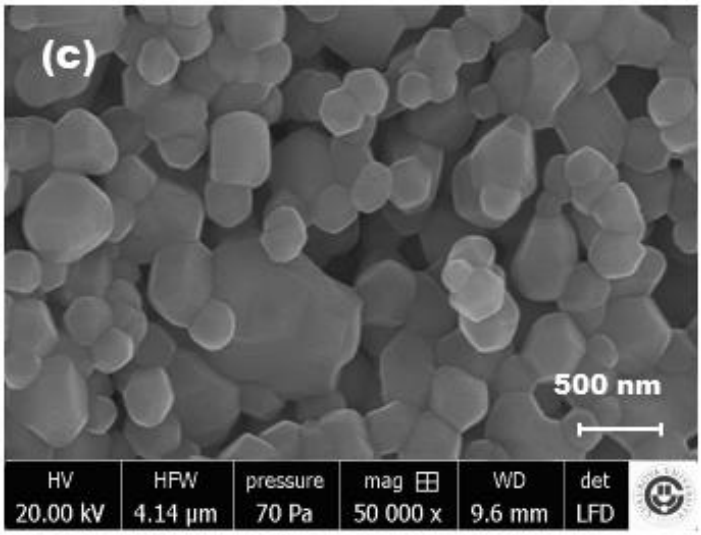

Figure 4.17. The SEM images of MgO:$Na_{5\%}$,$Li_{5\%}$ particles annealed at 800 °C for 4h with (a) 5000x, (b) 10000x and (c) 50000x magnifications. The homogeneous morphology can be seen clearly, in which the particles having almost spherical grains distributed regularly.

4.2.3. Basic RL, TL, and OSL Characteristics

The basic TL and OSL curves of the newly developed doped MgO:$Na_{5\%}$,$Li_{5\%}$ pellets which irradiated with 2 Gy beta doses are given in Figure 4.18a and Figure 4.18b. Further, Figure 4.18c presents the RL spectrum of the doped sample compared with the undoped.

Figure 4.18a presents the TL glow curve of both the newly developed MgO:Na,Li pellet and LiF:Mg,Ti chip, which is described as TLD-100, and well-known and commercially available, after exposure to a beta dose of 2 Gy. Here the TL glow curves are compared as counts recorded per mg. TL signals were recorded in the VIS region using the Schott BG-39 filter. The TL glow curve of MgO:Na,Li, which has 3 different peaks at 80, 245, and 345 °C, showed more than 10 times less intense than that of TLD-100.

As seen in Figure 4.18b, where the OSL signals of the newly developed MgO and the commercially used Al_2O_3:C chip (is known as TLD-500) are

comparatively given, the initial OSL signals are almost the same intensity. However, it is clear that the OSL decay curve of the MgO sample decays faster than Al_2O_3:C (Oliveira et al., 2013c).

The RL measurement was performed to determine the emission bands of the samples. The RL spectra of the undoped and doped MgO are given in Figure 4.18c. All the samples showed two emission bands. It is seen that the emission band located at 730 nm are dominant for all sample. However, the emission band of the doped sample compared to the undoped one showed an increase in the RL emission intensity, especially at 730 nm, with the effect of Na and Li combinations. We think that calcination and sintering processes can create an emission band (~730 nm) of Li centers in MgO. A similar emission spectrum has been reported by Tardio et al., (Tardío et al., 2002). They reported that the oxidation with the calcination or sintering process above 825 °C dispersed Li ions in the precipitate to form "micro-galaxies" containing substitute Li-ions. Since the OSL signals were recorded by the Hoya U-340 bandpass filter (290-390 nm, max 340 nm), however, it is considered that the dominant peak at 730 nm is not in the measurable range and thus contributes little (or no) to OSL signals.

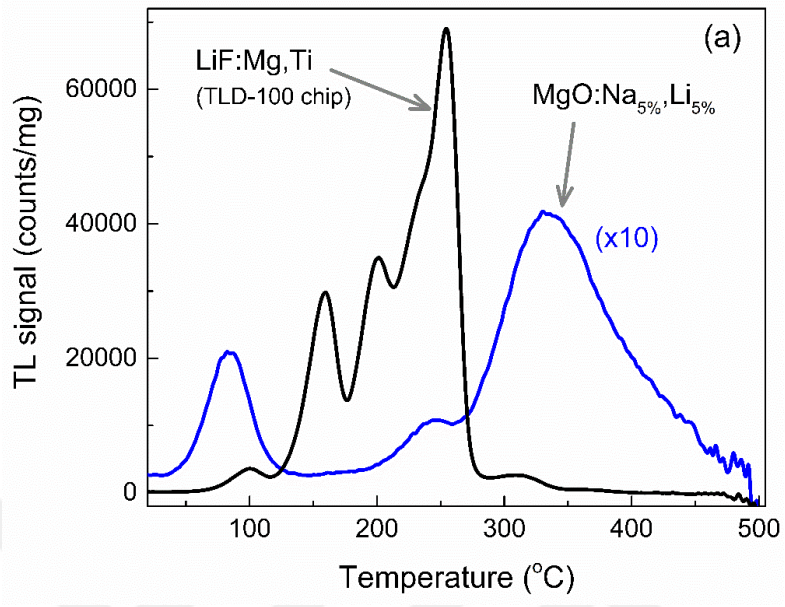
(a)
LiF:Mg,Ti
(TLD-100 chip)
MgO:Na5%,Li5%
(x10)
TL signal (counts/mg)
Temperature (°C)
0
20000
40000
60000
100
200
300
400
500

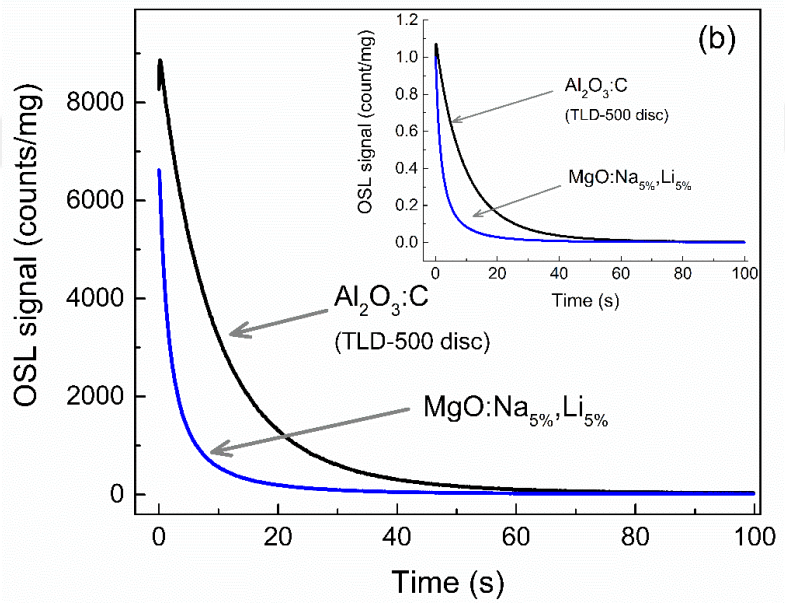
(b)
Al2O3:C
(TLD-500 disc)
MgO:Na5%,Li5%
OSL signal (counts/mg)
Time (s)
OSL signal (count/mg)
Time (s)
0
2000
4000
6000
8000
0
20
40
60
80
100
0.0
0.2
0.4
0.6
0.8
1.0
1.2

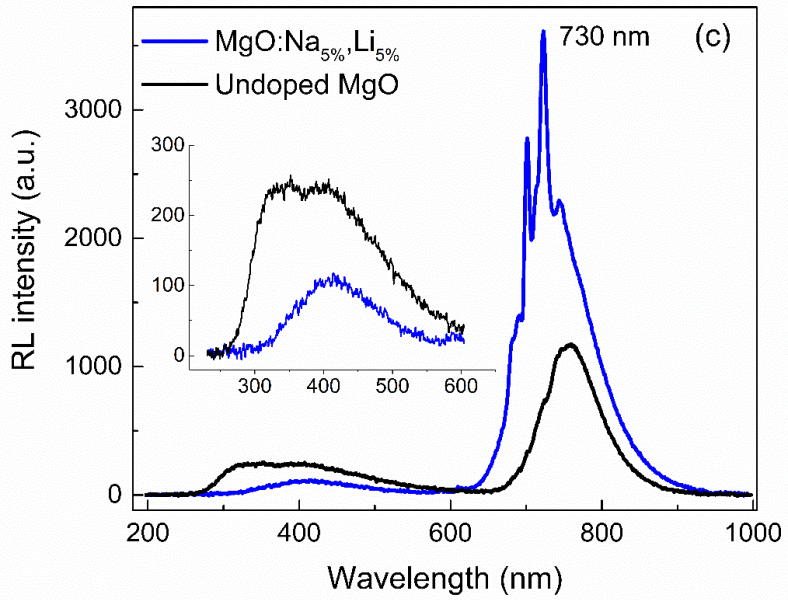

Figure 4.18. a) TL glow curves of MgO:$Na_{5\%}$,$Li_{5\%}$ pellets (sintered at 1200 °C for 4h) and LiF:Mg,Ti following 2 Gy beta exposure for comparison. (b) OSL decay curves of MgO:$Na_{5\%}$,$Li_{5\%}$, and Al_2O_3:C following 2 Gy beta exposure in a semi-log graph. (c) RL emission spectrum of undoped MgO and MgO:$Na_{5\%}$,$Li_{5\%}$ pellets. The emission for undoped and MgO:$Na_{5\%}$,$Li_{5\%}$ samples are from unidentified centers. The comparison of the sensitivity was done by using the counts per milligram sample.

4.2.4. Concentration Quenching of Dopant Elements

Concentration studies of Na and Li doping ions for MgO were systematically carried out in order to develop a high-intensity OSL material. Some of the OSL decay curves studied are given in Figure 4.19. It is not given for concentrations of all single doped samples where peak intensities and shapes do not change. Undoped samples exhibit a narrow TL peak at 90 °C (which is the characteristic peak of undoped MgO), while single-doped samples of Na and Li-ions exhibit TL peaks at 90 and 180 ° C. The single-doped samples MgO:$Na_{5\%}$ and MgO:$Li_{5\%}$ did not show a TL peak at 315 ° C. Binary combination of Na and Li ions on the MgO host material appears to have three different peaks located at 80, 155, and 315 °C.

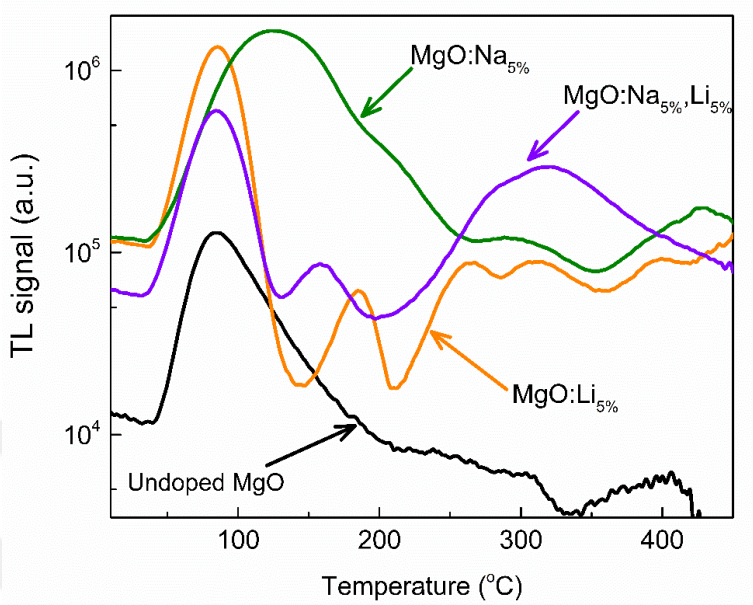

Figure 4.19. The comparison of the TL glow curves of undoped and doped MgO pellets.

The graph clearly shows the presence of an optimum OSL signal obtained with 10% Li doping (Figure 4.20a). OSL signals of the undoped MgO pellets were considerably weaker than the 10% Li concentration. The absence of significant changes in the MgO phase may indicate an increase of up to 10% of possible Li loss during synthesis. Similar improvements in Li-doped luminescence signal were reported by Oliviera et al. (2013). On the other hand, it shows that a 5% Na concentration increases TL and OSL signals 100 times and reaches saturation at luminescence densities for concentrations greater than 5% (see Figure 4.20b) In the case of the binary system of Na and Li dopants, it was observed that the TL and OSL intensities increased with the Li concentration increasing up to 5% and then decreased (Figure 4.20c). It can be said that the reason for the intensities increasing with the concentration of Li dopant could possibly be because it acts as a charge compensator and helps to replace Mg^{2+} with Na^{1+}.

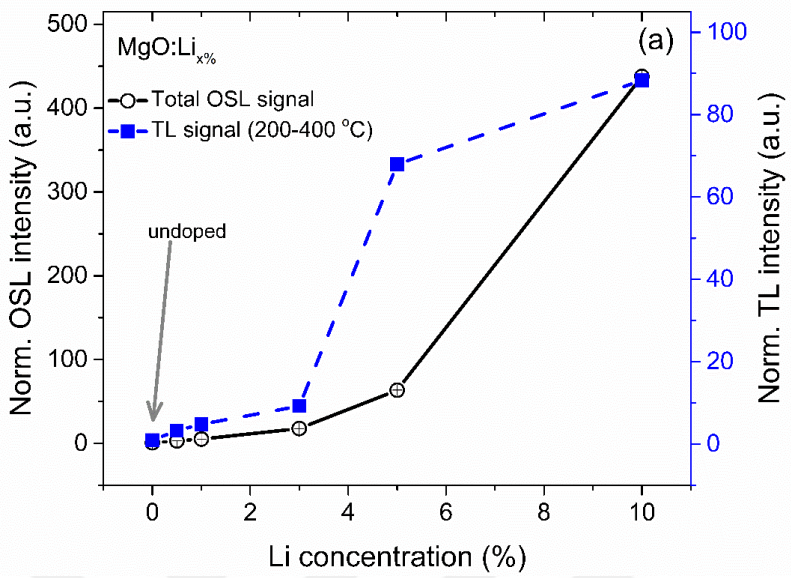
MgO:Li$_{x\%}$
(a)
Total OSL signal
TL signal (200-400 °C)
undoped
Norm. OSL intensity (a.u.)
Norm. TL intensity (a.u.)
Li concentration (%)
0
100
200
300
400
500
0
20
40
60
80
100
0
2
4
6
8
10

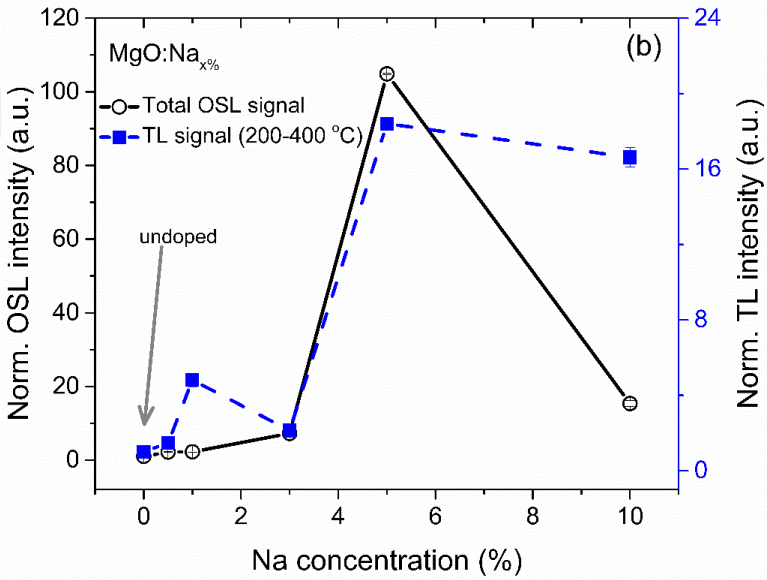
MgO:Na$_{x\%}$
(b)
Total OSL signal
TL signal (200-400 °C)
undoped
Norm. OSL intensity (a.u.)
Norm. TL intensity (a.u.)
Na concentration (%)
0
20
40
60
80
100
120
0
8
16
24
0
2
4
6
8
10

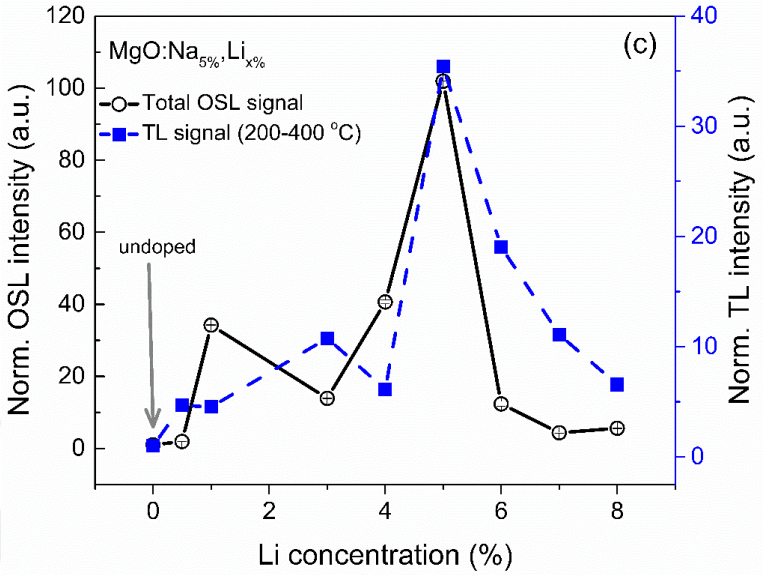

Figure 4.20. The integrated TL signal between 200-400 °C and total OSL signal of the (a) MgO:$Li_{x\%}$, (b) MgO:$Na_{x\%}$ and (c) MgO:$Na_{5\%}$,$Li_{x\%}$ pellets after 2 Gy beta irradiation as a function of dopant concentrations. Undoped is represented as the 0% concentration. Each data corresponds to the measurement of three samples. Li concentration of 10% was not preferred due to the high Li concentration causing structural changes and different phases in the material.

4.2.5. Correlation of TL and OSL signals

To understand the correlation between TL and OSL traps, the recommended and most useful method, the step-annealing experiment was performed and it was observed that the traps responsible for OSL signals did not affect up to 160 ° C. Thus, it can be concluded that shallow traps responsible for the TL signals observed at low temperatures do not contribute much to the OSL signal. When the sample was heated at 170 ° C and above, a significant decrease of OSL signals was detected, and when 250 ° C was reached, the OSL signal was at the background level. Thermally affected OSL traps in the range of 170-250 ° C and the sharp decrease of the OSL signal in this region indicate that TL traps after 250 ° C have no contribution to OSL (see Figure 4.21) (Guckan et al., 2017;

Kawano et al., 2017b; Morris et al., 1993). Further, it was determined that all the traps responsible for TL signals are affected by blue light as is seen in Figure 4.22.

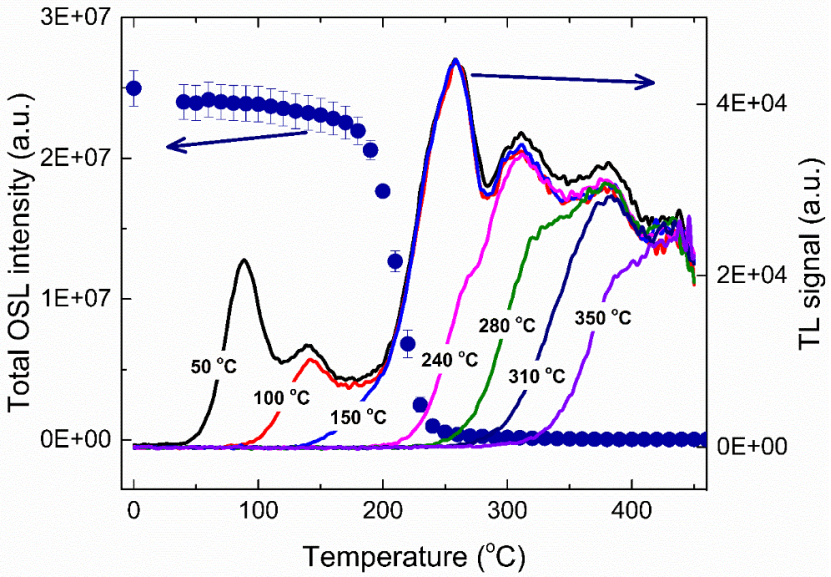

Figure 4.21. The step-annealing measurements were presented with total OSL intensity versus TL glow curve preheated at different temperatures for MgO:$Na_{5\%}$,$Li_{5\%}$. The experimental standard deviation presented as error bars were obtained from three pellets for each cycle. OSL readout was performed using blue light stimulation for 100 s. The samples were depleted using TL readout up to 500 °C for the probability of residual dose after each cycle.

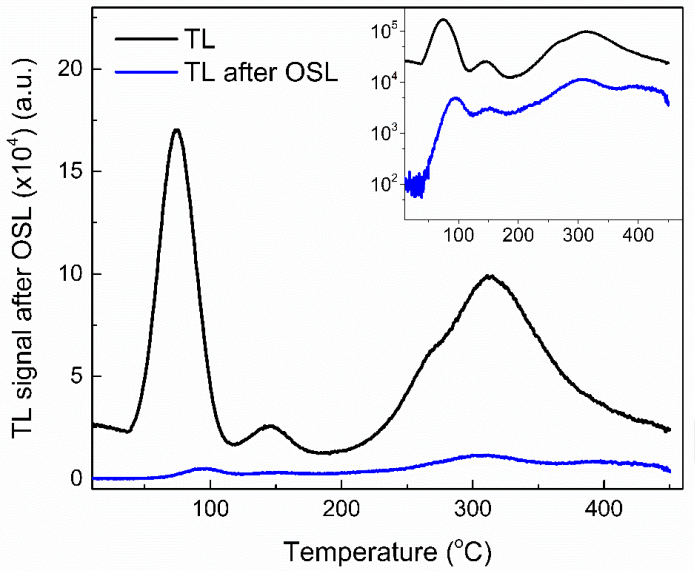

Figure 4.22. The effect of the blue light stimulation on the TL glow curve of the MgO:$Na_{5\%}$,$Li_{5\%}$. The power density of the blue light was ~90mWcm^{-2} during 100 s.

4.2.6. Storage of the OSL signal

Long and short fading experiments were carried out to investigate the storage time of the traps responsible for the OSL signals of MgO. After the samples were irradiated with a beta test dose of 10 Gy and kept in a laboratory room isolated from light, OSL fading tests were performed. Fading as a function of hours and weeks are given in Figure 4.23a ve Figure 4.23b, respectively. After the samples were exposed to beta dose were kept in the dark room. After a storage time of 6 hours, it was observed that there was a loss of approximately 6% in OSL signals. Fading in the OSL signal matched well with each other after 12 hours for the total OSL and initial OSL signal. Fading of the total OSL signal and the initial OSL signal was around 4% after 24 hours. As a result of the 5 weeks storage period, it was observed that both the total OSL signals and the initial OSL signal showed a reduction of approximately 15% and 19%, respectively, compared to readouts taken immediately after irradiation. The small deviations shown as the

shaded area in Figure 4.23a represent the fading and recovery, in principle explained by the various levels of energy storage involving time-sequential energy transfer. This may be due to unstable and shallow traps that release energy at room temperature and/or experimental uncertainties given as error bars (Guckan et al., 2017). While performing fading measurements, three MgO pellets were used as control samples and a correction coefficient was obtained based on the control samples. The usability of MgO:$Na_{5\%}$,$Li_{5\%}$ as control samples was checked by performing a reusability experiment and the samples were subjected to a 30-cycle test. In the 30-cycle experiment, the samples were observed to be reusable with a deviation of 3%.

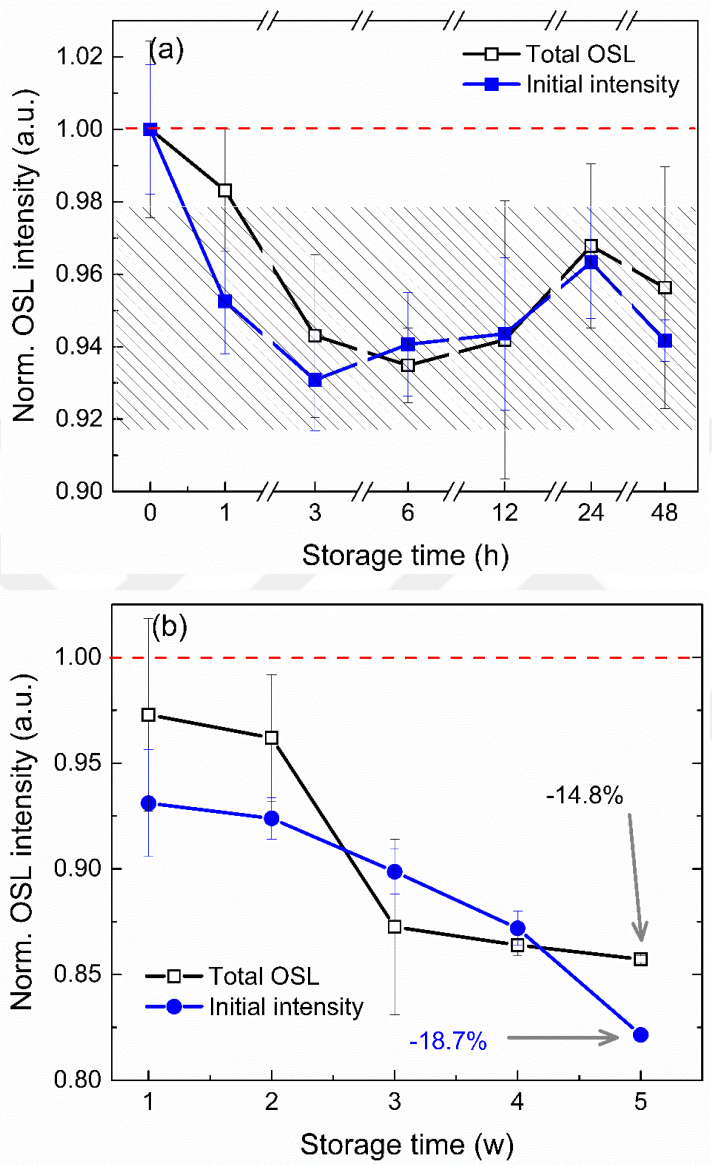

Figure 4.23. Initial OSL signals (in the first second) and total OSL signal as a function of (a) short-term and (b) long-term storage times in the darkroom. To remove the possible contributions that might come from shallow traps (unstable centers), the OSL readout was performed after preheating the sample at 130 °C for 10 s.

4.2.7. Determination and Investigation of the Kinetic Parameters

A typical OSL decay curve seen in Figure 4.24 was obtained from a MgO pellet after irradiation with a 10 Gy beta dose. The OSL curve was obtained with 470 nm blue light excitation used with a power density of 70mWcm^{-2} after preheating. Preheating was applied at 130 °C for 10 seconds to eliminate misleading signals caused by unstable shallow traps. Considering that the production under laboratory conditions will contain experimental errors, taking into account that the signals of the MgO pellets will vary slightly from production to production, fresh samples from the same batch were used in each experiment to increase the reliability of the experiments. It is noted in the literature that an OSL signal decreases as a function of time but does not deteriorate relative to a single exponential function because, during an OSL measurement, electrons may be transferred to the main OSL trap (Morris and Mckeever, 1993), or electron movement caused by deep traps can change the number of recombination centers present, thereby changing the number of OSL traps available. Such charge transfer processes can result in a combination of first and second-order effects, and such possibilities are modeled numerically by multiple exponential functions. In this analysis, the experimental OSL decay curve of the sample was analyzed using the general order kinetics described for isothermal TL as follows (Chen and McKeever, 1997; Kitis et al., 2016);

$$y = S_0(background) + S_1(fast\ component) + S_2(slow\ component)$$

$$I(t) = S_0 + I_1\left[1 + (b_1 - 1)\frac{t}{\tau_1}\right]^{-\frac{b_1}{b_1-1}} + I_2\left[1 + (b_2 - 1)\frac{t}{\tau_2}\right]^{-\frac{b_2}{b_2-1}} + \cdots \quad (4.3)$$

where $I(t)$ is the intensity, S_0 is the background signal, S_1 is the general-order decay function presenting the fast (S_1), medium (S_2) and slow (S_3) decay components of the OSL curve $\tau_{1,2,..} = {}^{1}/_{\lambda_{1,2,...}}$ (s) is the lifetime, and b is the order of kinetics. The kinetic order b was allowed to vary between $1.05 < \mathrm{b} < 2.05$. This general equation can describe many commonly used stimulation modes for luminescence signals like CW-OSL, linearly modulated OSL (LM-OSL), TL, isothermal TL, and TL measured using different heating rates (Kitis et al., 2013). By examining the experimental data, it was observed that the OSL signal could be estimated approximately by Equation (4.3 by applying curve fitting. The curve fitting process was performed using the parameters of amplitude, kinetic order parameters, and decay times, and the smallest figure of merit (FOM) value was obtained (see Table 4.1). It is seen that the OSL trap groups have general order kinetics $(1.05 < b < 2.05; b = 1.95)$ (Kitis et al., 1998). It was found that the time for the OSL signal reaches the background level was τ=4.06 s. It should be noted that fitting such a function does not reflect the actual OSL mechanism of the OSL decay curve and this is only a simplified approach.

Table 4.1. *τ_1 decay times, b_1 kinetic orders and FOM values of the curve fittings using the only component, it has.*

	S_1 (fast component)				
	I_1 (counts)	**τ_1(s)**	**$b_1(\mathrm{a.u.})$**	***S_0* (counts)**	***FOM* (%)**
MgO:$Na_{5\%}$,$Li_{5\%}$	7.67×10^5	4.06	1.95	160.95	2.71

Table 4.2. *Kinetic parameters of MgO:$Na_{5\%}$,$Li_{5\%}$ pellets determined using various methods.*

TL									***OSL***
CGCD					***Extended IRM***		***T_m-T_{stop}***		***Isothermal annealing***
Peak (°C)	**E (eV)**	**b**	**S (s^{-1})**	***life time (s)***	**Plateau region (^{o}C)**	**E (eV)**	**Plateau region (^{o}C)**	**E (eV)**	**E (eV)**
75	0.85	1.55	10^{11}	10^{3}	45-70	0.81	60-90	0.85	
144	0.95	1.75	10^{10}	10^{5}	95-130	0.93	100-140	0.92	
206	1.00	2.01	10^{09}	10^{7}	215-240	1.49	145-175	0.96	
263	1.30	1.47	10^{11}	10^{10}	260-330	1.61	195-220	1.12	1.37
313	1.42	2.01	10^{11}	10^{12}			250-300	1.28	
366	1.50	2.01	10^{10}	10^{15}			305-330	1.36	
432	1.55	2.01	10^{10}	10^{16}			340-370	1.43	
	FOM = 1.29%								

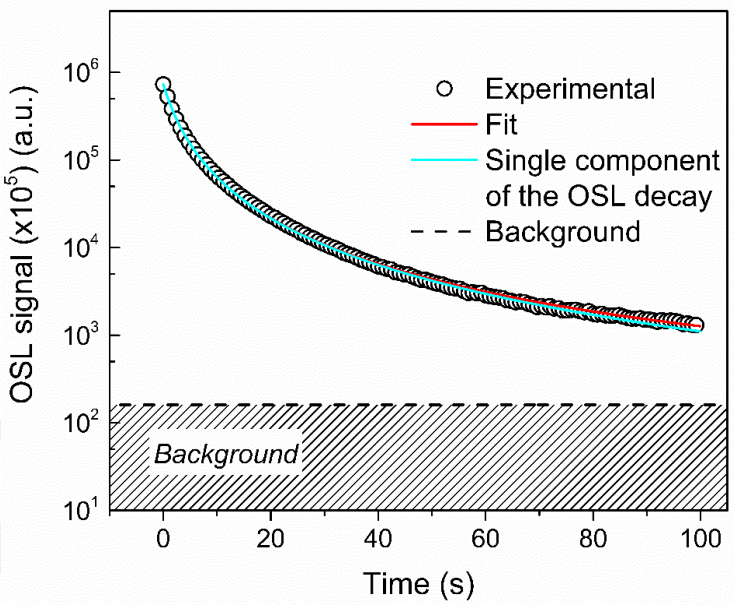

Figure 4.24. OSL signal of the MgO:$Na_{5\%}$,$Li_{5\%}$ as an experimental data after 100 s blue light stimulation following 130 °C preheating for 10 s and calculated data from analysis. S_1 is the single component of this curve from the curve fitting technique.

Kinetic parameters responsible for TL such as trap depth, E_a, frequency factor, s, and kinetic order, b, profoundly affect the dosimetric properties of a sample (Kitis et al., 2000). Moreover, these parameters are linked to the stability of the traps. For a sample with a low E_a, the glow peak will occur at a relatively lower temperature and the corresponding trap can be said to be unstable (Azorin et al., 1989). As a result, the TL signal is expected to fade at room temperature or lose signal. Fading can be pronounced if the frequency factor is high. The order of kinetics indicates whether the trapped charge carriers will be re-trapped in heating. There are several methods used to determine these parameters. The kinetic parameters of the TL glow curve of MgO sample were calculated by three different methods, using general order kinetic equation and/or methods independent of kinetic order.

For the first of these, the TL glow curve, which was thought to have the general order kinetics of a MgO pellet exposed to a 2 Gy beta dose, was deconvoluted by the CGCD method. This method was applied using the Microsoft Excel solver plug-in utility, which allows the analysis of complex TL signals consisting of overlapping peaks. This excel spreadsheet software draft was introduced by Afouxenidis et al. using a special software package (Afouxenidis et al., 2011). The kinetic parameters E_a, s and b values were determined with the help of this software, assuming general sequence kinetics (Kitis et al., 1998). The experimental TL glow curve and its components calculated using the CGCD method are given in Figure 4.25. The calculated approximate values of kinetic parameters are presented to the reader in Table 4.2. The activation energies calculated for each of the components are determined from 0.85 to 1.55 eV and exactly match those calculated using other methods.

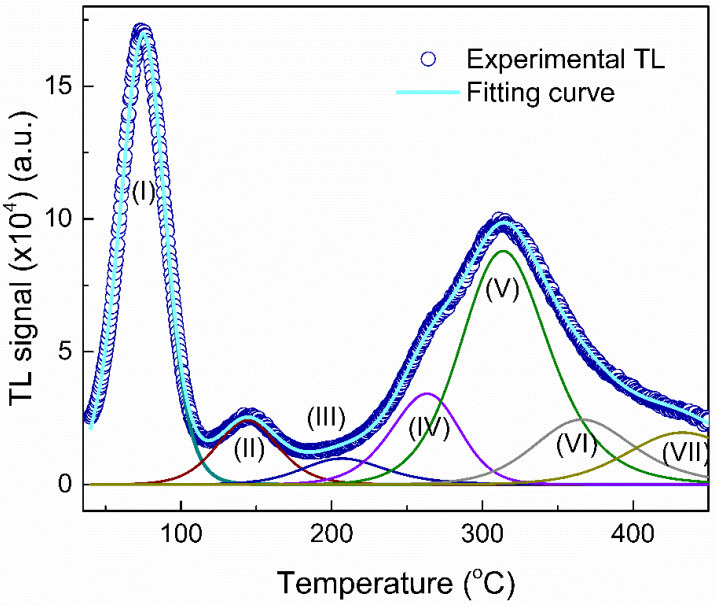

Figure 4.25. The TL glow curve deconvolution (CGCD) of the MgO:$Na_{5\%}$,$Li_{5\%}$. The composite TL glow curve was deconvoluted into seven individual glow peaks.

In another method, the kinetic parameters of the samples were examined using the Multiple Initial Rise Method (MIR). This method is recommended as an extended variance of the initial rise (*IR*) technique (Furetta, 2003). The method is defined as follows: When a single TL readout is applied to the level of 20% of the maximum intensity I, the slope value of the $ln\ (I)\ and\ 1\ /\ kT$ plot represents the activation energy of the corresponding trap. This process is described as the Initial Rise method (Furetta, 2003). As an extended variance of IRM (Chruścińska, 2001; Pietkun et al., 1992; Strickertsson, 1985) specified by Gobrecht and Hofmann (1966) and not dependent on kinetic order, sequential IRM application is applied by sequentially increasing T_{final} maximum measurement temperatures with a short step interval (Gobrecht et al., 1966). This method, available for overlapping peaks, was carried out using a series of sequential TL readouts and cooling at room temperature cycles detailed in one of our previous publications (Guckan et al., 2019). Plateau regions formed by a series of data within a temperature range are defined as indicative of a peak (McKeever, 1950). Five distinct plateau regions between 45-70 ° C, 93-130 ° C, 215-240 ° C and 260-330 ° C were observed as is seen in Figure 4.26. It is thought that the reason for this overlapping of the plateau may be the continuous distribution of trapping states or several closely trap centers with acomplex nature. Table 4.2 presents all E_a values calculated along with other methods in comparison with each other.

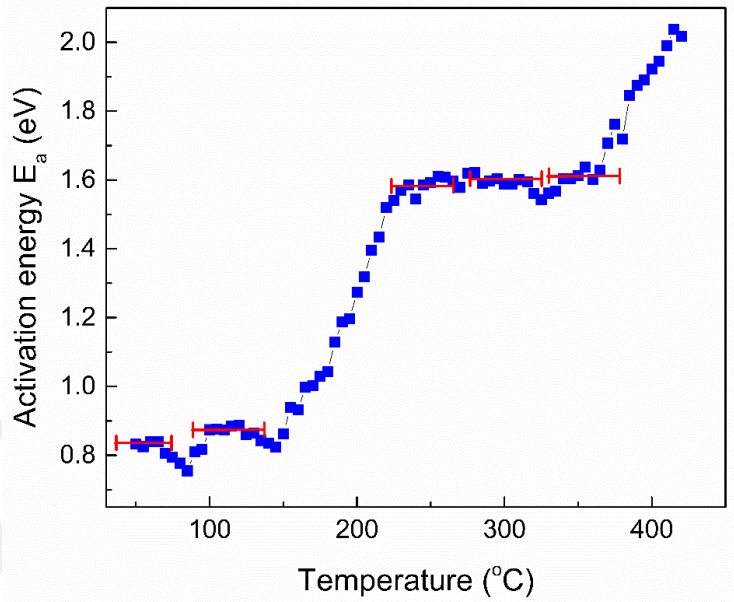

Figure 4.26. Plateaus representing TL traps throughout the temperature region between 50 and 500 °C for MgO pellets. The TL heating rate was 1 $°Cs^{-1}$ and the optical filter was Hoya U-340. The activation energy E_a values were obtained from the slopes of the initial rise curves.

Finally, we used a technique called $T_m - T_{stop}$, which is a very useful method for determining the TL peaks that coincide with their positions within a TL glow curve. This technique has been proposed by McKeever et al., (1980) and the experimental process is described in detail in one of our previous studies (Ozdemir et al., 2016). As can be seen in Figure 4.27, seven plateau regions were observed where activation energies between 0.85 eV and 1.43 eV were defined. The activation energies are given in Table 4.2 along with those obtained using other methods.

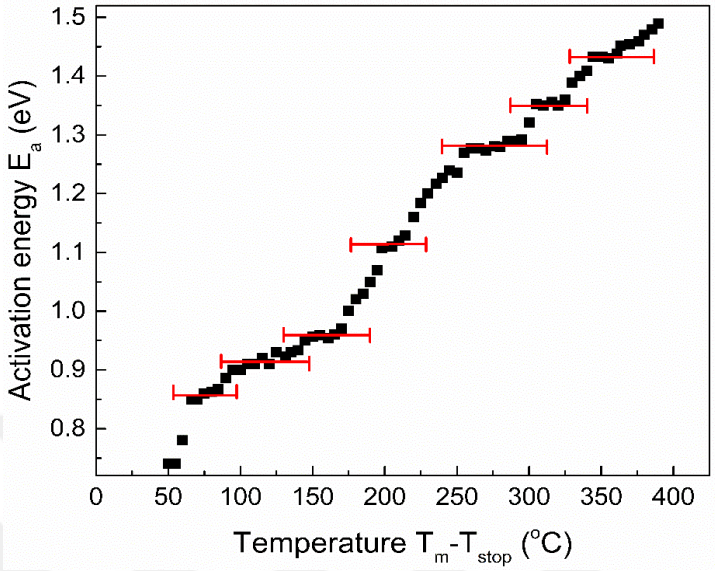

Figure 4.27. Activation energy (E_a) was obtained using the IR method after T_m–T_{stop} procedure from 50 °C to 400 °C.

The thermal stability of the trapping centers related to OSL signals was investigated using the Isothermal Annealing Method to determine the stability in dosimetric applications. Further, activation energy E_a, frequency factor s and kinetic parameters of the OSL signals were estimated using this technique. During the experimental process given in our previous study, three samples exposed to 10 Gy beta dose were kept at various annealing temperatures of 150, 160, 170, 180, 190 and 200 °C for various duration times and OSL signals were recorded after they reached to room temperature. Post-cycle samples were depleted using TL readout for possible residual dose. Since isothermal decay curves are exponential functions of time, we can plot the natural logarithms of the integrated OSL signals as a function of annealing time. The slope values of the isothermal decay curves are equal to the decay times of the signals presented in Figure 4.28a and were used to determine the trap parameters of the samples (Bulur et al., 1998a; Bulur et al., 1998b). Figure 4.28b presents the $ln|slope|$ as a function of $(1/kT)$. Thermal activation energy was obtained as $1.37\,eV$ and the frequency factor as $5.13x10^{12}\,Hz$.

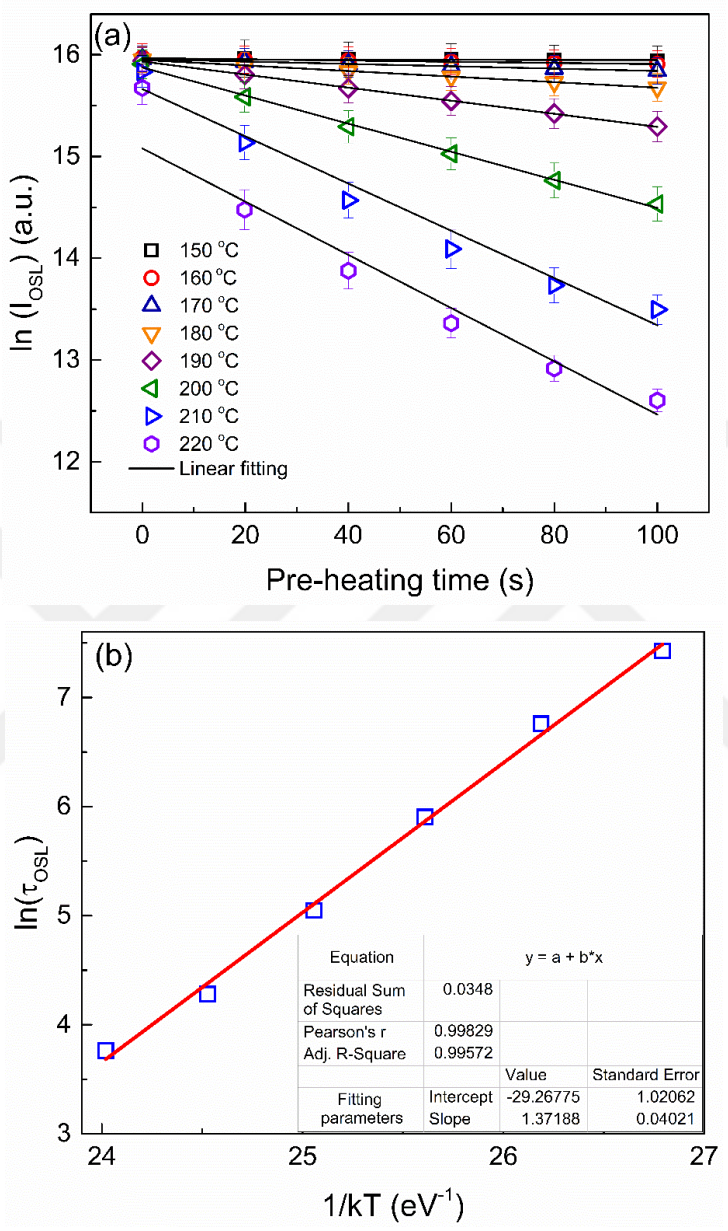

Figure 4.28. (a) Isothermal annealing of the OSL signal of the samples irradiated with 10 Gy beta dose. (b) The natural logarithms of the lifetimes of the OSL signals (ln|slope|) against the reciprocal of the k times preheating temperatures T (1/kT), and the corresponding thermal activation energies.

4.2.8. Conclusion

This study, in which the RL, TL, and OSL properties of the newly developed MgO dosimetric phosphorus were examined and compared with commercial dosimeters, showed that MgO synthesized by the SCS method has luminescence and dosimetric properties for a suitable and high intense OSL dosimeter. Thermally affected OSL traps were observed to be located between 170-250 °C and demonstrated to have an advantage in terms of signal stability due to this narrow region.

An increase in TL and OSL concentrations was detected while Na and Li ions were incorporated into the MgO host matrix. With Na and Li-ions doping of 5% molar concentration, a TL peak around 300 °C caused an increase in intensity and reach its maximum height. This work also includes the study of signal intensity as a function of the concentration ratio of Na and Li dopants that affect OSL signal intensity. The ratio of 5% of the Na and Li concentrations provided the most intense signal for the OSL signal.

It was observed that the newly developed MgO sample was very sensitive to visible light since all TL peaks observed in the TL luminescence curve were depleted after 100 seconds of exposure to 470 nm blue light excitation. Although this behavior suggests that the source of the OSL signal may be related to all observed TL peaks, it has been seen in the step-annealing analysis that the optically depleted charge from TL traps below 170 °C is likely to have some non-radiative transitions. It should also be noted that the luminescence emission may be beyond the detection window.

By using CGCD, IRM and $T_m - T_{stop}$ techniques, the kinetic parameters of the traps responsible for TL signals are presented to the reader comparatively. It was observed that the value of the activation energy obtained by $T_m - T_{stop}$ measurements and calculations were in agreement with those obtained by the multiple IRM and CGCD analysis methods. The activation energy of the traps

responsible for the OSL signal was determined as 1.37 eV by the isothermal annealing method. The fade capacity of the OSL signal was observed to exhibit 15% fading up to 5 weeks of storage.

4.3. Study of the Cu-, Li- and K- activated MgO

4.3.1. Preparation of MgO phosphors

MgO phosphors were synthesized using the SCS method as described above. The synthesis of the substance was performed with some amount of magnesium nitrate hexahydrate as a precursor and urea as a fuel (Guckan et al., 2020b; Oliveira et al., 2013c; Oliveira et al., 2016; Orante-Barrón et al., 2011). These chemicals were mixed in an aqueous medium and taken on a hot plate. The solution was stirred continuously on aplate. The mixture was left to dry at 250 °C for 2 hours after the solution became homogeneous. The temperature was raised to 350 °C and the combustion was observed. When the bulk material cooled down to the room temperature, the calcination procedure was performed at 1000 °C for 2h using an alumina crucible. The certain amount of the molar concentrations of the lithium nitrate, potassium hydroxide (Sigma Aldrich, KOH, ≥85%) and copper nitrate hydrate (Sigma-Aldrich, $Cu(NO_3)_2.xH_2O$, ≥99.0%,) solutions were used for the doping. The powder material after the calcination process was obtained and ground using a pestle and agate mortar. For pellet-shaped material, 30 mg Li, K, and Cu doped MgO powder sample was used and pellets were sintered at 1200 °C for 4 h before the luminescence measurements.

4.3.2. Structural Characterization

X-ray diffraction analysis of the MgO:Cu,Li,K pellets prepared using SCS technique and sintered at 1200 °C for 4h were carried out. The diffraction lines of the sample were presented with the Miller indices which are matched well with the cubic structure and Fm-3m space group (Periclase, ICSD: 98-015-9375). With the low concentration ratio of Cu, no apparent change in the XRD pattern of MgO:Cu

was observed. It can be said that Cu-doped samples are crystallized into the same phase. On the other hand, the XRD patterns of the Li and/or K doped MgO indicated small contributions from Li and K matched well with the ICSD file 98-015-1210 and ICSD file 98-042-6949. Further, this type of behavior was also observed for the Cu, Li, and K dopants as is seen in Figure 4.29.

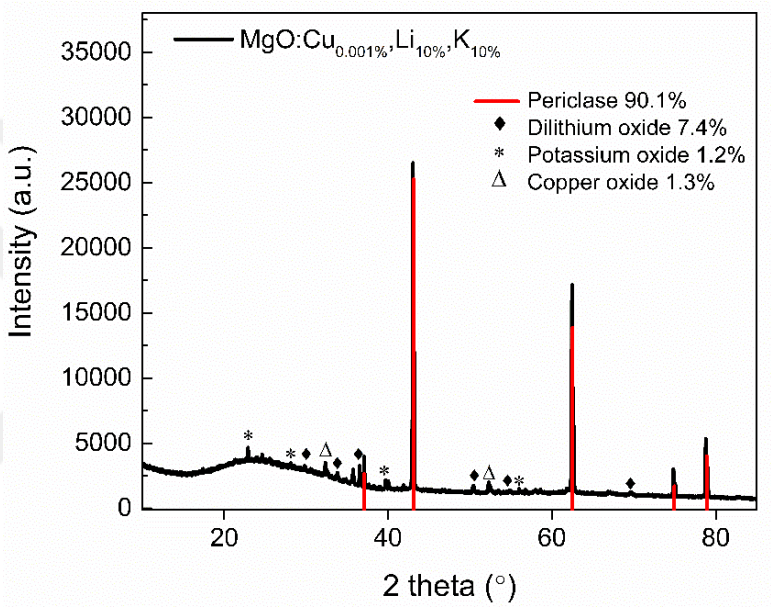

Figure 4.29. XRD patterns for $MgO:Cu_{0.001\%},Li_{10\%},K_{10\%}$ sample synthesized by SCS and annealed at 1200 °C for 4 h. The lines defined from ICSD file 98-015-9375 (Periclase, MgO, cubic structure, Fm-3m space group), ICSD file 96-151-4089 (Dilithium oxide, LiO), ICSD file 98-006-0438 (Potassium oxide, K_2O), and ICSD file 98-009-2364 (Copper oxide, CuO) were found to match well with the XRD pattern of the synthesized material via the Rietveld refinement.

The average crystallite size (D) of MgO:Cu,Li,K phosphors was determined with the Scherrer's equation using the XRD patterns using Equation (4.1 (Kroon, 2013). Crystallite size and FWHM of the MgO sample were calculated and they were found as 460 nm and 0.10 °, respectively.

The SEM images of the sample are given in Figure 4.30a, Figure 4.30b, and Figure 4.30c. The surface morphology of MgO:Cu,Li,K with different magnifications between 1000x and 10000x indicated the homogeneous distribution of the grains. Due to the uneven distribution of the mass in the temperature flow due to the exothermic reaction between metal ions and fuel during combustion, small agglomeration of the particles is observed in some areas and is perfectly normal (Tiwari et al., 2017). To determine the impurities or confirm the accuracy of the dopants indirectly, the EDS measurement was carried out (Figure 4.30d). It is known that the Li dopant could not be detected by EDS because the $Z < 5$. Due to the absorption of low energy X-rays by the beryllium window, Li content was not detected (Goldstein et al., 2017; Hovington et al., 2016).

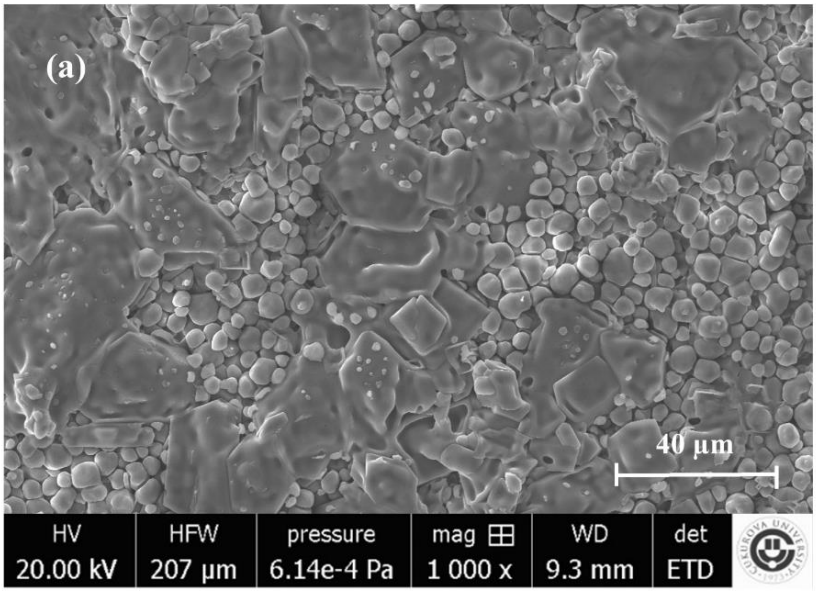

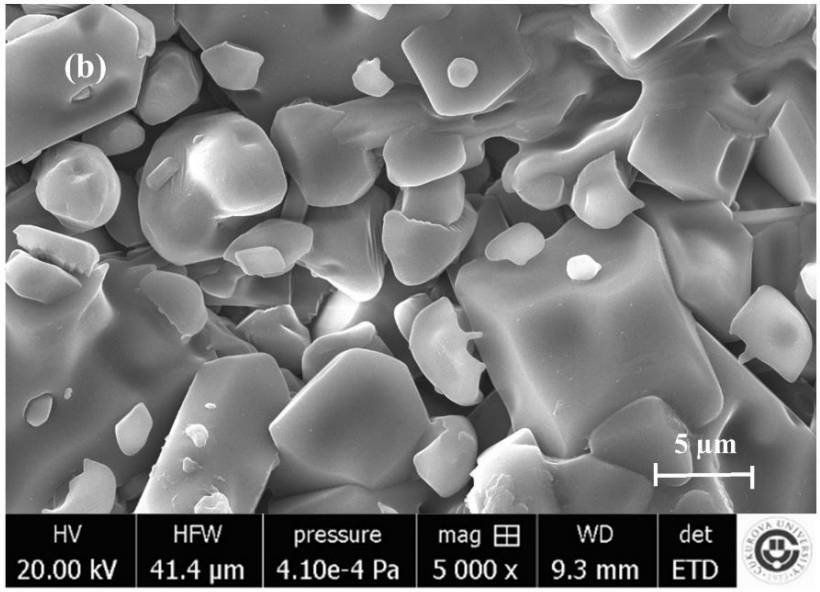
(b)
5 µm
HV
20.00 kV
HFW
41.4 µm
pressure
4.10e-4 Pa
mag
5 000 x
WD
9.3 mm
det
ETD

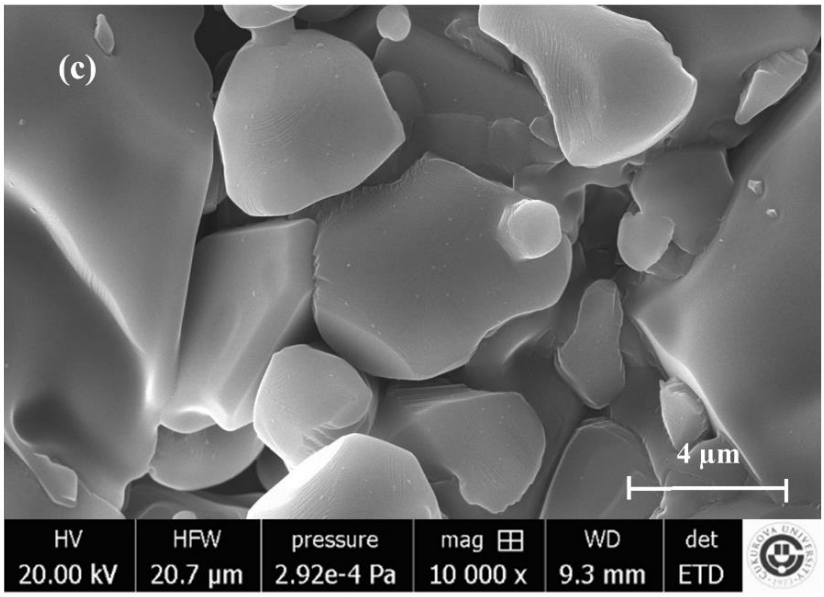
(c)
4 µm
HV
20.00 kV
HFW
20.7 µm
pressure
2.92e-4 Pa
mag
10 000 x
WD
9.3 mm
det
ETD

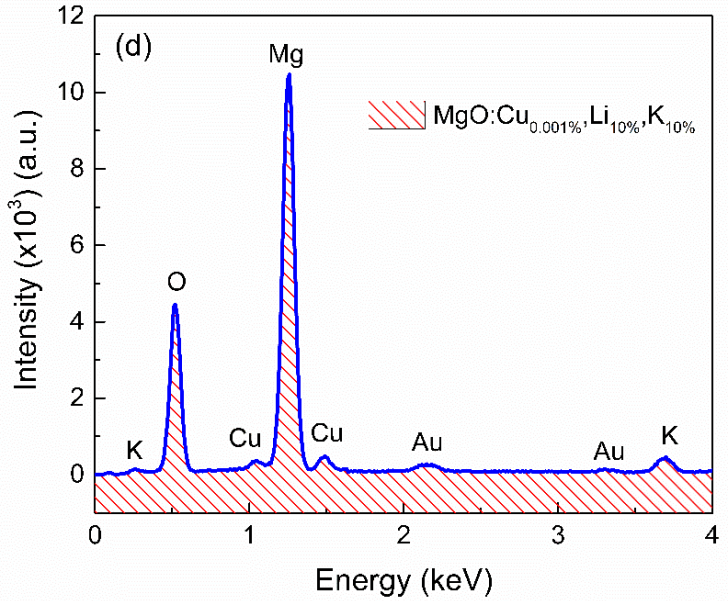

Figure 4.30. The SEM images of MgO:$Cu_{0.001\%}$,$Li1_{0\%}$,$K_{10\%}$ with (a) 1000x and (b) 5000x (c) 10000x magnifications. It has been observed that the cubic particles have a homogeneous morphology with regular distribution on the surface. d) EDS spectrum of the sample.

4.3.3. The Effect of Dopant Concentration

It is generally known that the dopant encourages luminescence by creating a luminescence center to collect and maintain excitation energy. It is also stated that changes in dopant concentration can cause "self-extinction" processes that can offset the emission gain and lead to a weakening of the overall emission intensity. This phenomenon, known as concentration quenching, must be studied in detail in order to create bright luminescence. The development of MgO dosimetry will be possible with systematic studies of concentrations of dopants. Therefore, concentration quenching studies were carried out and the results are presented in Figure 4.31. The TL signals of different doped MgO samples are presented comparatively as a function of temperature in Figure 4.31a. In order to observe different details, the specific TL glow curves for the main dopant concentrations are given in Figure 4.31b on the logarithmic scale. As can be observed from both

figures, the undoped MgO pellets showed a low-temperature peak caused by shallow traps at ~ 80-100 ° C. This peak is defined as the characteristic peak of undoped MgO. At the triple concentration of Cu, Li, and K, MgO appears to have four overlapping peaks with peak maxima found at ~ 97, 213, 276, and 344 ° C. TL intensities of triple dopant combinations as a function of concentration ratios are given in Figure 4.31c. TL readings for each sample exposed to a 2 Gy beta dose were performed under the same conditions with a heating rate of 5 °Cs^{-1} from room temperature to 450 °C. In the graph, undoped MgO is defined as 0%. As can be seen from Figure 4.31c, the undoped sample has the lowest TL density. Higher lithium concentration improved the energy transfer from host to dopant as expected, and the luminescence quenching was observed at a much higher concentration. It can be seen that the most intense emission was obtained when the concentration of Li is 10%.

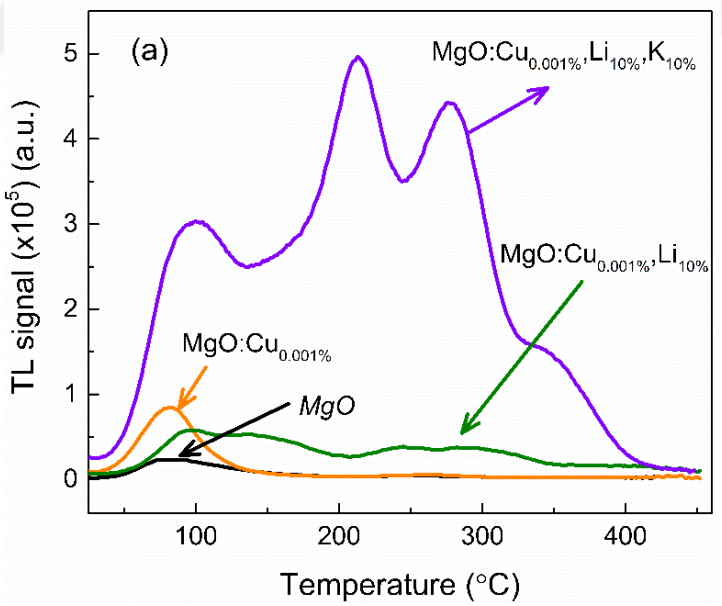

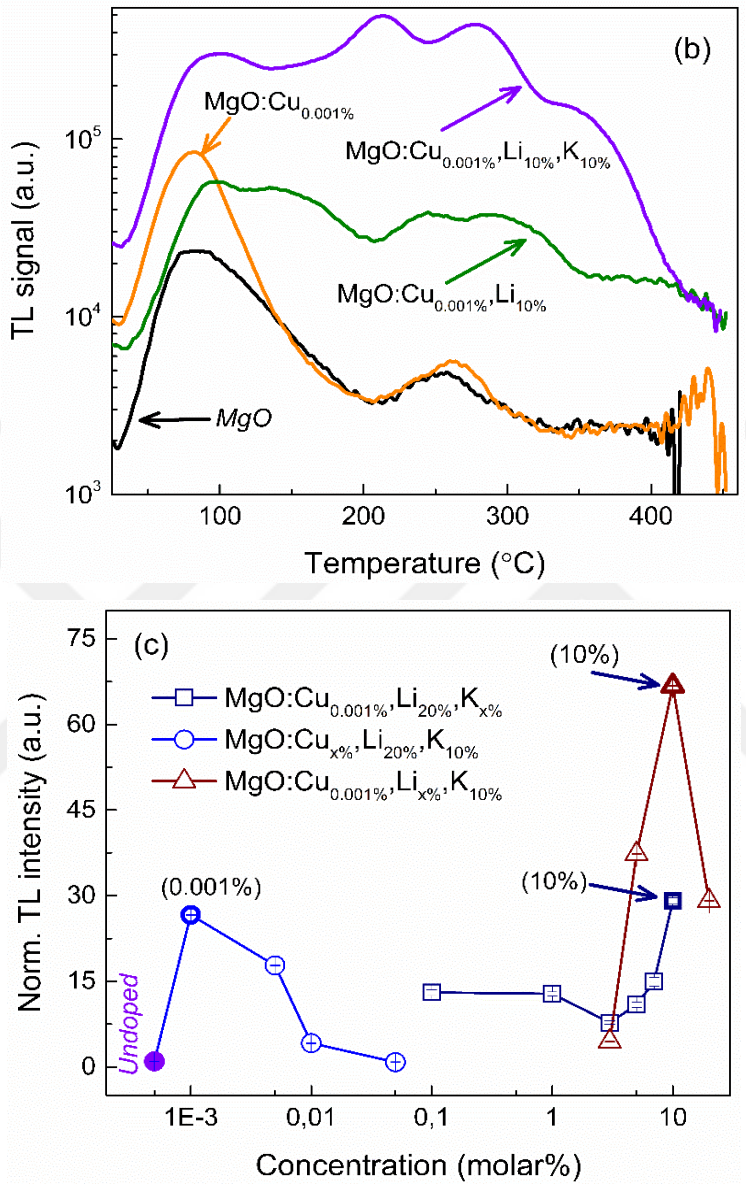

Figure 4.31. (a) TL glow curves of the undoped and doped MgO drown in linear graphic scale and (b) semi-log scale. All TL readouts were performed from room temperature to 450 °C following 2 Gy beta irradiation. (c) The integrated TL intensities of the MgO pellets as a function of dopant concentrations. The undoped MgO is represented by 0% concentration. Each data point corresponds to the mean values of the five pellets and the error bars represent the experimental standard deviations.

Figure 4.32 presents the RL spectra of different MgO samples, with and without dopants. The emergence of a wide and low-intensity peak between 650 and 800 nm is an expected result in terms of the characteristic emission of MgO. An emission band between 320 and 500 nm was also observed for doped MgO. The RL emission intensity increased with the addition of additives. It can be said the emission improved due to the Li co-dopant as a result of the increased intensity of structural defects. Considering that Li+ ions work as a sensitizer, it can be thought that the Li co-dopant homogenizes the distribution with the help of a K dopant in the MgO microcrystals, thereby increasing the luminescence emission in the effective detection range of the PM tube. Kadri et al. suggested that charge compensation was performed due to the substitution of Li^{+} ion in the Mg^{+2} region (Kadri et al., 2020). Therefore, it can be created $2Li_{Mg}^{\cdot\cdot}$ and would give rise to some oxygen vacancies $V_O^{\cdot\cdot}$.

$$Li^{\cdot\cdot} + 2Mg_{Mg}^{\cdot\cdot} \leftrightarrow 2Li_{Mg}^{\cdot\cdot} + O_o^x + V_O^{\cdot\cdot} \tag{4.4}$$

In some studies, it is clearly stated that these oxygen vacancies cause very efficient radiative energy transfer (Gupta et al., 2020; Oliveira et al., 2013c; Oliveira et al., 2019). Finally, in the case of Cu^{2+} dopant, no new TL peaks or any new emission bands were detected, but as can be seen from Figure 4.31 and Figure 4.32, a slight increase in the original TL peak intensity was observed thanks to Cu. Very weak TL signals (in the UV emission range) recorded using the Hoya U-340 filter are associated with the emission band between 320 and 380 nm. It is thought that the source of the TL signals received with the SCHOTT BG-39 filter is the wide emission band at 320-500 nm. The characteristic emission which is the dominant peak at 750 nm, is not within the range in which the filter can be detected, and emission from it cannot be measured as a TL signal or a small amount can be measured.

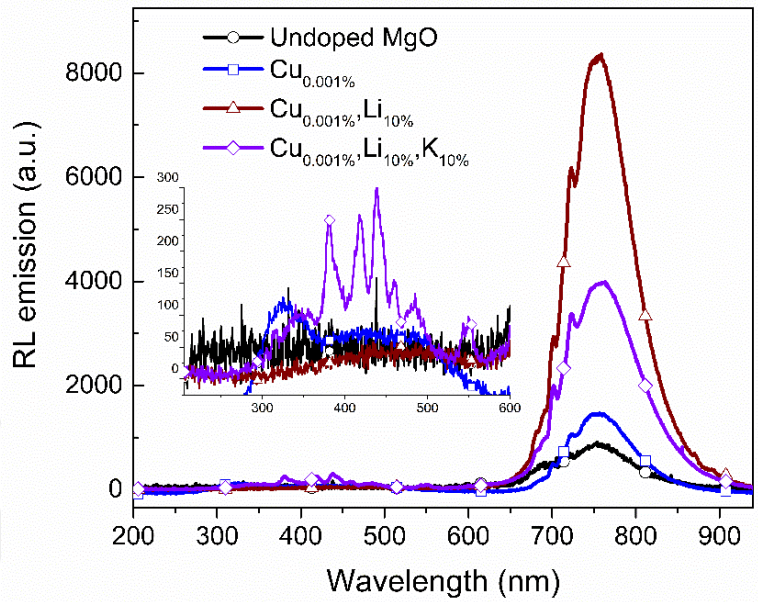

Figure 4.32. The RL emission spectra of the various dopant concentrations of MgO:Cu,Li,K.

4.3.4. TL Glow Curve Analysis

The TL glow curve obtained from the 2 Gy beta irradiated MgO pellet is given in Figure 4.33. TL measurements were carried out by using Schoot BG-39 filter (in the visible region) with a heating rate of 2 °Cs^{-1} from room temperature to 450 °C. It was observed that there were four peaks in the TL glow curve of the MgO pellet at 97, 213 and 276, and 344 °C with a peak maximum. The TL curves of the samples recorded using a HOYA U-340 filter in order to record the emission from the UV region under the same irradiation and reading conditions are given in Figure 4.33b. The sample has a low TL intensity in the UV region. In other parts of the study, all measurements were made using the Schott-BG-39 filter.

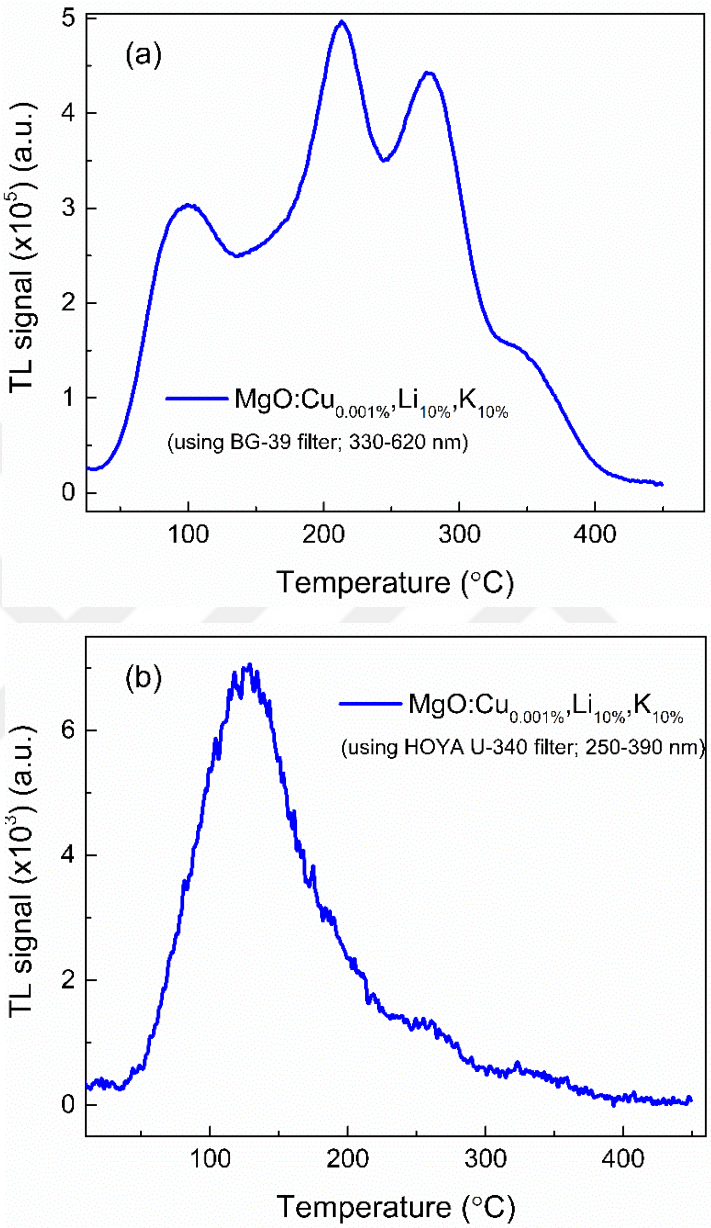

Figure 4.33. The TL glow curve of MgO:Cu,Li,K obtained from room temperature to 450 °C using an (a) SCHOTT BG-39 and (b) HOYA U-340 filter following 2 Gy irradiation.

4.3.5. Annealing and Reusability

The annealing procedures of dosimetric samples are achieved by applying heat treatment in a furnace or reader. However, in-reader annealing is easier to apply and saves time during routine dosimetric measurements with serial TL readings. Therefore, furnace and in-reader annealing processes must be compatible with each other and both procedures must be indistinguishable for MgO. In this study, the residual TL signals were compared after both in-furnace annealings and after annealing in the reader, after the samples were exposed to radiation. The results showed that the residual TL signals were completely depleted, the TL sensitivities and glow curve shapes were the same in both external and in-reader annealing. It showed that the deviation rate of the sample for both procedures was within less than 5% deviation (see Figure 4.34a and Figure 4.34b). Then in the reusability experiment, we performed an in-reader annealing procedure between the following readings, and the average value of the total TL signal of the MgO samples over 30 reading cycles was taken. The maximum deviation of the TL sensitivity of the samples between 30 cycles was measured as 2.5%. Considering these results, it appears that the in-reader annealing procedure is a suitable method for the TL signal and is much easier to save time than furnace annealing. Therefore, in-reader annealing was performed in all experiments in which a series of TL measurements were used for the remainder of the study.

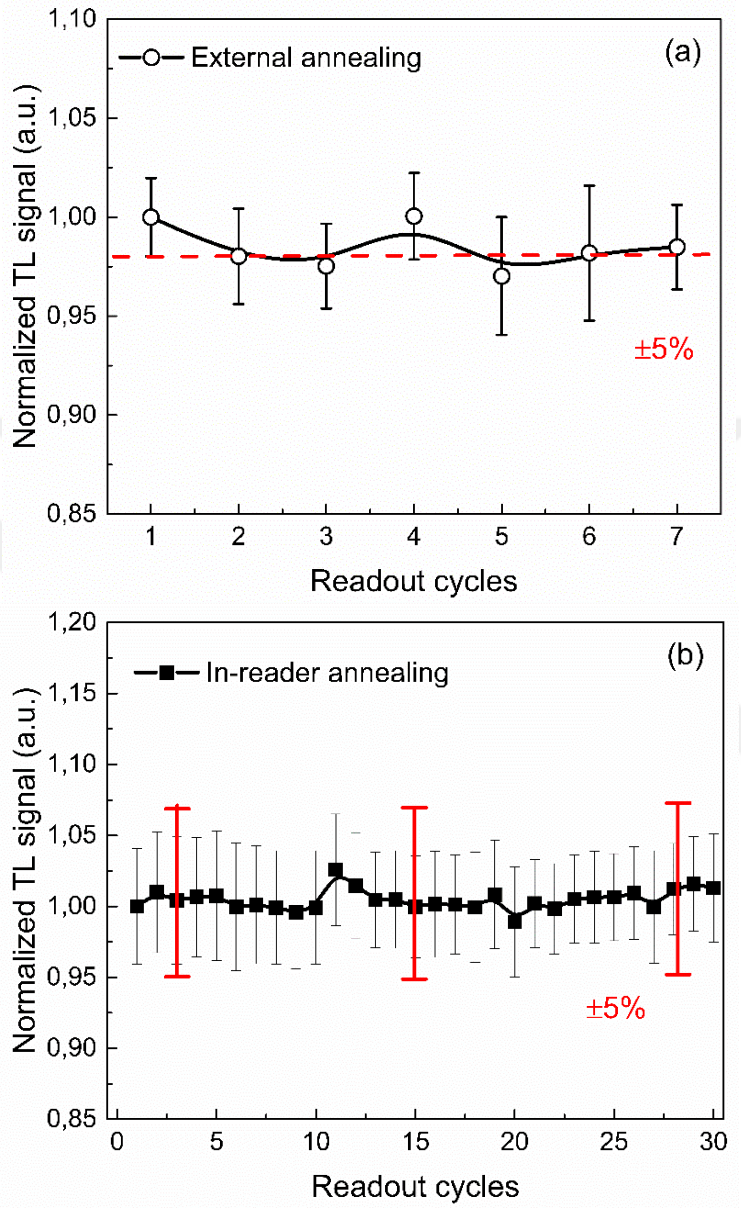

Figure 4.34. Reproducibility of the TL signal using (a) external annealing and (b) in-reader annealing as a function of the cycles. The total signals were normalized to the first readout cycle.

4.3.6. Storage of TL signals

The signal fading of the MgO:Cu,Li,K samples after 2 Gy irradiation was investigated in the darkroom. Regarding the probability that the sensitivities of samples or the reader may change, the three MgO samples were used for control during the readouts performed. These control samples were used to obtain a correction factor. As is shown in Figure 4.35a (short term fading) and Figure 4.35b (long term fading), for the integrated TL signal calculations, the stable TL peaks at 214 and 285 °C were used by taking 10 °C strips passing through the peak maximums of each. At least a 2% change in the TL signal was observed after three hours following irradiation. The fading of the TL signal was found about 3% after 48 hours of storage. The decrease in signal was determined as ~ 5% for two weeks storage period. As a result of the 4-week storage period, it was observed that total TL signals for the TL peaks located at 214 ad 285 °C the amounts of decrease were ~ 5 and 6%, respectively compared to that of the initial signals for both of the TL peaks.

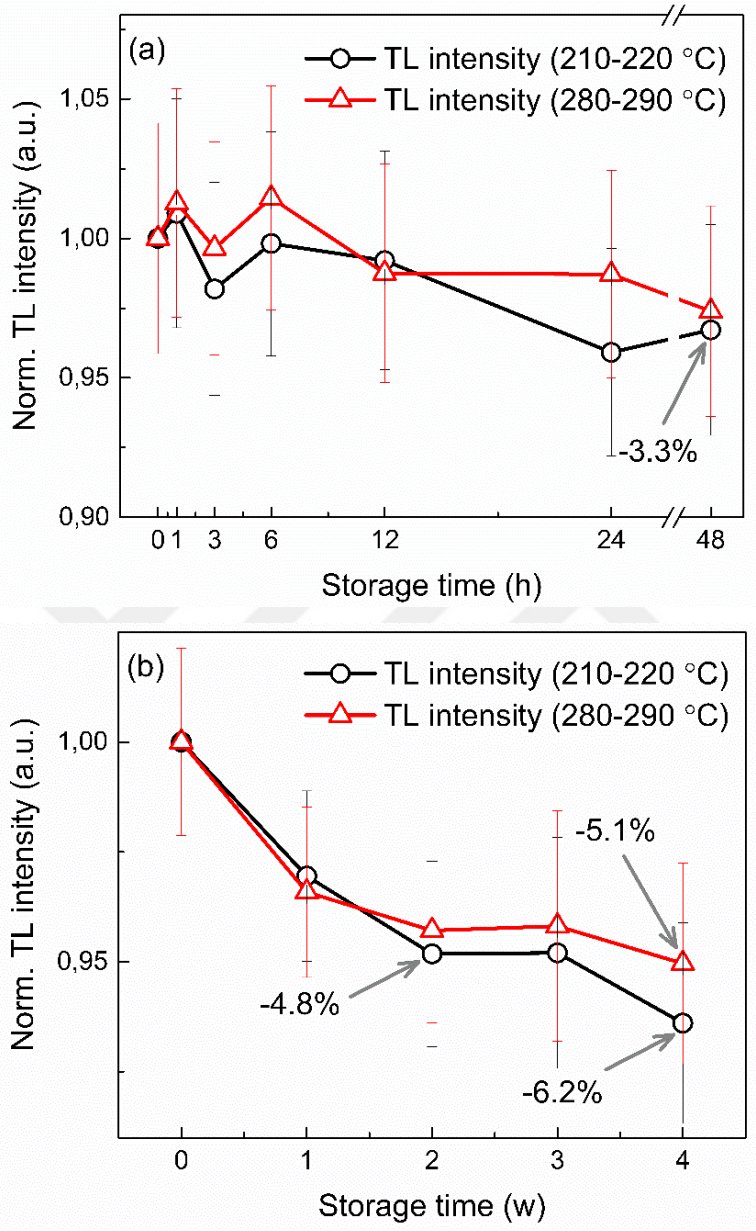

Figure 4.35. The TL intensity from stable traps between 210-220 °C (circles) and 280-290 °C (triangles) as a function of (a) short-term and (b) long-term storage times in a dark room.

4.3.7. Kinetic Parameters

To estimate the kinetic parameters of the studied sample, we used the T_m-T_{stop} method, initial rise method (IR) and computerized glow curve deconvolution analysis (CGCD) methods.

4.3.7.1. Tm -Tstop method

In T_m -T_{stop} measurements, the radiation exposed sample was heated up to a T_{stop} which is a point on the low-temperature tail of a peak. The sample was then allowed to cool down to room temperature and the TL readout was performed to obtain the whole TL peak. Then, the T_m position of the resulting peak was determined as a function of T_{stop}. This procedure was repeated on the same annealed and re-irradiated sample to the T_{stop} of the slightly higher value (T_{stop} was increased by 5 °C for each time). The peak maximum is expected to be independent of T_{stop} in the case of a first-order peak because the first-order TL peak position is reported as independent of the initial intensities of the trapped charge. In the case of the second-order kinetics, the temperature of the peak maximum increases with increasing T_{stop} (Kalita et al., 2017; Kitis et al., 2000; McKeever, 1950). In this experiment, the fresh sample irradiated with a 2 Gy beta dose was first heated to 40 °C, and then the TL readout was performed from room temperature to 450 °C after the sample cooled down. The T_{stop} temperature was increased by 5 °C up to 450 °C and repeated on the same sample irradiated again, each time. The T_m position of the resulting peak is given as a function of T_{stop} in Figure 4.36. As a result, the four peaks were observed in this experiment as in the thermal cleaning technique. Figure 4.36 also shows that all the glow peaks follow the first-order due to the independence of the peak maximum from T_{stop}.

The dose-response behavior of the sample also shows the order of kinetic of any TL peak. If the TL peak is first-order, its position is independent of the irradiation dose. In this experiment, the MgO pellets irradiated up to 0.5 kGy gave the same position Tm temperatures of the peaks as a function of irradiation dose

(data not shown). This result shows that the glow peaks of the MgO sample follow first-order kinetics and support the result of T_m-T_{stop} analysis.

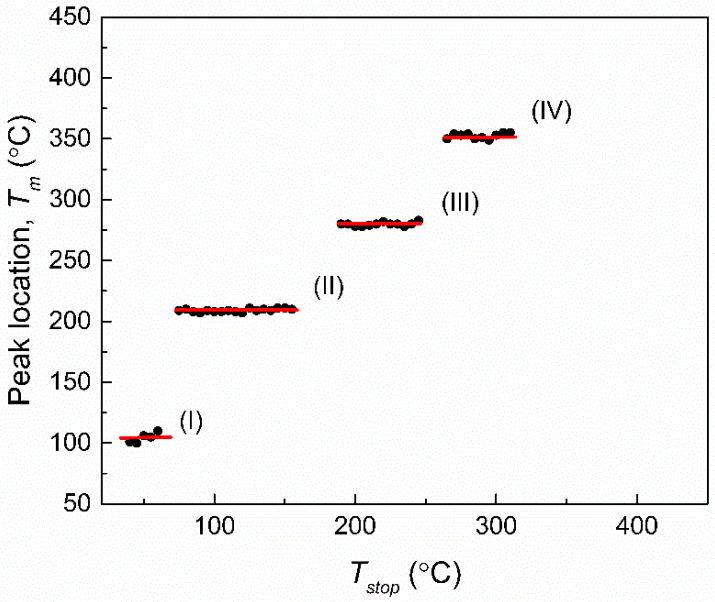

Figure 4.36. The T_m-T_{stop} graph for the MgO:$Cu_{0.001\%}$,$Li_{10\%}$,$K_{10\%}$. Similar to the thermal cleaning technique, four different peaks (denoted as I, II, III, and IV) were observed.

Table 4.3. Comparison of the kinetic parameters obtained by the CGCD, IR, and VHR methods.

CDCD					**IR**		
Peak (°C)	***E(eV)***	***b***	***S (s^{-1})***	***life time (s)***	***Plateu region (°C)***	***E (eV)***	***S (s^{-1})***
95	0.56	1.19	10^{05}	10^{04}	40-85	0.63	10^{12}
153	0.82	1.21	10^{06}	10^{07}	100-135	1.04	10^{14}
212	1.35	1.71	10^{10}	10^{12}	150-185	1.21	10^{16}
279	1.47	1.77	10^{11}	10^{13}	205-245	1.46	10^{19}
350	1.68	1.91	10^{12}	10^{16}	255-340	1.67	10^{20}

4.3.7.2. Computerized deconvolution analysis

The CGCD technique was used with the help of the Microsoft Excel add-in. This excel spreadsheet can be used for the analysis of the complex TL curves with overlapping peaks. Afouxenidis et al. presented this software using a special software package (Afouxenidis et al., 2011). Using this software, the kinetic parameters such as (Ea), (s), and (b) were calculated assuming the general order (Kitis et al., 1998). The TL glow curve and the components are given in Figure 4.37. The goodness of fit (FOM) was tested and determined as 1.84%. Ea, s, and b estimated with CGCD were shown in Table 4.3. Activation energies were observed to have an increasing tendency between 0.50 and 1.68 eV. The kinetic parameters obtained were found to be consistent with the parameters calculated using different methods in other parts of the study.

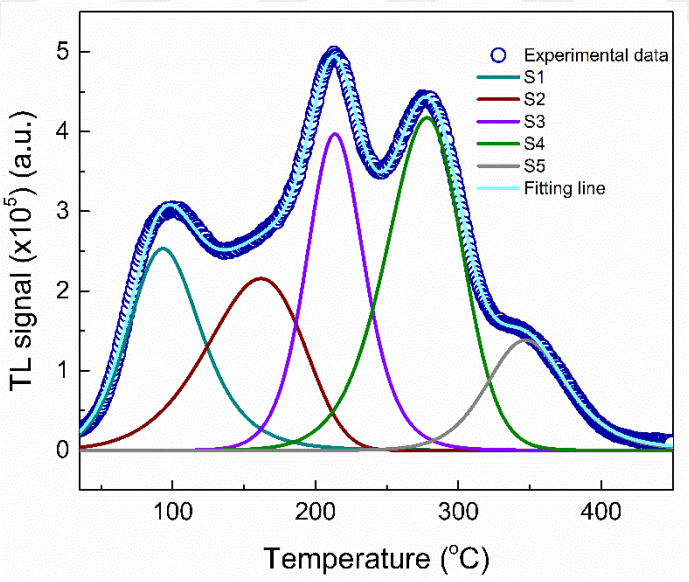

Figure 4.37. "The computerized glow curve deconvolution analysis" components for the TL glow curve of MgO:$Cu_{0.001\%}$,$Li_{10\%}$,$K_{10\%}$. The TL glow curve with overlapped peaks was deconvoluted into five individual peaks ($S_{1\text{-}5}$).

4.3.7.3. Initial rise method

The IR method was performed with a partial heating series that allows the location of the peaks to be recognized. Firstly, a freshly irradiated sample was heated to a temperature on the low-temperature tail of the peak. This was 40 °C for the MgO:Cu,Li,K sample. The sample was then allowed to cool down to room temperature in the reader and then reheated to a different value $T_1 > T_2$ under the same conditions. Then, T_{stop} was increased in small increments of 5 °C for each experimental step. The heating rate of TL readout was 2 °Cs^{-1}. Activation energy, E, was calculated for each temperature step from an $\ln(I)$ against $1/T$ graph. The activation energies for MgO:Cu,Li,K samples are shown in Figure 4.38. Corresponding to the position of the first peak located from 40 to 130 °C, the E values increase slowly between 0.60 and 1.00 eV. Corresponding to the second peak beyond 130 °C, the activation energy was ~1.30 eV. In the region of the third and fourth peaks, the activation energies increase up to 2 eV. The results obtained from the initial rise technique are in good agreement with the other studied techniques to determine kinetic parameters (Table 4.3).

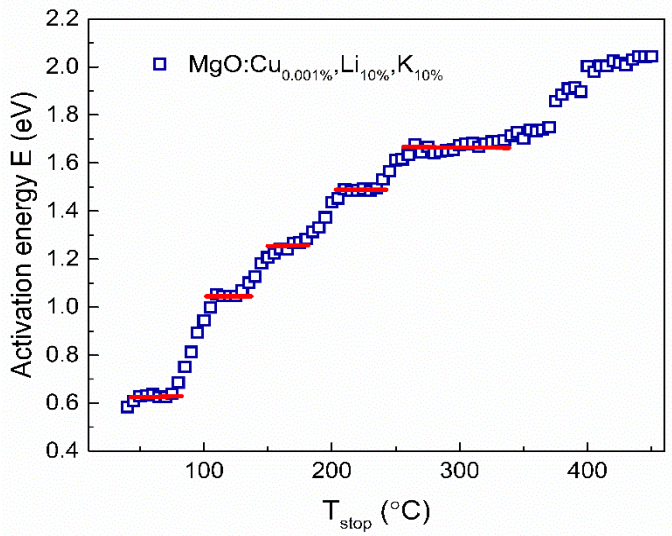

Figure 4.38. Activation energies obtained from initial rise method for MgO:$Cu_{0.001\%}$,$Li_{10\%}$,$K10_{\%}$ were highlighted with the red lines . T_{stop} was increased by 5 °C for each experimental step.

4.3.8. Dose-Response

The dose-response behaviors of the TL signals from MgO:Cu,Li,K pellets were presented by exposing the samples with beta particles, from 0.1 Gy to 500 Gy dose. The samples were irradiated with 0.1, 0.2, 0.5, 1, 2, 5, 10, 20, 50, 100, 200 and 500 Gy beta dose values. The samples were annealed using in-reader annealing at the end of each TL read-out to deplete the residual luminescent signals. The plot of integrated TL intensities as a function of absorbed dose was presented in Figure 4.39a. The integrated TL intensities were determined from the integrated counts of the strips (10 °C widths) passing through the maximum peak points of 214 and 285 °C TL peaks. The dose-response behavior of the MgO:Cu,Li,K pellets was found to be slightly linear with the 1.02 slope value in the dose range between 0.1 Gy and 500 Gy. The TL glow curves of the sample from different dose exposures from 0.1 Gy to 500 Gy were presented in Figure 4.39b. As is shown in the figure, the obtained TL glow curve shapes including high-temperature peaks did not vary significantly even with high doses. There isn't any specific high-temperature peak with higher doses. In this study, we did not read out the samples up to 650 °C which is the highest probable temperature for our Riso TL/OSL Reader because of the increasing background signal which prevents the record of the actual TL emission from the sample. Inconsistent with the dose-response behavior, the minimum detectable dose value (MDD) has been calculated using the following equation (Rawat et al., 2014);

$$MDD\ (Gy) = \frac{3\sigma(counts)}{a(counts * Gy^{-1})} \tag{4.5}$$

where σ is the standard deviation of the background signal of non-irradiated samples and a is the integrated TL signal counts from 1 Gy irradiated samples for the same integration regions of the dose responses. The MDD value of the MgO:Cu,Li,K pellet was calculated as ~ 5.9 μGy.

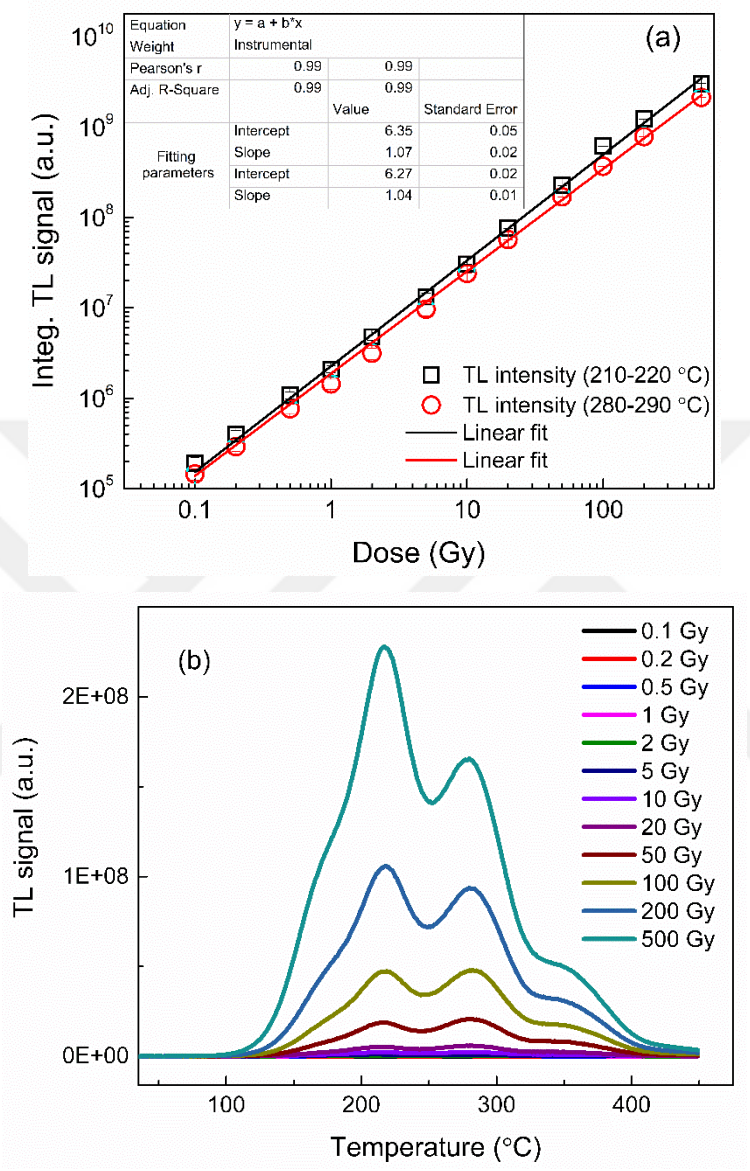

Figure 4.39. (a) Dose-response behavior of the total TL signals (200-300 °C stable traps) from MgO:Cu,Li,K pellets between 0.1 Gy and 0.5 kGy. The TL readout was performed from room temperature up to 450 °C for each cycle following the irradiation of the samples at the relevant dose value. (b) The TL glow curves of the sample from different dose excitation.

4.3.9. Conclusion

In this study, Cu, Li, K doped MgO samples were produced successfully by the SCS method and the results of the XRD analysis showed that the samples have a cubic structure. The dosimetric characteristics and kinetic parameters of beta irradiated MgO:$Cu_{0.001\%}$,$Li_{10\%}$,$K_{10\%}$ have been investigated for exploration of its potential as an alternative phosphor for dosimetry applications. Its glow curve consists of four overlapped peaks at 108, 214, 285, and 375 °C for TL readout performed with a 2 °C/s heating rate. Analysis of the peaks using T_m-T_{stop} and dose dependency methods shows that the peak follows first-order kinetics. The TL dose-response from stable traps was determined to be slightly linear with slope values of dose-response lines as 1.02 between 0.1 Gy and 0.5 kGy. Additionally, the MDD value was found ~5.9 μGy. The TL intensity decays nearly 3 and 3.3% for the peaks at 214 and 285 °C, respectively, in 48 h. Afterward, the same decays were determined as 5.1 and 6.2% for four weeks. The activation energy E of the main dosimetric peak located at around 214 °C is ~1.40 eV. The frequency factor s for this peak is 10^{14} s^{-1}.

4.4. Study of the Tb-, Gd-, and Li-doped MgO using Infrared-OSL

4.4.1. Material preparation

Undoped MgO phosphor was obtained in the polycrystalline powder form using the solution combustion synthesis (SCS) method as follows: The magnesium nitrate hexahydrate ($Mg(NO_3)_2.6H_2O$, *ACS Reagent, Sigma Aldrich)* as precursor and urea *(*CH_4N_2O, *Bioreagent, Sigma-Aldrich*) as fuel were mixed in purified water with stoichiometric amounts. The materials used as dopants in this study were lithium nitrate *(*$LiNO_3$, *ReagentPlus®, Sigma-Aldrich)*, terbium nitrate pentahydrate ($Tb(NO_3)_3.5H_2O$, *99.9% trace metals basis, Sigma-Aldrich*) and gadolinium nitrate hexahydrate *(*$Gd(NO_3)_3.6H_2O$, *99.99% trace metals basis, Sigma-Aldrich)*. All dopants were added with a certain ratio by calculating

according to the molar rate of the precursor material magnesium nitrate. The finely dispersed precursor containing a stoichiometric composite of used compounds was co-precipitated by stirring to achieve the desirable homogenous phosphor. The material was dried until the material became more viscous and clearer by complete evaporation of the water. The bulk material was burned at 350 ^{o}C and ultimately, a white hard solid was obtained. The dopant concentrations quoted in this study are nominal values used during synthesis; the actual concentration incorporated in the lattice is not known because of losses during the synthesis process. In this work, the grounded white powder was calcinated at 1000 °C for 2h (in the air atmosphere). Then, approximately 30 mg powder was filled into a die of 6 mm diameter and 0.8 mm thickness and prepared the pellet-shaped MgO. A Carver press was used for the pellet pressing. In this study, the sintering temperature was fixed at 1200 °C for 4 h. The sintering of the prepared pellets was undertaken in the air in a high-temperature furnace (Nabertherm GmbH, Lilienthal, Germany).

4.4.2. Structural characterization

X-ray diffraction analysis was performed to investigate the crystal structure and phase composition of doped MgO sintered at 1200 °C for 4 h. The XRD crystallographic pattern of the MgO phosphor doped with Li, Tb, and Gd is shown in Figure 4.40a. Miller indices were indicated for the peaks associated with MgO reported in the ICSD card numbered as ICSD:98-005-2026 and matched well with its Fm-3m space group and cubic structure. Although some peaks were observed due to dopants, no significant difference was identified in the crystallographic structure of the host material. In Figure 4.40a, the circles indicate peaks associated with Li_2O phases (ICSD file 98-064-2216, lithium oxide), stars indicate Tb_2O_3 phases (ICSD file 98-005-3635, terbium oxide) and triangles indicate Gd_2O_3 phases (ICSD file 98-016-0886, gadolinium oxide). For the Tb, Gd, and Li doped samples, the XRD indicates a small contribution from Tb_2O_3, Gd_2O_3, and Li_2O phases,

although of very low intensity, indicating the difficulty for Tb, Gd, and Li atoms to be introduced in the MgO crystal structure (Oliveira et al., 2013c).

The morphology and crystal surface of the MgO:Tb,Gd,Li samples in pellet form were analyzed through the SEM pictures. The SEM image of the MgO:Tb,Gd,Li sample in pellet form, thermally treated at 1200 °C for 4 h is presented in Fig.1b. SEM image (see Figure 4.40b) shows that all microparticles are uniform and a size of about < 0.1 μ. By prolonged thermal treatment, the sintering process is enhanced, but some micropores are still enclosed in the obtained dense samples (Figure 4.40b). It can be observed a heterogeneous microstructure with regions of small grains and regions of large grains of irregular shapes and this can be attributed to the different phases observed in the XRD pattern. The EDS analysis was performed to investigate the elemental impurities (see Figure 4.40c). The Li content (Z < 5) could not be detected by EDS due to the absorption of low-energy X-rays by the beryllium window which is located in front of the detector (Goldstein et al., 2017; Hovington et al., 2016).

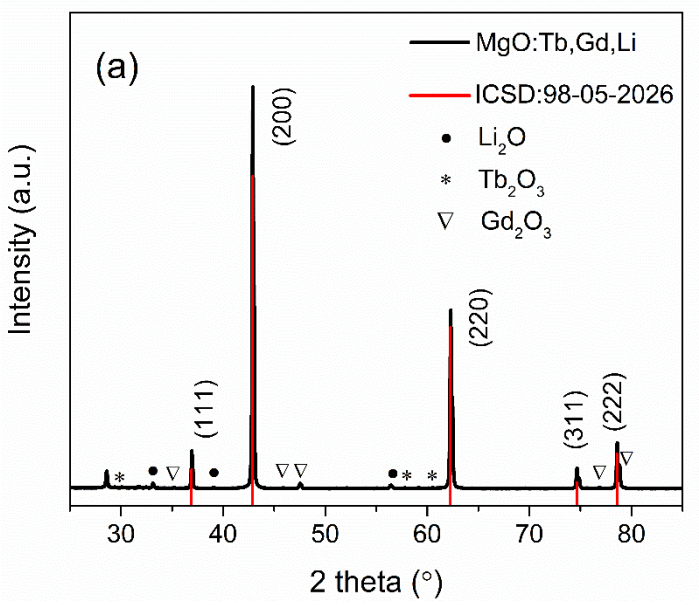

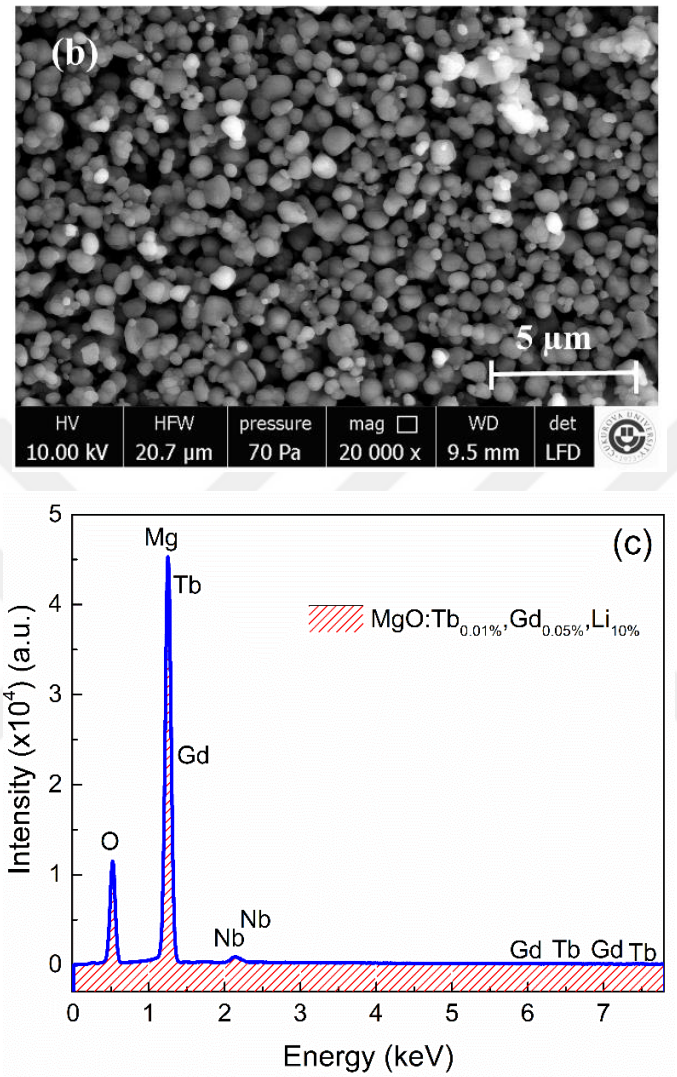

Figure 4.40. (a) XRD data for Tb, Gd and Li doped MgO phosphor synthesized using SCS method and sintered at 1200 °C for 4 h. The diffraction pattern was identified by the Miller indices match that from *ICSD:98-005-2026 (MgO, Fm-3m space group, cubic structure)*. The lines indicated by a circle, stars, and triangles are associated with the Li_2O *(ICSD file 98-064-2216, lithium oxide)*, Tb_2O_3 *(ICSD file 98-005-3635, terbium oxide)*, and Gd_2O_3 *(ICSD file 98-016-0886, gadolinium oxide)* phases, respectively. (b) The SEM image of Tb,Gd,Li doped MgO phosphor was calcined at 1000 °C for 2h and sintered at 1200 °C for 4h. Homogeneous morphology exists over all the sample surfaces. (c) EDS spectrum of the MgO:Tb,Gd,Li pellet.

4.4.3. Concentration quenching

During optimizing dopant concentration, one should avoid the concentration quenching, which can lead to increased non-radiative transitions responsible for the decrease in luminescence efficiency (Chen et al., 2016). To investigate the effect of dopants on Infrared-OSL (IRSL) intensities of MgO and achieve the highest luminescence intensity, concentration quenching studies were performed. Single and multiple doped MgO were prepared with various dopant concentrations (0.005, 0.01, 0.05, 0.1, 0.5, 1, 3, 5 mole%) and IRSL decay curves were recorded after 1 Gy beta dose exposure. Figure 4.41a shows the IRSL decay curves obtained from MgO, MgO:Tb, MgO:Gd, MgO:Tb,Gd and MgO:Tb,Gd,Li pellets. The IRSL signals showed that the Tb and Gd doped MgO samples were about 2 times higher than the single-doped MgO samples with Tb^{3+} or Gd^{3+}. This increase in IRSL intensity is about five orders of magnitude compared to the undoped MgO. Doping as MgO:$Tb_{0.01\%}$,$Gd_{0.05\%}$, $Li_{10\%}$ has a significant effect on the IRSL performance of the resulting microcrystalline powder (see Figure 4.41a). Figure 4.41b shows the concentration quenching study with different dopant concentrations of Tb and Gd on MgO:$Tb_{x\%}$,$Gd_{x\%}$,$Li_{10\%}$. A systematic decrease in IRSL was observed with increasing Gd concentration up to 5 mole%, and the highest IRSL (and TL) signals were obtained for 0.05 mole% Gd concentration. Similarly, the maximum IRSL (and TL) intensities were observed for 0.01 mole% of Tb concentration. For higher Tb or Gd concentrations, it is thought to exhibit a decrease (concentration quenching), possibly due to the formation of terbium oxide, gadolinium oxide, or both phases (Oliveira et al., 2013c). The phosphor exhibited the maximum luminescence intensity when we used the Li concentration as 10 mole% (see Figure 4.41b).

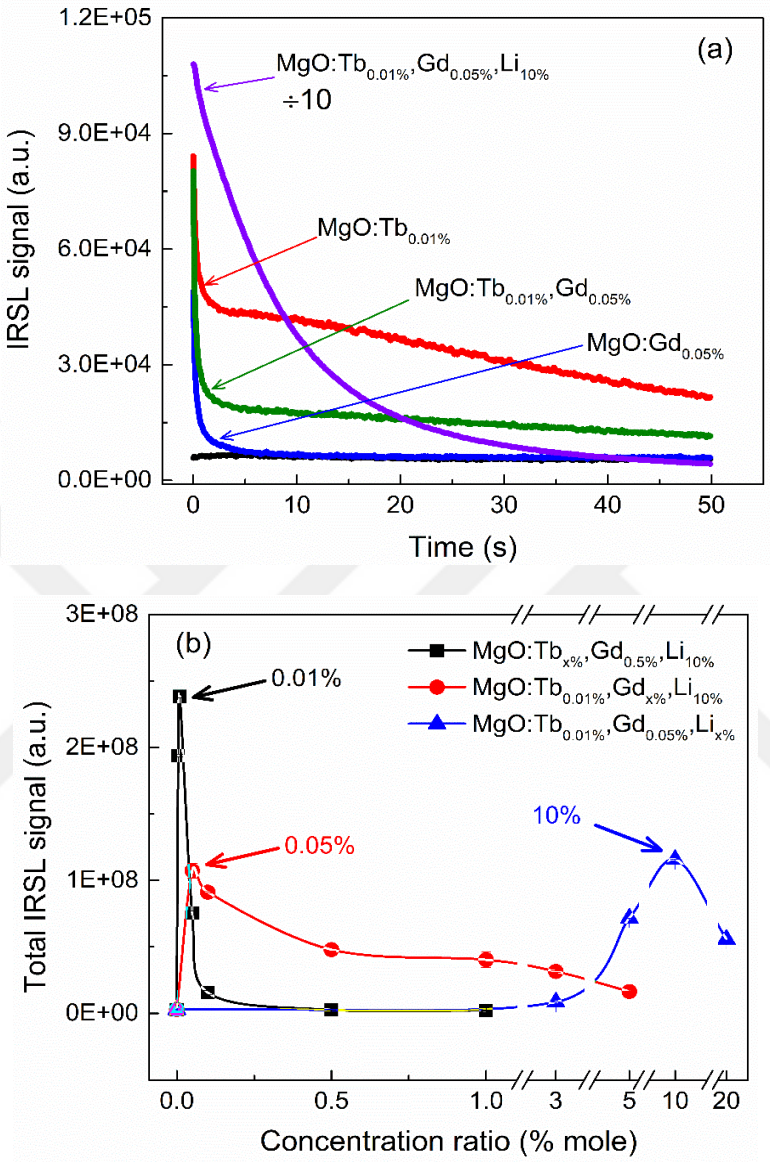

Figure 4.41. (a) IRSL decay curves of undoped MgO, MgO:Tb, MgO:Gd, MgO:Tb,Gd and MgO:Tb,Gd,Li. For the comparison, the IRSL decay curve of the MgO:Tb,Gd,Li sample was reduced by 10 times. (b) The IRSL intensities are integrated as a function of Gd concentration (keeping the Tb concentration fixed at 0.01%) and Tb concentration (keeping Gd concentration fixed at 0.5%). Li concentration was kept constant at 10% in both cases. The given concentrations were determined in mole%.

4.4.4. Determination of the background signals at various readout temperatures during the optical stimulation

During an optical stimulation with a certain wavelength at a certain sample temperature, the background signal is a parameter that should be considered, as it highly depends on the sample temperature. Because the background signal during optical stimulation will be significantly affected by the sample temperature, its identification and removal are critical for temperature-dependent OSL studies. Before studying the dosimetric properties of the MgO:Tb,Gd,Li samples, the influences of the experimental setting of readout temperature on the OSL signal were studied. In Figure 4.42a and Figure 4.42b, it can be easily seen that the background signal increases with increasing the temperature. The background signal with a sample temperature of 280 °C increases more than 7 times compared to room temperature. Therefore, it necessitates determining the optimum readout temperature value to undergo reproduction having maximum outputs by checking the temperature dependence of the luminescence signal.

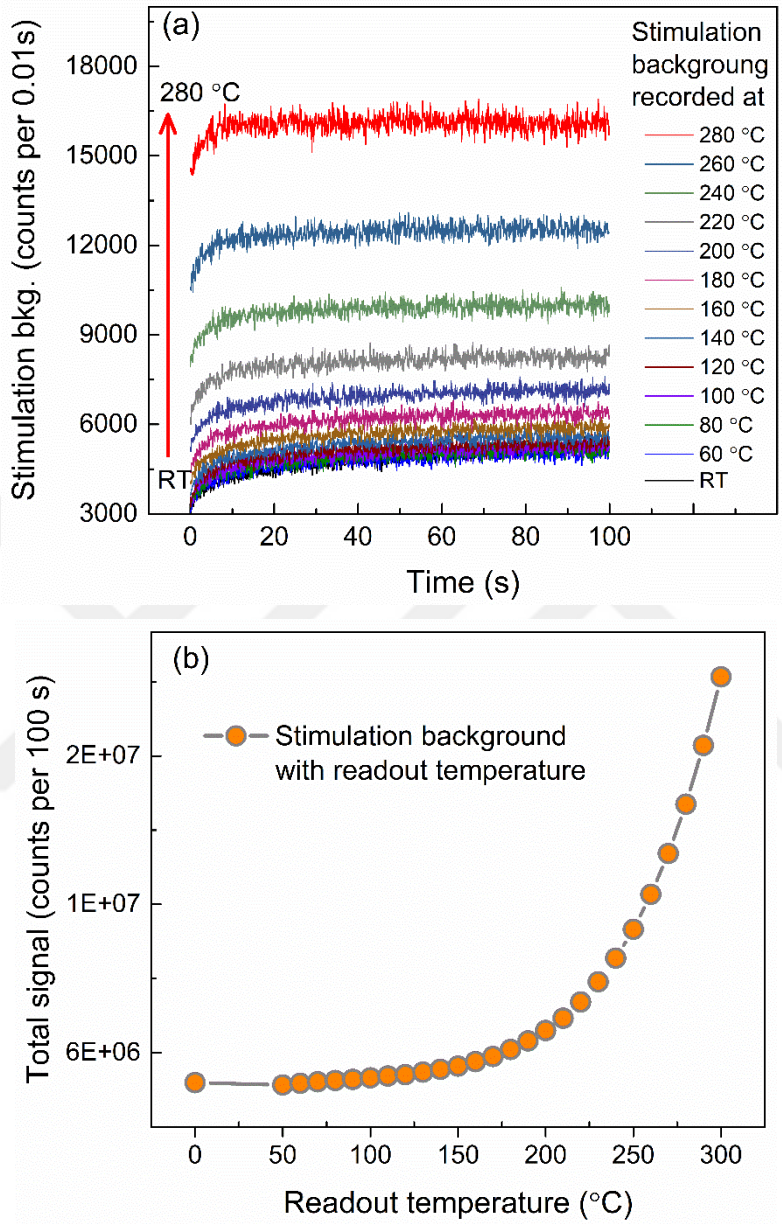

Figure 4.42 (a) Background signal curves of the MgO pellet during simultaneous IR stimulation and different readout temperatures up to 280 °C. (b) Total background signal for the 100 s IR stimulation with different readout temperatures.

To investigate the optimum readout temperature, we heated the sample which was previously irradiated at 1 Gy beta dose, to the constant temperatures of 60, 100, 120, 160, and 200 ^{o}C, subsequently and measured IRSL for each fixed temperature with pulsed excitations. In this work, the luminescence output was recorded during and following the excitation pulse (Bulur et al., 1998b; Duller et al., 1993). In our experiment (see Figure 4.43), firstly in 1 second, we measured the combination of IRSL and TL signals by holding the samples at different temperatures. During these measurements, in the next 1 second period, we measured only the TL signal originating from the same sample by cutting the infrared stimulation. We wanted the IRSL intensity with the minimum contribution of the TL signal. The chosen sample temperature (120 °C) was also provided to deplete the shallow traps associated with the 75 °C TL peak. The temperature dependence of the IRSL obtained by subtracting the TL signals after the excitation pulse, from these data is shown in Figure 4.43. The lifetime of the slow component due to temperature decreases as the temperature increases and causes the IRSL signal to grow faster. The increase in the tail of the decayed part of the luminescence output at temperatures up to 60 ° C is the contribution of the TL signal. The initial part of the luminescence output with readout temperature up to 120 °C increased sequentially and then decreased. The reading temperature at which both high initial IRSL signal and low TL contribution can be obtained at 120 °C. Therefore, one may suggest that the optimum readout temperature is 120°C if the luminescence intensity is going to be obtained by integrating the whole curve.

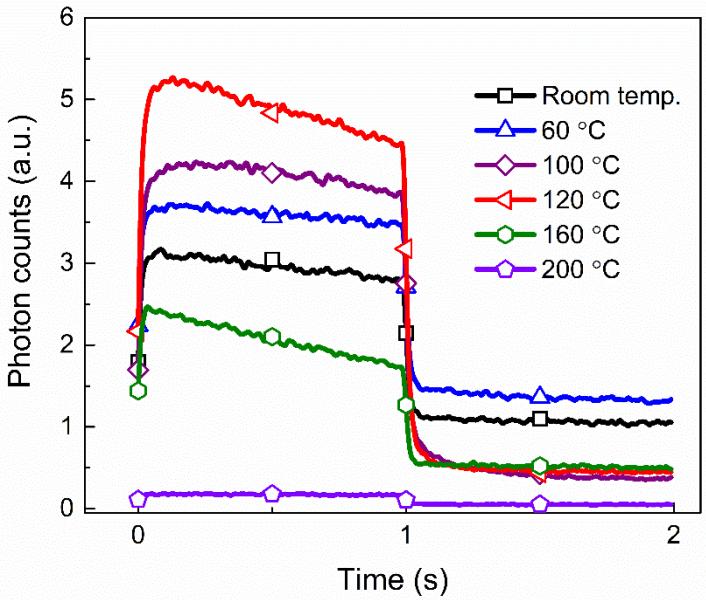

Figure 4.43. IRSL curves from 1 Gy irradiated sample at various readout temperatures during 2 s stimulation (IR stimulation of 1s on and 1s off). The TL contribution is observed when the sample's temperature is lower than 120°C.

4.4.5. Luminescence characteristics

Figure 4.44 shows the TL, OSL obtained for the blue and IR light stimulations and RL emissions of Tb,Gd,Li doped MgO. In this work, we explored the influence of dopant concentrations on IRSL emissions of Tb,Gd,Li doped MgO microcrystalline powders. A series of synthesized microcrystalline MgO powders with increasing amounts of Tb^{3+},Gd^{3+}, and Li^{+} were produced utilizing the SCS method. Doping Tb^{3+},Gd^{3+}, and Li^{+} in MgO lattice have a significant effect on the IRSL performance of the resulting microcrystalline powder. MgO:$Tb_{0.01\%}$,$Gd_{0.05\%}$, $Li_{10\%}$ showed the high crystallinity of the microparticles (see Figure 4.44b). The resultant data indicated that an optimum IRSL signal was achieved with 0.01% Tb and 0.05% Gd doping (data not shown). The IRSL signal increased with Li co-doping, which is possibly acting as a charge compensator and helping the substitution of Mg^{2+} by Tb^{3+} and Gd^{3+}. The increase in IRSL intensity for Li

concentrations up to 10% (data not shown) without significant changes in the MgO phase (see Figure 4.44b) is a further indication of possible Li loss during synthesis. Similar improvements in the luminescence signal with Li co-doping have been reported also in MgO (Oliveira et al., 2013c; Oliveira et al., 2013d; Oliveira et al., 2016; Orante-Barrón et al., 2011) and other luminescent materials (Altunal et al., 2020a; Kang et al., 2010a; Shi et al., 2008; Xie et al., 2010; Yukihara et al., 2014b).

The TL glow curves in Figure 5a are for the MgO:Tb,Gd,Li pellet samples from UV bandpass filter U-340 and VIS bandpass filter BG-39. The TL signal of the sample obtained using the UV transmitting filter was very weak compared to the TL signal received in the visible region. As is shown in Figure 4.44a, the TL glow curve of MgO:Tb,Gd,Li is characterized by two intense peaks at 75 and 170 °C overlapped with a neck at 140 °C and a high-temperature peak at 400 °C. One should keep in mind that the peak positions can be affected by the heating rate and detection window. In this work, the backgrounds were subtracted from the first TL readouts. Oliviera et al. studied MgO:Li,Gd using solution combustion technique and observed a TL glow curve with the TL peaks located at around 90, 140 and 300 ^{o}C. 90 and 140 ^{o}C TL peaks of their study can be correlated with the TL peaks at 75 and 140 ^{o}C. of our sample, MgO:Tb,Gd,Li. In another study by Oliviera et al., the obtained RL emission bands of MgO:Tb and MgO:Tb,Li are similar with the RL emission bands obtained in this study for the samples, MgO:Tb and MgO:Tb,Gd,Li (Oliveira et al., 2013c).

Figure 4.44b compares the OSL decay curves of MgO:Tb,Gd,Li after irradiation of the 1 Gy beta dose, measured with U-340 filter for 100 s blue light *(λ_{blue}= 470 nm)* illumination and BG-39 filter for 100 s infrared *(λ_{IR}=880 nm)* illumination. The OSL decay curve of the sample illuminated with blue light diodes was magnified 30 times to make it visible. It can be seen that the infrared stimulated luminescence of the sample in the VIS region is much more dominant than the blue light stimulated luminescence in the UV region. In the rest of the

study, OSL readings were performed using continuous-wave infrared light-emitting diodes and Schott BG-39 filter, unless otherwise stated.

To determine the effect of IR stimulation on the TL traps of an irradiated sample, a bleaching study was performed. Figure 4.44c shows that the TL glow curve is depleted completely by IR light exposure except for the 400 °C high-temperature peaks. According to this result, it can be said that all trapping centers (except the deep traps) associated with the TL peaks (shallow traps located at < 200 °C) are contributing to the IRSL signal.

Figure 4.44d shows the RL spectra for the undoped and doped MgO samples; namely, MgO:$Tb_{0.01\%}$, MgO:$Gd_{0.05\%}$, MgO:$Tb_{0.01\%}$,$Gd_{0.05\%}$ and MgO:$Tb_{0.01\%}$,$Gd_{0.05\%}$,$Li_{10\%}$ samples. The most intense RL was observed in the triply doped sample MgO:Tb,Gd,Li. The main emission bands or lines under x-ray excitation are identified in Figure 4.44d. It is can be seen that there exists dominant and characteristic broadband at 750 nm, which is observed even for undoped MgO samples. This emission band does not or only slightly associate with the IRSL stimulation because it is blocked by the Schott BG-39 filter. On the other hand, the emission band in Gd-doped samples is the 315 nm line due to the $^6P_{7/2} \rightarrow {}^8S_{7/2}$ transitions of Gd^{3+} (Dieke et al., 1968). Tb-doped samples show emission bands from 380 to 625 nm due to the $^5D_3 \rightarrow {}^7F_j$ and $^5D_4 \rightarrow {}^7F_j$ transitions. The strongest line appeared at 545 nm. It can be conclude that this line occurs due to the probability of magnetic dipole and electric dipole of Tb^{3+} $^5D_3 \rightarrow {}^7F_6$ transition (Tanimizu et al., 1999). For the MgO:Tb,Gd,Li sample, co-doping with Li enhances the Tb^{3+} emission several times. This increase in RL intensity from the lanthanides with Li co-doping is similar to many studies in the literature (Oliveira et al., 2013c; Orante-Barrón et al., 2011). It is thought that this behavior is that Li ions provide charge compensation for a nearby Tb^{3+} ion (Oliveira et al., 2013d). In a study by Oliviera et al., the obtained RL emission

bands of MgO:Tb and MgO:Tb,Li are similar to the RL emission bands of the studied samples, MgO:Tb and MgO:Tb,Gd,Li (Oliveira et al., 2019).

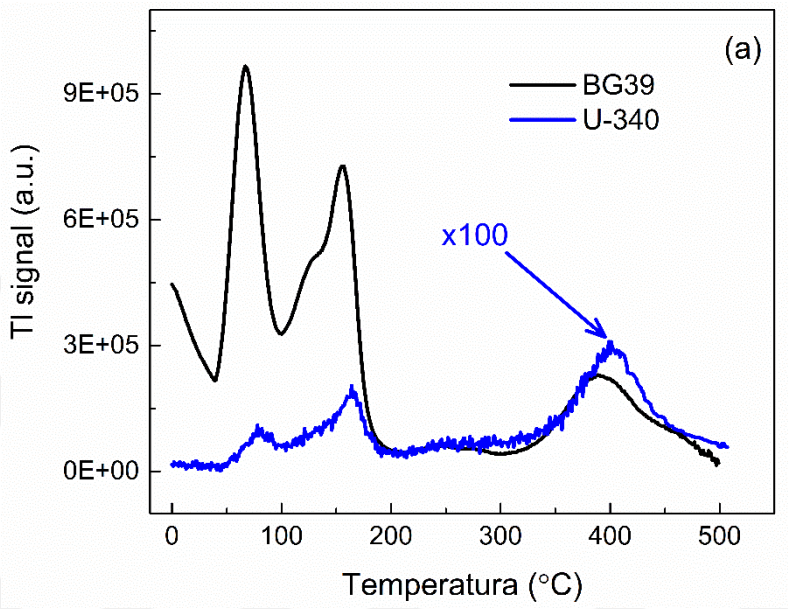

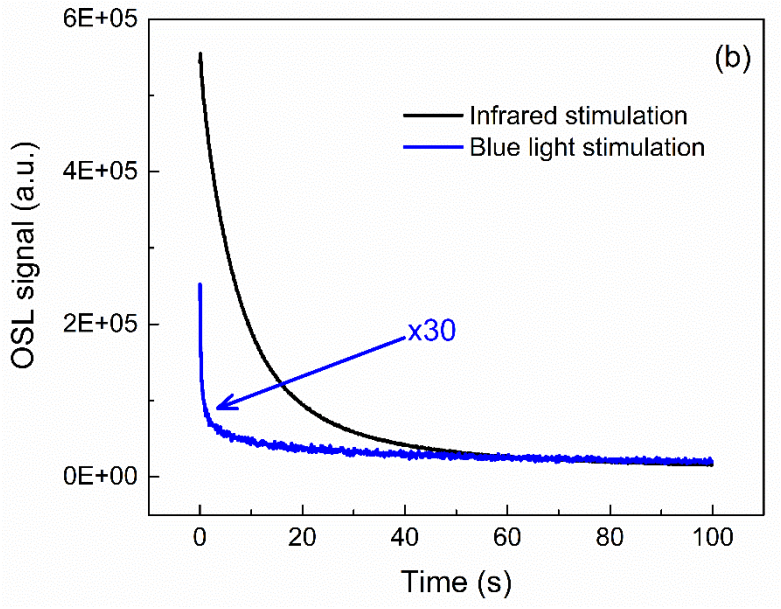

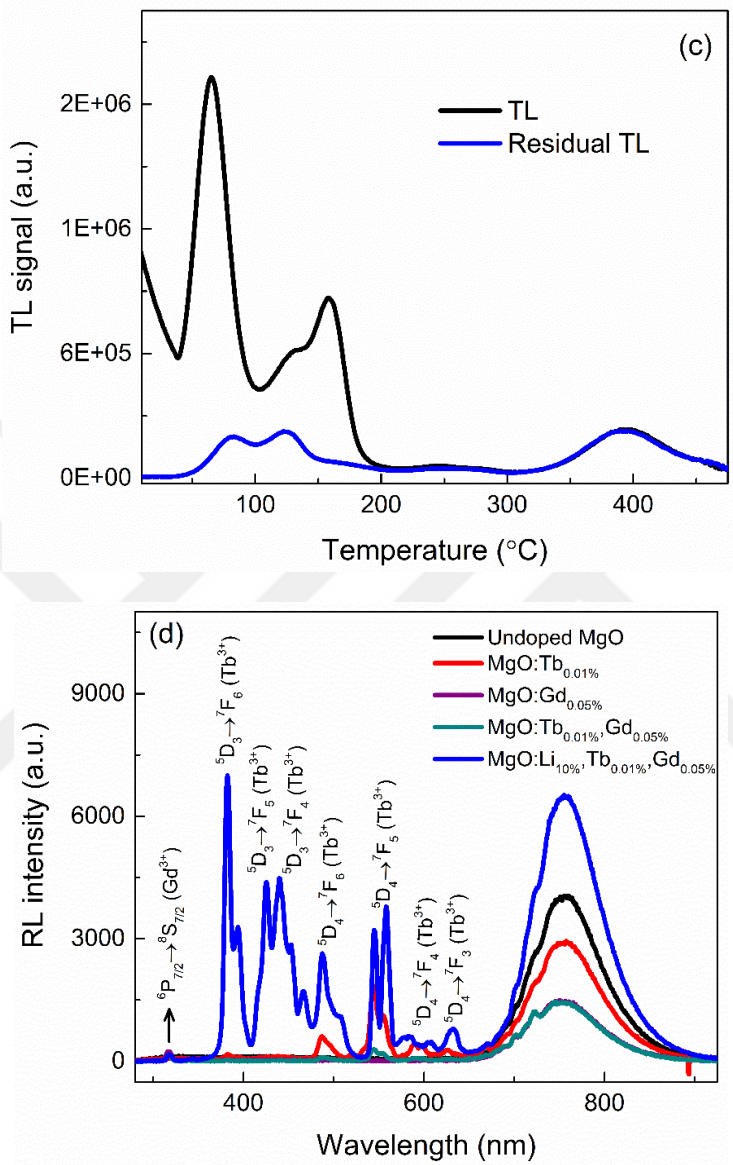

Figure 4.44. Luminescence curves of pellet-shaped MgO:Tb,Gd,Li synthesized using SCS method. (a) TL glow curves of a sample using different bandpass filters of Hoya U-340 and Schott BG-39. (b) OSL decay curves of a sample using blue light and IR stimulations. (c) Comparison of the TL readout immediately after irradiation and after the IRSL stimulation. TL after IRSL gives the residual TL. (d) RL emission spectrum of undoped MgO samples and that of MgO samples with different dopants. The dose amount is 1 Gy.

4.4.6. Isolating the TL glow curve

For precise determination of the number of TL peaks and locations in the TL glow curve by thermal cleaning, the overlapped peaks were successively preheated just beyond each peak maximum. This process was carried out on the same sample, which was re-irradiated under the same conditions each time and TL reading was carried out. TL signal of a freshly irradiated sample each time was recorded to a temperature just beyond the peak maximum of each TL peak after preheating. The result of this procedure revealed the glow curves measured after partial heatings to 65, 127, 158, 252, and 395 °C (see Figure 4.45). After this procedure, a total of five peaks located at 65 (I), 85 (II), 125 (III), 160 (IV), and 387 °C (V) were observed.

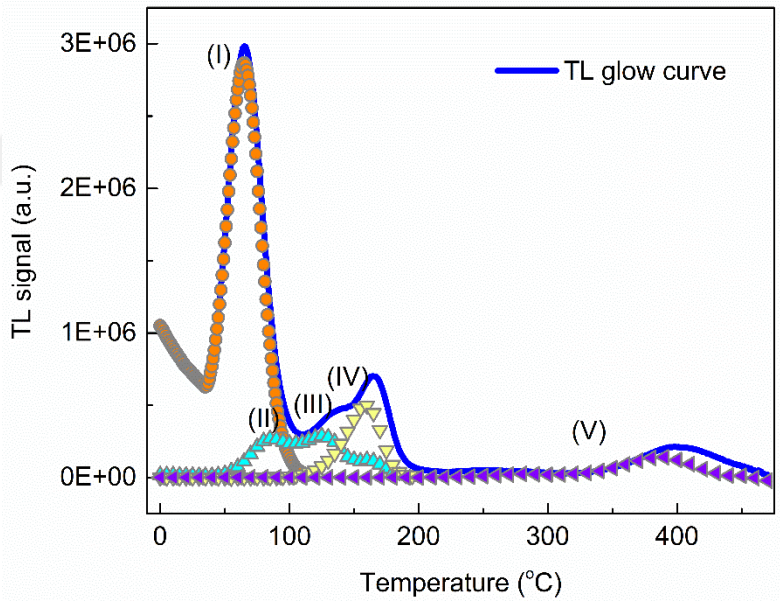

Figure 4.45. Determination of the TL glow curve components using the thermal cleaning technique. Five peaks were obtained following 1 Gy dose exposure and preheating to just beyond each peak as 65, 127, 158, 252, and 395 °C, respectively. The peak maximums of the components were determined at 90, 160, 65, 85, 125, 160, and 387 °C.

4.4.7. IRSL signals varying with readout temperatures

The IRSL decay curves of MgO:Tb,Gd,Li recorded at various readout temperatures between RT and 260 °C are given in Figure 4.46a and Figure 4.46b, and normalized IRSL curves for the same data are given in Figure 4.46c. To determine the lifetimes ($\boldsymbol{\tau}$) and kinetic orders ($\boldsymbol{b}$), of the OSL decay curves the studied samples were analyzed using linear integration of the two-time decaying functions. In this study, the fitting technique which was used for phosphorescence decay by Chen and McKeever (1997), was performed using the general kinetic approach with Equation (4.3 given the previous section. For MgO:Tb,Gd,Li pellet samples, it was observed that to increase the reading temperature from RT to 160 °C, IRSL decay became faster with decreasing lifetimes, but at temperatures higher than 160 °C it began to be slower again with increasing lifetimes. The lifetimes of both the slow and fast components of the decay curves according to the changing sample temperatures were given in Table 4.4. Furthermore, the FOM (Figure of Merit) values for the given data were calculated to determine the goodness of the fitting process (Balian et al., 1977) and presented in

Table 4.4. The data obtained from the IRSL curves of MgO:Tb,Gd,Li was recorded at various sample temperatures. Curve fitting was applied to determine the components of OSL decay curves.

Readout temp. (°C)	S_1 $(fast\ component)$	S_2 $(slow\ component)$	
	$life\ time, \tau_1\ (s)$	$life\ time, \tau_2\ (s)$	$FOM\ (\%)$
30	16.13 ± 0.50	40.14 ± 3.22	2.14
60	7.36 ± 0.21	81. 54 ± 4.41	1.07
100	3.88 ± 0.07	91.63 ± 0.55	0.82
120	3.81 ± 0.20	170.91 ± 17.58	1.20
160	1.94 ± 0.05	350.13 ± 93.09	1.74
180	5.25 ± 0.73	484.90 ± 12.73	1.01
200	7.64 ± 0.13	540.18 ± 17.79	0.65
220	7.04 ± 0.97	469.47 ± 40.98	0.70
240	11.71 ± 0.51	653.57 ± 6.08	0.65
260	24.67 ± 2.85	898.38 ± 50.64	0.54

The variation of the total IRSL signals during 100 s stimulation for each readout temperature is shown in Figure 4.47. This curve implies the change in the OSL signal as the sample temperature increases during optical stimulation. The error bars are the standard deviations of three pellets for the same measurements. Figure 4.47 shows that the total IRSL signal decreases sharply with increasing sample temperature up to 90 °C. Beyond 90 °C, the IRSL signal decays slowly, and the tending of this curve toward the downward direction continues when the IRSL reading temperature between 120 and 175°C after a shorth flat region around 100 °C.

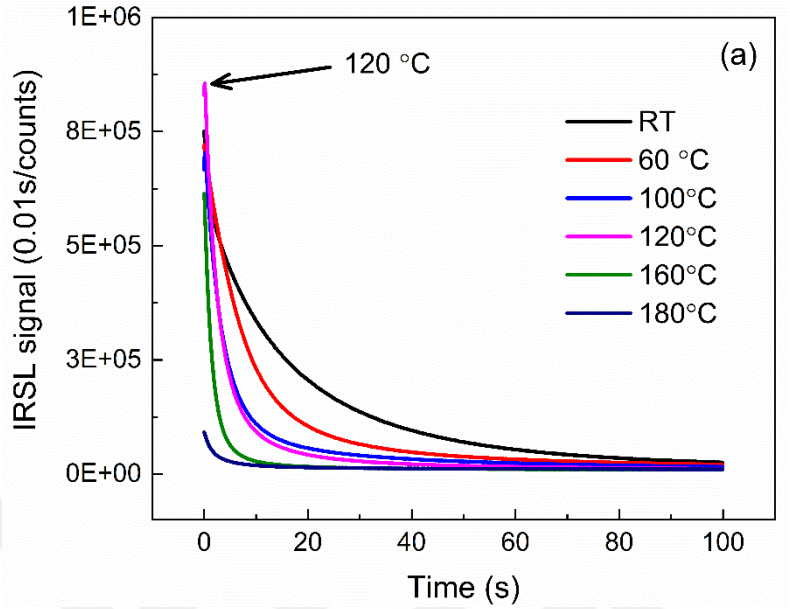
(a)
120 °C
RT
60 °C
100°C
120°C
160°C
180°C
IRSL signal (0.01s/counts)
Time (s)
1E+06
8E+05
5E+05
3E+05
0E+00
0
20
40
60
80
100

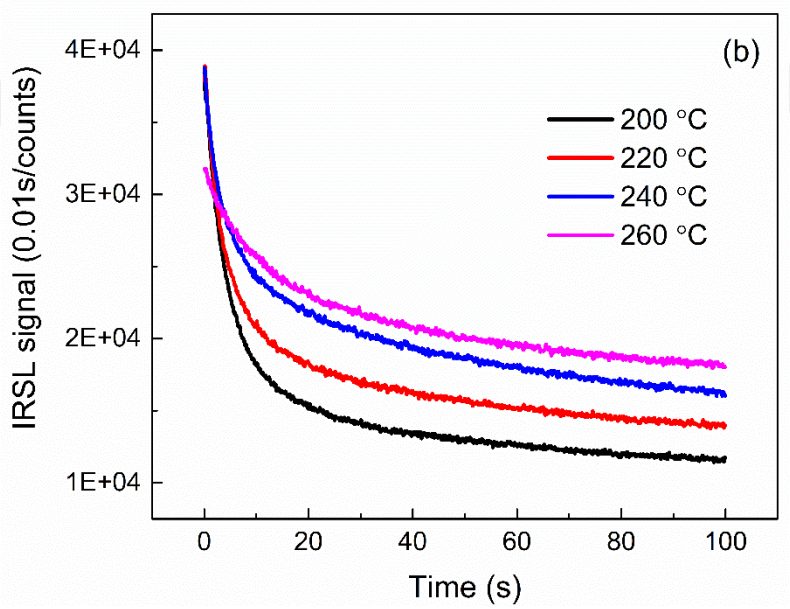
(b)
200 °C
220 °C
240 °C
260 °C
IRSL signal (0.01s/counts)
Time (s)
4E+04
3E+04
2E+04
1E+04
0
20
40
60
80
100

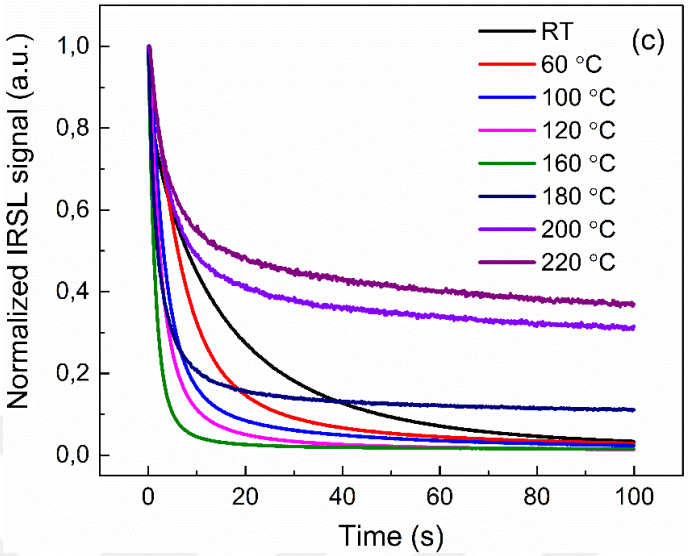

Figure 4.46. IRSL curves of MgO:Tb,Gd,Li pellets were performed with readout temperature at (a) RT to 180 °C and (b) 200 to 260 °C. (c) Normalized IRSL signals measured at the same readout temperatures.

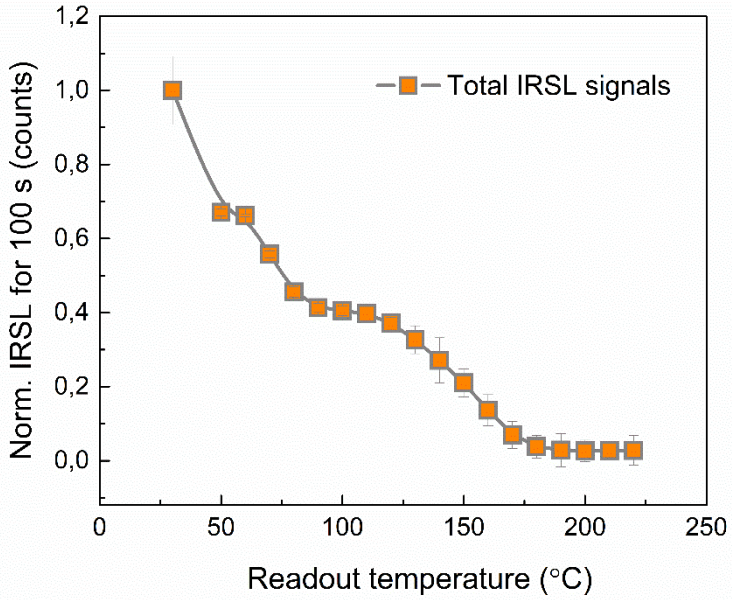

Figure 4.47. Normalized IRSL signal values were obtained by integrating the total luminescence output over 100 s IR stimulation with readout temperatures from RT to 220 °C.

4.4.8. Correlation of TL and OSL traps

The correlation between the TL glow curve and IRSL decay signal was also studied with the step annealing procedure described by Yukihara and McKeever (2011). In our study, the samples were first irradiated at room temperature and preheated to the predetermined T_{stop} value. The IRSL signals were recorded after the IRSL readouts were made at room temperature and 120 °C. After these IRSL readouts, annealing was performed with a TL reading up to 500 °C to deplete the deep traps in the crystal structure. In this experiment, each measurement cycle was performed using three pellets and error bars were plotted using their standard deviations. The step-annealing curves shown in Figure 4.48 were obtained for different T_{stop} values between 50 and 250 °C with increments of 10 °C each. In this procedure, a test dose of 1 Gy and a heating rate of 2 °Cs^{-1} were used. It was an expected result that the IRSL signal would gradually decrease up to around 200 ^{o}C for both conditions. However, it was observed that the unstable signal caused by shallow traps was removed from the depicted step annealing curve of the IRSL signals recorded at a sample temperature of 120 °C. It was investigated that the TL peak at 400 °C did not contribute to the IRSL signal (see Figure 4.44c). It shows that the obtaining mechanism of the IRSL signal is relatively simple concerning the fact that the IRSL signal originates from shallow and relatively deep traps associated with the TL peaks up to 200 °C for IR stimulation at 870 nm used in our measurements.

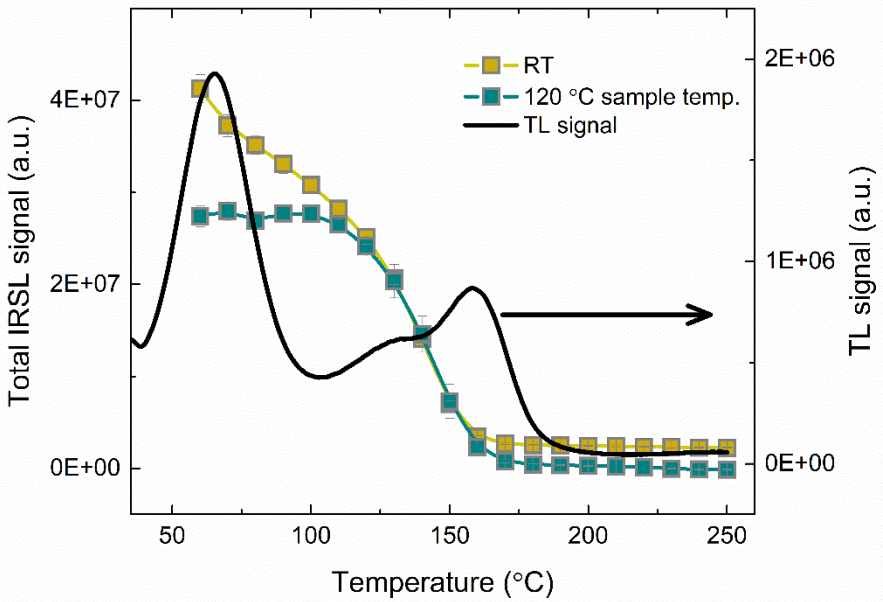

Figure 4.48. Step annealing measurement and the TL glow curve of the MgO:Tb,Gd,Li pellets. In the step-annealing line, each data point corresponds to the total OSL signal from the 100 s IRSL decays after irradiation and pre-heating to the preset temperature. The error bars were plotted based on the measurement of three

4.4.9. Re-producibility of luminescence signals and multi-readability

The reusability of radiation dosimeters is one of the most important features expected in the field of dosimetry. The reusability measurement was performed to investigate the stability of the dosimetric data. The MgO:Tb,Gd,Li samples were exposed to 1 Gy beta test dose, and IRSL measurements were made 20 times. At the end of each cycle, the depletion of the charge traps was performed by TL readout up to 500 °C at a 5 °Cs^{-1} heating rate for deleting the probable residual dose. After 20 cycling processes, it was found that the deviation of the signal was ~2% at the end of the 20th readout (see Figure 4.49).

Multi-readability refers to the ability to read the dosimetric sample several times without significant depletion of the signal intensity which is the most desirable property of the OSL technique. The multi-readability of the IRSL signal

for MgO:Tb,Gd,Li was checked by sequential readings of a sample irradiated 1 Gy beta dose using short stimulations of 1 s. The multi-readability measurements using the total integrated luminescence signals are shown in Figure 4.49. After the Multi-readability experiment, it was seen that as a result of the second readout, the luminescence signals decreased to approximately 55% of the initial IRSL signal count. 20 readouts were conducted to observe ~95% reduction in the luminescence signal obtained for the first reading of the sample (see Figure 4.49).

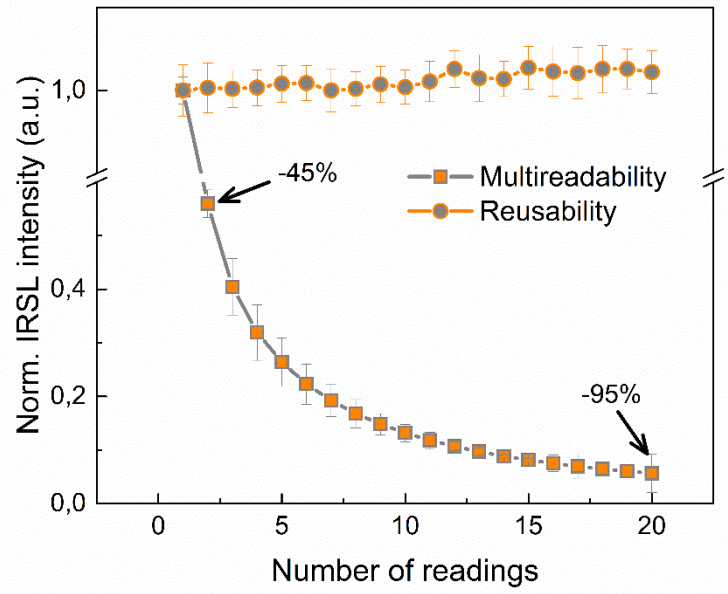

Figure 4.49. Reusability and multi-readability of normalized total IRSL signals for the MgO:Tb,Gd,Li pellets. The reusability investigated with 20 identical cycles was obtained by integrating the 100 s IRSL signal of each cycle. Multireadability was investigated with the pulse illuminations of 1 s each.

4.4.10. Dose-response behavior of the sample

To determine the IRSL application of MgO:Tb,Gd,Li for dosimetric purposes the IRSL response per Gy as a function of the dose was checked for beta irradiation in the dose range of 0.1 Gy to 1 kGy. IRSL measurements were

performed using 100 s of IR stimulation. The same group of samples consisting of three pellets were used for all dose values delivered. After each reading, the samples were warmed up to 500 ° C by TL readout so that the residual signal could be erased. Figure 4.50 summarizes the results of these determinations and indicates that the response per Gy of the phosphor is essentially a linearly increasing function over this dose range since the slope of the line is equal to 1.01. A sublinear behavior is observed after 50 Gy dose exposure using total IRSL decaying signal counts.

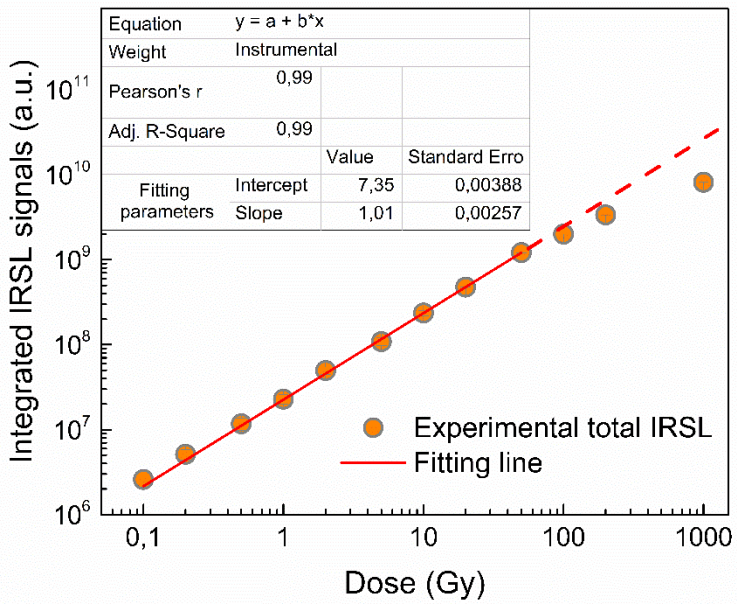

Figure 4.50. Total IRSL signals from MgO:Tb,Gd,Li pellets exposed to different beta dose values ranging from 0.1 to 1000 Gy.

4.4.11. Signal storage capacity

The capability of a phosphor synthesized for dosimetric purposes, to store exposed dose information over long periods (until it is read) is very important. In this study, the fading behavior of the MgO:Tb,Gd,Li pellets were investigated up to 4 weeks at RT and 120 °C (Figure 4.51a and Figure 4.51b). A fading experiment was performed using MgO:Tb,Gd,Li pellets which were kept in dark at RT after being exposed to 2 Gy beta radiation. These measurements were made in two different ways of readout. For the first group, after irradiation and keeping in a dark room, the IRSL readouts were performed at room temperature after each storage period. For the second group, the IRSL readouts were carried out at 120 °C readout temperature after the irradiated samples were stored in dark. Three samples were used for each storage time and error bars were obtained from the standard deviations of these samples. The fading signals are given by the ratio between the IRSL signals from the stored samples and the signals taken from the samples' readout immediately after irradiation. IRSL readout at room temperature exhibited a fading of approximately 15% at the end of the first 10 hours; it was followed by a loss of approximately 20% signal intensity over 1-day storage time. These reductions were observed as 15% and 25%, respectively, for samples that were read out at 120 °C. At the end of the 4 weeks, it appears that the fading of the luminescence signal of the IRSL readout at 120 °C is less than that of RT. It might be the result of the reduction of the shallow trap intensity concerning the heat applied to the samples.

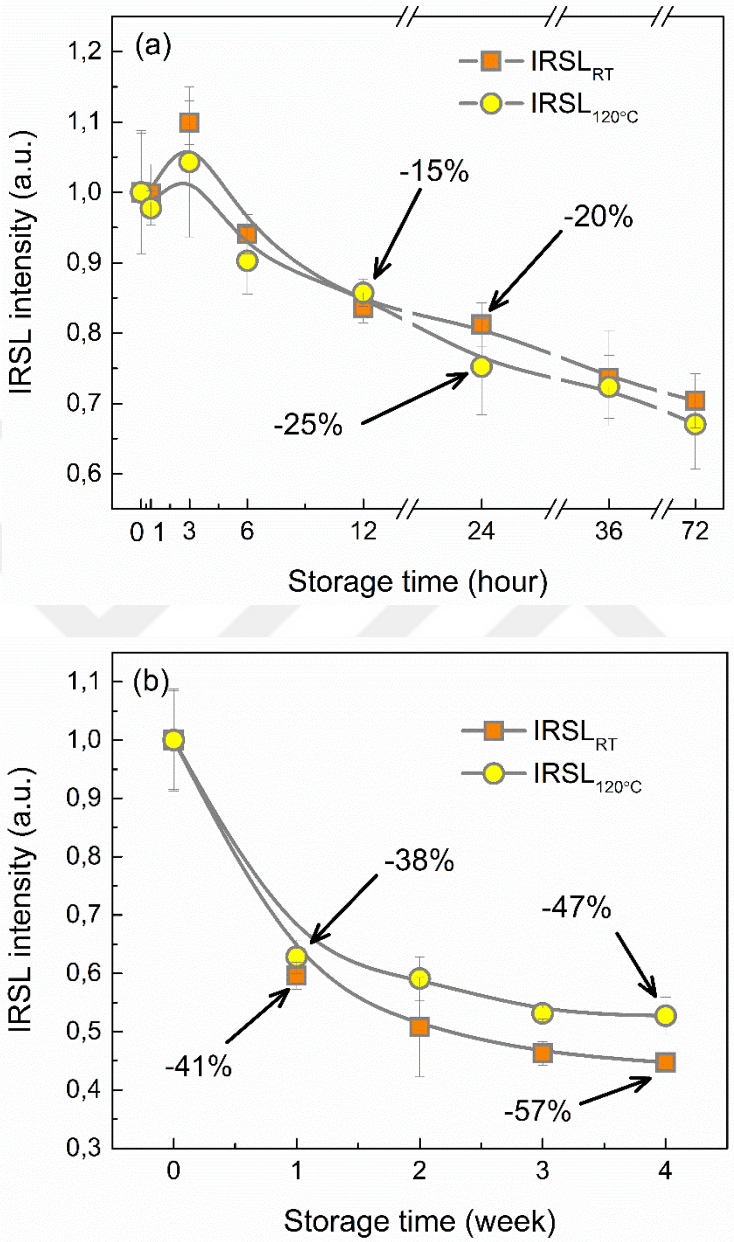

Figure 4.51. Effect of storage time on IRSL signals from 1 Gy irradiated samples. (a) short storage time (b) storage time in weeks. IRSL readings were performed both at room temperature (squares) and 120 ° C readout temperature (circles).

4.4.12. Thermal stability of the sample

To understand the thermal stability of the IRSL signal of MgO:Tb,Gd,Li, the isothermal annealing method was carried out and demonstrated the suitability of the phosphor for radiation dosimetry (Bulur et al., 1998b). The thermal stability of the IRSL signal was investigated using isothermal decay measurements to determine the trap parameters. In this experiment, the MgO:Tb,Gd,Li pellets were pre-heated at various temperatures for various duration of times following the irradiation of 1 Gy beta dose. The IRSL signals were measured after cooling the samples to room temperature in each cycle. During each cycle, in the end, samples were depleted by TL reading (500 °C, 5 °C/s) to prevent the contribution of residual dose to the next cycle. The isothermal decay curves of the samples are exponential functions of time with the assumption of first-order kinetics. It can be seen that the isothermal decays from the natural logarithms of the integrated IRSL curves (0–100 s) as the function of annealing times appeared to slope downwards (see Figure 4.52a). The slope values of each decay equaling the decay times of the signals were used to determine the activation energy and frequency factor of the MgO:Tb,Gd,Li sample. Figure 4.52b presents the $\ln|slope|$ values, which are obtained from $ln(I_{IRSL})$ curves vs. pre-heat temperature, as a function of $1/kT$. The resultant activation energy and the frequency factor of the TL traps responsible for the TL peak at <200 °C were obtained to be 0.62 eV and 10^6 Hz, respectively.

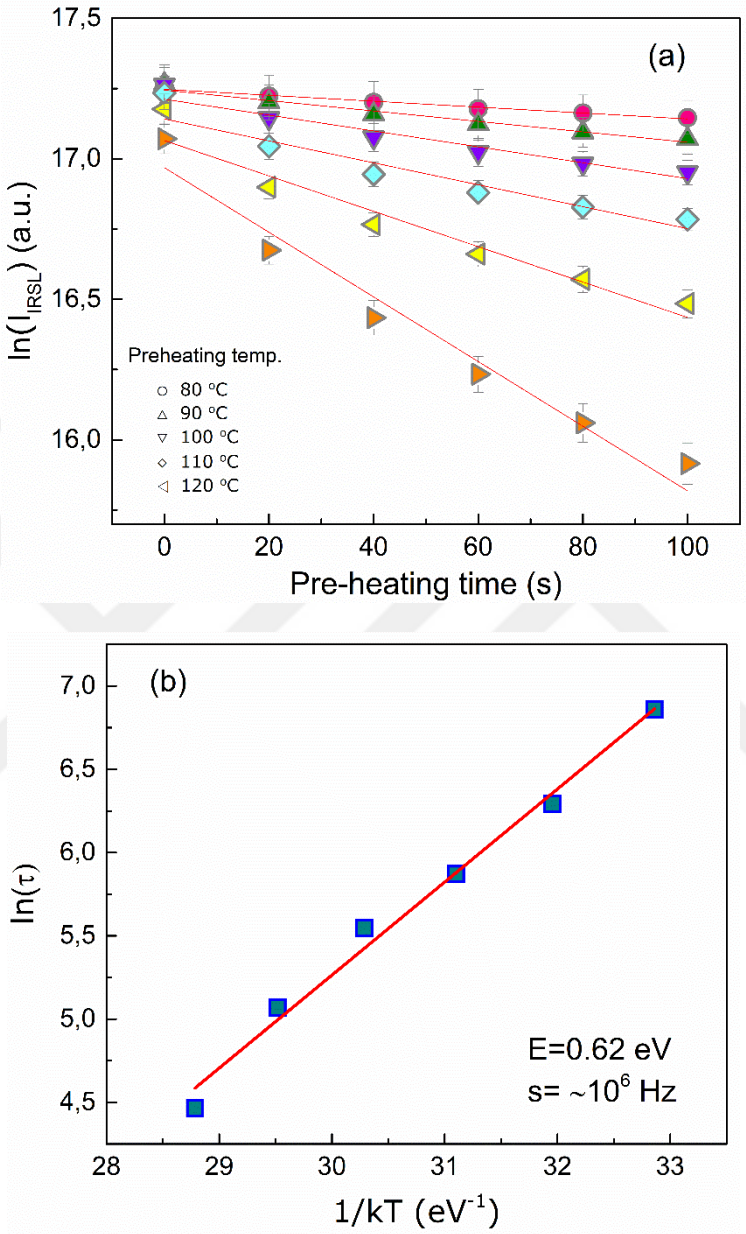

Figure 4.52. (a) Isothermal annealing of the IRSL signal originated from TL peaks located at <200 °C. IRSL intensities were taken as the integral of the whole luminescence decay. (b) The natural logarithms of the lifetimes of the IRSL signals ln|$slope$| against the reciprocal of the k times preheating temperatures T $(1/kT)$, and the corresponding activation energy.

The results for co-doped MgO presented here must be discussed from the point of view of the underlying luminescence mechanism. Co-doping with impurities such as Gd^{3+} ions may be an effective way to enhance upconversion (UC) efficiency. The incorporated impurities may generally serve as sensitizers like Gd^{3+}, or modify the local crystal field (CF) environment around activators (Dou et al., 2011), or dissociate the ion clusters in polycrystalline which in consequence leads to the UC enhancement. Gd^{3+} ions may also participate in energy transfer (ET) within the matrix. In our experiments, we demonstrated simultaneous optical and luminescence properties control of MgO through Gd^{3+} doping. A new UC mechanism, (energy migration-mediated UC: EMU) is based on gadolinium sublattice-mediated energy migration, which facilitates efficient UC emissions from Tb^{3+} without intermediary energy levels (Wang et al., 2011a). Unlike the active co-dopants, other impurities, for example, alkali ions, intentionally incorporated into UC polycrystals do not directly participate in the optical process (e.g., ET) within the hosts, but are capable of enhancing UC efficiency as well. In this study, the reason for the remarkable increase in IRSL intensity obtained from MgO:Tb,Gd,Li compared to the MgO:Tb,Gd is described that Li^{+} ions act as a charge compensator to increase upconversion quantum yield (Chen et al., 2016). Similar improvements in the luminescence signal with Li co-doping have been reported also in MgO (Oliveira et al., 2013c; Oliveira et al., 2013d; Oliveira et al., 2016; Orante-Barrón et al., 2011) and other host materials (Altunal et al., 2020a; Kang et al., 2010b; Shi et al., 2008; Xie et al., 2010; Yukihara et al., 2014b).

4.4.13. Conclusion

In this work, MgO:Tb,Gd,Li phosphor was successfully produced using the SCS method, and their crystallographic structure and phase composition was confirmed by XRD and SEM analyzes. The TL glow curve consists of four TL peaks located at around 75, 140, 170, and 400 °C. As a result of IR stimulation in

optically stimulated luminescence signals, when this phosphor was stimulated with IR light it exhibited 30 times more intense signal than that of blue light. Furthermore, it was found that all TL traps except the traps responsible for the 400 °C TL peak were affected by IR stimulation. It was shown that the IRSL reading at 120 °C was the reading with the highest luminescence signal intensity. It was observed that when increasing the readout temperature from RT to 160 °C, IRSL decay became faster, but at temperatures higher than 160 °C its decaying speed became slower. This result can be associated with the presence of shallow traps that are interfering during IRSL readout. Charge traps responsible for the IRSL signal were found to be the TL traps below 200 °C in both step-annealing and TL after IRSL experiments. The reusability of the sample was tested by applying the identical successive cycles and an acceptable deviation of 2% was observed after 20 readings. In the measurements made for multiple IRSL readings, it was shown that at the end of the second reading, there was a 45% signal loss compared to the initial signal, and the signal was almost completely faded at the end of the 20^{th} reading. With the assumption of the first-order kinetics, the activation energy and frequency factor of trapping centers responsible for IRSL signals were determined using isothermal annealing measurements as 0.62 eV and 10^6 Hz, respectively.

4.5. Study of Ce- and Li- doped MgO

4.5.1. Material Preparation

A solid-state reaction process was used to prepare Ce^{3+} and Li^+ co-doped MgO phosphors. Analytical grade reagents MgO (Sigma Aldrich 98%), Li_2CO_3 (Sigma Aldrich 99%), and CeO_2 (Sigma Aldrich 98%) were used as the starting materials. Stoichiometric amounts of the starting materials were well-grounded together using an agate mortar and pestle to form a homogeneous solid solution. Temporary defects and charges, which may cause triboluminescence, can occur during grinding. To minimize any contribution of such a case to the luminescence signal, the samples were annealed after grinding (Garcia-Guinea et al., 2000;

Rodriguez-Lazcano et al., 2012). The solid solution was loaded into alumina crucibles and a standard heating ramp of 5 K min^{-1} up to a temperature of 700 °C with 4 h dwell time was used. The process was followed by air cooling in the furnace. The obtained products were milled into fine powder. Three samples with different contents of Ce and Li dopants were prepared respectively *via* this method for comparison: Ce (0.01 mole%) and Li (1 mole%); Ce (1 mole%) and Li (1 mole%) and Ce (1.5 mole%) and Li (10 mole%).

4.5.2. Compositional analysis and crystal structure

The XRD spectra of the as-prepared sample are given in Figure 4.53. The sharp peaks related to the MgO cubic structure of the periclase phase with the Fm-3m (225) space group are visible and match well with the JCPDS card number 45-0946. Some Ce and Li-related impurity peaks in the spectra show that a significant amount of the dopants is not incorporated into the MgO lattice. These peaks matched with the peaks observed in JCPDS #15-0401 for Li and 31-0325 for Ce (metallic). The sharpness of the peaks demonstrates the high crystallinity whereas very small peaks in the spectra show low-level impurity incorporations during crystallization of MgO:Ce,Li powder. Moreover, the absence of any prominent peak shift suggests that the dopants (Ce and Li) are well-incorporated into the MgO lattice.

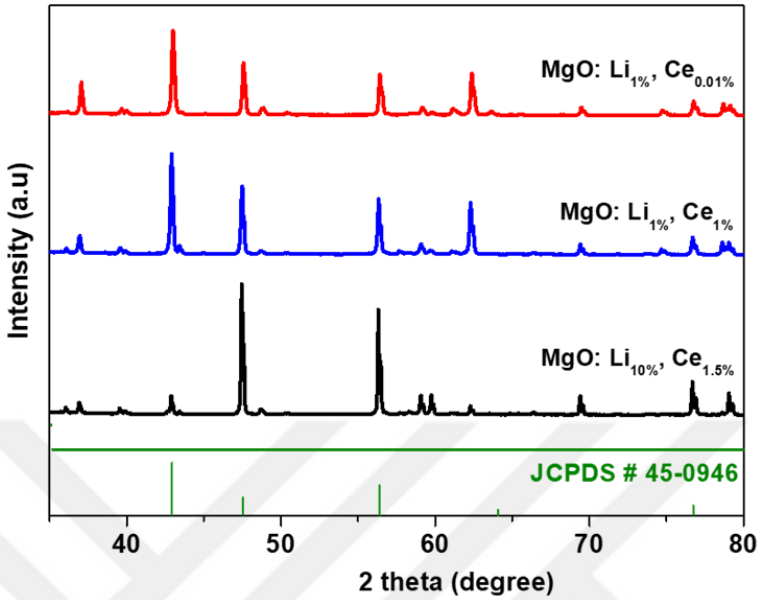

Figure 4.53. Crystallographic studies: XRD patterns of the Ce^{3+} and Li^{1+}doped MgO ceramics.

4.5.3. Morphological study

SEM images of the samples at different magnifications are given in Figure 4.54. The material crystallinity and well-shaped crystal grains can be observed with isolated pores. Sintering at 700 °C for 4 hours led to clear boundaries between particles. The grain sizes are between 70-200 nm (data not shown) with uniform morphology.

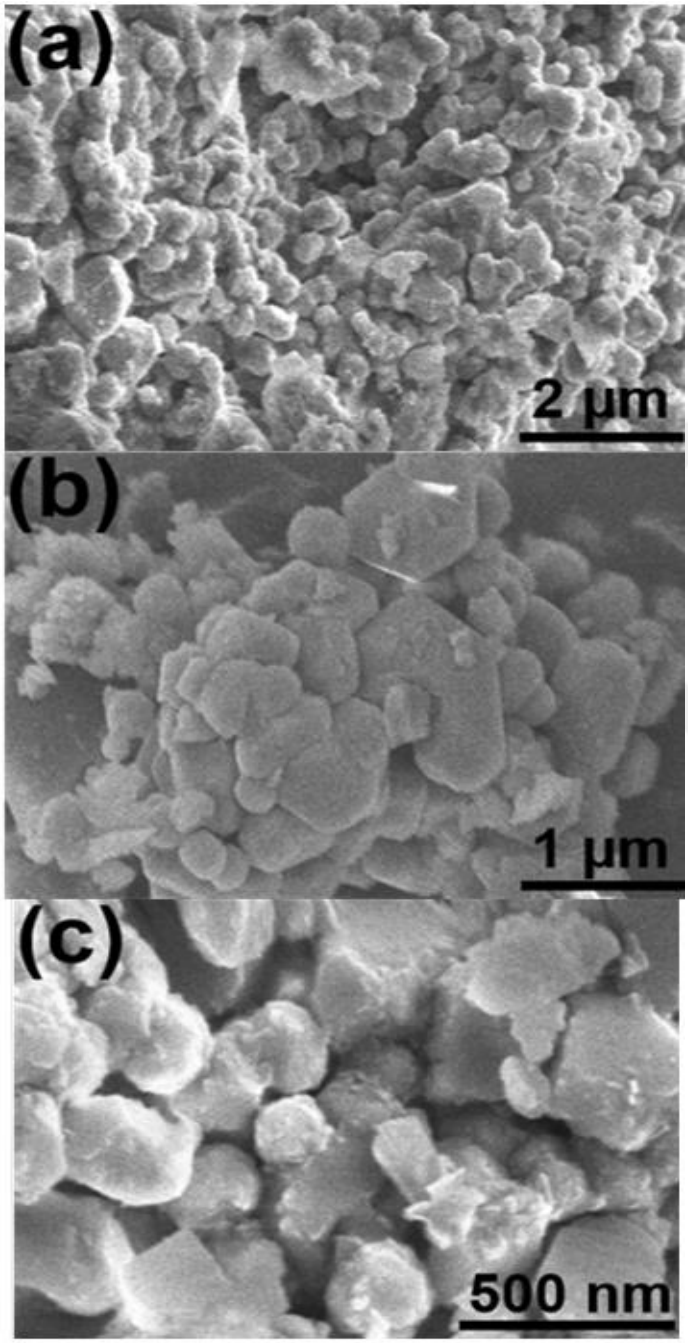

Figure 4.54. SEM micrographs showing the grain structure of MgO:Ce^{3+} (1 mole%), Li^{1+} (1 mole%) phosphor with magnifications (a) 25000x, (b) 50000x and (c) 80000x.

4.5.4. Photoluminescence

PL spectroscopy was performed as an essential tool to study the optical properties of the designed phosphors. The as-prepared samples were excited by 365 nm UV light and the PL emission (PL) was recorded. The PL excitation (PLE) spectra were obtained from the samples with emission at 635 nm. The PL and PLE of undoped MgO are presented in Figure 4.55a. The PL of undoped MgO has three strong bands at 566, 617, and 648 nm. Whereas two strong PLE bands were found at 409 nm and 440 nm attributable to the surface defects. The PL and PLE results of Ce and Li doped MgO are presented in Figure 4.55b. The intensities of the PL and PLE bands changed with different dopant concentrations. However, the peak positions remain the same due to the reported fact that the emission of MgO is due to the charge transfer on the surface state and not from the MgO itself (El-Shaer et al., 2020). The strong PL bands were obtained at 573, 591, 617, and 649 nm with a weak band at around 560 nm for all the samples. The band at 591 nm can be ascribed to the interband transition after doping with Ce and Li as these ions can only occupy the interstitial positions and MgO sites. But they cannot occupy the anionic oxygen sites in the MgO crystal lattice due to the high energy of formation (Shakti et al., 2018). As a result, the additional defects (O_i and V_o) are created in MgO for charge compensation.

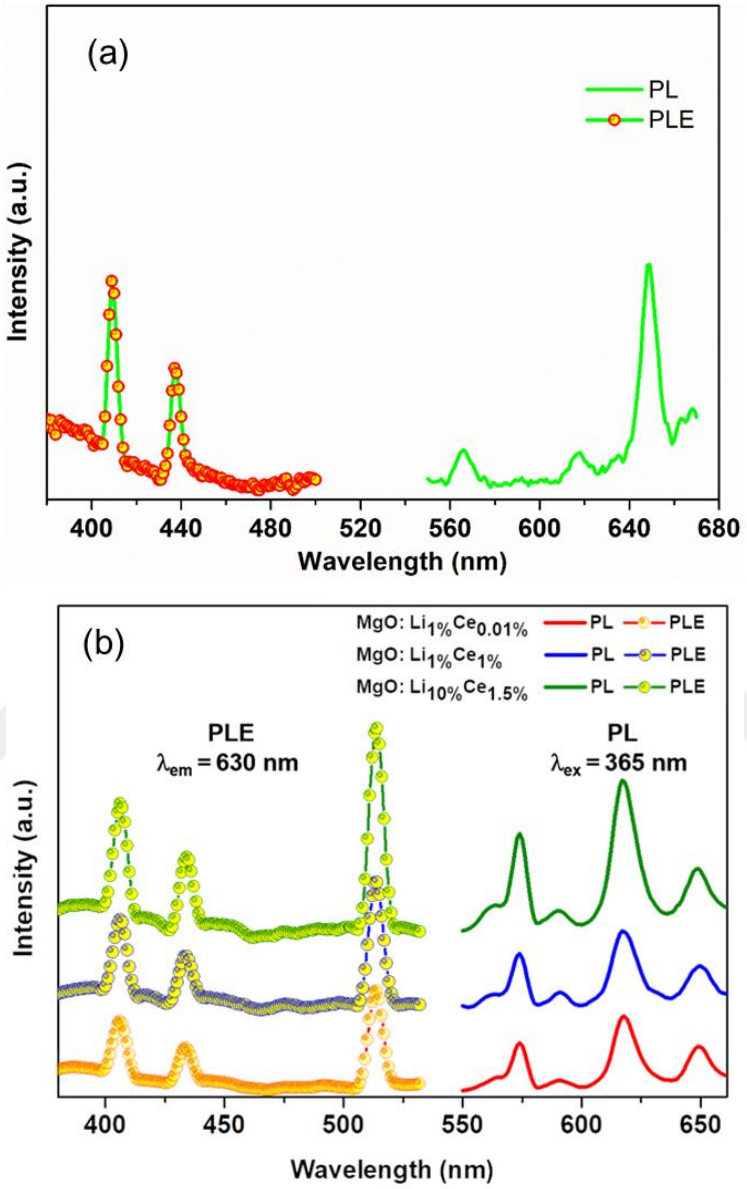

Figure 4.55. Photoluminescence studies: PL emission and PL excitation spectra of (a) undoped MgO and (b) MgO:Ce^{3+} (0.01 mole%), Li^{1+} (1 mole%); MgO:Ce^{3+} (1 mole%), Li^{1+} (1 mole%) and MgO:Ce^{3+} (1.5 mole%), Li^{1+} (10 mole%) samples.

In contrast, the PLE spectra consisted of three strong bands at 405, 433, and 513 nm for all samples. The strong band at 405 nm is ascribed to 4f-5d transitions (Zhang et al., 2018). The less intense bands at 433 and 513 nm can be attributed to the surface modifications by the carbonate precursors used during the synthesis process. The excitation band at 433 nm can also be ascribed to the hydroxylated low coordination oxygen, and the excitation beyond 450 nm can be ascribed to the generation of different kinds of F centers on MgO (Bailly et al., 2005; Xie et al., 2011). Overall, the PLE bands can be attributed to the surface states and structural defects, such as oxygen vacancies in MgO (Kaur et al., 2020).

4.5.5. Radioluminescence

Figure 4.56 shows the RL spectrum of X-ray irradiated MgO:Ce,Li phosphors with different dopant concentrations. Five emission bands located at 526, 575, 617, 752, and 900 nm can be identified in the RL spectra. Although Ce^{3+} emission between 300-450 nm is originated from 5d-4f transitions (Bünzli et al., 2010), the positions of the emission bands are known to be affected by the surrounding anions and so the main emission can range from UV (e.g., 314 nm in CaF_2) to red (e.g., 670 nm in Y_2O_2S) (Dorenbos, 2000; Van Uitert, 1984). As seen in Figure 4.56, Ce^{3+} emission was observed as two bands at 580 and 620 nm. This may be caused by Ce^{3+} emission associated with 5d-4f transitions and typically featured by a double band due to the splitting of $4f^1$ ground state into $^2F_{5/2}$ and $^2F_{7/2}$ states. Similar RL emission bands located at 525 and 605 nm obtained from MgO:Ce,Li phosphor were reported by Orante-Barrón *et al.* (Orante-Barrón et al., 2011). It can be observed that the Li^+ co-doping can significantly improve the luminescence efficiency by acting as a probable charge compensator and increasing the incorporation of Ce^{3+} dopant. Furthermore, a negative effective charge defect (Li_{Mg}) occurs with the Li^+ substitution for Mg^{2+}. Oliviera *et al.* reported that the emission band located at ~530 nm in the RL spectrum obtained from the Li, Ce, and Sm doped MgO sample relates to Ce^{3+} emission [14]. The authors noted that in

the MgO:Ce,Sm sample, the emission of Ce^{3+} was barely detected, but when the sample was co-doped with Li, the emission of Ce^{3+} increased by several orders of magnitude. Hence, this negative charge defect can compensate for the positive effective charge defect $(Ce_{Mg})^{+}$ formed by Ce^{3+} instead of Mg^{2+} (Guckan et al., 2021a; Yukihara et al., 2013b). In our study, all MgO samples showed similar strong RL emissions of broad bands located at 750 nm as this emission band is due to Cr ions which are typical contaminants in MgO (Kato et al., 2016). Since the strong RL emission band at 750 does not coincide with the spectral range of the filter used during the measurements. Therefore, it does not contribute to the TL signals.

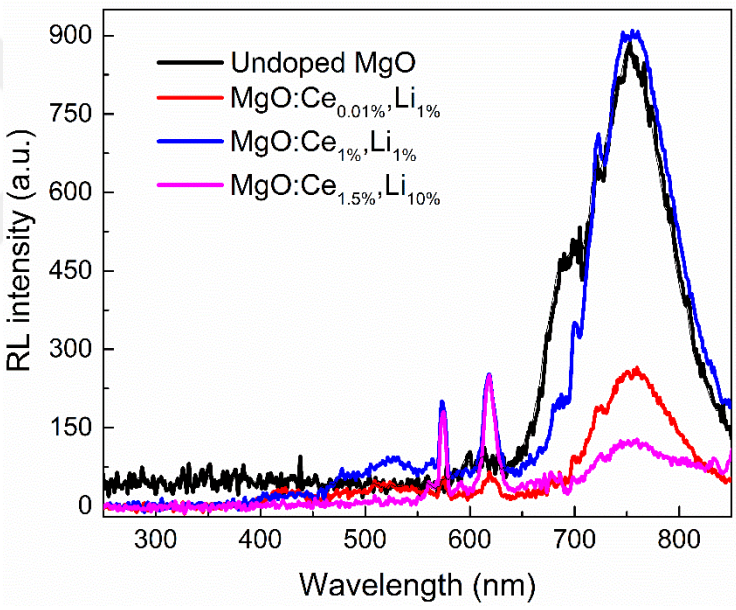

Figure 4.56. Dependence of RL intensity on different dopant concentrations: Undoped MgO; MgO:Ce^{3+} (0.01 mole%), Li^{1+} (1 mole%); MgO:Ce^{3+} (1 mole%), Li^{1+} (1 mole%) and MgO:Ce^{3+} (1.5 mole%), Li^{1+} (10 mole%) phosphors.

4.5.6. TL glow curve analysis

The compositional study of MgO:Ce,Li samples was conducted by employing the previously described solid-state technique at 700°C for 2 hours.

Low purity reagents of polycrystalline powder samples were consistently obtained in the following molar compositional range: Ce, 0.01 to 1.5 mole%; Li, 1 to 10 moles%. The effects of Ce and Li concentrations on the TL glow curves of these polycrystalline powder materials are shown in Figure 4.57. The degradation caused by Ce^{3+} replacing Mg^{2+} ions in the crystal lattice can be attributed to the new capture centers. The role of Li co-doping and substitution Li^{+} in Mg^{2+} site acts as a charge compensator promoting the inclusion of Ce^{3+} in the lattice, resulting in luminescence bands of 526, 573, and 615 nm, thereby increasing the TL sensitivity (Altunal et al., 2020b; Altunal et al., 2020c; Gu et al., 2006; Oliveira et al., 2013d; Orante-Barrón et al., 2011).

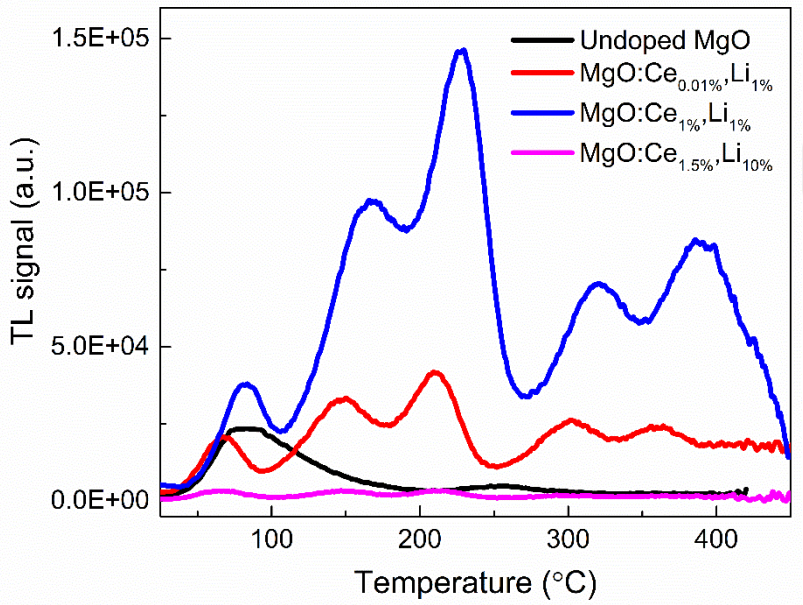

Figure 4.57. TL glow curves of MgO samples activated with different concentrations of Ce and Li after 1 Gy β-ray exposure with a heating rate of 5 °C/s.

As seen in Figure 4.58a, the TL glow curve obtained from MgO:Ce^{3+} (1 mole%), Li^{+} (1 mole%) exposed to 1 Gy β dose include five overlapping peaks located at ~80, 165, 228, 318, and 387°C with the heating rate of 5 K/s. For better identification of the TL peaks, the thermal cleaning technique was used to determine the individual peak temperatures in the TL glow curve (Guckan et al., 2019; Kalita and Chithambo, 2017; Ozdemir et al., 2021; Shivaramu et al., 2021). In this technique, the TL of a re-irradiated sample was recorded each time after preheating to a temperature just beyond a peak maximum. Each time the sample was irradiated with a 1 Gy β dose, repeatedly. To show each TL peak as an isolated and simple-shaped peak, we eliminated the other peaks by using the thermal cleaning method. Through this method, the first thermally cleaned curve (I) was obtained by subtracting the 80 °C preheated TL glow curve from the non-preheated TL glow curve. When we subtracted the TL glow curve preheated at 165 °C from the TL glow curve preheated at 80 °C, we obtained curve (II) (Figure 4.58b). This procedure was subsequently repeated to obtain the other thermally cleaned curves (curves III, IV, and V), respectively. As a result of this analysis, the isolated TL peaks given in Figure 4.58b were obtained at 77, 159, 223, 308, and 382 °C, respectively.

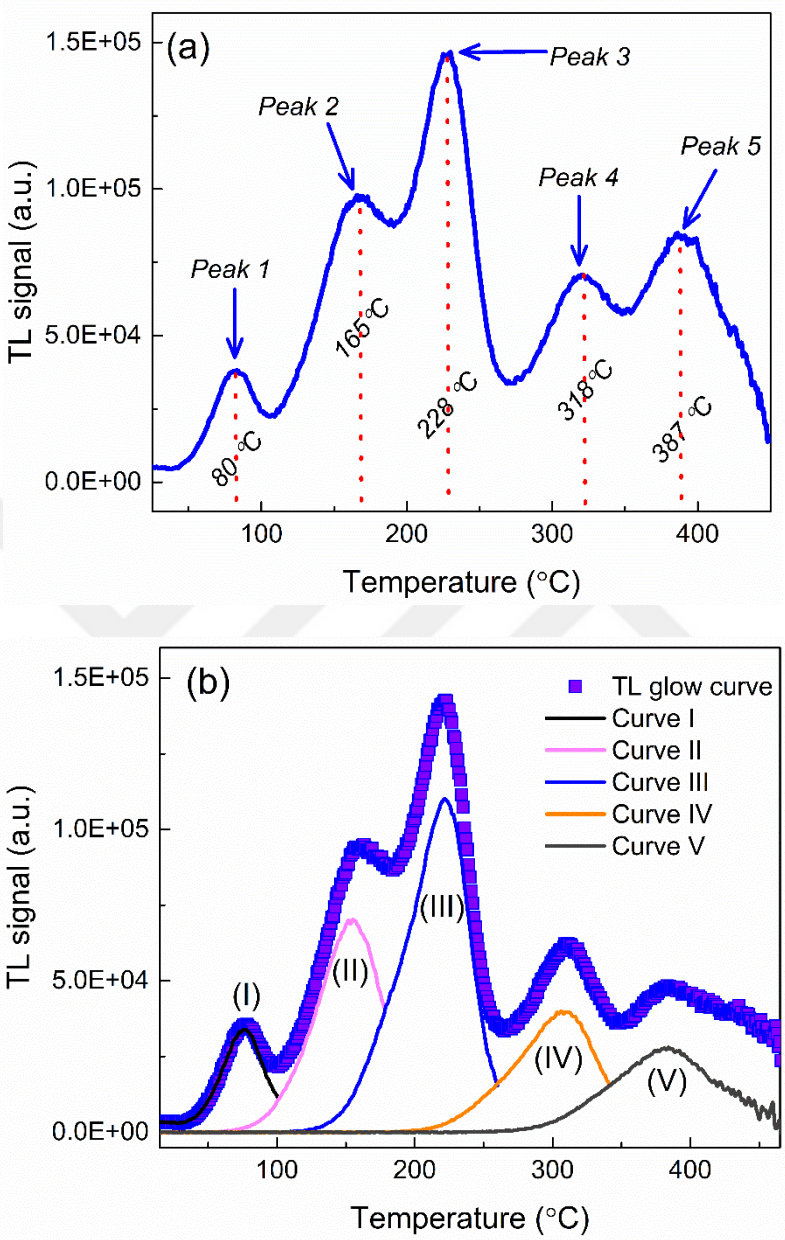

Figure 4.58. (a) TL glow curve of MgO:Ce^{3+} (1 mole%), Li^{1+} (1 mole%) exposed to 1 Gy β-dose. (b) The difference curves calculated by subtracting the corresponding preheated curves by pre-heating to 70 °C (I), 140 °C (II), 220 °C (III), 300 °C (IV) and 390 °C (V), respectively. The irradiation dose is 1 Gy.

4.5.7. Step-annealing measurement

Figure 4.59 shows the step annealing data and the associated TL intensities as a function of temperature comparatively. TL intensity is given on the left axis as a function of T_{stop}, and the TL curve as a function of the readout temperature on the right-hand coordinate. In the beginning, TL intensity appears to decrease sharply from room temperature to around 100 °C, indicating that the shallow traps associated with the low-temperature TL peaks might be depleted by preheating at 100 °C. With this preheating, the misleading signal from unstable traps will be prevented and more consistent results could be expected. TL intensity exhibits a progressive decay from 120 to 200 °C preheating. After 200 °C preheating, the TL signals up to 280 °C exhibits a slow decreasing behavior (Figure 4.59). This sample is considered promising because its main glow peak is at about 223 °C, a temperature high enough to provide stability upon storage following exposure. Its glow curve has a component at low temperatures where stability upon storage is not obtained. In addition, the high-temperature portion of the glow curve is not completely exhausted even at 400 °C, a temperature region in which interference from incandescence of the heating apparatus becomes serious, particularly in the detection of the small doses.

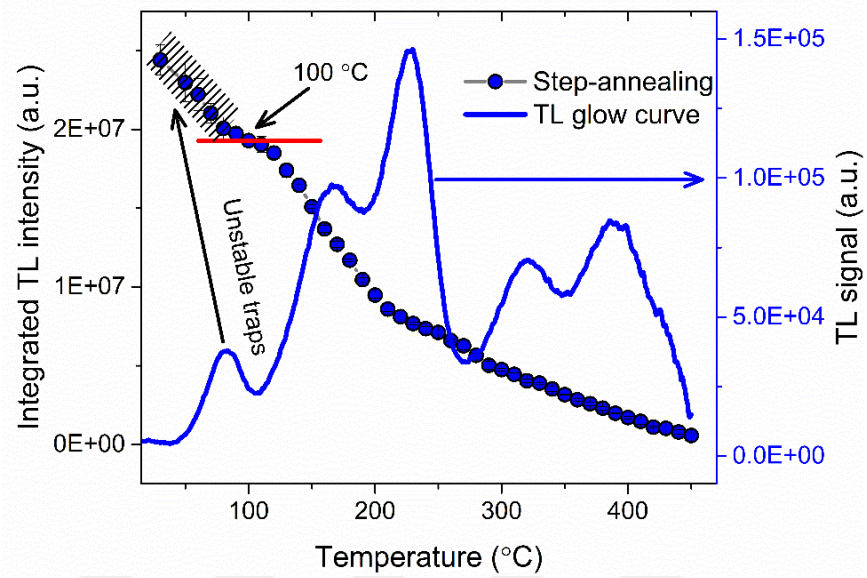

Figure 4.59. Step-annealing curve as a function of T_{stop} (left hand) and TL glow curve as a function of read-out temperature (right hand).

4.5.8. Dose-response of TL peaks

To examine the radiation dose-response of MgO:Ce^{3+} (1 mole%), Li^{+} (1 mole%) phosphor, the dose-dependence of TL peaks was investigated. TL read-outs were performed from RT to 450 °C with a heating rate of 5 Ks^{-1} from the samples exposed to doses between 0.2 Gy and 2 kGy. Before the TL readouts, the samples were preheated to 100 °C following β irradiation to minimize the influence of the shallow traps for each cycle. Increasing dose exposure caused the shallow peak at 165 °C to start increasing immediately reaching its maximum height with ~10^3 orders of magnitudes greater than its initial height with 0.2 Gy dose exposure (Figure 4.60a). Mean values of TL signals were calculated from the TL readout data of three equally weighted samples, and the procedure given in Table 4.5 was applied for each sample used. The dose responses of the integrated TL of all aforementioned five peaks appear on the deconvolved glow curve, specifically the TL peak at 223 °C (Peak III), the main dosimetric peak in this study, and peak at 308 °C (Peak IV) were carried out. Luminescence signals obtained by total TL

integration and Peak III (the temperatures of 210–240 °C were selected in order to present Peak III) and Peak IV were given in Figure 4.60b. The behavior of Peak III exhibits a linear dose-response up to 10 Gy with increasing exposure. After that, it tends to exhibit saturation. Similarly, the signals from Peak IV (300–330 °C was selected to present Peak IV) exhibited linear behavior up to 10 Gy, then showed a saturation trend. The linearity of the total field signals was up to 20 Gy and later found to saturate.

Table 4.5. Dose-response protocol applied to MgO:Ce,Li samples.

Step	**Cycle**
1	Preheating to 500 °C with 5 °Cs^{-1} to deplete traps due to residual dose.
2	Dose exposure to the preheated samples with D_i= 0.2, 0.5, 1, 2, 5, 10, 20, 50, 100, 200, 500, 1000 and 2000 Gy.
3	Preheating up to 100 °C at 5 °Cs^{-1} eliminates the unstable shallow traps.
4	TL readout up to 450 °C at 5 °Cs^{-1}, with Schott BG-39 bandpass optical filter.

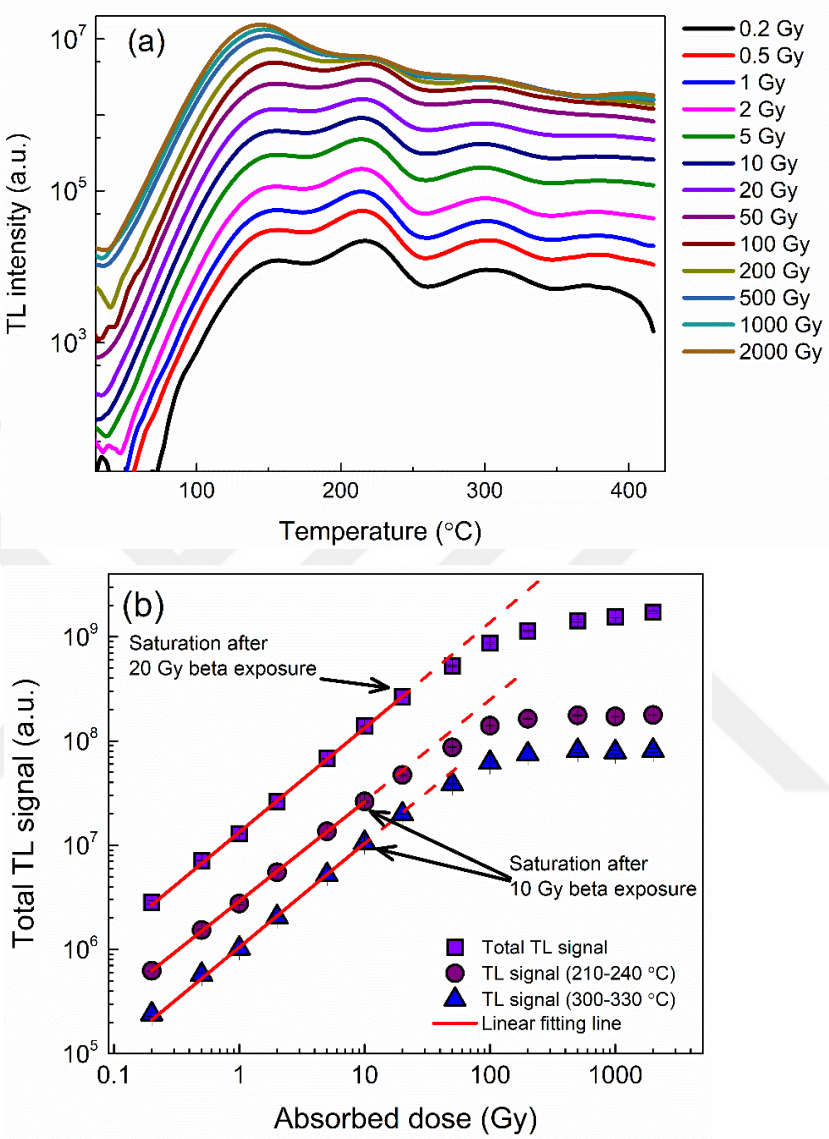

Figure 4.60. (a) TL glow curves measured at 5 °Cs^{-1} following preheating at 100 °C after irradiation to doses between 0.2 Gy and 2 kGy. (b) Dose-response behavior of MgO:Ce,Li phosphor as a function of absorbed doses. Total TL signal and the stable TL peaks were compared (210-240 °C and 300-330 °C peaks by getting 30 °C strips passing through the peak maximums of each). The dashed lines show linearity. The data points were determined by calculating the average values of the three samples exposed. The error bars show the experimental standard deviation, which are not visible in this scale in the graph.

4.5.9. Fading

The fading of the TL signals as a function of the storage time is shown in Figure 4.61. In the present work, MgO:Ce,Li samples exposed to 1 Gy β dose were put on the stainless-steel cups and stored at room temperature in dark for various time intervals of 1, 3, 6, 12, 24, and 72 hours (short-term) and 1, 2, 3 and 4 weeks (long-term). The reason for the dark storage is that a luminophore would have to be shielded from light. In general, dosimetric materials are sensitive to light. so the exposure to sunlight or room light causes light-induced fading of the main TL signal (Yukihara and McKeever, 2011). In fading experiments, three aliquots were used to determine the data for each storage time for better statistical accuracy. Figure 4.61a shows that the TL intensities of glow curves decrease as a function of storage time in short-term storage. Reduction in TL signals of Peak III (the temperatures of 210–240 °C were selected to present Peak III) was observed by 6% after three hours, 13% after 1 day, and 25% after 7 days of dark storage. Peak III lost 40% of its signal in four weeks. The fading curve of TL Peak IV (the temperatures of 300–330 °C was selected to present Peak IV) was recorded with a similar rate of decay during these four weeks. But the short-term fading of Peak IV appeared as a ~4% increase when compared with the TL intensity recorded after half an hour following the dose delivery.

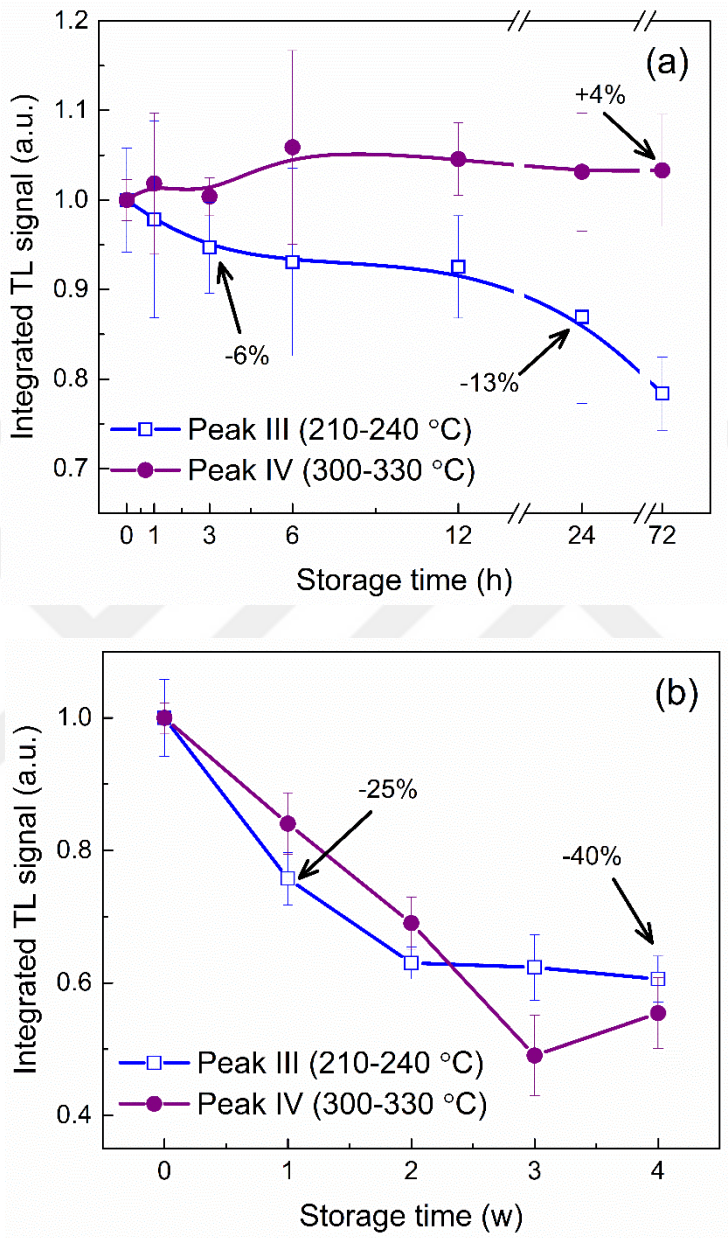

Figure 4.61. Decay of stored energy in MgO:Ce,Li phosphor after 1 Gy β dose exposure in (a) 72 hours (b) four weeks.

4.5.10. Determination of the TL kinetic parameters

In this study, CGCD, VHR methods and T_m-T_{stop} method in combination with the Initial Rise (IR) method were used to determine the kinetic parameters of the TL glow curve of MgO:Ce^{3+} (1 mol%), Li^+ (1 mole%) sample. The kinetic parameters were determined and compared using these methods to show advantages and disadvantages. Experimental methods other than CGCD require that the TL glow peaks should be fully or partially isolated from the neighboring TL peaks. In this study, the isolated TL peaks of the complex TL glow curve of MgO:Ce,Li were obtained by the CGCD method. The CGCD method is widely used for the calculation of the trap parameters without requiring experimental procedures, and it does not matter whether the TL glow curve is complex or not. The advantage of the IR method is that it is a method used to estimate the activation energy independently from the kinetic order (b). But in this method, since 10% of the signal value corresponds to the peak maximum of the TL signal is of interest, the TL peaks must be isolated. The VHR method also has the advantage of being independent of the kinetic order (b). For the details of the methods, the reader can refer to the cited papers (Aitken, 1985a; Azorín, 1986; Chen and McKeever, 1997; Chen et al., 2011; Kirsh, 1992; McKeever et al., 1985; Pagonis et al., 2006). Although not included in this study, several simple methods have been used to analyses TL glow curves, assuming the arbitrary recombination and re-trapping rates suit for evaluating the kinetic parameters of the phosphorus (Gomez-Ros et al., 2006).

4.5.10.1. Glow curve deconvolution

The glow curve deconvolution (CGCD) method is widely used to analyze and determine the components of a complex TL glow curve (Chen and McKeever, 1997). However, the CGCD could not be singly used for determining the number of peaks in a TL glow curve and their kinetic parameters (Horowitz et al., 2013). Additional analysis such as isothermal decay, T_m-T_{stop}, initial rise, and various

heating rates, etc. should be used to test the accuracy of the results obtained using CGCD (McKeever, 1988).

The TL glow curve of MgO:Ce^{3+} (1 mol%), Li^{+} (1 mole%) phosphor irradiated with 1 Gy β dose was deconvoluted into five peaks using the CGCD approach, considering that its TL glow curve has general order kinetics. The TL glow curve was deconvoluted using the Microsoft Excel add-in utility in the tab of solver, which can analyze the overlapped TL peaks. Kinetic parameters such as activation energies (E_a), kinetic orders (b), and frequency factors (s) values were evaluated using the general order kinetic equation with the excel spreadsheet software which is a special software package from Afouxenidis *et al.* (Afouxenidis et al., 2011). The goodness of fit is tested by the Figure of Merit (FOM) (Balian and Eddy, 1977). Figure 4.62a shows the five calculated components using the CGCD method with 1.35% FOM and the experimental TL glow curve. Kinetic parameter values are given in Table 4.6. The activation energies almost continuously increased from 0.60 to 1.55 eV. Since this method is applied by calculating and theoretical matching to a function, it might not exactly correspond to the actual E_a and *s* values. Contrary to this expectation, Table 4.6 shows the E_a values obtained by CGCD agree with the VHR method.

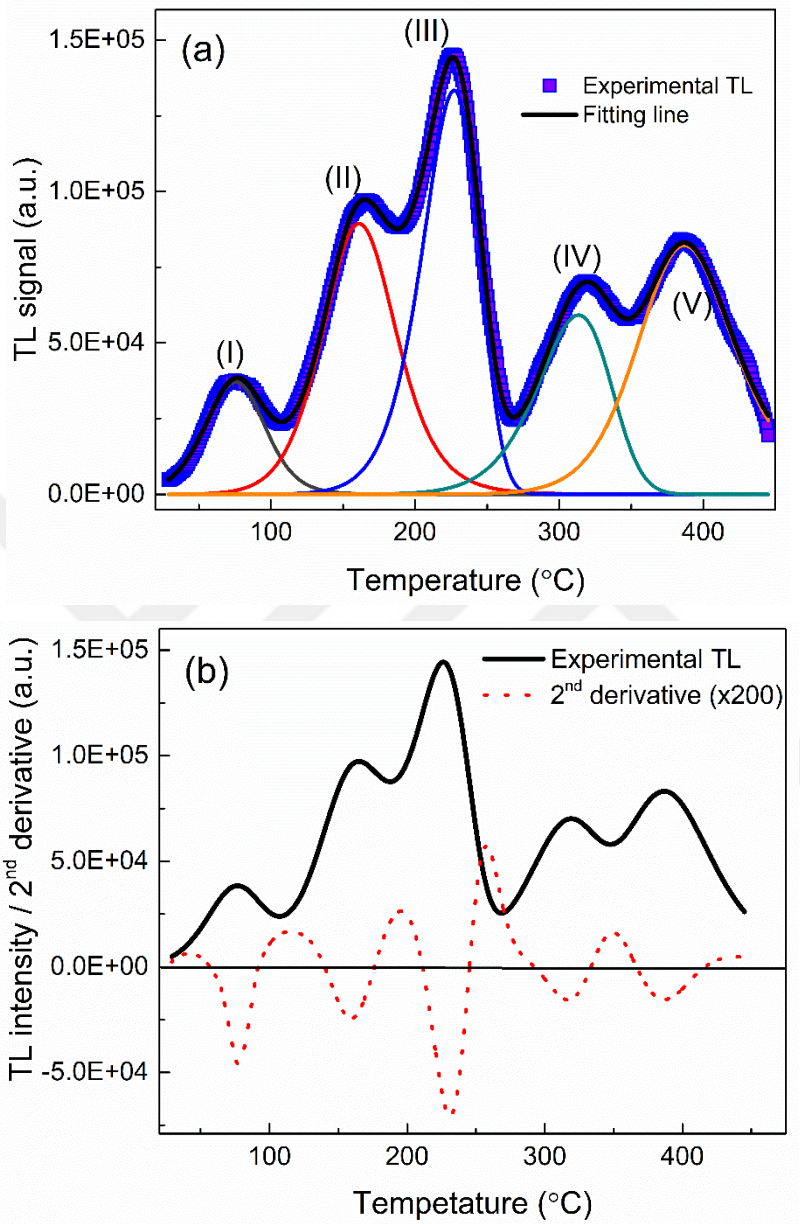

Figure 4.62. (a) The computerized glow curve deconvolution (CGCD) analysis of TL glow curve of MgO:Ce^{3+} (1 mol%), Li^{1+} (1 mole%) phosphor. The TL glow curve contains five individual glow peaks. (b) Schematic diagram of TL glow curve and its second derivatives.

If the number of TL peaks is not known before analyzing the complex TL glow curve, the number of glow peaks deconvoluted in the CGCD could be changed. Therefore, many possible kinetic parameters can be fitted to the same glow curve. The quality of this deconvolution increases if the complex TL curve is fitted with the exact number of component peaks (Karmakar et al., 2017; Sadek, 2013). The exact number of peaks of this complex TL curve can be determined by the second derivative of the intensity (d^2I/dT^2) with respect to the temperature, *T* (Karmakar et al., 2017). In this way, apparently hidden peaks with no local maxima in the I-T radiation curve, together with peaks with local maxima, provide local minima in the second derivative plot, allowing the total number of peaks with their respective locations to be estimated. We observed that each of the peaks in the experimental TL glow curve corresponds to a negative minimum in the second derivative curve (d^2I/dT^2). So that the number of minimums in (d^2I/dT^2) gives the number of TL peaks in the TL glow curve. In our study, it was determined as five, and this number was accepted as a predetermined number of the peaks for CGCD calculations (Figure 4.62b).

Table 4.6. Activation energies E_a, frequency factors s and kinetic order b determined using computerized glow curve deconvolution (CGCD), T_m-T_{stop}, and variable heating rate (VHR) methods.

Method	**CGCD**				**T_m-T_{stop}**	**VHR**	
	E (eV)	s (Hz)	b (a.u.)	FOM (%)	E (eV)	E (eV)	s (Hz)
Peak I	0.60	1.45E+08	1.54		0.56 ± 0.03	0.65 ± 0.03	8.87E+08
Peak II	0.82	9.60E+08	1.78		0.82 ± 0.02	0.82 ± 0.07	1.90E+09
Peak III	1.11	4.44E+10	1.09	1.35	1.11 ± 0.07	1.17 ± 0.10	2.97E+11
Peak IV	1.20	1.20E+11	1.12		1.22 ± 0.03	1.43 ± 0.09	9.95E+12
Peak V	1.55	1.36E+11	2.00		1.53 ± 0.09	N/A	N/A

4.5.10.2. T_m-T_{stop} method in combination with the Initial Rise method

T_m-T_{stop} analysis was performed to determine the total number of peaks in the TL glow curve, which is by heating an irradiated sample to a temperature T_{stop} corresponding to a point on the low-temperature tail. Subsequently, the sample is cooled and the TL readout is performed to obtain the peak point. The peak position T_m obtained from the preheated sample is noted. This procedure is repeated with the slightly increased T_{stop} values each time with 5 K increments in temperature. In our study, firstly MgO:Ce,Li sample was exposed to 1 Gy dose, and TL measurements were performed after 30 °C preheating. Then the subsequent measurements were performed by re-irradiating the same sample each time, and the T_{stop} temperature was increased by 5 K for each cycle from 30 to 450 °C. The positions of the peaks corresponding to each T_{stop} temperature on the TL glow curve were noted. Figure 4.63a presents the T_m-T_{stop} plot obtained from the experiments, showing five peak positions in the TL glow curve of the studied sample. This result is in good agreement with the results obtained from both Thermal Cleaning and CGCD methods.

The T_m–T_{stop} method together with the IR method is known as a useful technique to obtain components of the composite TL glow curves and activation energies of each component. Analysis of composite TL glow curve was carried out using the IR method after T_m–T_{stop} measurements. The area of interest in this analysis is the rising edge of the low-temperature tail of the glow peak. The initial rise of the relevant TL peak will follow exponential independence given in Equation (4.6 regardless of the kinetic order and the applicability of the quasi-equilibrium.

$$I_{TL} \alpha \exp {}^{-E}/_{kT} \tag{4.6}$$

where k is the Boltzmann constant and T is the absolute temperature at which recombination occurs. I_{TL} is the TL intensity of the respective initial rise area, E is the activation energy, i.e., the depth of the respective traps. As a result, a semi-logarithmic plot of TL intensity $ln(I)$ as a function of $1/kT$ by considering up to 10% of the low-temperature side of the peak will have a linear slope, and the magnitude of this slope equals the activation energy E (Kitis et al., 2000). In this method, it is not possible to calculate the frequency factor s and it is independent of the kinetic order b (Chen and McKeever, 1997; Taylor et al., 1978). Five plateau regions, each corresponding to a TL peak, were observed with the activation energies between 0.56 eV and 1.53 eV as a function of T_{stop} temperatures. In Figure 4.63b, it was evident that the distribution of E value with cut-off temperature followed some specific trend. As is seen in Figure 4.63b, the value of E was consistent at 0.56 eV for T_x between 80 and 100 ˚C. Similarly, within 110–150 ˚C, E was consistent at 0.82 eV, within 220–270 ˚C at 1.11 eV, within 250–350 ˚C at 1.22 eV, and within 370–450 ˚C at 1.53 eV. This analysis implies that the sample had a discrete distribution of electron traps. Moreover, the analysis also suggested that there were at least five electron trap groups in the phosphor with the activation energies of 0.56 (Peak I), 0.82 (Peak II), 1.11 (Peak III), 1.22 (Peak IV), and 1.53 (Peak V) eV, respectively. Table 4.6 shows the kinetic parameters obtained using this method for comparison.

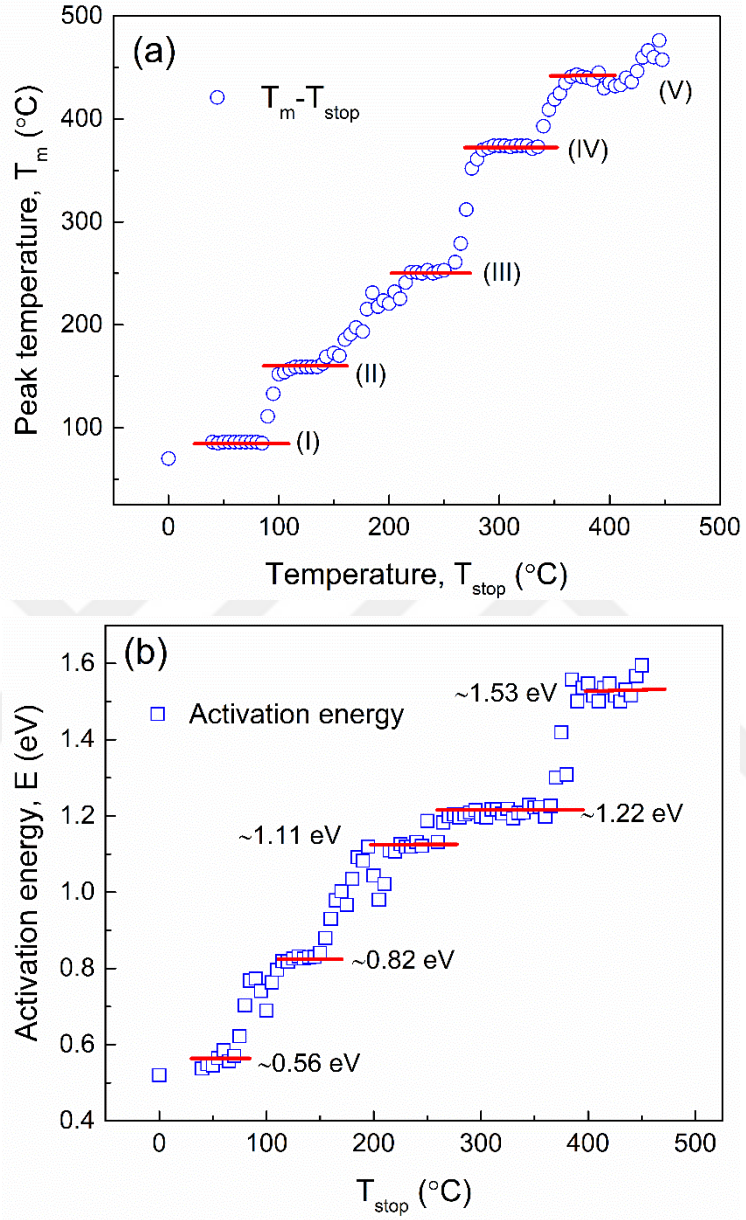

Figure 4.63. (a) The T_m–T_{stop} graph of the MgO:Ce,Li sample. Each plateau presents a TL peak in the TL glow curve. (b) Activation energies as a function of related T_{stop} temperatures.

4.5.10.3. Variable heating rate method

From the TL glow curves obtained by applying the variable heating rate method, the activation energy of Ce and Li doped MgO phosphor can be estimated using Equation (4.7. This method is based on the shift of the peak maxima to higher temperatures with increasing heating rate, as predicted by the Randall and Wilkins model (Randall and Wilkins, 1945).

$$E\beta/kT_m^2 = S\exp(-E/kT_m) \quad (4.7)$$

where β is the heating rate, E is the activation energy of traps corresponding to TL peak, T_m is the temperature at the maximum intensity of the glow peak and k is Boltzmann constant. Figure 4.64a shows the TL glow curves measured at different heating rates. Consistent with the theory, when the heating rate increases, the peak maxima of the TL glow curves shift towards higher temperatures. The activation energies and frequency factors can be obtained from the $ln\ (T_m^2/\beta)$ versus $1/\ kT_m$ plots as seen in Figure 4.64b. The values of the activation energies were calculated as 0.65, 0.82, 1.17, and 1.43 eV for Peaks I, II, III, and IV with the frequency factors of 8.87×10^8, 1.90×10^9, 2.97×10^{11}, and 9.95×10^{12}, respectively. Due to the strong background signals, calculations could not be made for the high-temperature peak, Peak V.

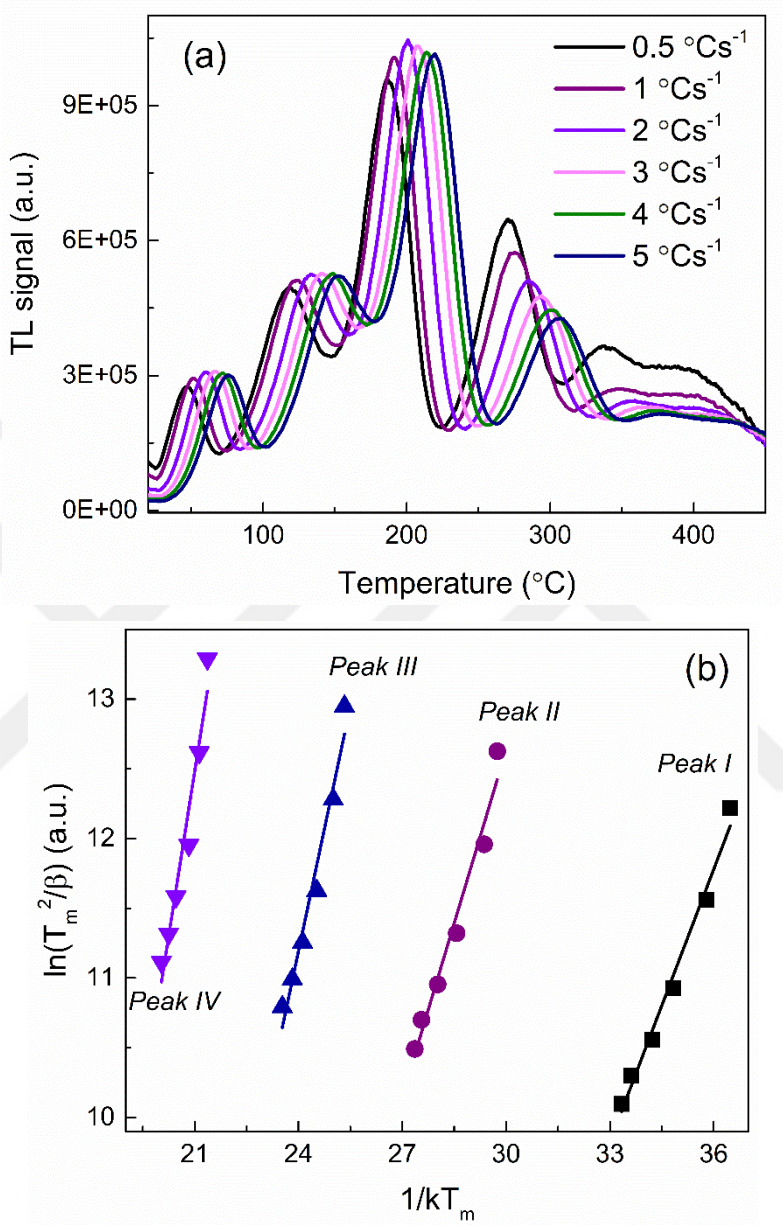

Figure 4.64. (a) TL glow curves of MgO:Ce^{3+} (1 mol%), Li^{1+} (1 mole%) phosphor measured from RT to 450 °C at different heating rates. (b) Plots of $\ln(T_m^2/\beta)$ as a function of $1/kT_m$. Each slope value indicates the activation energy of the relevant TL peak and the exp (intercept) value indicates the frequency factor of this TL peak. The delivered β dose amount is 10 Gy.

4.5.11. Conclusions

In the present study, Ce^{3+} and Li^{+} co-doped MgO phosphors were synthesized using the solid-state reaction technique, and their luminescence properties were investigated. The MgO:Ce,Li phosphor was determined as polycrystalline with a cubic structure of periclase phase with Fm-3m space group. It was observed that MgO:Ce^{3+} (1 mole%), Li^{+} (1 mole%) phosphor possess considerably high PL, RL, and TL intensities when compared to the other studied concentrations. The samples were characterized with the TL peaks at 223 (Peak III) and 308 °C (Peak IV). The dose-response of the phosphor (Peak III and Peak IV) as a function of the β-ray exposure is essentially linear for exposures below 10 Gy. At higher exposures, the response becomes distinctly saturating. After the first day in dark storage, the fading of TL intensity of Peak III was ~13% whereas Peak IV presented a slight increase of ~4% in the same period.

The kinetic parameters of MgO:Ce^{3+} (1 mole%), Li^{+} (1 mole%) were determined using standard methods including CGCD, variable heating rate, and T_m-T_{stop} method in combination with the IR method. The activation energies were found in agreement with each other. T_m-T_{stop} method revealed five activation peaks. Using these activation centers spreading between ~0.6 and ~1.5 eV, it was determined that the main contributions are from these energy levels for radiation storage.

4.6. Study of Li effect on Eu- and Yb- doped $KMgF_3$ for OSL dosimetry

4.6.1. Material Preparation

Inspired by Eu doped $KMgF_3$, which has been extensively studied in the literature and presented with superior dosimetric properties (Andrade et al., 2019; Daniel et al., 2016; Schuyt and Williams, 2018), and also has a very bright OSL (and TL) signal, Eu ion in this study was chosen as the activator. In addition, following the information presented in the literature, the Yb ion was included in the $KMgF_3$ perovskite structure as a sensitizer (Gambarini et al., 1999; Wu et al.,

2016a). Since alkali metal ions are known to play an important role in increasing the luminescence efficiency even in very small amounts as a co-dopant (Bae et al., 2005; Balakrishnaiah et al., 2011; Dhananjaya et al., 2012), Li^+ was added to the Eu^{3+} and Yb^{3+} doped $KMgF_3$. $KMgF_3$ (Parascandolaite) based perovskite-type fluoride were prepared in polycrystalline powder using the sol-gel synthesis method to examine the changes in the perovskite structures by testing different concentrations of Li ions as a result of the significant improvement in the luminescence efficiency of the samples using Li co-dopant, The potassium fluoride (*KF, ACS reagent, ≥99.0%, Sigma Aldrich)* and magnesium fluoride (*MgF_2, ≥99.99% trace metals basis, random crystals, optical grade, Sigma-Aldrich)* were used as the precursors. Ethylene glycol solution (*$C_2H_6O_2$, 99.8% purity, Sigma-Aldrich*) and citric acid (*$C_6H_8O_7$, 99.5% purity, Sigma-Aldrich*) were used as a solvent and a reactant, respectively. The dopant ions were taken from nitrate forms which were lithium nitrate *($LiNO_3$, ReagentPlus®, Sigma-Aldrich)*, ytterbium nitrate (*$Yb(NO_3)_3$, 99.9% trace metals basis, Sigma-Aldrich)* and europium nitrate (*$Eu(NO_3)_3$, 99.9% trace metal basis, Sigma-Aldrich*). Deionized water used for the solution medium was prepared using the New Human Power ultra-purification system (Human Corporation, Korea). The doping ratios of Eu and Yb dopants were optimized by a concentration quenching study and kept constant at 0.5% mole and 0.1% mole, respectively, and the molar ratios of $Li_{x\%}$ was increased (x: 1, 3, 5, 10, 15, 20) by reducing MgF_2 in the precursor from the $KMgF_3$. After the whole mixture was mixed until it became homogeneous, it was kept at low temperature on the hot plate to remove the water from the environment and to obtain a gel form. As the aqueous environment decreased, the gel form began to be observed, and then it was taken into an alumina crucible. The calcination process was carried out in a Protherm branded (max 1800 °C) high-temperature furnace at 800 °C for 2 h. To minimize oxidation, argon gas was passed through the furnace during the calcination process.

4.6.2. Powder X-Ray Diffraction

We performed XRD analyses to identify the crystalline phase formations of the synthesized perovskites as a function of Li co-doping concentration. Figure 4.65 shows XRD patterns (black circle) and Rietveld refinement analysis (red line) results of as-prepared $KMgF_3$ and $KMgF_3$: $Eu_{0.5\%}$,$Yb_{0.1\%}$,$Li_{x\%}$ samples, respectively. As is seen in Figure 4.65, we observed two major phases: $KMgF_3$ with a space group of cubic-$Pm\bar{3}m$ and cell parameters of a=b=c=3.9907 Å fluoroperovskite-like structure and MgF_2 phase with a space group of tetragonal-*P42/mnm* structure and cell parameters of a=b=4.6211 Å and c=3.0505 Å (see Table 4.7) (Andrade et al., 2019; Wu et al., 2016b). In these perovskite structures, Mg^{2+} and K^{+} ions occupy the central sites of MgF_6 octahedral and KF_{12} tetrakaidecahedrons, respectively. We have also determined the secondary oxide peaks such as MgO, KO, and SiO_2 at low degrees for the undoped-$KMgF_3$ sample (Andrade et al., 2019). The unit cell of $KMgF_3$ fluoroperovskite compound is given in Figure 4.66.

Our purpose is to determine a relationship between the changing Li co-dopant concentration and optical and luminescence properties of $KMgF_3$:$Eu_{0.5\%}$,$Yb_{0.1\%}$ and study in detail the possibility of obtaining maximum luminescence intensity. Therefore, the XRD analyses of $KMgF_3$:$Eu_{0.5\%}$,$Yb_{0.1\%}$,$Li_{x\%}$ structures were studied to observe the structural transformation as a function of the pre-determined Li co-doping concentrations. Figure 4.65f shows the XRD data and Rietveld refinement analysis of 15% Li co-doped $KMgF_3$: $Eu_{0.5\%}$, $Yb_{0.1\%}$, polycrystalline by reducing the amount of MgF precursor. Along with the main $KMgF_3$ and MgF_2 phases, we were observed Li_2O_2 formation with hexagonal-P63/mmc and clear MgO phase with cubic-$Fm\bar{3}m$ structures for all samples. Increasing Li ratio and decreasing Mg ratio in the structure resulted in more dense unit cell volume through reducing cell parameters and bond lengths.

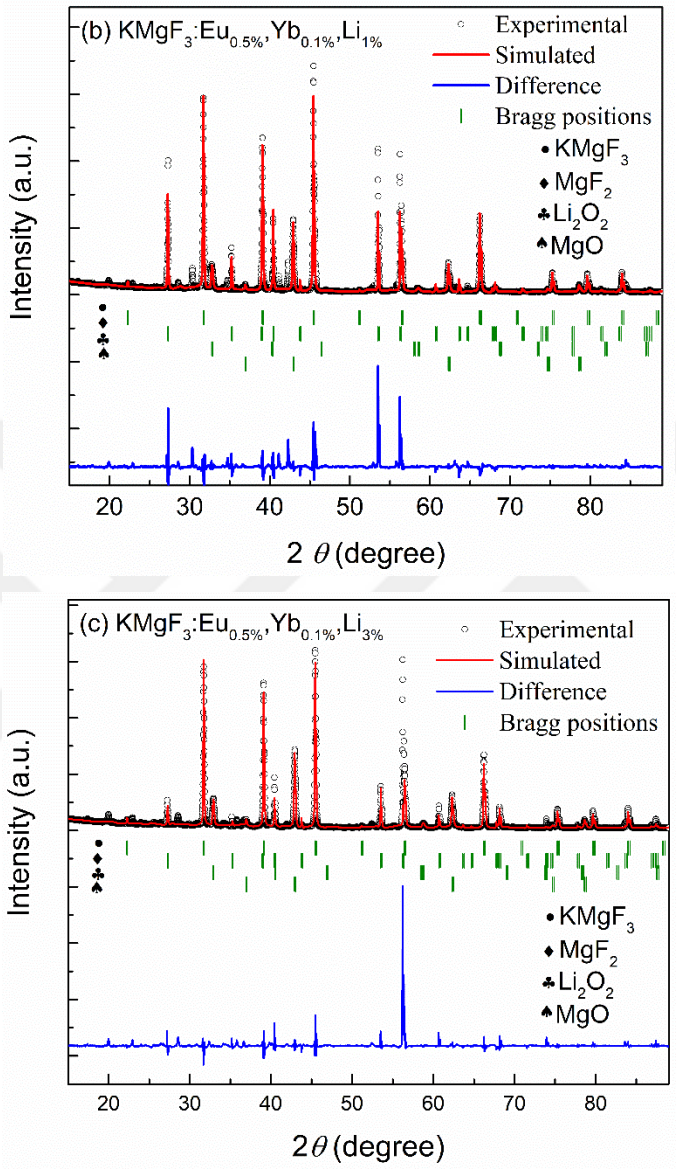
(b) KMgF3:Eu0.5%,Yb0.1%,Li1%
Experimental
Simulated
Difference
Bragg positions
KMgF3
MgF2
Li2O2
MgO
Intensity (a.u.)
20
30
40
50
60
70
80
2 θ (degree)
(c) KMgF3:Eu0.5%,Yb0.1%,Li3%
Experimental
Simulated
Difference
Bragg positions
KMgF3
MgF2
Li2O2
MgO
Intensity (a.u.)
20
30
40
50
60
70
80
2θ (degree)

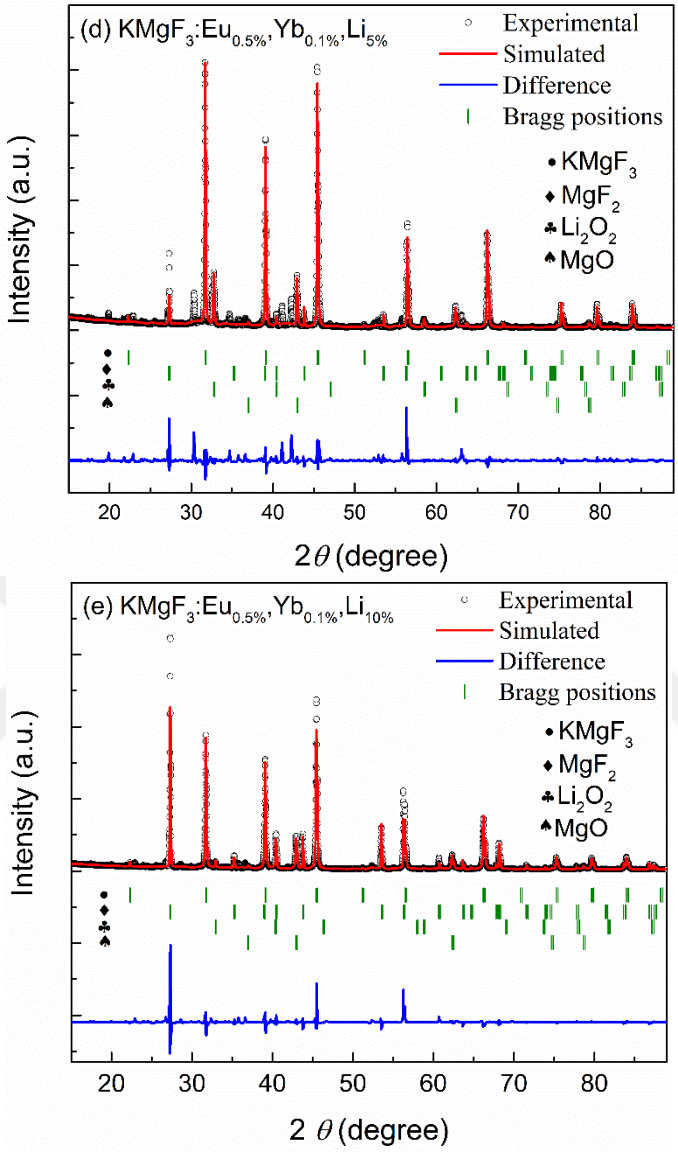
(d) KMgF3:Eu0.5%,Yb0.1%,Li5%
Experimental
Simulated
Difference
Bragg positions
KMgF3
MgF2
Li2O2
MgO
Intensity (a.u.)
20
30
40
50
60
70
80
2θ (degree)
(e) KMgF3:Eu0.5%,Yb0.1%,Li10%
Experimental
Simulated
Difference
Bragg positions
KMgF3
MgF2
Li2O2
MgO
Intensity (a.u.)
20
30
40
50
60
70
80
2 θ (degree)

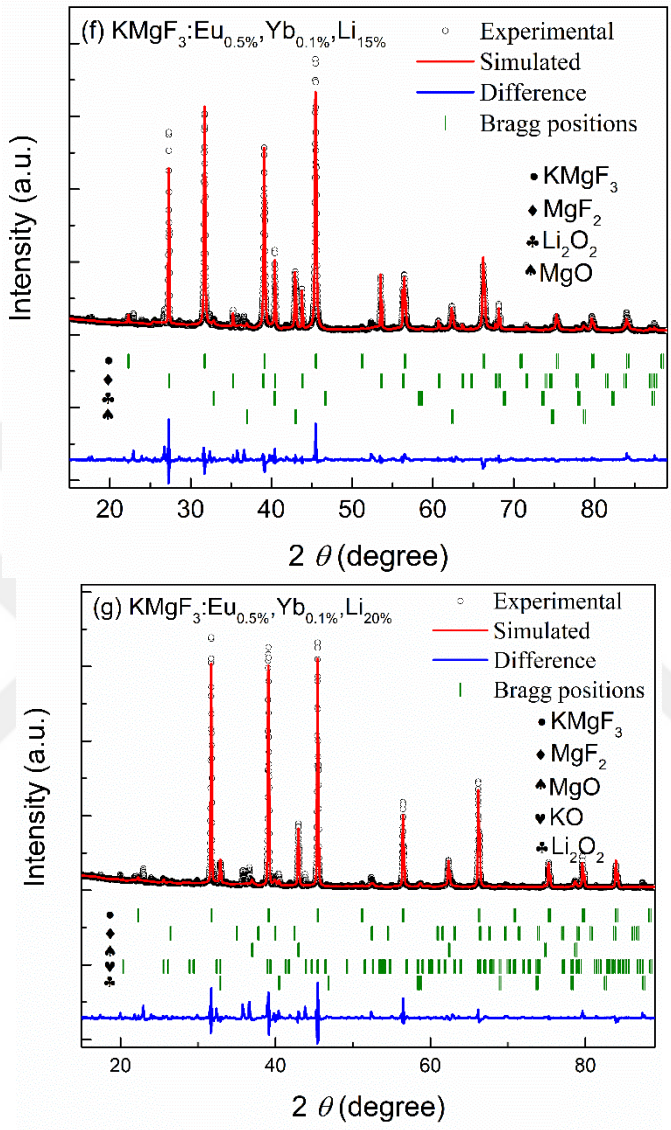

Figure 4.65. (a)XRD data of as-prepared $KMgF_3$ phosphors with $KMgF_3$ (●) and MgF_2 (♦) phases, (b) 1%, (c) 3%, (d) 5%, (e) 10%, (f) 15% and (g) 20% Li doped $KMgF_3$: $Eu_{0.5\%}$, $Yb_{0.1\%}$ sample, with $KMgF_3$ (●), MgF_2 (♦), Li_2O_2 (♣), and MgO (♠) phases. Experimental data (black circle), Rietveld refinement simulation (red line), differences (blue line), and Bragg positions (green bars).

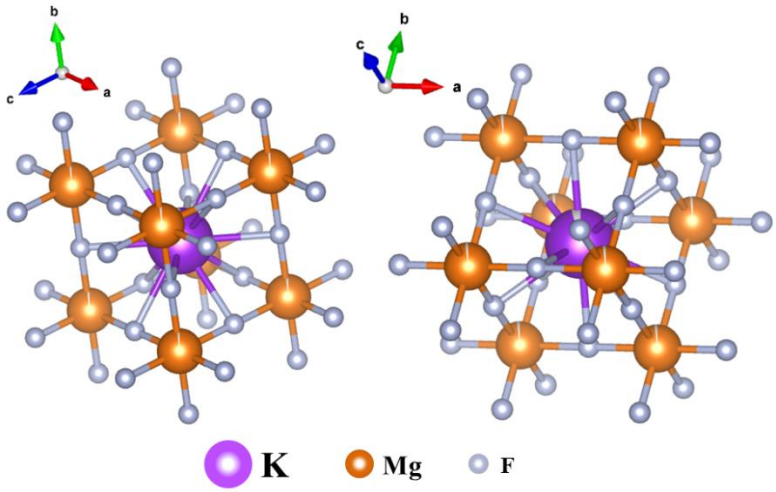

Figure 4.66. Cubic perovskite structure of $KMgF_3$ with space group $Pm\bar{3}m$.

Structure refinement of undoped $KMgF_3$ and Li co-doped $KMgF_3$: Eu, Yb polycrystalline samples, space groups, lattice parameters (a=b=c), unit cell volume (V), and bond lengths of K-F and Mg-F bonds were given in Table 4.7. The addition of 15 mole% Li resulted in a reduction in the unit cell size due to a decrease in the lattice parameters from a=b=c=3.9907 Å to a=b=c=3.9891 Å and the unit cell volume from 63.5555 Å to 63.4763 Å. Consequently, we discovered the K-F and Mg-F bond lengths decreasing from 2.8219 Å to 2.8197 Å and from 1.9954 Å to 1.9939 Å, respectively in the fluoroperovskite structure. In another work, similar values were reported for the K-F bond length of 2.8305 Å (Demartin et al., 2014) and the Mg-F bond length of 1.996 Å (Mitchell et al., 2006). Furthermore, we observed a similar tendency to densification of perovskite samples due to a reduction in the structural parameters. Increasing Li percentage to 20 mole% reduced the other oxide formations (MgO, KO, and SiO_2) in the sample structure. We did not observe the Eu and Yb phases in the XRD due to the small amount of $Eu_{0.5\%}$ and $Yb_{0.1\%}$ ions which might preferentially substitute with Mg^{+2} ions in the $KMgF_3$ crystalline structure (Wu et al., 2016b).

Table 4.7. Structural parameters of undoped $KMgF_3$ and Li co-doped $KMgF_3$: Eu, Yb polycrystalline phases obtained from Rietveld refinement: Space groups, Lattice parameters (*a*=*b*=*c*), unit cell volume (*V*), and bond lengths of K-F and Mg-F bonds.

Phases	Space Group	Lattice Parameters (Å)	V (Å^3)	K–F bond Length (Å)	Mg-F bond Length (Å)
Undoped $KMgF_3$	Cubic-$Pm\bar{3}m$	a=b=c=3.9907	63.5555	2.8219	
MF_2	Tetragonal-*P42/mnm*	a=b=4.6211 c=3.0505	65.1407		1.9954
1% Li doped $KMgF_3$:Eu,Yb	Cubic-*Pm-3m*	a=b=c=3.9891	63.4763	2.8207	
MF_2	Tetragonal-*P42/mnm*	a=b=4.6211 c=3.0505	65.1407		1.9945
Li_2O_2	Hexagon-*P63/mmc*	a=b=3.1524 c=3.8999	38.7563		
MO	Cubic-*Fm-3m*	a=b=c=4.2122	74.737		
3% Li doped $KMgF_3$:Eu,Yb	Cubic-*Pm-3m*	a=b=c=3.9882	63.4763	2.8201	
MF_2	Tetragonal-*P42/mnm*	a=b=4.6214 c=3.0494	65.1276		1.9941
Li_2O_2	Hexagon-*P63/mmc*	a=b=3.1420 c=3.8751	38.256		
MO	Cubic-*Fm-3m*	a=b=c=4.2116	74.7062		
5% Li doped $KMgF_3$:Eu,Yb	Cubic-*Pm-3m*	a=b=c=3.9897	63.5083	2.82117	
MF_2	Tetragonal-*P42/mnm*	a=b=4.6188 c=3.0568	65.2117		1.9947
Li_2O_2	Hexagon-*P63/mmc*	a=b=3.1553 c=3.8646	38.4748		
MO	Cubic-*Fm-3m*	a=b=c=4.2108	74.6614		

Table 4.7. Continue

10% Li doped $KMgF_3$:Eu,Yb	Cubic-*Pm-3m*	a=b=c=3.9889	63.4711	2.8206	
MF_2	Tetragonal-*P42/mnm*	a=b=4.6209 c=3.0500	65.1263		1.9945
Li_2O_2	Hexagon-*P63/mmc*	a=b=3.1412 c=3.9186	38.6672		
MO	Cubic-*Fm-3m*	a=b=c=4.2115	74.7026		
15% Li doped $KMgF_3$:Eu,Yb	Cubic-$Pm\bar{3}m$	a=b=c=3.9891	63.4763	2.8197	
MF_2	Tetragonal-*P42/mnm*	a=b=4.6197 c=3.0499	65.0927		1.9939
Li_2O_2	Hexagon-*P63/mmc*	a=b=3.1498 c=3.8929	38.6228		
MO	Cubic-$Fm\bar{3}m$	a=b=c=4.2103	74.6337		
20% Li doped $KMgF_3$:Eu,Yb	Cubic-*Pm-3m*	a=b=c=3.9890	63.4763	2.8213	
MF_2	Tetragonal-*P42/mnm*	a=b=4.6197 c=3.0499	65.0927		1.9949
Li_2O_2	Hexagon-*P63/mmc*	a=b=3.1498 c=3.8929	38.6228		
MO	Cubic-*Fm-3m*	a=b=c=4.2103	74.6337		

We have calculated crystal size (D), dislocation density (δ), microstrain (ε), and d-space for selected main Miller indices of the structure. These parameters were summarized in Table 4.8 for the undoped sample, $KMgF_3$ and its MgF_2 phase, together with a 15 mole% Li co-doped sample $KMgF_3$: $Eu_{0.5\%}$, $Yb_{0.1\%}$, and its MgF_2, Li_2O_2, and MgO phases. The crystal sizes were calculated as the averages of the crystal sizes found from the full width at half maximum (FWHM) values of the characteristic diffraction lines using the selected Miller indices. In a 15 mole% Li co-doped sample, the crystal sizes of all phases were reduced due to a reduction in the cell parameters. Whereas, we observed an increase of the δ and ε values in the same samples following the addition of Li to the host material (Kunkel et al., 2014). We also reported the D, δ, ε, and the d-space values in Table 4.8 in which a decrease in the calculated d-space was caused by reduced cell parameters for various Li co-dopings.

Table 4.8. Structural parameters of undoped $KMgF_3$ and Li co-doped $KMgF_3$: Eu, Yb polycrystalline phases obtained from Rietveld refinement: Diffraction angle (2θ), Miller indices, Crystal size of selected peaks (D), Dislocation density (δ), Microstrain (ε), and d-space.

Phases	2θ (°)	Plane	D (nm)	δ x 10^{-3} (nm^{-2})	ε x 10^{-3}	d-space (Å)
Undoped $KMgF_3$	31.68	(110)	72.53	0.1901	1.8299	2.822
	39.06	(111)	77.56	0.1662	1.3973	2.304
	45.42	(200)	82.43	0.1472	1.1386	1.995
MgF_2	27.37	(110)	181.07	0.0305	0.8458	3.268
	38.95	(200)	77.53	0.1664	1.4018	2.311
	40.42	(111)	136.97	0.0533	0.7657	2.230
1% Li $KMgF_3$	31.70	(110)	41.24	0.5879	3.2171	2.821
	39.08	(111)	82.27	0.1477	1.3168	2.303
	45.44	(200)	88.52	0.1276	1.0599	1.995
MgF_2	27.26	(110)	116.25	0.0740	1.3224	3.268
	38.94	(200)	82.23	0.1479	1.3219	2.311
	40.42	(111)	185.50	0.0291	0.5654	2.230
Li_2O_2	32.77	(100)	37.02	0.7297	3.4691	2.730
	40.26	(101)	130.44	0.0588	0.8072	2.238
	58.50	(110)	20.78	2.3148	3.5673	1.576
MgO	36.93	(111)	75.86	0.1738	1.5079	2.432
	42.91	(200)	61.19	0.2671	1.6189	2.106
	62.29	(220)	64.99	0.2368	1.0779	1.489
3% Li $KMgF_3$	31.70	(110)	76.59	0.1705	1.7319	2.820
	39.09	(111)	86.98	0.1322	1.2451	2.303
	45.45	(200)	75.46	0.1756	1.2430	1.994
MgF_2	27.27	(110)	172.27	0.0337	0.8923	3.268
	38.94	(200)	86.94	0.1323	1.2501	2.311
	40.42	(111)	178.04	0.0315	0.5890	0.229
Li_2O_2	32.89	(100)	38.74	0.6664	3.3040	2.721
	40.47	(101)	178.07	0.0315	0.5882	2.227
	58.72	(110)	25.60	1.5253	2.8860	1.571
MgO	36.94	(111)	46.44	0.4636	2.4627	2.432
	42.91	(200)	58.97	0.2876	1.6797	2.106
	62.30	(220)	58.95	0.2878	1.1882	1.489
5% Li $KMgF_3$	31.69	(110)	87.90	0.1294	1.5097	2.821
	39.07	(111)	91.59	0.1192	1.1830	2.304
	45.43	(200)	93.87	0.1135	0.9996	1.995
MgF_2	27.28	(110)	116.26	0.0740	1.3214	3.266
	38.97	(200)	82.24	0.1478	1.3208	2.309
	40.38	(111)	185.48	0.0291	0.5660	2.232
Li_2O_2	32.76	(100)	37.02	0.7297	3.4701	2.733
	40.39	(101)	130.50	0.0587	0.8042	2.231
	58.45	(110)	20.78	2.3160	3.5714	1.578

Table 4.8. Continue

	36.94	(111)	75.86	0.1737	1.5073	2.431
MgO	42.92	(200)	61.20	0.2670	1.6183	2.105
	62.32	(220)	64.99	0.2367	1.0774	1.489
	31.70	(110)	41.24	0.5879	3.2170	2.821
10% Li $KMgF_3$	39.08	(111)	82.27	0.1477	1.3167	2.303
	45.44	(200)	88.52	0.1276	1.0598	1.995
	27.34	(110)	116.27	0.0740	1.3186	3.268
MgF_2	38.95	(200)	82.24	0.1479	1.3215	2.311
	40.42	(111)	185.50	0.0291	0.5653	2.230
	32.90	(100)	37.03	0.7292	3.4554	2.720
Li_2O_2	40.33	(101)	130.47	0.0587	0.8057	2.235
	58.74	(110)	20.81	2.3095	3.5503	1.571
	36.94	(111)	75.86	0.1738	1.5076	2.432
MgO	42.91	(200)	61.19	0.2670	1.6186	2.106
	62.30	(220)	64.99	0.2368	1.0777	1.489
	31.71	(110)	65.34	0.2342	2.0297	2.820
15% Li $KMgF_3$	39.09	(111)	70.27	0.2025	1.5412	2.302
	45.45	(200)	72.37	0.1909	1.2959	1.994
	27.28	(110)	94.84	0.1112	1.6202	3.267
MgF_2	38.96	(200)	70.24	0.2027	1.5469	2.310
	40.43	(111)	101.71	0.0967	1.0310	2.229
	32.80	(100)	35.37	0.7992	3.6272	2.728
Li_2O_2	40.34	(101)	101.68	0.0967	1.0334	2.234
	58.56	(110)	51.33	0.3796	1.4433	1.575
	36.95	(111)	81.90	0.1491	1.3961	2.431
MgO	42.93	(200)	63.96	0.2444	1.5481	2.105
	62.33	(220)	57.05	0.3073	1.2273	1.489
	31.69	(110)	75.12	0.1772	1.7665	2.821
20% Li $KMgF_3$	39.07	(111)	72.82	0.1886	1.4880	2.304
	45.43	(200)	75.46	0.1756	1.2436	1.995
	27.27	(110)	67.33	0.2206	2.2823	3.267
MgF_2	38.95	(200)	72.79	0.1887	1.4928	2.310
	40.42	(111)	96.71	0.1069	1.0845	2.230
	32.77	(100)	100.00	0.3096	2.2600	2.731
Li_2O_2	40.40	(101)	96.70	0.1069	1.0852	2.238
	58.50	(110)	25.57	1.5295	2.9000	1.573
	36.98	(111)	81.98	0.1488	1.3935	2.429
MgO	42.96	(200)	66.94	0.2231	1.4779	2.103
	62.38	(220)	60.37	0.2744	1.1589	1.487

4.6.3. SEM and EDS

The surface morphology of Li co-doped $KMgF_3:Eu_{0.5\%},Yb_{0.1\%}$ fluoroperovskite was analyzed using SEM images at different magnifications. A series of SEM images with pre-determined Li contents (x=1, 3, 5, 10, 15, and 20 %) were recorded at 5.000, 10.000 and 20.000x magnification (see Figure 4.67). Increasing Li content in the $KMgF_3:Eu_{0.5\%},Yb_{0.1\%}$ structure improved the crystallinity of $KMgF_3$ powders. the SEM images show that the 15 mole% Li co-doped sample provides homogeneous structures with approximately <0.1 μ grain size owing to a clear cubic formation. These results can also be correlated with XRD data by the comparison of the calculated crystal size of samples reducing with the increasing Li percentage concentration. Nevertheless, the clustering of microcrystals in some regions and the relatively larger formations are attributed to the uneven temperature flow in the mass due to the exothermic reaction between metal ions and fuel (Tiwari et al., 2017).

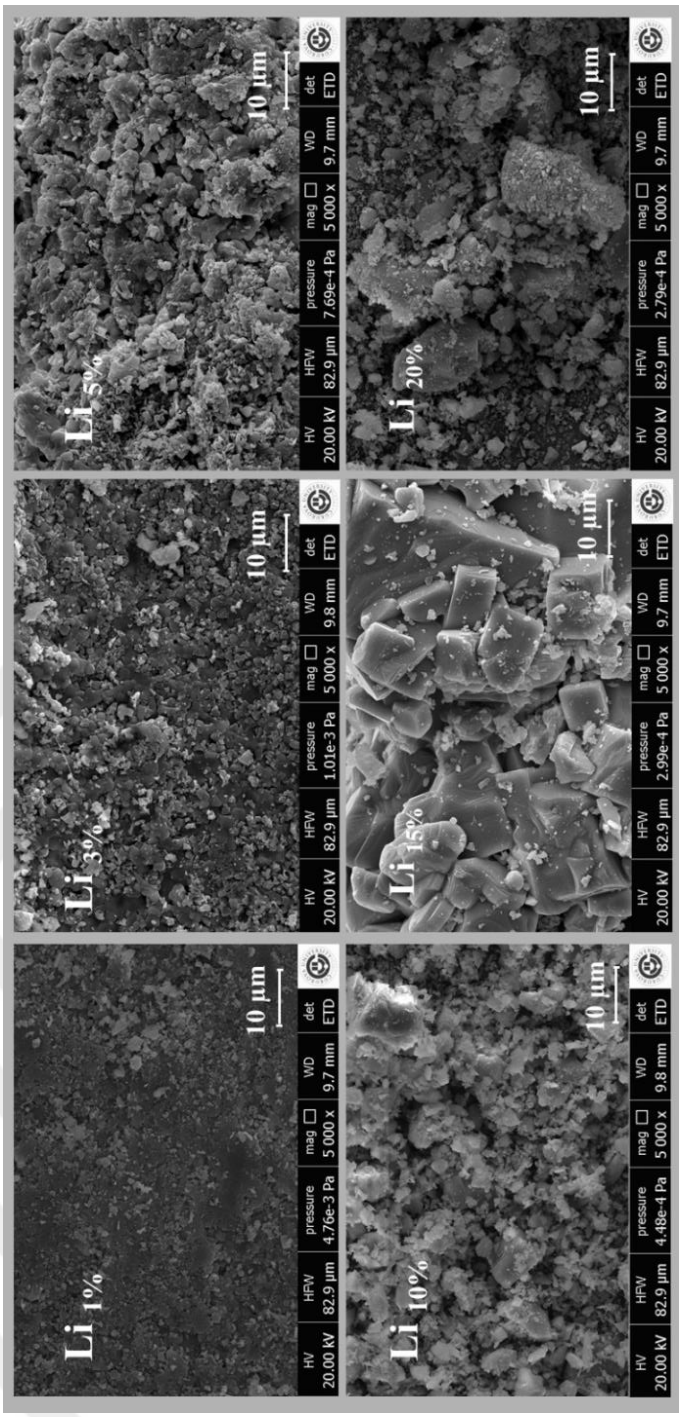
Li 1%
Li 3%
Li 5%
Li 10%
Li 15%
Li 20%
10 µm
HV 20.00 kV
HFW 82.9 µm
pressure 4.76e-3 Pa
pressure 1.01e-3 Pa
pressure 7.69e-4 Pa
pressure 4.48e-4 Pa
pressure 2.99e-4 Pa
pressure 2.79e-4 Pa
mag 5 000 x
WD 9.7 mm
WD 9.8 mm
det ETD

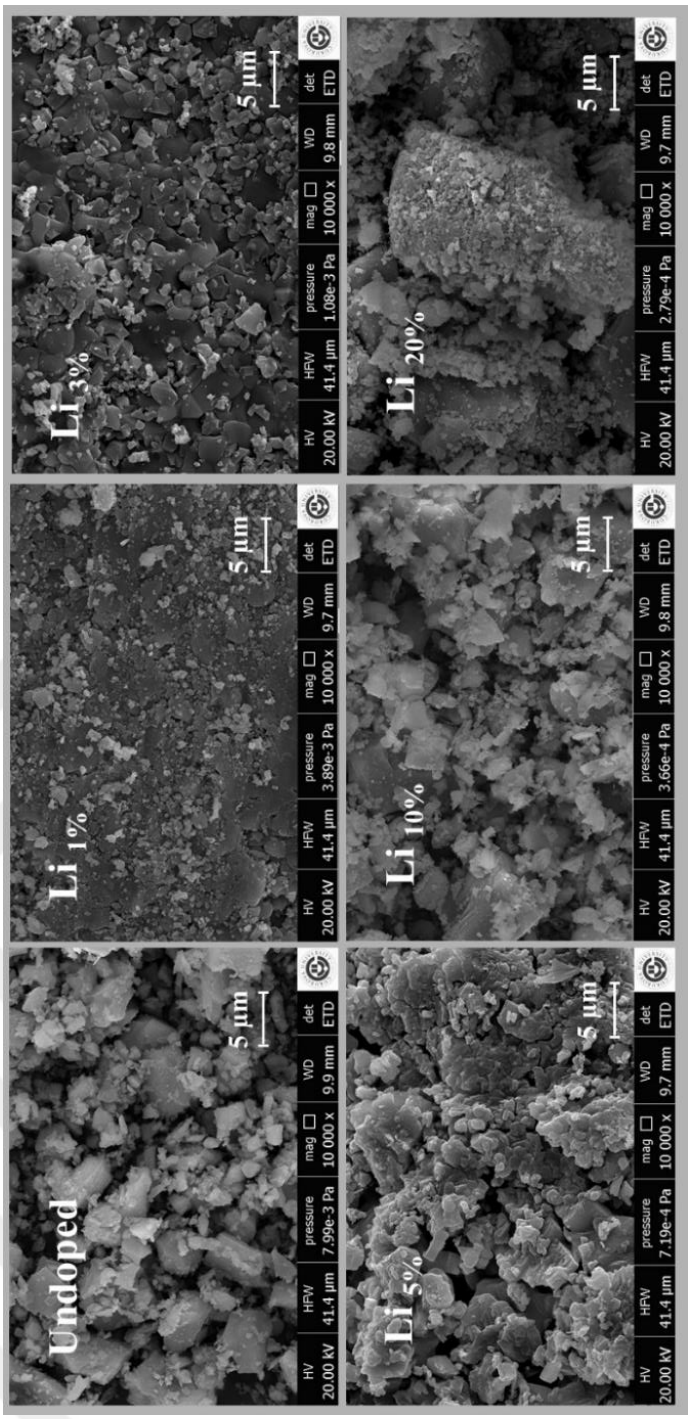
Undoped
Li 1%
Li 3%
Li 5%
Li 10%
Li 20%
5 µm
HV 20.00 kV
HFW 41.4 µm
pressure 7.99e-3 Pa
pressure 3.89e-3 Pa
pressure 1.08e-3 Pa
pressure 7.19e-4 Pa
pressure 3.66e-4 Pa
pressure 2.79e-4 Pa
mag 10 000 x
WD 9.9 mm
WD 9.7 mm
WD 9.8 mm
det ETD

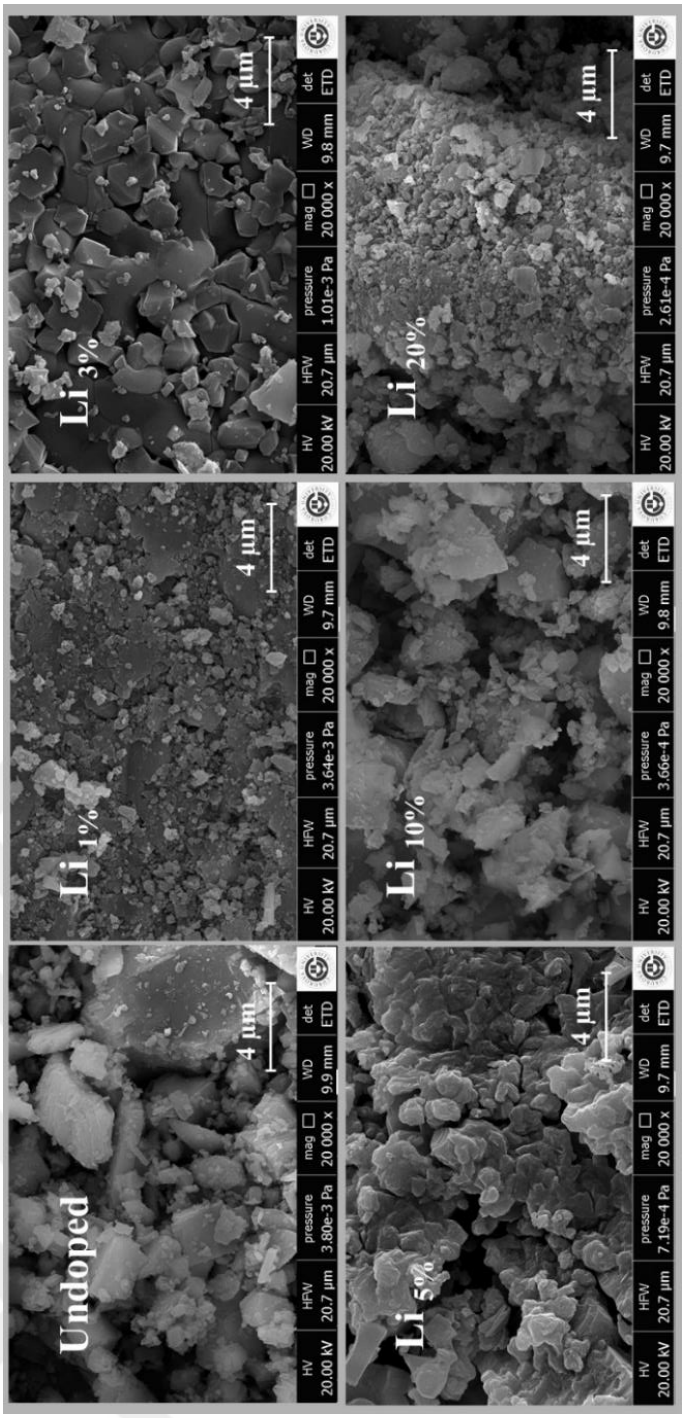

Figure 4.67. SEM micrographs with the (a) 5.000x, (b) 10.000x and (c) 20.000x magnification of $KMgF_3$:$Eu_{0.5\%}$,$Yb_{0.1\%}$,$Li_{x\%}$ (x=1, 3, 5, 10, 15, and 20) samples prepared using sol-gel method and calcined at 800 °C for 2 h in argon atmosphere.

The chemical compositions seen by EDS on different areas confirmed the basic impurities and additives. Figure 4.68 show EDS analysis of undoped $KMgF_3$ and doped $KMgF_3$ with electron shell of potassium (K), magnesium (Mg), fluorine (F), oxygen (O), europium (Eu), and ytterbium (Yb) in the host structure atomic detection, respectively. The elemental analyses of undoped and Li co-doped samples were presented in Table 4.9 with the distributions of atomic percentages which are normalized for each Li content by the percentage of K atom. As XRD and Rietveld refinement analyses confirmed oxide formation in the structure, the averaged EDS results indicate the oxygen content in the sample structures. This result is attributed to the fact that the high-temperature furnace used in the calcination process is not fully isolated from the atmosphere and most probably contains a low amount of oxygen together with the argon gas inside the furnace. We also detected Si atoms in the EDS spectra of all samples. This undesired impurity may come from the potassium fluoride precursor (impurity of ≤0.1% K_2SiF_6). Li-ions (Z<5) could not be detected by EDS because of the beryllium window in front of the detector (Goldstein et al., 2017; Hovington et al., 2016).

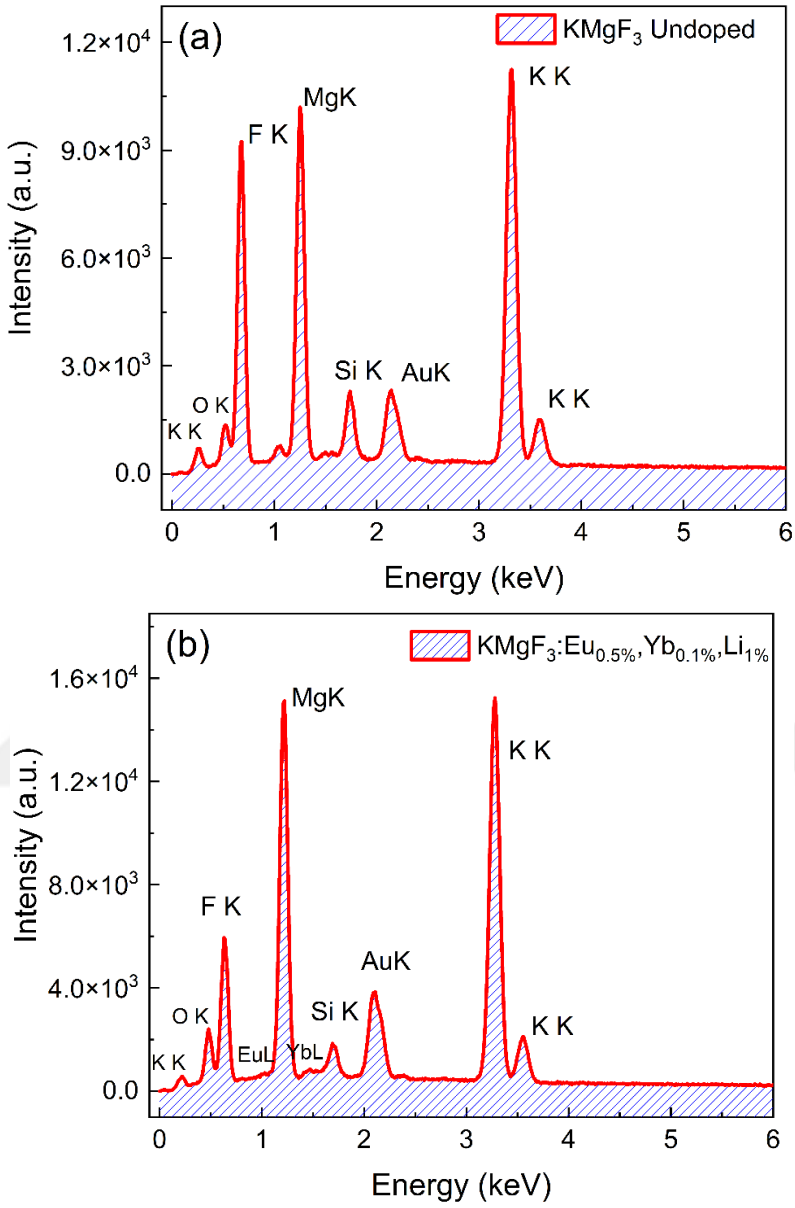
(a)
KMgF3 Undoped
Intensity (a.u.)
Energy (keV)
O K
K K
F K
MgK
Si K
AuK
K K
K K
(b)
KMgF3:Eu0.5%,Yb0.1%,Li1%
Intensity (a.u.)
Energy (keV)
K K
O K
F K
EuL
YbL
MgK
Si K
AuK
K K

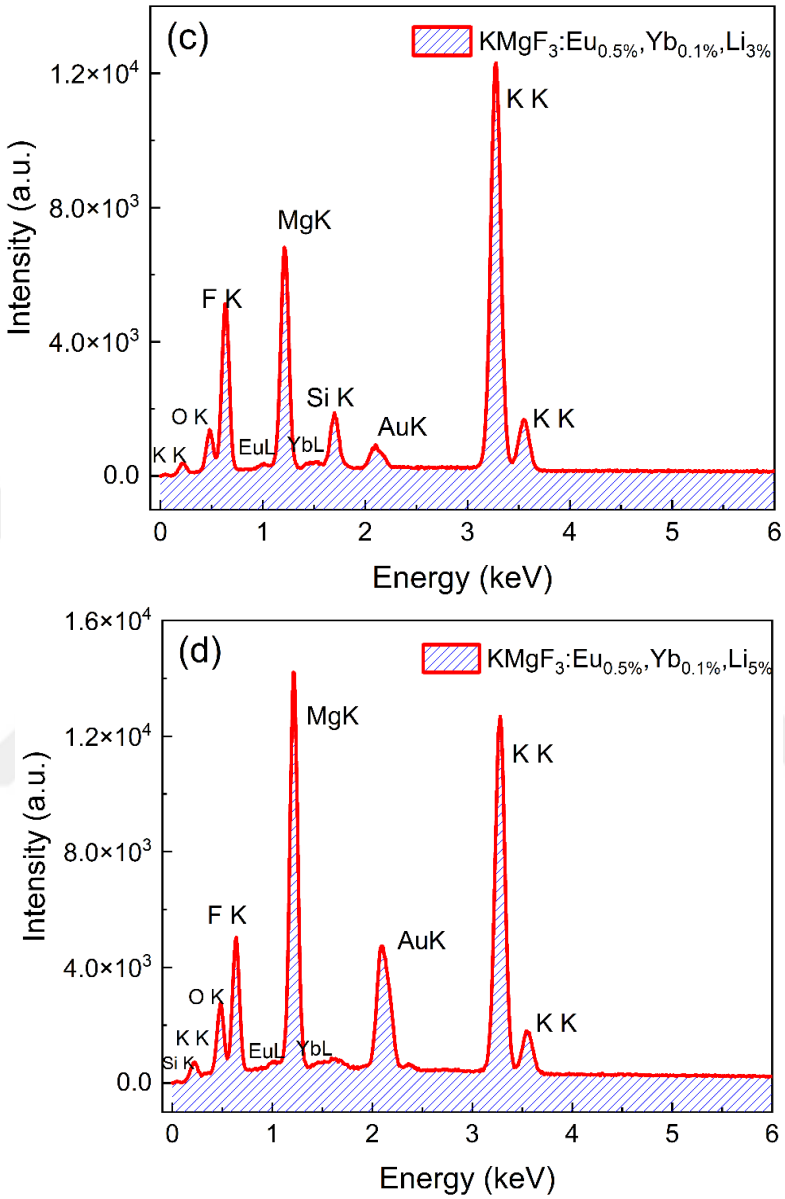
(c)
KMgF3:Eu0.5%,Yb0.1%,Li3%
1.2×10^4
8.0×10^3
4.0×10^3
0.0
Intensity (a.u.)
K K
MgK
F K
O K
K K
EuL
YbL
Si K
AuK
K K
0
1
2
3
4
5
6
Energy (keV)
(d)
KMgF3:Eu0.5%,Yb0.1%,Li5%
1.6×10^4
1.2×10^4
8.0×10^3
4.0×10^3
0.0
Intensity (a.u.)
MgK
K K
F K
AuK
O K
K K
Si K
EuL
YbL
K K
0
1
2
3
4
5
6
Energy (keV)

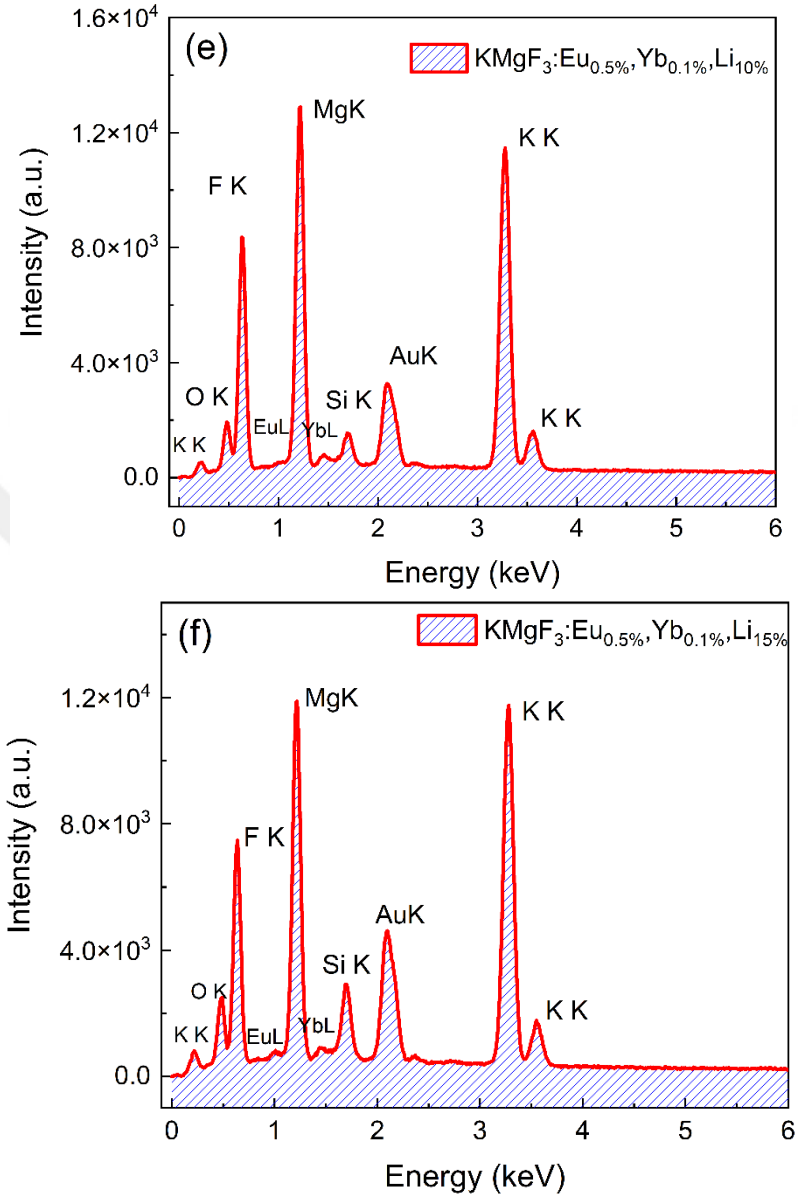
(e)
KMgF3:Eu0.5%,Yb0.1%,Li10%
MgK
K K
F K
AuK
O K
Si K
EuL
YbL
K K
K K
Intensity (a.u.)
Energy (keV)
(f)
KMgF3:Eu0.5%,Yb0.1%,Li15%
MgK
K K
F K
AuK
O K
Si K
EuL
YbL
K K
K K
Intensity (a.u.)
Energy (keV)

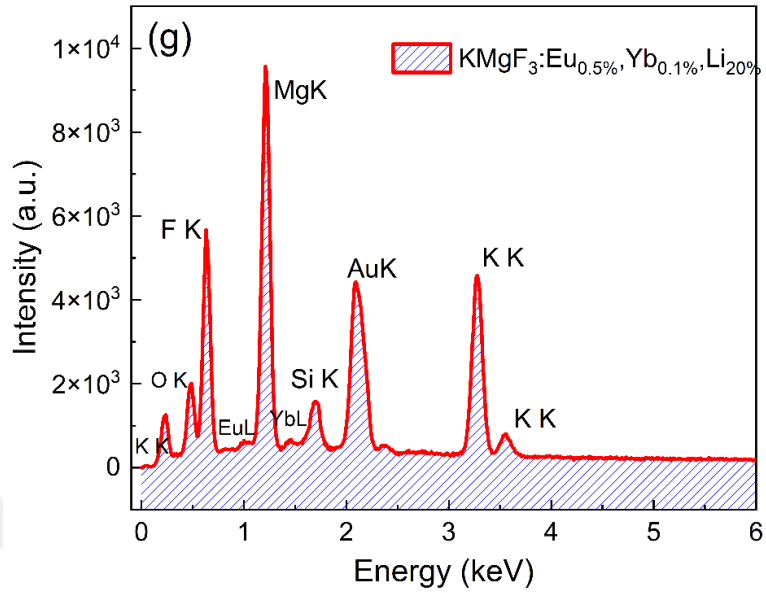

Figure 4.68. EDS analysis of (a) undoped $KMgF_3$, (b) $KMgF_3$:$Eu_{0.5\%}$,$Yb_{0.1\%}$,$Li_{1\%}$, (c) $KMgF_3$:$Eu_{0.5\%}$,$Yb_{0.1\%}$,$Li_{3\%}$, (d) $KMgF_3$:$Eu_{0.5\%}$,$Yb_{0.1\%}$,$Li_{5\%}$, (e) $KMgF_3$:$Eu_{0.5\%}$,$Yb_{0.1\%}$,$Li_{10\%}$, (f) $KMgF_3$:$Eu_{0.5\%}$,$Yb_{0.1\%}$,$Li_{15\%}$ and (g) $KMgF_3$:$Eu_{0.5\%}$,$Yb_{0.1\%}$,$Li_{20\%}$.

Table 4.9. Elemental analysis of the Li doped $KMgF_3$ phosphors as atomic% distribution which is normalized by the percentage of K atom.

	Experimental atomic%						
Element	**K**	**Mg**	**F**	**O**	**Eu**	**Yb**	**Si**
Undoped $KMgF_3$	1.000	1.195	2.758	1.696	-	-	0.470
$KMgF_3$:Eu,Yb,$Li_{1\%}$	1.000	1.167	1.996	0.926	0.003	0.003	0.037
$KMgF_3$:Eu,Yb,$Li_{3\%}$	1.000	3.556	2.300	4.389	0.005	0.005	0.233
$KMgF_3$:Eu,Yb,$Li_{5\%}$	1.000	2.647	1.795	3.313	0.004	0.005	0.195
$KMgF_3$:Eu,Yb,$Li_{10\%}$	1.000	0.522	0.895	0.374	0.042	0.024	0.033
$KMgF_3$:Eu,Yb,$Li_{15\%}$	1.000	1.210	2.565	0.868	0.004	0.005	0.868
$KMgF_3$:Eu,Yb,$Li_{20\%}$	1.000	7.035	9.7329	2.338	0.012	0.016	0.285

4.6.4. FT-IR

The FT-IR spectra of undoped (black line) and Li co-doped (red line) $KMgF_3:Eu_{0.5\%},Yb_{0.1\%}$ fluoroperovskite are presented in Figure 4.69a. All determined peaks are associated with the Mg-F bond stretching mode of vibration as the characteristic peak of $KMgF_3$. The spectral band at 1020 cm^{-1} is due to the stretching mode vibration of the Mg-F bond. The FT-IR analysis of the undoped sample reveals that the frequency envelope around 1300 cm^{-1} consists of two-component bands at 1230 and 1400 cm^{-1} due to the Mg-F bond. The predominant absorption peak at 430 cm^{-1} observed for all samples shows the K-F bond (Chantry et al., 1981). The FT-IR spectra of 1, 3, 5, 10, and 20% Li co-doped $KMgF_3:Eu_{0.5\%},Yb_{0.1\%}$ samples were presented in Figure 4.69b-f . We observed a reduction of Mg-F bands by FT-IR spectra for all samples due to Mg^{+2} ion substitution with Eu, Yb, and Li atoms in the sample structure which was also confirmed with XRD analysis. The peak at 2903 and 2970 cm^{-1} belongs to aliphatic C-H stretching and the peak at 3666 cm^{-1} assigns to O-H stretching.

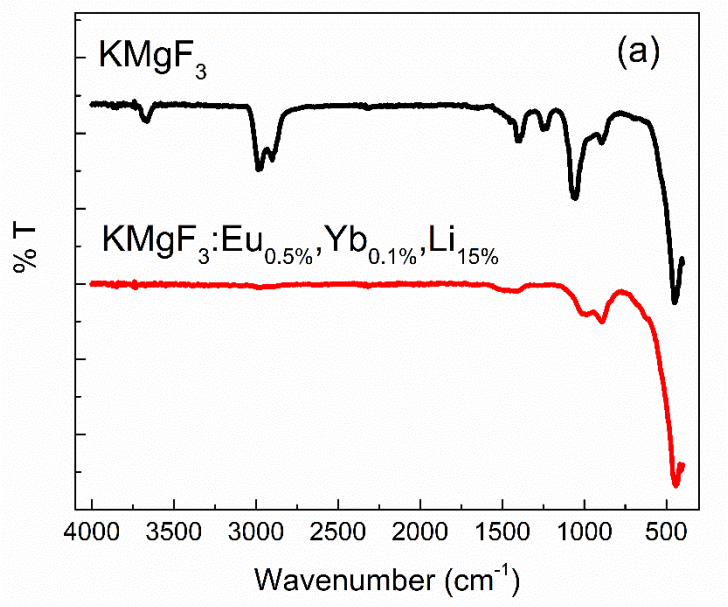

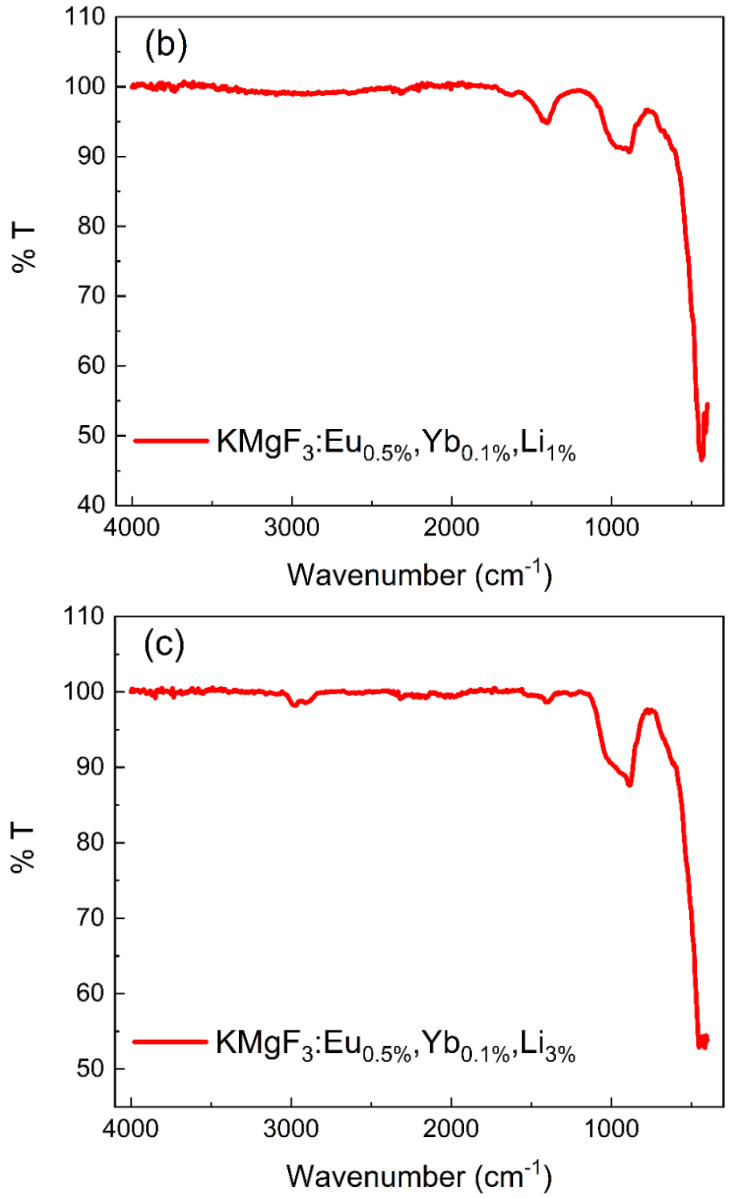
(b)
% T
110
100
90
80
70
60
50
40
4000
3000
2000
1000
Wavenumber (cm-1)
KMgF3:Eu0.5%,Yb0.1%,Li1%
(c)
% T
110
100
90
80
70
60
50
4000
3000
2000
1000
Wavenumber (cm-1)
KMgF3:Eu0.5%,Yb0.1%,Li3%

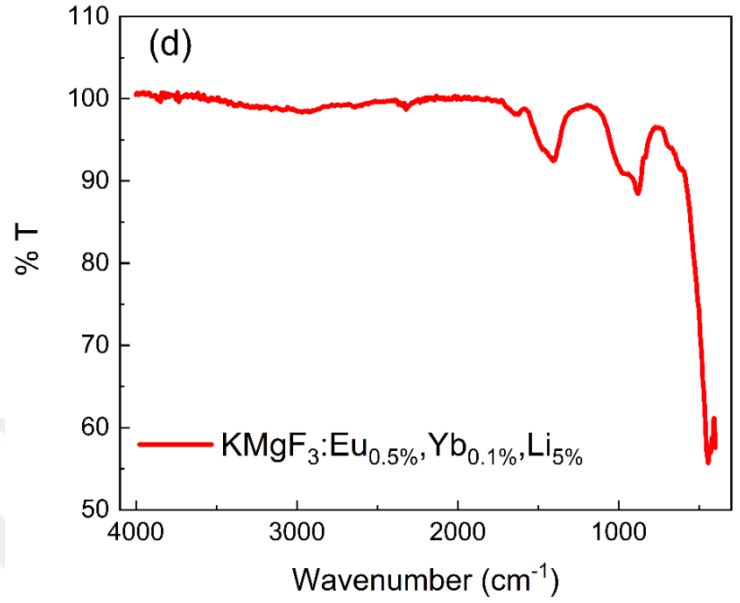
(d)
110
100
90
80
70
60
50
% T
KMgF3:Eu0.5%,Yb0.1%,Li5%
4000
3000
2000
1000
Wavenumber (cm-1)

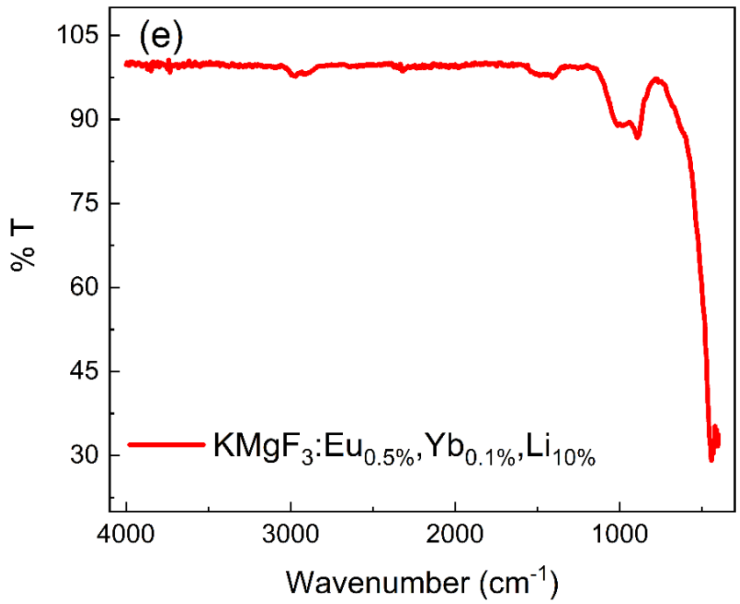
(e)
105
90
75
60
45
30
% T
KMgF3:Eu0.5%,Yb0.1%,Li10%
4000
3000
2000
1000
Wavenumber (cm-1)

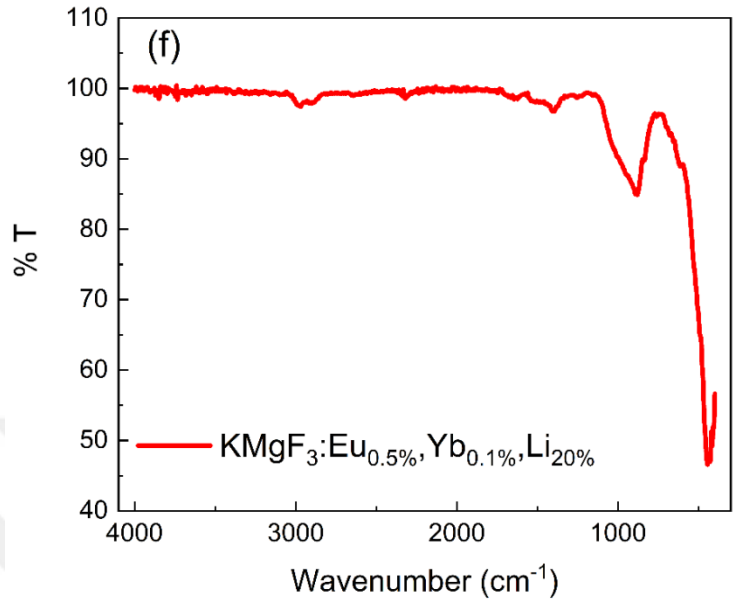

Figure 4.69. (a) Comparison the FT-IR spectra of $KMgF_3$ (black line) and $KMgF_3$:$Eu_{0.5\%}$,$Yb_{0.1\%}$,$Li_{15\%}$ (red line) samples. (b) The FT-IR spectra of $KMgF_3$:$Eu_{0.5\%}$,$Yb_{0.1\%}$,$Li_{1\%}$, (c) $KMgF_3$:$Eu_{0.5\%}$,$Yb_{0.1\%}$,$Li_{3\%}$, (d) $KMgF_3$:$Eu_{0.5\%}$,$Yb_{0.1\%}$,$Li_{5\%}$, (e) $KMgF_3$:$Eu_{0.5\%}$,$Yb_{0.1\%}$,$Li_{10\%}$ and (f) $KMgF_3$:$Eu_{0.5\%}$,$Yb_{0.1\%}$,$Li_{20\%}$.

4.6.5. Radioluminescence

The behavior of the radioluminescence (RL) emission spectra obtained from the different dopant combinations is given in Figure 4.70Figure 4.70. The RL measurements demonstrate no emission from the undoped sample and emissions from the incorporation of the dopants especially Eu in the host. The characteristic Eu^{2+} and Eu^{3+} emissions are evident from the $KMgF_3$:$Eu_{0.5\%}$ sample (see Figure 4.70). $KMgF_3$:$Eu_{0.5\%}$ exhibits the emission from Eu^{3+} ions with two broad emission bands just below and above 600 nm. Eu^{2+} ions give a band around 350-400 nm. UV emission bands located between 355-430 nm with peak maximums at 362 and 400 nm were observed for all Eu doped $KMgF_3$ phosphors. These bands can be attributed to the f→f $^6P_{7/2}$→ $^8S_{7/2}$ transitions of Eu^{2+} in the blue range (Hua et al., 2007; Huang et al., 2011) because of the reduction of Eu^{3+} to Eu^{2+} through the

calcination process carried out in an argon atmosphere. Similar results have been published for various host materials in the literature (Hua et al., 2007; Schuyt and Williams, 2018). Hua et al. studied the optical properties of $KMgF_3$:Eu^{2+} and they presented the emission spectrum of the sample which has the sharp emission line located at 362 nm (Hua et al., 2007). They suggested that this emission has been arisen from f→f transition of Eu^{2+} ions in the host lattice substituting for K^+ ions. On the other hand, the results are similar to Eu emissions in different hosts. The broad spectrum of the Eu-doped $NaMgPO_4$ sample with a maximum at 450 nm was associated with the Eu^{2+} emission responsible for the 5d → 4f transitions by Huang et al. (Huang et al., 2011). UV-VIS emission bands with the peak maximums at 591, and 613 nm were detected too, for Eu doped samples (see Figure 4.70). These emissions are composed of the characteristic 4f→4f $^5D_0 \rightarrow {}^7F_j$ with j=0, 1 red emission transitions of Eu^{3+}. Pathak et al. presented similar emission bands, such as orange emission in the 590–600 nm range due to the $^5D_0 \rightarrow {}^7F_{0,1}$ magnetic dipole transition and red emission in the 610-630 nm wavelength region due to the $^5D_0 \rightarrow {}^7F_{1,2}$ electric dipole transition by examining the different defect clusters of Eu-doped $KMgF_3$ (Pathak et al., 2020). It is known that the emission of Eu^{3+} at 690 nm is blocked by the Schott BG-39 filter and can be considered that this emission band contributes little or no to TL intensities of the studied samples. On the other hand, the luminescence of Yb^{3+} is relatively weak due to parity-forbidden 4f–4f transitions (Dhoble et al., 2018; Sun et al., 2012). Because 4f electrons do not lead to high recombination of electron-hole pairs, accordingly, in this study, the Yb dopant did not amplify the RL emission from $KMgF_3$. To solve this problem, we used Eu^{3+} for Yb activation. In the literature, several research groups have used other luminescent species with higher absorption coefficients to sensitize the Yb ions (Fu et al., 2012; Otmar et al., 2011; Zhang et al., 2011). In addition, ions such as Ce^{3+}, Eu^{2+}, Bi^{3+}, and Mn^{2+} and/or combinations with intrinsic absorption of the host itself (e.g., YVO_4 and ZnO) have also been studied for Yb^{3+} activation (Gao et al., 2013; Huang et al., 2010; Li et al., 2013; Wei et al., 2010).

To provide more information about the locations of the emission bands of Eu and Yb dopants and the general appearance influenced by the Li co-doping, the RL emission spectra of the undoped and $KMgF_3:Eu_{0.5\%},Yb_{0.1\%},Li_{x\%}$ fluoroperovskites were investigated. All of the relative RL intensities as a function of varying Li co-dopant concentrations are presented in Figure 4.71 ($KMgF_3:Eu_{0.5\%},Yb_{0.1\%},Li_{1\%}$, $KMgF_3:Eu_{0.5\%},Yb_{0.1\%},Li_{3\%}$, $KMgF_3:Eu_{0.5\%},Yb_{0.1\%},Li_{5\%}$, $KMgF_3:Eu_{0.5\%},Yb_{0.1\%},Li_{10\%}$ and $KMgF_3:Eu_{0.5\%},Yb_{0.1\%},Li_{20\%}$). The RL emission bands of $KMgF_3$ doped with 0.1 mole% Yb and 0.5 mole% Eu and co-doped with various Li concentrations were obtained at room temperature using 1 nm resolution. Figure 4.70 shows that the addition of Li increases the emission intensity of Eu as is seen in the $KMgF_3:Eu_{0.5\%},Li_{5\%}$ sample. Additionally, the RL emission increased approximately four times with the addition of Li co-dopant in $KMgF_3:Eu_{0.5\%},Yb_{0.05\%}$ sample. Figure 4.71a shows the comparison of the RL emission spectra of undoped $KMgF_3$ and $KMgF_3:Eu_{0.5\%},Yb_{0.1\%},Li_{15\%}$ samples. All emission bands and lines under x-ray excitation were similar to each other and associated with the Eu^{2+} and Eu^{3+} transitions (see Figure 4.71a-f). As the concentration of Li^+ co-dopant increased, the Eu^{2+} emission bands from $KMgF_3:Eu_{0.5\%},Yb_{0.1\%},Li_{15\%}$ perovskite are up to three times more intense. It can be considered that the RL signal increases by Li co-doping possibly acting as a charge compensator for nearby Eu ions and helping the substitution for K^+ or Mg^{2+} sites which are also predicted by the XRD and FT-IR analysis in this work. This resultant increase in the RL intensity from the RE dopants with Li co-doping is consistent with many studies in the literature (Altunal et al., 2020a; Guckan et al., 2021b; Oliveira et al., 2019; Pathak et al., 2020).

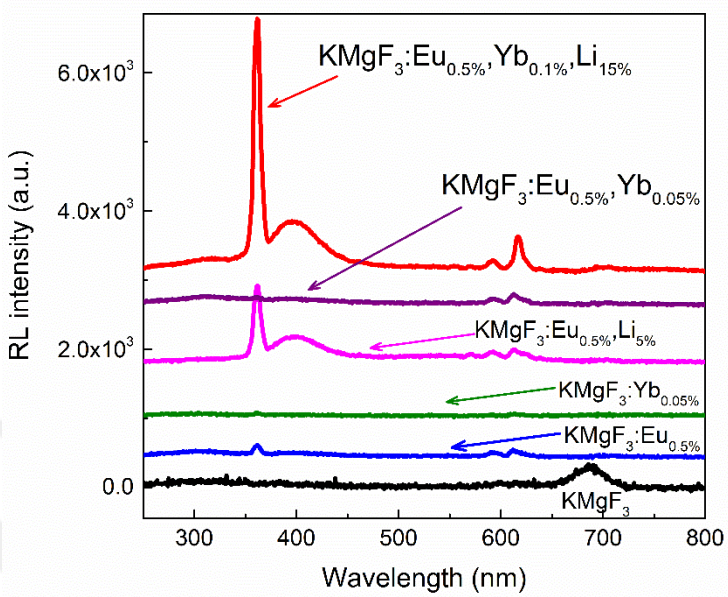

Figure 4.70. The RL emission spectra of the $KMgF_3$ samples from the concentration quenching study.

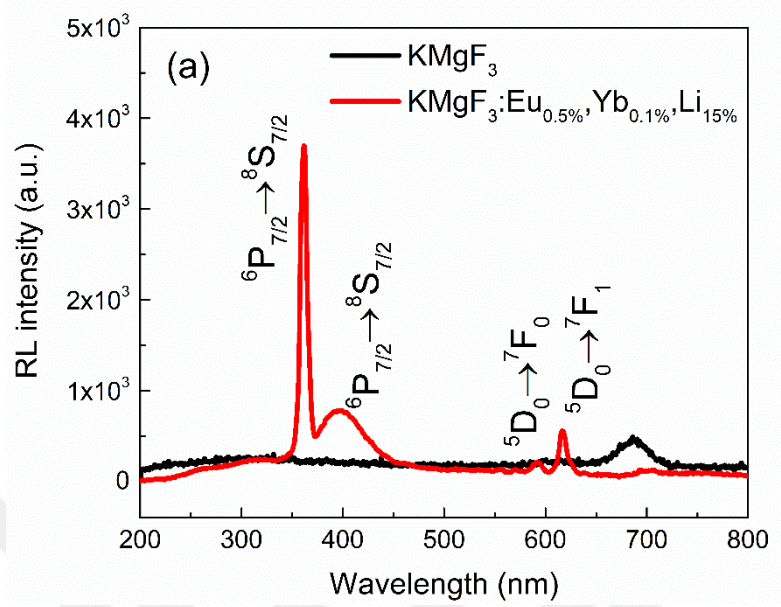
(a)
KMgF3
KMgF3:Eu0.5%,Yb0.1%,Li15%
6P7/2→8S7/2
6P7/2→8S7/2
5D0→7F0
5D0→7F1
RL intensity (a.u.)
Wavelength (nm)
5x10^3
4x10^3
3x10^3
2x10^3
1x10^3
0
200
300
400
500
600
700
800

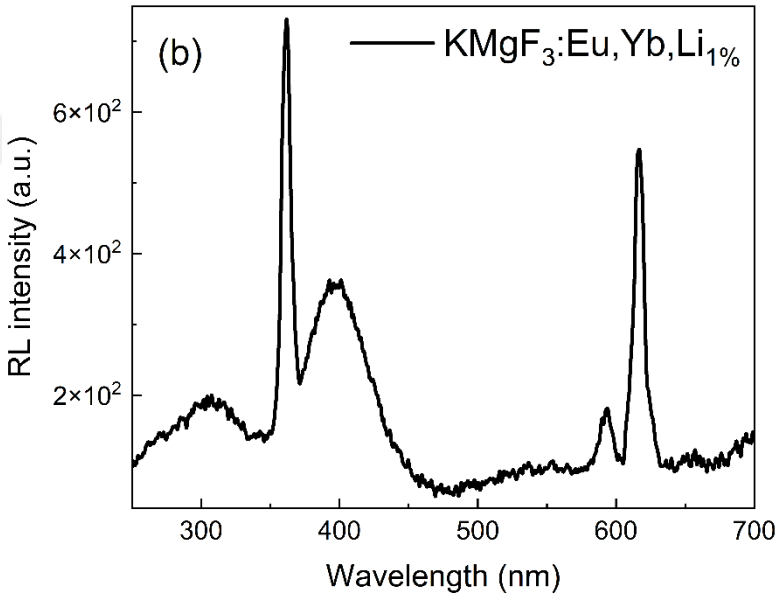
(b)
KMgF3:Eu,Yb,Li1%
RL intensity (a.u.)
Wavelength (nm)
6×10^2
4×10^2
2×10^2
300
400
500
600
700

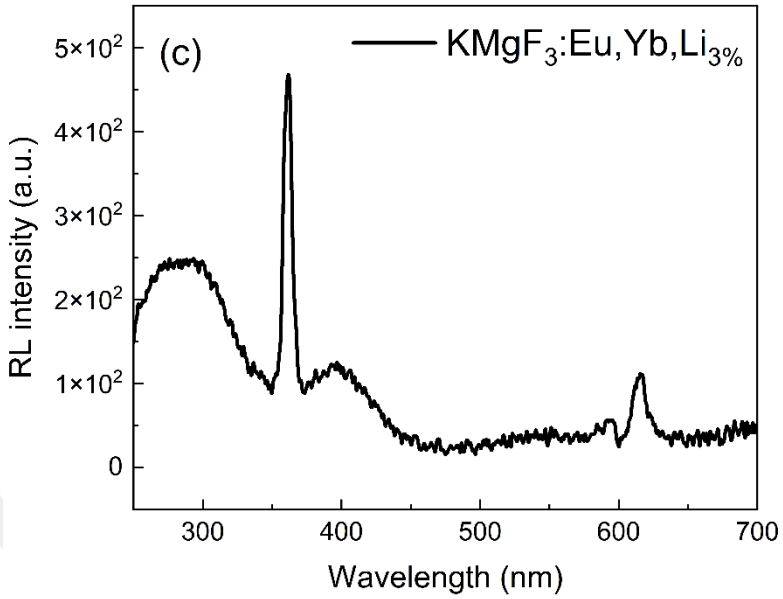
(c)
KMgF3:Eu,Yb,Li3%
RL intensity (a.u.)
5×10²
4×10²
3×10²
2×10²
1×10²
0
300
400
500
600
700
Wavelength (nm)

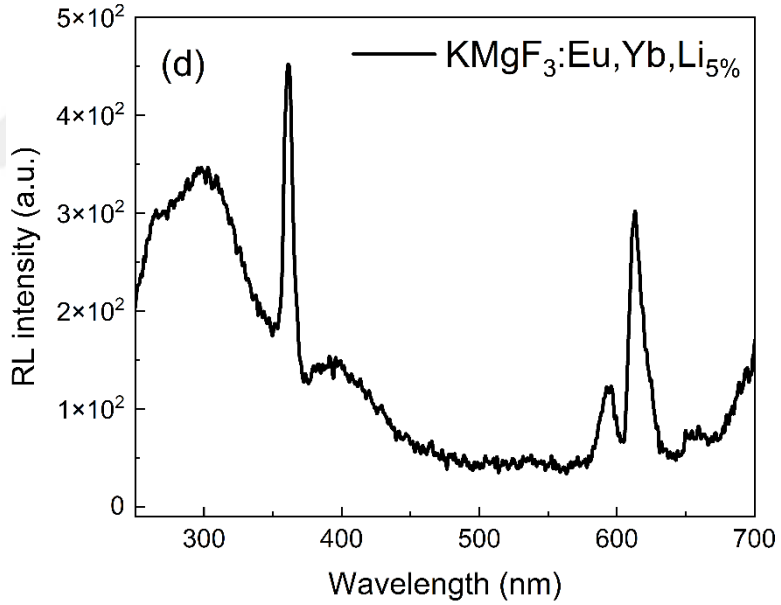
(d)
KMgF3:Eu,Yb,Li5%
RL intensity (a.u.)
5×10²
4×10²
3×10²
2×10²
1×10²
0
300
400
500
600
700
Wavelength (nm)

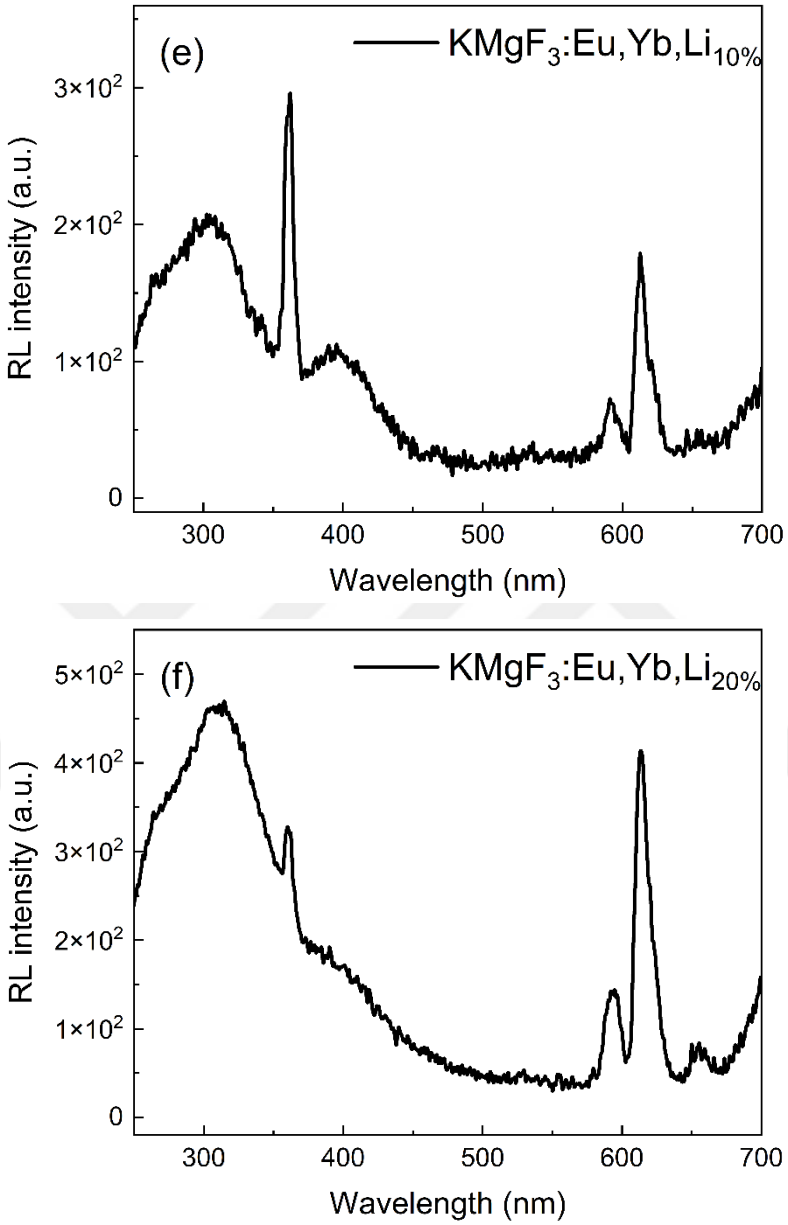

Figure 4.71. (a) Comparison of the RL emission spectra between undoped $KMgF_3$ and $KMgF_3:Eu_{0.5\%},Yb_{0.1\%},Li_{15\%}$ phosphors. (b) The RL emission spectra of $KMgF_3:Eu_{0.5\%},Yb_{0.1\%},Li_{1\%}$, (c) $KMgF_3:Eu_{0.5\%},Yb_{0.1\%},Li_{3\%}$, (d) $KMgF_3:Eu_{0.5\%},Yb_{0.1\%},Li_{5\%}$, (e) $KMgF_3:Eu_{0.5\%},Yb_{0.1\%},Li_{10\%}$ and (f) $KMgF_3:Eu_{0.5\%},Yb_{0.1\%},Li_{20\%}$.

4.6.6. Effect of dopant concentration and concentration quenching

A concentration quenching study was carried out for improvement in luminescence efficiency of $KMgF_3$ with Eu and Yb dopants and Li co-dopant. The total OSL signals obtained from the concentration quenching studies by testing the most intense luminescence signals were used. The effect of Eu, Yb, and Li doping was investigated for concentration values between 0.001 and 3%; 0.001 and 0.5%; and 1 and 20%, respectively. It should be noted that these concentrations are nominal values, not the actual fractions added into the host matrix. As can be seen from the EDS analysis, these values may differ after the product is created. The OSL intensity in Figure 4.72 indicates that an optimum OSL signal was achieved with 0.5% Eu and 0.1% Yb doping when the Li was kept constant as 5%. It was observed that the OSL signal increases as the Li concentration increases, possibly because it acts as a charge compensator and helps replace Mg^{2+} with Eu^{3+} or Yb^{3+}. It was observed that the OSL signals of the samples reached saturation and then drastically decreased after a certain signal increase was observed for each dopant. The most intense OSL signal was obtained at concentration ratios of 0.5%, 0.1% and 15% for Eu, Yb and Li-ions ($KMgF_3$:$Eu_{0.5\%}$,$Yb_{0.1\%}$,$Li_{15\%}$), respectively.

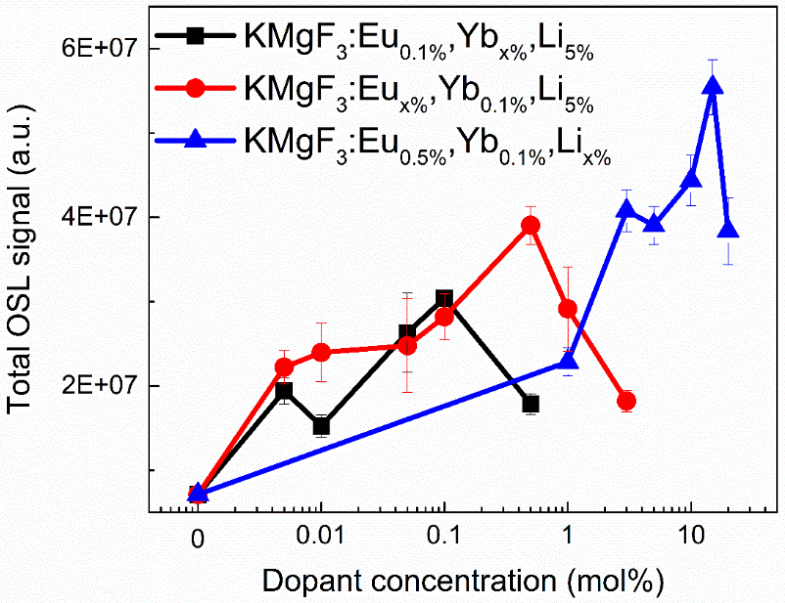

Figure 4.72. Total OSL signal of $KMgF_3$ as a function of Eu, Yb, and Li dopant concentrations. Uncertainties were presented with the error bars using the experimental standard deviation associated with three aliquots from the same batch. All samples were obtained under the same laboratory conditions using the same method and using the same precursors.

4.6.7. Thermoluminescence

RE dopants Eu and Yb were studied regarding the influence on luminescence (TL and OSL) properties. In our work, it was accomplished to produce $KMgF_3$ perovskite samples which gave the suitable TL and OSL curves for dosimetric purposes by testing various contents of Eu, Yb dopants, and Li co-dopant. It was found that the presence of Li ions together with the RE dopants has an impact mainly on the TL glow curve and OSL decay signal of the studied perovskite.

The TL glow curves of undoped, and some of the doped $KMgF_3$ obtained using single, double, or triple dopant combinations are given in Figure 4.73a. TL intensities of both $KMgF_3$:$Yb_{0.05\%}$ and $KMgF_3$:$Eu_{0.1\%}$, were weaker when compared with the undoped sample. There was an increase in TL intensities when we doubly doped $KMgF_3$ in terms of different combinations of dopants. Figure 4.73a shows no

TL glow curves of $KMgF_3:Eu_{0.5\%},Yb_{0.05\%}$ or $KMgF_3:Eu_{0.5\%},Li_{5\%}$ samples. All these samples obtained are featured by a dominant TL peak at around 130 °C. We obtained a 4-fold increase in the total TL signal of the $KMgF_3:Eu_{0.5\%},Yb_{0.1\%},Li_{15\%}$ sample when we co-doped the sample with Li, and extra TL peaks were observed at 83, 180, 254, and 357°C, as well as the TL peak at 133°C. It is known that trivalent RE impurities can replace Mg^{2+} ions in MgF_2 or $KMgF_3$, resulting in a perturbation in the charge distribution surrounding RE ions (Nagpal et al., 1981). It is thought that the incorporation of Li into the medium may have acted as a charge compensator and thus the charge distribution was increased and caused an increase in TL signal (Furetta et al., 1990; Yukihara et al., 2017).

To study the effect of Li^+ co-doping on the shape of the TL glow curve of $KMgF_3$:Eu,Yb,Li perovskite, the TL readouts were performed by heating from room temperature to 500 °C with a heating rate of 2 $°Cs^{-1}$. Comparison of the TL glow curves of undoped and $KMgF_3:Eu_{0.5\%},Yb_{0.1\%},Li_{15\%}$ samples are given in Figure 4.73b. The TL glow curves were obtained using a Schott BG-39 bandpass filter in the VIS region (between 330-620 nm). The TL glow curve of the $KMgF_3:Eu_{0.5\%},Yb_{0.1\%},Li_{15\%}$ revealed five peaks located at ~83, 133, 180, 254, and 357 °C, close to the peak maxima of the undoped $KMgF_3$.. The total TL signal of the undoped sample was determined as four times weaker than that of $KMgF_3:Eu_{0.5\%},Yb_{0.1\%},Li_{15\%}$. It can be suggested that the main TL peaks of both undoped and doped $KMgF_3$ at around 83, 133, 180, 254, and 357 °C are consistent with each other, and the dopants only affect the sensitivity of these peaks. This result is in agreement with the TL peaks of $KMgF_3$ perovskite recorded in different studies (Furetta et al., 2001; Perez C et al., 2015). Some of the differences in TL peak maxima can be attributed to the heating rate used to record the TL glow curves and differences in the synthesis processes in different laboratories. It was observed that high-temperature TL peaks at 254 and 357 °C became more pronounced at 3 mole% and higher Li concentrations. The intense TL signal was obtained from 15 mole% Li concentration. A more detailed investigation is required to determine the kinetic parameters of the mentioned traps and their dosimetric properties for monitoring radiation doses.

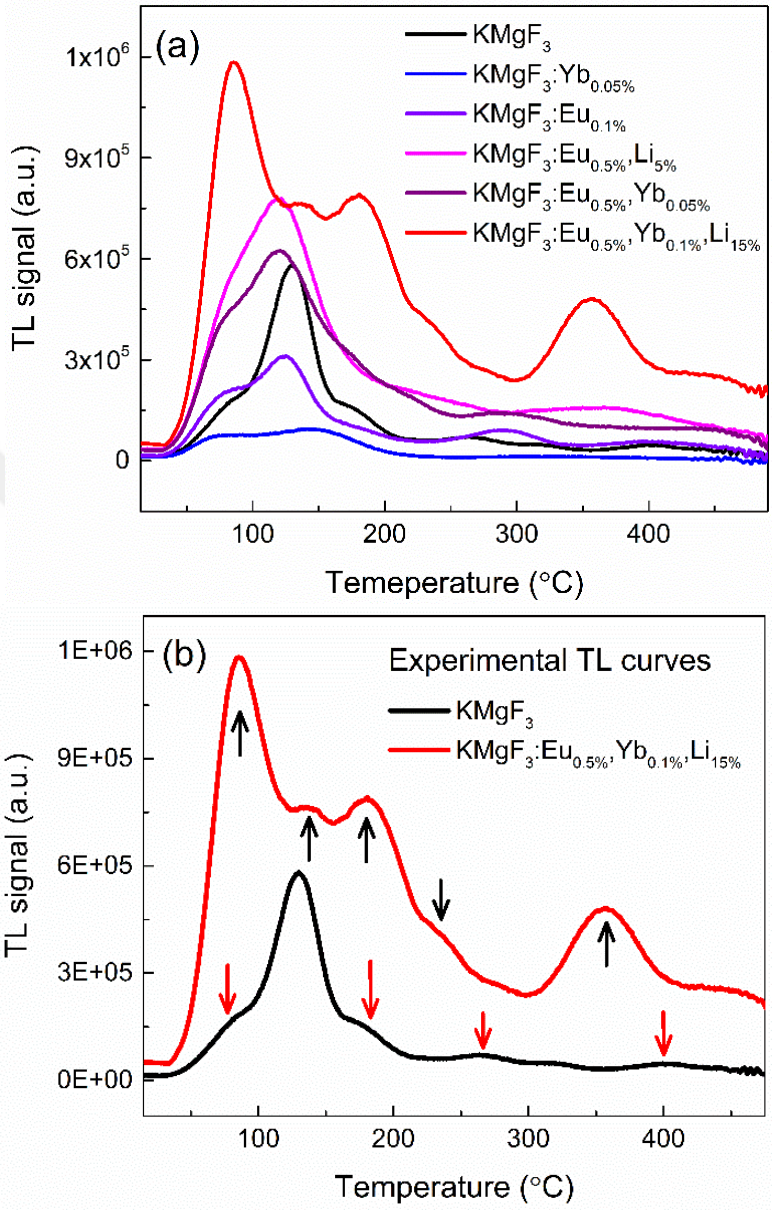

Figure 4.73. (a) Comparison of TL glow curve of undoped and doped $KMgF_3$ with single, double or triple dopant combination. (b) Effect of Li^+ co-doping on TL glow curves of $KMgF_3$ and $KMgF_3$:$Eu_{0.5\%}$,$Yb_{0.1\%}$,$Li_{15\%}$ samples obtained by sol-gel technique and calcined at 800 °C for 2h. Each TL glow curve is derived from the averages of TL signals of three samples under the same measurement conditions following 0.2 Gy beta dose.

4.6.8. Continuous-wave OSL (CW-OSL)

CW-OSL decay curves of the 0.2 Gy pre-irradiated perovskite samples were obtained using 50 s blue LEDs stimulation (λ_{blue}= 470 nm). The OSL decay curves of the $KMgF_3$ and $KMgF_3$:$Eu_{0.5\%}$,$Yb_{0.1\%}$,$Li_{15\%}$ perovskites are compared in Figure 4.74a. The total OSL signal of $KMgF_3$:$Eu_{0.5\%}$,$Yb_{0.1\%}$,$Li_{15\%}$ is about eight times brighter when compared to that of the undoped sample. Further, the effect of Li co-doping possessing different concentrations on the OSL decay curves was observed and can be seen in Figure 4.75.

Analyses of the OSL decay curves and their components with associated decaying times are important for luminescence dosimetry. The three-time decay functions of undoped $KMgF_3$ and $KMgF_3$ doped with different Li concentrations were analyzed by linear integration and given in Figure 4.74b and Figure 4.74c. The fitting was conducted by using the general kinetic equation (Eq. (4.3) (Bøtter-Jensen et al., 2003) of the luminescence decays. This technique was also used in the literature for many dosimeters (Altunal et al., 2020b; Chen and McKeever, 1997; Guckan et al., 2021b; Kalita et al., 2021). All components were calculated using Equation (4.3 and given with the FOM values (goodness of the fitting) in

Table 4.10. The effect of the Li concentration on the OSL curves was better understood when the lifetimes of the OSL decay components were controlled. $KMgF_3$:$Eu_{0.5\%}$,$Yb_{0.1\%}$,$Li_{15\%}$ appeared to have 0.55, 8.45 and 125.45 μs signal decay rates of the fast, medium, and slow components of its OSL curve, respectively. A maximum lifetime of the fast components is observed for 15 mole% Li concentration. On the other hand, although there are big differences between the lifetimes of the medium and slow components of the undoped and Li co-doped samples, no systematic change in fast components is observed. Although the results indicate the existence of different types of defect centers and a complex luminescence mechanism in $KMgF_3$:$Eu_{0.5\%}$,$Yb_{0.1\%}$,$Li_{15\%}$ perovskite, this technique is an oversimplified approach to the real situation. More information about the traps and transitions related to improving the OSL signal is possible with studies focusing on numerical solutions of the charge mechanism equations.

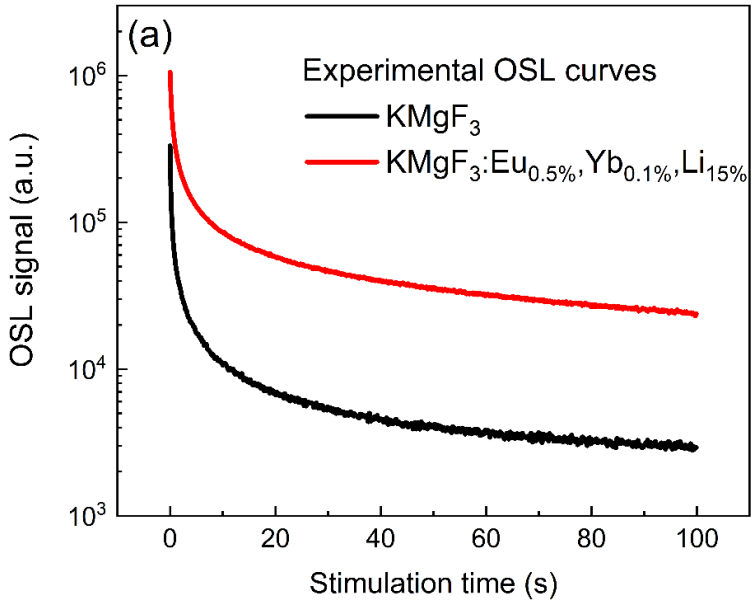
(a)
Experimental OSL curves
KMgF3
KMgF3:Eu0.5%,Yb0.1%,Li15%
OSL signal (a.u.)
Stimulation time (s)

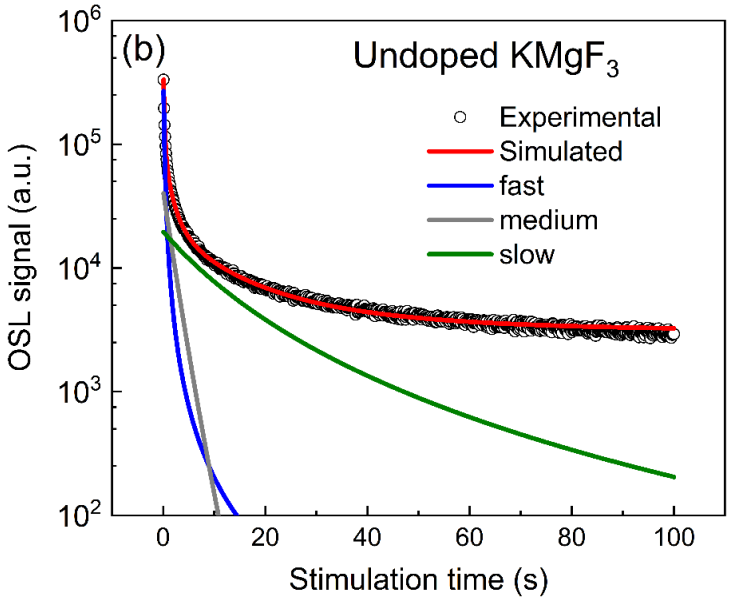
(b)
Undoped KMgF3
Experimental
Simulated
fast
medium
slow
OSL signal (a.u.)
Stimulation time (s)

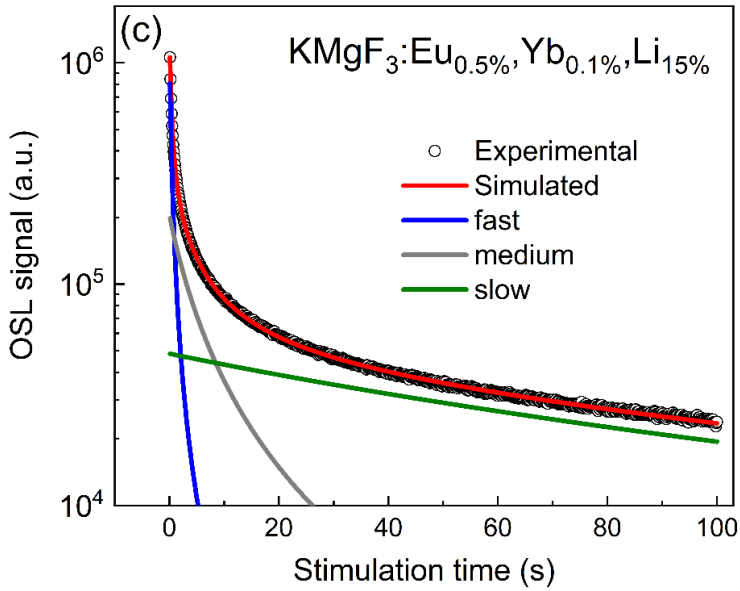

Figure 4.74. (a) Typical OSL decay curves from 0.2 Gy irradiated undoped $KMgF_3$ and $KMgF_3$:$Eu_{0.5\%}$,$Yb_{0.1\%}$,$Li_{15\%}$ phosphors following the preheating at 100 °C for 10 s. Analysis of experimental OSL decay curve described by Eq. ((4.3) along with the resolved components of (b) undoped $KMgF_3$ and (c) $KMgF_3$:$Eu_{0.5\%}$,$Yb_{0.1\%}$,$Li_{15\%}$.

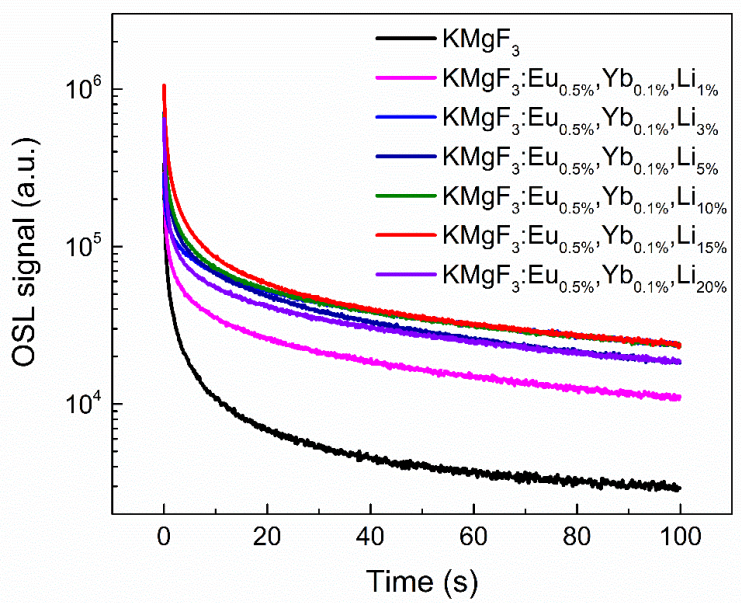

Figure 4.75. After doping with Eu^{3+} (0.5 mole%), Yb^{3+}(0.1 mole%) and co-doped with Li^{+} (x mole%), OSL decay curves of $KMgF_3$ phosphors.

Table 4.10. The decaying parameters of the OSL components after fitting the OSL decay curve of $KMgF_3:Eu_{0.5\%},Yb_{0.1\%},Li_{x\%}$ phosphors using general order kinetics.

	Fast component		**Medium component**		**Slow component**			
Perovskite	τ_1*(s)*	b_1*(a.u.)*	τ_2*(s)*	b_2*(a.u.)*	τ_3*(s)*	b_3*(a.u.)*	*bkg (count)*	*FOM* (%)
Undoped $KMgF_3$	0.17	2.04	1.62	1.05	13.79	1.52	2998.90	2.75
$KMgF_3$:Eu,Yb,$Li_{1\%}$	0.25	1.34	4.69	2.05	100.08	2.01	3069.37	1.63
$KMgF_3$:Eu,Yb,$Li_{3\%}$	0.39	2.05	11.82	1.94	162.73	1.69	3050.48	0.89
$KMgF_3$:Eu,Yb,$Li_{5\%}$	0.39	1.67	7.34	1.97	112.04	2.05	3067.55	1.19
$KMgF_3$:Eu,Yb,$Li_{10\%}$	0.45	2.05	7.52	2.05	147.73	1.67	3067.47	1.05
$KMgF_3$:Eu,Yb,$Li_{15\%}$	0.55	2.05	8.45	2.05	125.45	1.06	3058.82	1.16
$KMgF_3$:Eu,Yb,$Li_{20\%}$	0.24	1.33	4.62	2.05	127.50	2.05	3094.01	1.50

4.6.9. Correlation of traps responsible for TL and OSL

As mentioned in Section 4.2.5, the step annealing experiment was performed to understand the relationship between TL and OSL traps of $KMgF_3:Eu_{0.5\%},Yb_{0.1\%},Li_{15\%}$ sample. It was observed that the charge traps responsible for the OSL signals were not affected up to 100 °C heating (see Figure 4.76). It was observed that a decrease in OSL signals started when the sample was heated to 100 °C up to 150 °C. The decay rate of intensity increased after 150 °C and the OSL signal was at the background level when 310 °C was reached. The existence of a wide range of thermally affected OSL traps in the 100-310 °C range has been proven. It can be said that TL traps have no contribution to OSL after 310 °C.

It would be better to confirm these results with TL after OSL analysis. As seen in Figure 4.77, when we compare TL signals without blue light excitation with TL signals after blue light stimulation (residual TL), it is clear that blue light stimulation affects the TL glow curve up to 310 °C and does not affect the high-temperature peak caused by electrons in deeper traps.

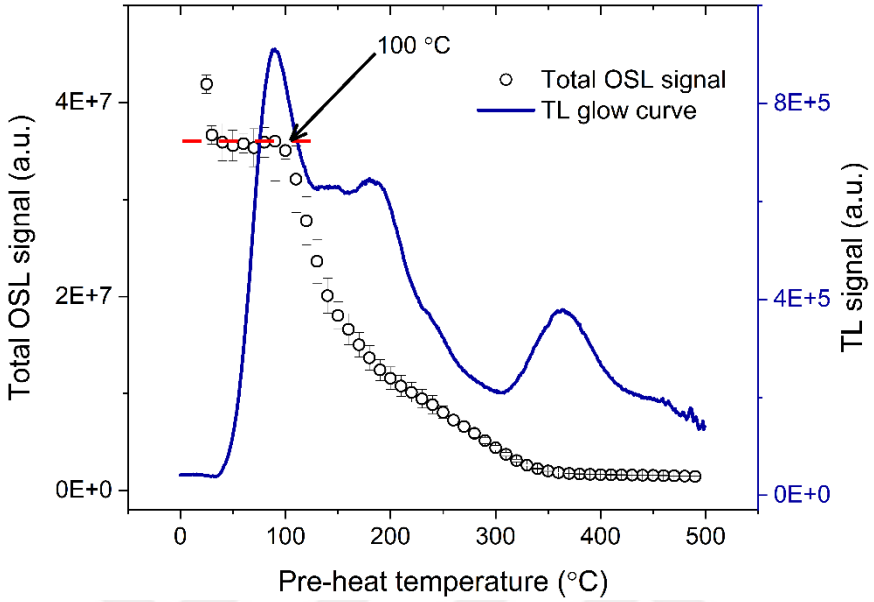

Figure 4.76. Total OSL intensity versus TL glow curve preheated at different temperature for $KMgF_3:Eu_{0.5\%},Yb_{0.1\%},Li_{15\%}$. The error bars were obtained from three pellets for each cycle. Blue light stimulation was used during 100 s. The samples were depleted using TL readout up to 500 °C for the probability of residual dose after each cycle.

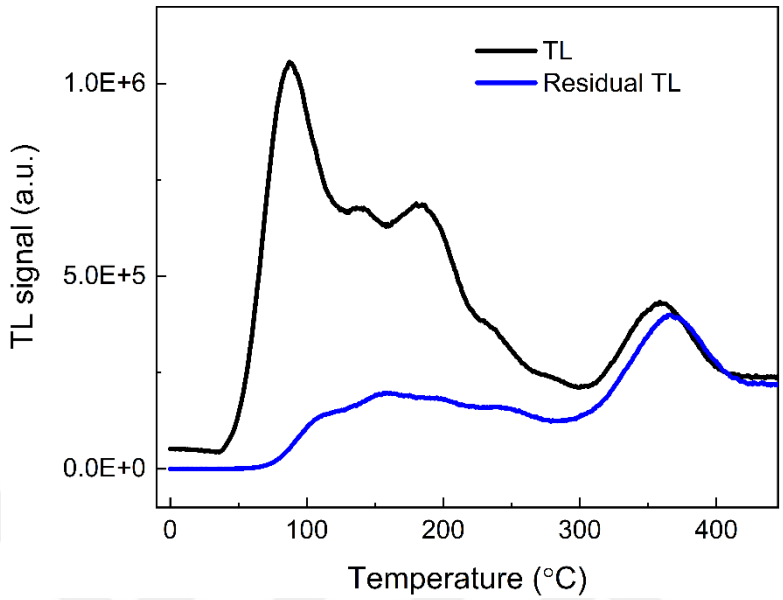

Figure 4.77. The effect of the blue light stimulation on the TL glow curve of the $KMgF_3:Eu_{0.5\%},Yb_{0.1\%},Li_{15\%}$. The power density of the blue light was about 90 $mWcm^{-2}$ during 100 s.

4.6.10. Dosimetric characteristics

4.6.10.1. Fading

The fading of the trapped electrons responsible for OSL signals was checked as a function of the storage time. The $KMgF_3:Eu_{0.5\%},Yb_{0.1\%},Li_{15\%}$ samples exposed to 0.2 Gy β-dose were put on the stainless-steel cups and stored in a dark room for various time intervals as mentioned in Figure 4.78. In the experiments, three samples were used to determine the data for each storage time for better statistical accuracy. Figure 4.78 shows that the OSL intensities of decay curves decrease as a function of storage time in short-term and long-term storage up to six weeks. Reduction in OSL signals was observed by 5% after a day and 6 % after a day. But the long-term fading of six weeks appeared as a ~10% increase when compared with the OSL intensity recorded after half an hour following the dose delivery. This may be due to charge transfer from deep traps to shallower ones, as mentioned in Section 4.5.9.

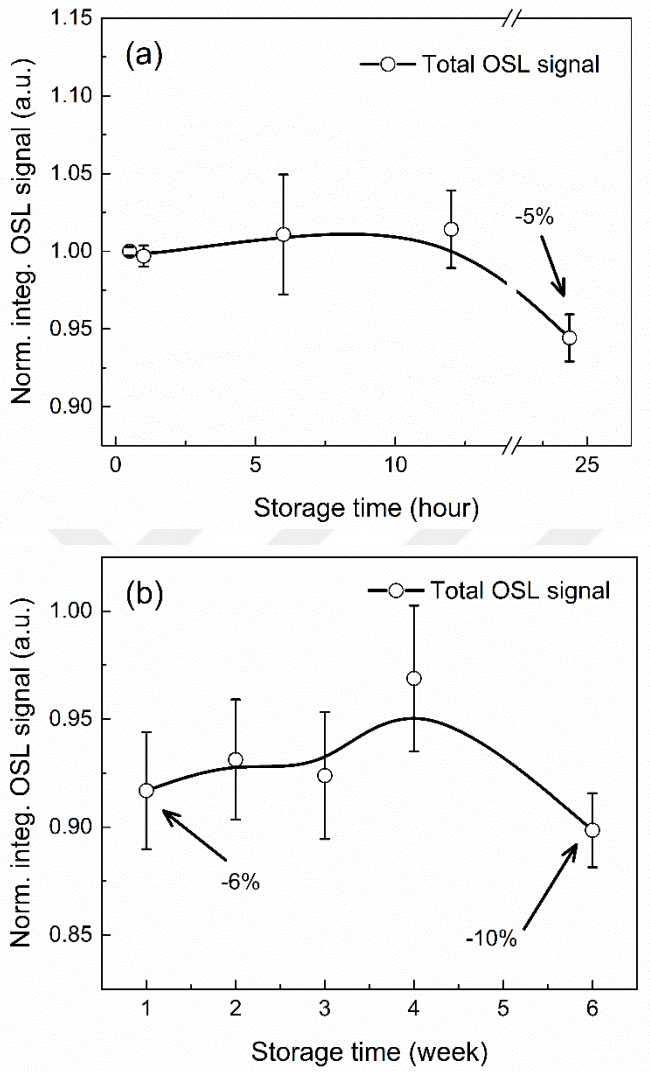

Figure 4.78. Effect of storage time on OSL signals from 0.2 Gy irradiated $KMgF_3:Eu_{0.5\%},Yb_{0.1\%},Li_{15\%}$ samples as a function of (a) short and (b) long term storage time. OSL measurements were performed at room temperature. Three samples were used for each cycle to obtain standard deviation and error bars.

4.6.10.2. Dose-response

The dose-response behavior of the OSL signals of the $KMgF_3:Eu_{0.5\%},Yb_{0.1\%},Li_{15\%}$ samples was presented from 0.1 Gy to 500 Gy dose

exposure. The samples were annealed using TL read-out at the end of each OSL read-out to deplete the residual luminescence signals. The plot of integrated OSL intensities as a function of absorbed dose was presented in Figure 4.79. The dose-response of the $KMgF_3:Eu_{0.5\%},Yb_{0.1\%},Li_{15\%}$ sample was found to be linear with the 1.00 slope value in the dose range between 0.1 Gy and 500 Gy. The MDD value has been calculated using Equation (4.5 and it was calculated as ~ 1.68 mGy. The fact that it gives high signals even at a very low dose (the lowest possible dose value was 0.1 Gy) allows this sample to be used in many areas such as medical dosimetry, personal dosimetry, or emergency dosimetry. Since the signals obtained from the samples exceeded the capacity of the PMT, two different apertures (signal blocker) were used at 0.5 Gy and 100 Gy, and coefficient values were determined for each and the total signal values were calculated.

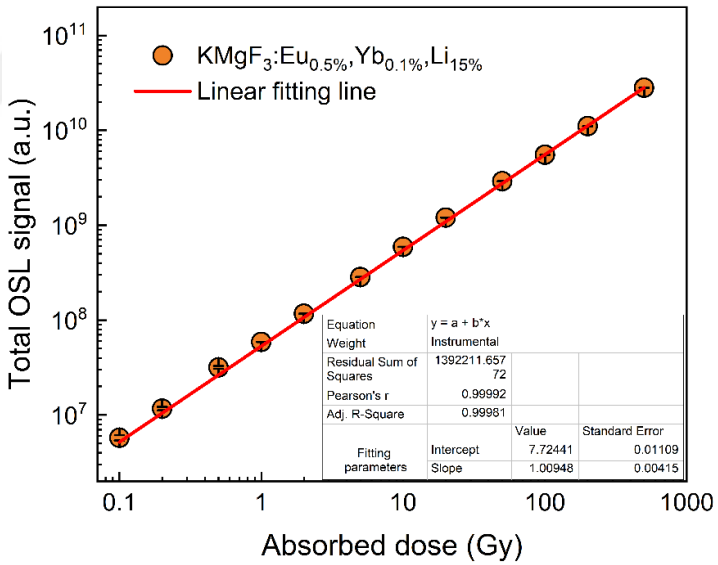

Figure 4.79. Dose-response behavior of $KMgF_3:Eu_{0.5\%},Yb_{0.1\%},Li_{15\%}$ phosphor as a function of absorbed doses. The dashed lines show the linearity of the total OSL signal. The data points were determined by calculating the average values of the three samples exposed. The error bars show the experimental standard deviation, but they are not visible in this scale in the graph.

4.6.11. Kinetic parameters

Kinetic parameters such as activation energies (E), frequency factor (s-1), order of kinetic (b) of $KMgF_3:Eu_{0.5\%},Yb_{0.1\%},Li_{15\%}$ crystal was estimated using various methods: various heating rate (VHR), T_m-$T_{stop,}$ and Computerized Glow Curve Deconvolution (CGCD). The theoretical explanation/procedure for these methods was given in the previous sections (see Section 4.5.10).

4.6.11.1. CGCD analysis

The TL curve of the $KMgF_3:Eu_{0.5\%},Yb_{0.1\%},Li_{15\%}$ phosphor was recorded with a heating rate of 5 °Cs^{-1} from room temperature up to 450 °C without preheating after 0.2 Gy beta dose. Theoretical information about CGCD analysis was given in previous sections (see Section 4.3.7). TL glow curve of the crystal was fitted according to the equation assuming the general order kinetic given by Kitis et al. (Kitis et al., 1998). The glow curve was fitted with spreadsheet software given by Afouxenidis et al. (Afouxenidis et al., 2011), and the fit standard was evaluated using FOM. The deconvoluted TL fitting curve of the crystal was given in Figure 4.80.

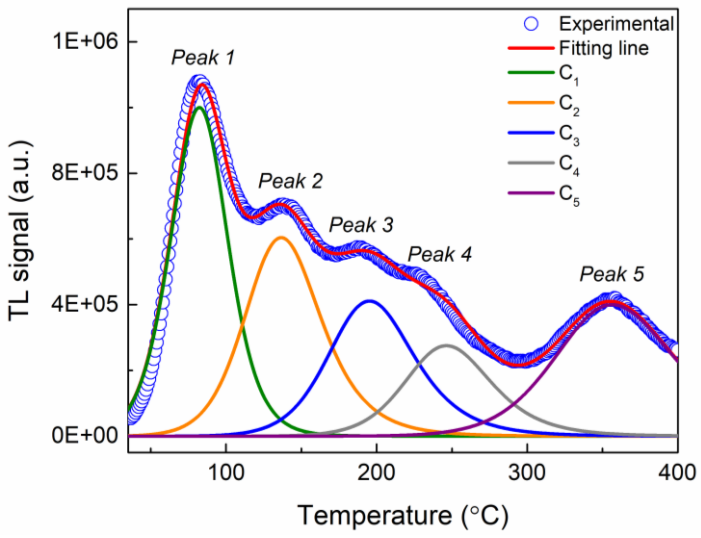

Figure 4.80. Deconvolution of CGCD for the $KMgF_3:Eu_{0.5\%},Yb_{0.1\%},Li_{15\%}$ phosphor.

As seen in Figure 4.80, the deconvolved TL curve of the crystal consists of individual five TL Peaks labeled as C_1, C_2, C_3, C_4 and C_5. The activation energies and frequency factor corresponding to these individual TL Peaks (C_1, C_2, C_3, C_4 and C_5) were found as 0.72 (corresponding to Peak 1), 0.80 (corresponding to Peak 2), 0.92 (corresponding to Peak 3) and 1.14 eV (corresponding to Peak 4) and 1.20 eV (corresponding to Peak 5), $6.21x10^{09}$, $1.42x10^{9}$, $1.96x10^{09}$, $2.27x10^{10}$ and $5.37x10^{8}$ s^{-1}, respectively. The obtained kinetic parameters using CGCD analysis were represented in Table 4.11.

Table 4.11. Comparison of the kinetic parameters of the $KMgF_3:Eu_{0.5\%},Yb_{0.1\%},Li_{15\%}$ phosphor.

Method	**CGCD**				**T_m-T_{stop}**	**VHR**	
	E (eV)	s (Hz)	b (a.u.)	FOM (%)	E (eV)	E (eV)	s (Hz)
Peak I (C_1)	0.72	$6.21x100^{9}$	1.67	1.92	1.06 ± 0.03	1.02 ± 0.03	N/A
Peak II (C_2)	0.80	$1.42x10^{9}$	2.00		1.12 ± 0.02	1.10 ± 0.07	N/A
Peak III (C_3)	0.92	$1.96x10^{9}$	2.00		1.40 ± 0.07	N/A	N/A
Peak IV (C_4)	1.14	$2.27x10^{10}$	2.00		1.47 ± 0.03	N/A	N/A
Peak V (C_5)	1.20	$5.37x10^{8}$	2.00		N/A	1.80± 0.03	N/A

4.6.11.2. T_m-T_{stop} analysis

The T_m-T_{stop} procedure previously given in Section 4.5.10.2. was applied on the $KMgF_3:Eu_{0.5\%},Yb_{0.1\%},Li_{15\%}$ phosphor to determine activation energies. The sample was heated from room temperature to a temperature T_{stop} which corresponds to a position on the low-temperature tail of the first TL peak in the glow curve. In this study, $KMgF_3:Eu_{0.5\%},Yb_{0.1\%},Li_{15\%}$ crystal was exposed to 0.2 Gy β-dose. The temperature varied from 40-350 °C in 10 °C intervals was used with a heating rate of 2 °C/s. After each TL readout, the crystal was again exposed to the same test dose. Following a series of processes (see Section 4.5.10), the T_m value was measured for each T_{stop} value, and a graph of T_m as a function of T_{stop} was

drawn in Figure 4.81a. In the Figure 4.81a has five plateau regions located at ~40–60 °C (centered at 50 °C), ~70–100 °C (centered at 85 °C) and ~110–160 °C (centered at 135 °C), ~200–220 °C (centered at 210 °C),. ~230–300 °C (centered at 265 °C). Therefore, it means each region corresponds to the presence of an individual peak in the phosphor.

The graph of ln (I_{TL}) versus 1/kT was plotted after performing the T_m-T_{stop} procedure in detail previously given in Section 4.5.10 after each TL readout. The data for each TL readout was fitted to the linear function given y=a+bx. The slope of the plot was correlated to activation energies. As seen in Figure 4.81a, there are four plateau regions located at ~40–80 °C (centered at 60 °C), ~90–120 °C (centered at 105 °C) and ~160–210 °C (centered at 185 °C), and ~220–260 °C (centered at 240 °C) activation energy corresponding to these plateaus was found to be 1.06 eV, 1.12 eV, 1.40 eV, and 1.47 eV, respectively. The kinetic parameters obtained using T_m-T_{stop} method are given in Table 4.11. Figure 4.81b shows the graph of activation energies vs T_{stop}. In general, the E-T_{stop} is expected to yield specific stability areas, which are also known as plateaus.

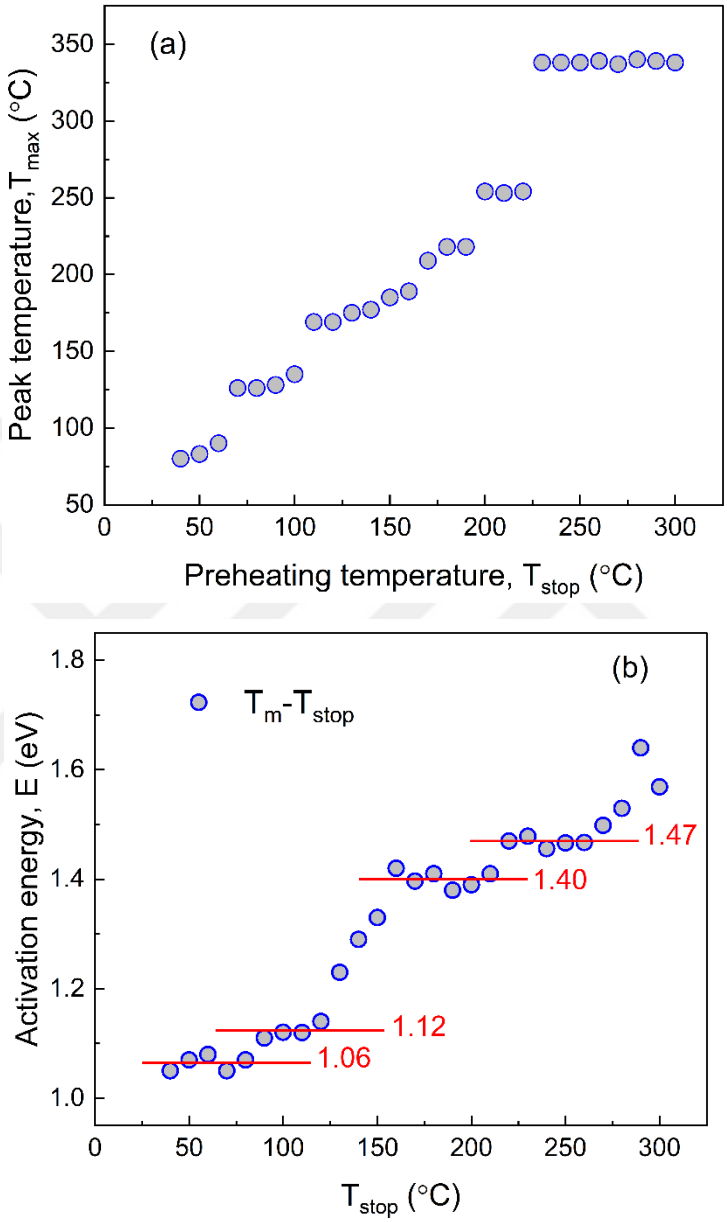

Figure 4.81. (a) The T_m–T_{stop} graph of the $KMgF_3$:$Eu_{0.5\%}$,$Yb_{0.1\%}$,$Li_{15\%}$. Each plateau presents a TL peak in the TL glow curve. (b) Activation energies as a function of related T_{stop} temperatures.

4.6.11.3. Various heating rate

The TL glow curve of the $KMgF_3:Eu_{0.5\%},Yb_{0.1\%},Li_{15\%}$ phosphor consists of five TL peak maxima located ~83, 133, 180, 254, and 357 °C when using heating rate of 5 °C/s (see Section 4.6.7). TL glow curves of the $KMgF_3:Eu_{0.5\%},Yb_{0.1\%},Li_{15\%}$ crystal were recorded using pre-determined heating rates of 1, 2, 3 and 4 °C/s after 0.2 Gy β-dose.

Regarding the TL theory, it was observed that the position TL peak maxima curve shifted towards higher temperatures as the heating rate increased except for Peak 1 (see Figure 4.82a). Since the maxima temperature (T_m) of the TL peaks (Peak 1, Peak 2 and Peak 5) of $KMgF_3:Eu_{0.5\%},Yb_{0.1\%},Li_{15\%}$ crystal could be determined, the VHR method to determine kinetic parameters was applied only to these TL peaks. The other TL peak (i.e, Peak 3 and Peak 4) were not calculated considering that statistical errors would be high in T_m determination.

The maxima temperature corresponding to positions of peak maxima were noted visually in Origin 8.6 to the nearest degree for Peak 1, Peak 2 and Peak 5 each heating rate cycle. Using Equation (4.7, the graph of the $\ln (T_m^2/\beta)$ vs $1/kT_m$ was plotted, then the data's corresponding Peak1, Peak 2 and Peak 5 were separately fitted to linear function given y=a+bx (see Figure 4.82b). The results of the fit were used to calculate E and s from Equation (4.7. The kinetic parameters obtained using the VHR method were given in Table 4.11.

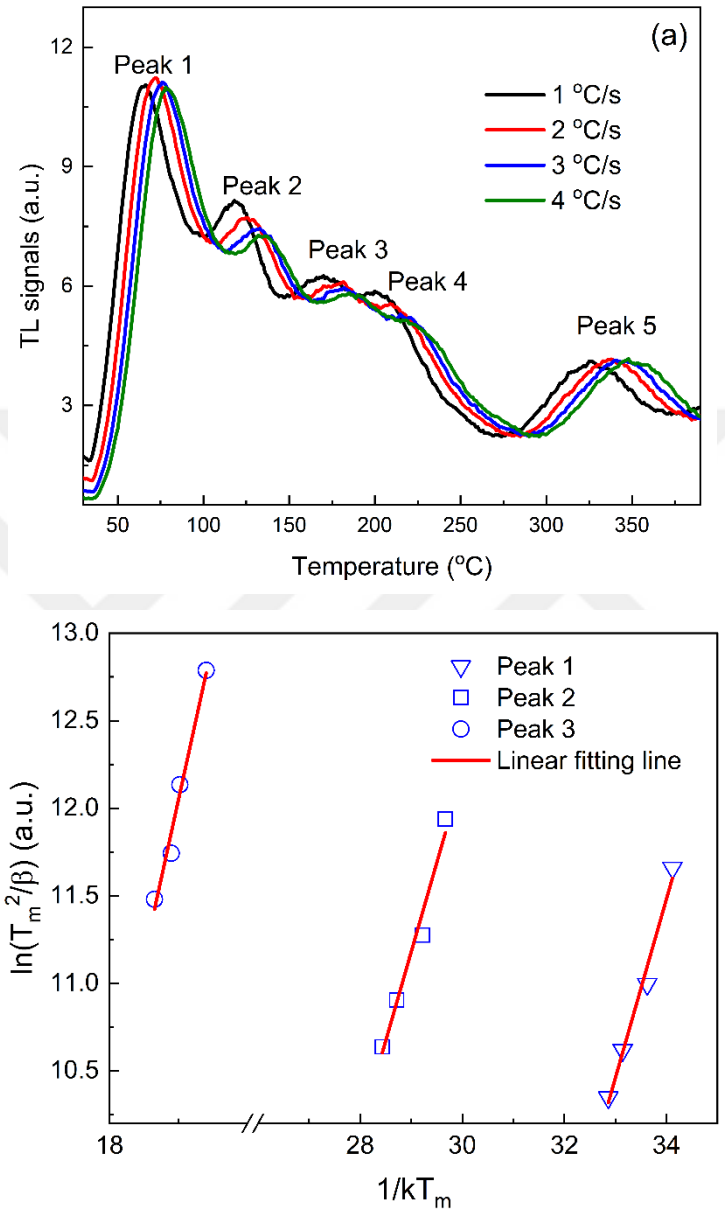

Figure 4.82. (a) TL glow curves of $KMgF_3:Eu_{0.5\%},Yb_{0.1\%},Li_{15\%}$ phosphor measured from RT to 450 °C at different heating rates. (b) Plots of ln (T_m^2/β) as a function of $1/kT_m$. Each slope value indicates the activation energy of the relevant TL peak and the exp (intercept) value indicates the frequency factor of this TL peak. The delivered β dose amount is 0.2 Gy.

4.6.12. Conclusion

In this work, undoped $KMgF_3$ and Li co-doped $KMgF_3$:Eu,Yb samples were prepared in polycrystal powder form via the sol-gel method. We investigated the role of individual and binary dopants of Eu and Yb, and co-dopant of Li on the luminescence and optical properties of $KMgF_3$. The Rietveld refinement was applied to the entire as-synthesized and doped $KMgF_3$ X-ray diffraction data for taking suitable structural information of the perovskite samples. We calculated the unit cell parameters of the undoped and Li co-doped samples and found a decrease in these values from $a=b=c$=3.9907 Å to $a=b=c$=3.9891 Å when doped with 15 mole% Li. The surface morphology of the samples was checked by SEM analyses and it was observed that the crystalline formation increased as the Li concentration increased. RL study of $KMgF_3$ and $KMgF_3$:$Eu_{0.5\%}$,$Yb_{0.1\%}$,$Li_{15\%}$ revealed the presence of various emission bands related to Eu^{3+} and Eu^{2+} being red- and blue-emissions. It has been showed that the $KMgF_3$:$Eu_{0.5\%}$,$Yb_{0.1\%}$,$Li_{x\%}$ samples have five TL peaks located at ~83, 133, 180, 254, and 357 $^{\circ}$C were recorded with varying intensities. The most intense TL signals were obtained at 15 mole% Li concentration. The OSL signal of the $KMgF_3$:$Eu_{0.5\%}$,$Yb_{0.1\%}$,$Li_{15\%}$ sample was approximately 8 times brighter than the neat sample. The OSL decay curves of the samples were analyzed. The OSL decay curve of the fast, medium and slow components of the undoped $KMgF_3$ and $KMgF_3$:$Eu_{0.5\%}$,$Yb_{0.1\%}$,$Li_{x\%}$ perovskites were calculated to determine the electron-hole recombination lifetimes for the related traps.

5. GENERAL CONCLUSION

5.1. Conclusions

Luminophores have been researched and developed for years to gain a better basic understanding of their properties and uses or to develop new and superior dosimeters. Currently, some groups around the world are involved in research on doped-MgO, ZnO, or doped-$KMgF_3$ phosphors due to their superior luminescence properties compared to conventional dosimetric materials. This thesis study has clearly shown that the doped MgO and $KMgF_3$ phosphors have a very high potential for use in radiation dosimetry. This thesis study also guides the determination of suitable calcination conditions for Eu-doped ZnO phosphors to be used as high-dose dosimeters.

This thesis is based on six main experimental studies of the doped ZnO, MgO, and $KMgF_3$ with different dopants, each having different aims. These experimental studies were carried out to develop the new high intense TL or OSL dosimeter for the radiation dosimetry.

In the first investigation in this thesis, we studied the effects of precipitation and sol-gel methods and different calcination conditions on the basic PL, TL, and OSL curves and the intensities of the relevant signals. ZnO phosphors were successfully produced by both of the methods and the calcination conditions were applied afterward. The XRD patterns of all samples are matched well to the ICSD card:98-019-5803 with a space group of hexagonal P63mc wurtzite structure. We obtained SEM images of the samples with well-defined grains. It was observed that the porous structures became more pronounced after 1000 °C with increasing calcination temperatures in both samples. The green emission from defects was observed from the PL spectra with $\lambda_{ex} = 350\,nm$. With the excitation of 464 nm, the sharp emission peaks, which are located at 579, 615, 650, and 700 nm, due to $^5D_0 \rightarrow {}^7F_1$, $^5D_0 \rightarrow {}^7F_2$, $^5D_0 \rightarrow {}^7F_3$ and $^5D_0 \rightarrow {}^7F_4$ transitions were detected in

the spectra. Two well-separated and simple TL peaks, located at 130 and 300 °C, were observed in the TL glow curve of ZnO:Eu pellets exposed to 20 Gy β-dose. In the TL measurements, we observed that TL peak positions or TL curves do not shift or change shape with the change of calcination conditions. In terms of luminescence efficiency, we determined that the optimum conditions of the calcination process in sol-gel and precipitation methods were at 800 °C - 10h and 900 °C - 4h, respectively. We also observed that the linear dose-response behavior of these samples ranged from 1 Gy to 0.2 kGy for both sample types. In this study, in which the optimum calcination conditions of Eu-doped ZnO samples that can be used in high dose dosimetry were determined, it was shown that both synthesis methods and calcination conditions could be applied, and comparative results were brought to the literature.

In the second work of this thesis, we have tried to develop the newly synthesized MgO dosimetric phosphorus as an OSL dosimeter and compare it with commercial dosimeters. We detected an increase in both TL and OSL intensities when Na and Li ions were incorporated into the MgO host matrix. We observed that, with the doping of Na and Li-ions at 5% molar concentration ratios, a TL peak around 300 °C caused an increase in intensity, and we also observed that the OSL signal intensity was likewise affected. Therefore, in this study, we presented the OSL signal intensity study as a function of the concentration ratio of Na and Li additives. We observed that 5% of Na and Li concentrations provided the most intense signal for OSL signal. We observed that the thermally affected OSL traps are located between 170-250 °C, which means that this narrow region is advantageous in terms of OSL signal stability. It was observed that the newly developed MgO:Na,Li sample was very sensitive to visible light as all TL peaks were completely depleted when exposed to 470 nm blue light excitation. Although this behavior suggested that the source of the OSL signal may be related to all observed TL peaks, the optically depleted charge from TL traps below 170 °C was seen to be by non-radiative transitions in the step-annealing measurement. It should

also be noted that the luminescence emission may be beyond the detection window. In this study, in which kinetic parameter calculations were performed for both TL and OSL traps, the activation energy of OSL traps was calculated as 1.37 eV using the isothermal annealing method. Further, by using CGCD, IRM, and T_m-T_{stop} techniques, the kinetic parameters of the traps responsible for TL signals were determined. TL activation energies were almost the same for all methods and were calculated as ~0.85 eV for 75 °C, ~0.95 eV for 144 °C, ~1.28 eV for 260 °C and ~1.50 eV for 366 °C. Detailed results are given in Table 4.2 comparatively. The stability of the OSL signals was examined in the darkroom for up to about 5 weeks, and at the end of 5 weeks, it was observed that the OSL signals decreased by 15% compared to the signals immediately after the radiation exposure. It can be said that with in-depth investigations such as different synthesis parameters or dopant concentrations, Na and Li doped MgO phosphors can be developed to exhibit better dosimetric properties in the future. It can be said that Na and Li doped MgO phosphors, which will exhibit better dosimetric properties in the future, can be developed as OSL dosimeters with in-depth studies such as different synthesis parameters or additive concentrations.

In this study, Cu, Li, K doped MgO samples were tested for their suitability for TL dosimetry. The samples were produced successfully by the SCS method and the XRD analysis results showed that the samples had a cubic structure and Fm-3m space group (Periclase, ICSD: 98-015-9375). The dosimetric characteristics and kinetic parameters of beta irradiated MgO:$Cu_{0.001\%}$,$Li_{10\%}$,$K_{10\%}$ have been investigated for exploration of its potential as an alternative phosphor for dosimetry applications. TL glow curve of MgO:$Cu_{0.001\%}$,$Li_{10\%}$,$K_{10\%}$ have four overlapped peaks located at 108, 214, 285, and 375 °C for TL readout performed with a 2 °C/s heating rate. The TL dose-response from stable traps was determined to be slightly linear with a slope value of 1.02 between 0.1 Gy and 0.5 kGy. The MDD value was estimated as ~5.9 μGy. The TL intensity decays nearly 3 and 3.3% for the peaks at 214 and 285 °C, respectively, in 48 h. Afterward, the same

decays were determined as 5.1 and 6.2% for four weeks. The activation energy *E* of the main dosimetric peak (214 °C) and the frequency factor *s* were calculated as ~1.40 eV and 10^{14} s^{-1}, respectively. The comparison of the kinetic parameters obtained by the CGCD, IR and VHR methods was presented in Table 4.3 in detail. As these results suggeste, the luminescence properties of the MgO:Cu,Li,K are such that they deserve more attention as a possible dosimeter in the field of radiation dosimetry.

In another study for MgO host matrix, dosimetric properties of Tb, Gd, and Li doped MgO were investigated for the IRSL technique. In this work, MgO:Tb,Gd,Li phosphor was successfully produced using the SCS method, and their crystallographic structure and phase composition were confirmed by XRD and SEM analyzes. The miller indices determined for the peaks associated with MgO proved to agree with the ICSD card:98-005-2026, which is in the Fm-3m space group and cubic structure. It was observed that all microparticles were uniform and had a size of about <0.1 μ on the SEM image. It was observed that the TL glow curve of MgO consisted of the combination of four TL peaks at 75, 140, 170, and 400 °C. It was reported that IR stimulation showed a 30 times more intense signal compared to blue light stimulation, and all TL traps were affected by IR stimulation, except for the traps responsible for the 400 °C TL peak. The IRSL readout at 120 °C was the reading with the highest luminescence signal intensity. When increasing the readout temperature from RT to 160 °C, IRSL decay became faster, but at temperatures higher than 160 °C its decaying speed became slower. This result can be associated with the presence of shallow traps that are interfering during IRSL readout. Charge traps responsible for the IRSL signal were found to be the TL traps below 200 °C in both step-annealing and TL after IRSL experiments. We tested the reusability of the samples over 20 sequential cycles and observed an acceptable deviation of 2%. In multiple IRSL readings, we observed a 45% loss of signal compared to the first signal at the end of the second reading, and we found that the signal was almost completely depleted at the end of the 20th

cycle. In the kinetic parameter calculations, the activation energy and frequency factor of the trap centers responsible for the IRSL signals were determined as 0.62 eV and 10^6 Hz, respectively, using isothermal annealing measurements. This result is a research study for a newly developed phosphor of MgO:Tb,Gd,Li, where the properties required for a radiation dosimeter have been investigated with the basic experiments. When properly heated MgO:Tb,Gd,Li pellet proved satisfactory for the IRSL dosimetry. This sample needs to be improved for its use in radiation dosimetry.

In the last work of the MgO sample, MgO matrix was activated with Ce and Li ions using the solid-state reaction technique to investigate and develop their luminescence properties. The sharp peaks related to the MgO cubic structure of the periclase phase with the Fm-3m (225) space group were determined and were observed to match well with the JCPDS card:45-0946. The TL glow curve of the samples was characterized with the TL peaks at 223 (Peak III) and 308 °C (Peak IV). The dose-response of the phosphor is essentially linear for exposures below 10 Gy β-dose. The dose-response becomes distinctly saturating at higher doses. Reduction in total TL signals between 210 and 240 °C (Peak III) was observed by 6% after three hours, 13% after 1 day, and 25% after 7 days dark storage. We observed a 40% depletion of the total TL signal in four weeks in the strip of 210-240 °C. The fading curve of the total TL signal between 300 and 330 °C (Peak IV) was recorded with a similar rate of decay during these four weeks. But the short-term fading of Peak IV appeared as a ~4% increase when compared with the TL intensity recorded after half an hour following the dose delivery. It might be due to a charge transfer from Peak III to Peak IV during those periods, appearing that the fading of the TL signal is relatively high for MgO:Ce,Li compared to the loss for other commercial TLD phosphors for the same period (Furetta, 2003). In the determination of the kinetic parameters, activation energy, frequency factors, and kinetic orders were determined using standard methods including CGCD, variable heating rate, and T_m-T_{stop} method, and all the activation energies were found in

agreement with each other (see Table 4.6). T_m-T_{stop} method revealed five plateaus. Using these activation centers spreading between ~0.6 and ~1.5 eV, it was determined that the main contributions are from these energy levels for radiation storage. The TL glow curve was analyzed by CGCD analysis, and the activation energies for Peak I, II, III, IV, and V were calculated as 0.60, 0.82, 1.11, 1.20, and 1.55 eV, respectively, in computerized analysis with a FOM value of 1.35. These energies are in agreement with those obtained in the T_m-T_{stop} analysis. On the other hand, the activation energies, obtained using the VHR method, corresponding to Peaks I, II, III, and IV were calculated as 0.65, 0.82, 1.17, and 1.43 eV, respectively.

In the last study of this thesis, we investigated the effect of Li concentration on crystallography and luminescence properties of $KMgF_3$:Eu,Yb. The absence of such a study for Parascandolaite in the literature encouraged us to investigate in detail, especially in terms of structural analysis, and we tried to interpret the increase in luminescence efficiency with detailed structural characterizations. Firstly, undoped and doped-$KMgF_3$ phosphorus were prepared in polycrystal powder form using the sol-gel method. We investigated the role of individual and binary dopants of Eu and Yb, and co-dopant of Li on the luminescence and optical properties of $KMgF_3$. For this purpose, we measured the TL and OSL luminescence curves, and RL emissions by testing different Li concentrations. The Rietveld refinement was applied to the entire as-synthesized and doped $KMgF_3$ X-ray diffraction data for taking suitable structural information of the perovskite samples. We calculated the unit cell parameters of the undoped and Li co-doped samples and found a decrease in these values from $a=b=c$=3.9907 Å to $a=b=c$=3.9891 Å when doped with 15 mole% Li. The surface morphology of the samples was checked by SEM analyses and it was observed that the crystalline formation increased as the Li concentration increased. The elemental configuration of the samples with EDS spectra has been reported. FT-IR spectra confirmed a reduction of the Mg-F bond due to the addition of Li, Eu, and Yb substitutions. RL

study of $KMgF_3$ and $KMgF_3$:$Eu_{0.5\%}$,$Yb_{0.1\%}$,$Li_{15\%}$ revealed the presence of various emission bands related to Eu^{3+} and Eu^{2+} being red- and blue-emissions. The $KMgF_3$:$Eu_{0.5\%}$,$Yb_{0.1\%}$,$Li_{x\%}$ samples were readout following the 0.2 Gy beta dose exposure, and the five TL peaks located at ~83, 133, 180, 254, and 357 $^{\circ}$C were recorded with varying intensities. It was observed that changing Li concentration did not affect the peak maxima of these TL peaks whereas it affected the TL-peak intensities. The most intense TL signals were obtained at 15 mole% Li concentration. The OSL signal of the $KMgF_3$:$Eu_{0.5\%}$,$Yb_{0.1\%}$,$Li_{15\%}$ sample was approximately 8 times brighter than the neat sample. The OSL decay curves of the samples were analyzed, too using the general order kinetic equation. The OSL decay curve of the fast, medium, and slow components of the undoped $KMgF_3$ and $KMgF_3$:$Eu_{0.5\%}$,$Yb_{0.1\%}$,$Li_{x\%}$ perovskites were calculated to determine the electron-hole recombination lifetimes for the related traps. This study stimulates further research for an understanding of the structure−property-luminescence relationship as a basis to improve the dosimetric capabilities of $KMgF_3$:$Eu_{0.5\%}$,$Yb_{0.1\%}$,$Li_{15\%}$ perovskite.

This thesis, which investigates many dosimetric properties of the ZnO, MgO, and $KMgF_3$, such as characterization and identification of the samples, defining RL emissions, determining PL emissions, solving simple "TL and OSL" glow curves, determining dose-response curves, fading studies, showing the relationship between "TL and OSL" traps, calculating activation energies of electron traps, has brought many results to the literature that will contribute to the research of these luminescent materials in the field of radiation dosimetry and will pave the way for the future development and its use in the industry.

5.2. List of Publications

The results of the present thesis have been presented in national and international conferences, and also have been published in international peer-reviewed scientific journals. Following is a list of them:

- Publications in SCI index Journals concerning present thesis:

1. Guckan, V., Altunal, V., Ozdemir, A., Tsiumra, V., Zhydachevskyy, Y., and Yegingil, Z., 2020. Calcination effects on europium doped zinc oxide as a luminescent material synthesized via sol-gel and precipitation methods. Journal of Alloys and Compounds, 823, 153878, 10.1016/j.jallcom.2020.153878.
2. Guckan, V., Altunal, V., Ozdemir, A., and Yegingil, Z., 2020. Optically stimulated luminescence of MgO:Na,Li phosphor prepared using solution combustion method. Journal of Alloys and Compounds, 835, 155253, 10.1016/j.jallcom.2020.155253.
3. Guckan, V., Altunal, V., Ozdemir, A., Kurt, K., and Yegingil, Z., 2021a. Cu, Li and K activated MgO: A metal oxide thermoluminescent synthesized using solution combustion technique for dosimetry. Journal of Luminescence, 230, 117751, 10.1016/j.jlumin.2020.117751.
4. Guckan, V., Altunal, V., Ozdemir, A., Kurt, K., and Yegingil, Z., 2021b. Use of infrared light-emitting diodes to determine dosimetric characteristics of MgO:Tb,Gd,Li via the optically stimulated luminescence technique. Journal of Luminescence, 235, 118005, 10.1016/j.jlumin.2021.118005.
5. Guckan, V., Bokhari, S.W., Altunal, V., Ozdemir, A., Gao, W., and Yegingil Z., 2021. Luminescence of Ce3+ and Li+ co-doped MgO synthesized using solid-state reaction method, Nuclear Instruments and Methods in Physics Research Section B: Beam Interactions with Materials and Atoms, 503, 53-61.

6. V. Guckan, D. Kaya, V. Altunal, A. Ekicibil, F. Karadag, A. Ozdemir and Z. Yegingil, 2021. Impact of Li concentration in $KMgF_3$:Eu,Yb fluoroperovskite on structure and luminescence properties, Journal of Alloys and Compounds, xxx (Under Review).

- Oral presentations in International Conferences concerning present thesis:
  1. Guckan, V., Ozdemir A., Altunal V. and Yegingil Z, 2019. A preliminary study of TL and OSL properties of MgO doped with Gd and Tb. 5th Internatıonal conference on materials science and nanotechnology for next generation (MSNG2018), 04-06 October 2018, NEVŞEHİR, Cappadocia, TURKEY.
  2. Guckan, V., Altunal, V., Ozdemir, A., Yegingil, Z., 2019. Structure characterization and luminescence studies of MgO:Li calcinated at different temperatures via solution combustion and sol-gel methods. International Conference on Condensed Matter and Materials Science (ICCMS-2019), October 14-19, 2019, Adana, TURKEY.
  3. Guckan, V. Altunal, A. Ozdemir, A., Erunal E. and Yegingil Z., 2019. Developing new MgO luminophors with different dopants for dosimetry applications and determination of ESR properties. 6th International Conference on Materials Science and Nanotechnology For Next Generation (MSNG2019) October 16-18, 2019, Niğde, TURKEY.
  4. Guckan, V., Altunal, V., Abusaid, W., Ozdemir, A., Yegingil, Z., 2021. Study of Enhancement the TL/OSL Intensities of $KMgF_3$ Perovskites. 6th International Conference on Oxide Materials for Electronic Engineering – Fabrication, Properties and Application (OMEE-2021) September28- October 2, 2021, Lviv, UKRAINE.

- Publications in scientific journals concerning other applications of luminescence:
  1. Güçkan, V., Altunal, V., Özdemir, A., and Yeğingil, Z., 2019. Structure Characterization and Luminescence Studies of MgO:Li Calcinated at Different Temperatures via Solution Combustion and Sol-Gel Methods. Journal of Investigations on Engineering and Technology, 2(2), 45-48, https://dergipark.org.tr/en/pub/jiet/issue/51030/637291.

REFERENCES

Afouxenidis, D., Polymeris, G., Tsirliganis, N., and Kitis, G., 2011. Computerised curve deconvolution of TL/OSL curves using a popular spreadsheet program. *Radiation Protection Dosimetry, 149*(4), 363-370,

Ahmed, F., Kumar, S., Arshi, N., Anwar, M., Koo, B. H., and Lee, C. G., 2012. Doping effects of Co2+ ions on structural and magnetic properties of ZnO nanoparticles. *Microelectronic Engineering, 89*, 129-132,

Aitken, M. J., 1985b. *Thermoluminescence dating*.

Aitken, M. J., and Smith, B. W., 1988. Optical Dating - Recuperation after Bleaching. *Quaternary Science Reviews, 7*(3-4), 387-393, Doi 10.1016/0277-3791(88)90034-0.

Aitken, M. J., Tite, M. S., and Reid, J., 1964. Thermoluminescent dating of ancient ceramics. *Nature, 202*(4936), 1032-1033,

Aitken, M. J., Zimmerman, D. W., and Fleming, S. J., 1968. Thermoluminescent dating of ancient pottery. *Nature, 219*(5153), 442-445,

Aitken, M., 1985a. Thermoluminescence dating: past progress and future trends. *Nuclear Tracks and Radiation Measurements (1982), 10*(1-2), 3-6,

Akselrod, M. S., Botter-Jensen, L., and McKeever, S. W. S., 2006. Optically stimulated luminescence and its use in medical dosimetry. *Radiation Measurements, 41*, S78-S99, 10.1016/j.radmeas.2007.01.004.

Altunal, V., Guckan, V., Ozdemir, A., and Yegingil, Z., 2020b. Radiation dosimeter utilizing optically stimulated luminescence of BeO:Na,Tb,Gd ceramics. *Journal of Alloys and Compounds, 817*, 152809, 10.1016/j.jallcom.2019.152809.

Altunal, V., Guckan, V., Ozdemir, A., Kurt, K., Ekicibil, A., and Yegingil, Z., 2020a. Investigation of luminescence properties of BeO ceramics doped with metals for medical dosimetry. *Optical Materials, 108*, 110436, 10.1016/j.optmat.2020.110436.

Altunal, V., Guckan, V., Ozdemir, A., Sotelo, A., and Yegingil, Z., 2019. Effect of sintering temperature on dosimetric properties of BeO ceramic pellets synthesized using precipitation method. *Nuclear Instruments & Methods in Physics Research Section B-Beam Interactions with Materials and Atoms, 441*, 46-55, 10.1016/j.nimb.2018.12.036.

Altunal, V., Guckan, V., Yu, Y., Dicker, A., and Yegingil, Z., 2020c. A newly developed OSL dosimeter based on beryllium oxide: BeO:Na,Dy,Er. *Journal of Luminescence, 222*, 117140, 10.1016/j.jlumin.2020.117140.

Andrade, A. B., Macedo, Z. S., Valerio, M. E. G., and Yukihara, E. G., 2019. Thermoluminescence and optically stimulated luminescence properties of the Eu2+-doped KMgF3 produced by a hydrothermal microwave method. *Journal of Luminescence, 206*, 302-307, https://doi.org/10.1016/j.jlumin.2018.10.012.

Ashraf, R., Riaz, S., Kayani, Z. N., and Naseem, S., 2015. Effect of Calcination on properties of ZnO nanoparticles. *Materials Today: Proceedings, 2*(10), 5468-5472,

Atuchin, V. V., Gavrilova, T. A., Grivel, J. C., and Kesler, V. G., 2008. Electronic structure of layered titanate Nd2Ti2O7. *Surface Science, 602*(19), 3095-3099, 10.1016/j.susc.2008.07.040.

Atuchin, V. V., Subanakov, A. K., Aleksandrovsky, A. S., Bazarov, B. G., Bazarova, J. G., Gavrilova, T. A., Krylov, A. S., Molokeev, M. S., Oreshonkov, A. S., and Stefanovich, S. Y., 2018. Structural and spectroscopic properties of new noncentrosymmetric self-activated borate Rb3EuB6O12 with B5O10 units. *Materials & Design, 140*, 488-494, 10.1016/j.matdes.2017.12.004.

Atuchin, V., Aleksandrovsky, A., Chimitova, O., Gavrilova, T., Krylov, A., Molokeev, M., Oreshonkov, A., Bazarov, B., and Bazarova, J., 2014. Synthesis and spectroscopic properties of monoclinic α-Eu2 (MoO4) 3. *The Journal of Physical Chemistry C, 118*(28), 15404-15411,

Atuchin, V., Galashov, E., Kozhukhov, A., Pokrovsky, L., and Shlegel, V., 2011. Epitaxial growth of ZnO nanocrystals at ZnWO4 (0 1 0) cleaved surface. *Journal of Crystal Growth, 318*(1), 1147-1150,

Avilés-Monreal, R., Cruz-Vázquez, C., Bernal, R., and Brown, F., 2018. Thermoluminescence of ZnO: Na phosphors exposed to beta particle irradiation. *Optical Materials, 83*, 78-81,

Azorín, J., 1986. Determination of thermoluminescence parameters from glow curves. *Nuclear Tracks and Radiation Measurements, 11*(3), 159-166,

Azorin, J., 2014. Preparation methods of thermoluminescent materials for dosimetric applications: an overview. *Appl Radiat Isot, 83 Pt C*, 187-191, 10.1016/j.apradiso.2013.04.031.

Azorin, J., Furetta, C., and Gutierrez, A., 1989. Evaluation of the kinetic parameters of CaF2: Tm (TLD-300) thermoluminescence dosemeters. *Journal of Physics D: Applied Physics, 22*(3), 458,

Azorín-Vega, J., Azorín-Nieto, J., García-Hipólito, M., and Rivera-Montalvo, T., 2007. Thermoluminescence properties of TiO2 nanopowder. *Radiation Measurements, 42*(4-5), 613-616,

Bacci, C., Fioravanti, S., Furetta, C., Missori, M., Ramogida, G., Rossetti, R., Sanipoli, C., and Scacco, A., 1993. Photoluminescence and Thermally Stimulated Luminescence in Kmgf3-Eu2+ Crystals. *Radiation Protection Dosimetry, 47*(1-4), 277-280,

Bae, J. S., Kim, S. B., Jeong, J. H., Park, J. C., Kim, D. K., Byeon, S. H., and Yi, S. S., 2005. Photoluminescence characteristics of Li-doped Y2O3 : Eu3+ thin film phosphors. *Thin Solid Films, 471*(1-2), 224-229, 10.1016/j.tsf.2004.05.133.

Bailiff, I. K., 1995. The Use of Ceramics for Retrospective Dosimetry in the Chernobyl Exclusion Zone. *Radiation Measurements, 24*(4), 507-511, Doi 10.1016/1350-4487(95)00020-F.

Bailiff, I., and Poolton, N., 1989. The use of LEDs as an excitation source for photoluminescence dating of sediment. *Ancient TL, 7*, 18-20,

Bailly, M.-L., Costentin, G., Lauron-Pernot, H., Krafft, J. M., and Che, M., 2005. Physicochemical and in situ photoluminescence study of the reversible transformation of oxide ions of low coordination into hydroxyl groups upon interaction of water and methanol with MgO. *The Journal of Physical Chemistry B, 109*(6), 2404-2413,

Balakrishnaiah, R., Yi, S. S., Jang, K., Lee, H. S., Moon, B. K., and Jeong, J. H., 2011. Enhanced luminescence properties of YBO3:Eu3+ phosphors by Li-doping. *Materials Research Bulletin, 46*(4), 621-626, 10.1016/j.materresbull.2010.09.012.

Balian, H. G., and Eddy, N. W., 1977. Figure-of-merit (FOM), an improved criterion over the normalized chi-squared test for assessing goodness-of-fit of gamma-ray spectral peaks. *Nuclear Instruments and Methods, 145*(2), 389-395,

Bapat, M., and Sivaraman, S., 1985a. Role of Ce 3+ in the luminescence of MgO. *Indian Journal of Pure and Applied Physics, 23*(10), 535-536,

Bapat, M., Sivaraman, S., and Nambi, K., 1985b. Thermoluminescence of MgO: Li (Ce, Eu). *Indian journal of pure and applied physics. New Delhi, 23*(11), 558-560,

Barros, V., De Azevedo, W., Khoury, H., Andrade, M., and Linhares Filho, P., 2010. Thermoluminescence study of aluminum oxide doped with therbium and thulium. *Radiation Measurements, 45*(3-6), 435-437,

Berrezoug, H., Merad, A., Zerga, A., and Hassoun, Z. S., 2015. Simulation and modeling of structural stability, electronic structure and optical properties of ZnO. *Energy Procedia, 74*, 1517-1524,

Bhadane, M. S., Mandlik, N., Patil, B. J., Dahiwale, S. S., Sature, K. R., Bhoraskar, V. N., and Dhole, S. D., 2016. CaSO4:Dy microphosphor for thermal neutron dosimetry. *Journal of Luminescence, 170*, 226-230, 10.1016/j.jlumin.2015.10.025.

Bhargava, A., Alarco, J. A., Mackinnon, I. D., Page, D., and Ilyushechkin, A., 1998. Synthesis and characterisation of nanoscale magnesium oxide powders and their application in thick films of Bi2Sr2CaCu2O8. *Materials Letters, 34*(3-6), 133-142,

Blair, M. W., Jacobsohn, L. G., Bennett, B. L., Tornga, S. C., Yukihara, E. G., McKigney, E. A., and Muenchausen, R. E., 2009. Luminescence and structural properties of oxyorthosilicate and Al2O3 nanophosphors. *Physica Status Solidi a-Applications and Materials Science, 206*(5), 904-909, 10.1002/pssa.200881275.

Blair, M. W., Jacobsohn, L. G., Tornga, S. C., Ugurlu, O., Bennett, B. L., Yukihara, E. G., and Muenchausen, R. E., 2010. Nanophosphor aluminum oxide: Luminescence response of a potential dosimetric material. *Journal of Luminescence, 130*(5), 825-831,

Borbón-Nuñez, H., Cruz-Vázquez, C., Bernal, R., Kitis, G., Furetta, C., and Castaño, V., 2014. Thermoluminescence properties of sintered ZnO. *Optical Materials, 37*, 398-403,

Bos, A. J. J., 2006. Theory of thermoluminescence. *Radiation Measurements, 41*, S45-S56, 10.1016/j.radmeas.2007.01.003.

Bos, A., Prokić, M., and Brouwer, J., 2006. Optically and thermally stimulated luminescence characteristics of MgO: Tb3+. *Radiation Protection Dosimetry, 119*(1-4), 130-133,

Bøtter-Jensen, L., and Duller, G., 1992. A new system for measuring optically stimulated luminescence from quartz samples. *International Journal of Radiation Applications and Instrumentation. Part D. Nuclear Tracks and Radiation Measurements, 20*(4), 549-553,

Bøtter-Jensen, L., Ditlefsen, C., and Mejdahl, V., 1991. Combined OSL (infrared) and TL studies of feldspars. *International Journal of Radiation Applications and Instrumentation. Part D. Nuclear Tracks and Radiation Measurements, 18*(1-2), 257-263, 10.1016/1359-0189(91)90120-7.

Bøtter-Jensen, L., Markey, B., Poolton, N., and Jungner, H., 1996. Luminescence properties of porcelain ceramics relevant to retrospective radiation dosimetry. *Radiation Protection Dosimetry, 65*(1-4), 369-372,

Bøtter-Jensen, L., McKeever, S. W., and Wintle, A. G., 2003. *Optically stimulated luminescence dosimetry*: Elsevier.

Bulur, E., 1996. An alternative technique for optically stimulated luminescence (OSL) experiment. *Radiation Measurements, 26*(5), 701-709, Doi 10.1016/S1350-4487(97)82884-3.

Bulur, E., and Goksu, H. Y., 1998a. OSL from BEO ceramics: New observations from an old material. *Radiation Measurements, 29*(6), 639-650, Doi 10.1016/S1350-4487(98)00084-5.

Bulur, E., Göksu, H. Y., and Wahl, W., 1998b. Infrared (IR) stimulated luminescence from α□Al2O3:C. *Radiation Measurements, 29*(6), 625-638, 10.1016/s1350-4487(98)00076-6.

Bünzli, J.-C. G., and Eliseeva, S. V. (2010). Basics of lanthanide photophysics. In *Lanthanide Luminescence* (pp. 1-45): Springer.

Calabrese, E., and Fowler, W. B., 1978. Electronic energy-band structure of α quartz. *Physical Review B, 18*(6), 2888,

Camargo Jimenez, L. A., Pérez Cruz, L., Cruz Zaragoza, E., Martinez Ovalle, S. A., and Marcazzo, S. J., 2018. OSL properties of KMgF3: Tm3+ for dosimetric applications as OSL dosimeter.

Chantry, G. W., Nicol, E. A., Willis, H. A., and Cudby, M. E. A., 1981. Far Infrared Studies of the Formation of Potassium Fluoride Dihydrate in and Its Interaction with Low-Molecular Weight Polytetrafluorethylene. *International Journal of Infrared and Millimeter Waves, 2*(1), 97-105, Doi 10.1007/Bf01007474.

Chen, C., Liu, P., and Lu, C., 2008. Synthesis and characterization of nano-sized ZnO powders by direct precipitation method. *Chemical Engineering Journal, 144*(3), 509-513,

Chen, R., and McKeever, S. W., 1997. *Theory of thermoluminescence and related phenomena*: World Scientific.

Chen, R., and Pagonis, V., 2011. *Thermally and optically stimulated luminescence: a simulation approach*: John Wiley & Sons.

Chen, X., Liu, Y., and Tu, D., 2016. *Lanthanide-doped luminescent nanomaterials*: Springer.

Chen, Y., Kernohan, R., Boldu, J., Abraham, M., Eisenberg, D., and Crawford Jr, J., 1980. Enhancement of electrical conductivity in MgO due to lithium impurities. *Solid state communications, 33*(4), 441-443,

Chruścińska, A., 2001. THE FRACTIONAL GLOW TECHNIQUE AS A TOOL OF INVESTIGATION OF TL BLEACHING EFFICIENCY IN K-FELDSPAR. *Geochronometria: Journal on Methods & Applications of Absolute Chronology, 20*,

Cohen, R. E., 1992. Origin of Ferroelectricity in Perovskite Oxides. *Nature, 358*(6382), 136-138, DOI 10.1038/358136a0.

Copp, A., 1995. Magnesia/magnesite. *American Ceramic Society Bulletin, 74*(6), 135-137,

Correcher, V., Sanchez-Munoz, L., Garcia-Guinea, J., Gomez-Ros, J. M., and Delgado, A., 2006. On the blue thermoluminescence emission of synthetic Li-rich aluminosilicates. *Nuclear Instruments & Methods in Physics Research Section a-Accelerators Spectrometers Detectors and Associated Equipment, 562*(1), 456-460, 10.1016/j.nima.2006.02.134.

Cruz-Vázquez, C., Bernal, R., Burruel-Ibarra, S., Grijalva-Monteverde, H., and Barboza-Flores, M., 2005. Thermoluminescence properties of new ZnO nanophosphors exposed to beta irradiation. *Optical Materials, 27*(7), 1235-1239,

Dalal, M., Taxak, V. B., Chahar, S., Khatkar, A., and Khatkar, S. P., 2016. A promising novel orange-red emitting SrZnV2O7:Sm3+ nanophosphor for phosphor-converted white LEDs with near-ultraviolet excitation. *Journal of Physics and Chemistry of Solids, 89*, 45-52, 10.1016/j.jpcs.2015.10.017.

Dallas, G., Polymeris, G., Afouxenidis, D., Tsirliganis, N., Tsagas, N., and Kitis, G., 2010. Correlation between TL and OSL signals in KMgF 3: Ce 3+: Bleaching study of individual glow-peaks. *Radiation Measurements, 45*(3), 537-539,

Daniel, D. J., Madhusoodanan, U., Annalakshmi, O., Jose, M. T., and Ramasamy, P., 2015. Thermoluminescence dosimetric characteristics on cubic fluoroperovskite single crystal (KMgF3:Eu2+, Ce3+). *Optical Materials, 45*, 224-228, 10.1016/j.optmat.2015.03.043.

Daniel, D. J., Raja, A., Madhusoodanan, U., Annalakshmi, O., and Ramasamy, P., 2016. OSL studies of alkali fluoroperovskite single crystals for radiation dosimetry. *Optical Materials, 58*, 497-503, 10.1016/j.optmat.2016.06.019.

Daniels, F., Boyd, C. A., and Saunders, D. F., 1953. Thermoluminescence as a research tool. *Science, 117*(3040), 343-349,

Davini, P., and Tartarelli, R., 1985. Emissions from the combustion of heavy oils: effect of granulometry and surface area of MgO additive. *Fuel, 64*(3), 380-383,

Dawber, M., Rabe, K. M., and Scott, J. F., 2005. Physics of thin-film ferroelectric oxides. *Reviews of modern physics, 77*(4), 1083-1130, DOI 10.1103/RevModPhys.77.1083.

Demartin, F., Campostrini, I., Castellano, C., and Russo, M., 2014. Parascandolaite, KMgF3, a new perovskite-type fluoride from Vesuvius. *Physics and Chemistry of Minerals, 41*(6), 403-407, 10.1007/s00269-014-0668-y.

Denisenko, Y. G., Atuchin, V. V., Molokeev, M. S., Aleksandrovsky, A. S., Krylov, A. S., Oreshonkov, A. S., Volkova, S. S., and Andreev, O. V., 2018. Structure, Thermal Stability, and Spectroscopic Properties of Triclinic Double Sulfate AgEu(SO4)2 with Isolated SO4 Groups. *Inorg Chem, 57*(21), 13279-13288, 10.1021/acs.inorgchem.8b01837.

Dhananjaya, N., Nagabhushana, H., Nagabhushana, B. M., Rudraswamy, B., Shivakumara, C., and Chakradhar, R. P. S., 2011. Effect of Li+-ion on enhancement of photoluminescence in Gd2O3:Eu3+ nanophosphors prepared by combustion technique. *Journal of Alloys and Compounds, 509*(5), 2368-2374, 10.1016/j.jallcom.2010.11.023.

Dhananjaya, N., Nagabhushana, H., Nagabhushana, B. M., Rudraswamy, B., Shivakumara, C., Narahari, K., and Chakradhar, R. P., 2012. Enhanced photoluminescence of Gd2O3:Eu3+ nanophosphors with alkali (M=Li+, Na+, K+) metal ion co-doping. *Spectrochim Acta A Mol Biomol Spectrosc, 86*, 8-14, 10.1016/j.saa.2011.05.072.

Dhannia, T., Jayalekshmi, S., Kumar, M. C. S., Rao, T. P., and Bose, A. C., 2010. Effect of iron doping and annealing on structural and optical properties of cerium oxide nanocrystals. *Journal of Physics and Chemistry of Solids, 71*(7), 1020-1025, 10.1016/j.jpcs.2010.04.011.

Dhoble, S. J., Raju, B. D. P., and Singh, V., 2018. *Phosphors: Synthesis and applications*: CRC Press.

Dieke, G. H., Crosswhite, H. M., and Crosswhite, H., 1968. Spectra and energy levels of rare earth ions in crystals.

Dinka, P., and Mukasyan, A., 2006. Solution Combustion Synthesis of Nano Materials. *Nano Science and Technology Institute, Cambridge, MA, 2139*, 7-11,

Dolgov, S., Isakhanyan, V., Kärner, T., Liblik, P., Maaroos, A., and Nakonechnyi, S., 2004. Luminescence of [Be]+ centre in MgO: Be. *Radiation Measurements, 38*(4-6), 699-702,

Dolgov, S., Kärner, T., Lushchik, A., Maaroos, A., Mironova-Ulmane, N., and Nakonechnyi, S., 2002. Thermoluminescence centres created selectively in MgO crystals by fast neutrons. *Radiation Protection Dosimetry, 100*(1-4), 127-130,

Dorenbos, P., 2000. The 5d level positions of the trivalent lanthanides in inorganic compounds. *Journal of Luminescence, 91*(3-4), 155-176, Doi 10.1016/S0022-2313(00)00229-5.

Dotzler, C., Williams, G., Rieser, U., and Edgar, A., 2007. Optically stimulated luminescence in Na Mg F 3: Eu 2+. *Applied Physics Letters, 91*(12), 121910,

Dou, Q., and Zhang, Y., 2011. Tuning of the structure and emission spectra of upconversion nanocrystals by alkali ion doping. *Langmuir, 27*(21), 13236-13241,

Duller, G. A. T., and Botterjensen, L., 1993. Luminescence from Potassium Feldspars Stimulated by Infrared and Green Light. *Radiation Protection Dosimetry, 47*(1-4), 683-688, 10.1093/oxfordjournals.rpd.a081832.

Dunphy, K., and Duley, W., 1990. Multiphoton excitation of Mn4+ and Cr3+ luminescence in MgO. *Journal of Physics and Chemistry of Solids, 51*(9), 1077-1082,

Dyshlyuk, L., Babich, O., Ivanova, S., Vasilchenco, N., Atuchin, V., Korolkov, I., Russakov, D., and Prosekov, A., 2020. Antimicrobial potential of ZnO, TiO2 and SiO2 nanoparticles in protecting building materials from biodegradation. *International Biodeterioration & Biodegradation, 146*, 104821,

Efstathopoulos, E. P., Makrygiannis, S. S., Kottou, S., Karvouni, E., Giazitzoglou, E., Korovesis, S., Tzanalaridou, E., Raptou, P. D., and Katritsis, D. G., 2003. Medical personnel and patient dosimetry during coronary angiography and intervention. *Phys Med Biol, 48*(18), 3059-3068, 10.1088/0031-9155/48/18/307.

Ellens, A., Meijerink, A., and Blasse, G., 1994. 6I emission and vibronic transitions of Eu2+ in KMgF3. *Journal of Luminescence, 59*(5), 293-301, 10.1016/0022-2313(94)90056-6.

El-Shaer, A., Abdelfatah, M., Mahmoud, K. R., Momay, S., and Eraky, M. R., 2020. Correlation between photoluminescence and positron annihilation lifetime spectroscopy to characterize defects in calcined MgO nanoparticles as a first step to explain antibacterial activity. *Journal of Alloys and Compounds, 817*, 152799, ARTN 152799 10.1016/j.jallcom.2019.152799.

Faghihi-Sani, M.-A., and Yamaguchi, A., 2002. Oxidation kinetics of MgO–C refractory bricks. *Ceramics International, 28*(8), 835-839,

Fang, T. H., Chang, Y. S., Ji, L. W., Prior, S. D., Water, W., Chen, K. J., Fang, C. F., Fang, C. N., and Shen, S. T., 2009. Photoluminescence characteristics of ZnO doped with Eu3+ powders. *Journal of Physics and Chemistry of Solids, 70*(6), 1015-1018, 10.1016/j.jpcs.2009.05.012.

Fox, M. (2002). Optical properties of solids. In: American Association of Physics Teachers.

Fu, H. Y., Cui, S., Luo, Q., Qiao, X. S., Fan, X. P., and Zhang, X. H., 2012. Broadband downshifting luminescence of Cr3+/Yb3+-codoped fluorosilicate glass. *Journal of Non-Crystalline Solids, 358*(9), 1217-1220, 10.1016/j.jnoncrysol.2012.02.024.

Furetta, C., 2003. *Handbook of thermoluminescence*: World Scientific.

Furetta, C., Bacci, C., Rispoli, B., Sanipoli, C., and Scacco, A., 1990. Luminescence and Dosimetric Performances of Kmgf3 Crystals Doped with Metal Impurity Ions. *Radiation Protection Dosimetry, 33*(1-4), 107-110,

Furetta, C., Ramogida, G., Scacco, A., Martini, M., and Paravisi, S., 1994. Spectroscopy of complex defects in crystals of KMgF3: Tl+. *Journal of Physics and Chemistry of Solids, 55*(11), 1337-1345,

Furetta, C., Santopietro, F., Sanipoli, C., and Kitis, G., 2001. Thermoluminescent (TL) properties of the perovskite KMgF3 activated by Ce and Er impurities. *Appl Radiat Isot, 55*(4), 533-542, 10.1016/s0969-8043(01)00085-9.

Gai, M. Q., Chen, Z. Y., Fan, Y. W., Yan, S. Y., Xie, Y. X., Wang, J. H., and Zhang, Y. G., 2015. Synthesis of LiMgPO4:Eu,Sm,B phosphors and investigation of their optically stimulated luminescence properties. *Radiation Measurements, 78*, 48-52, 10.1016/j.radmeas.2014.09.009.

Gambarini, G., Marchesi, P., Scacco, A., Roy, M. S., and Marchesini, R., 1999. Thermoluminescent response of KMgF3 : Yb single crystals in gamma radiation fields. *Radiation Protection Dosimetry, 84*(1-4), 211-214, DOI 10.1093/oxfordjournals.rpd.a032720.

Gao, G., and Wondraczek, L., 2013. Near-infrared down-conversion in Mn 2+–Yb 3+ co-doped Zn 2 GeO 4. *Journal of Materials Chemistry C, 1*(10), 1952-1958,

Garcia M, J., Sibley, W. A., Hunt, C. A., and Spaeth, J. M., 1988. Optical properties of Eu2+, Eu3+ and Mn2+ in cubic perovskite crystals. *Journal of Luminescence, 42*(1), 35-42, 10.1016/0022-2313(88)90063-4.

Garcia-Guinea, J., and Correcher, V., 2000. Luminescence spectra of alkali feldspars: Influence of crushing on the ultraviolet emission band. *Spectroscopy Letters, 33*(1), 103-113, Doi 10.1080/00387010009350062.

Garg, V., Sengar, B. S., Awasthi, V., Kumar, A., Singh, R., Kumar, S., Mukherjee, C., Atuchin, V. V., and Mukherjee, S., 2018. Investigation of dual-ion beam sputter-instigated plasmon generation in TCOs: a case study of GZO. *ACS applied materials & interfaces, 10*(6), 5464-5474,

Gektin, A. V., 2000. Scintillators and storage phosphors based on ABX3 crystals. *Journal of Luminescence, 87-89*, 1283-1285, 10.1016/s0022-2313(99)00579-7.

Gektin, A. V., Komar, V. K., Shiran, N. V., Shlykhturov, V. V., Nesterenko, N. P., Krasovitskaya, I. M., and Kornienko, V. V., 1995. Radiation damage of pure and doped KMgF/sub 3/ crystals. *IEEE Transactions on Nuclear Science*, *42*(4), 311-314, 10.1109/23.467830.

Gektin, A. V., Krasovitskaya, I. M., and Shiran, N. V., 1997. High-temperature thermoluminescence of KMgF3-based crystals. *Journal of Luminescence, 72-4*, 664-666, Doi 10.1016/S0022-2313(96)00231-1.

Gektin, A. V., Krasovitskaya, I. M., and Shiran, N. V., 1998. UV-dosimetric material based on KMgF3 perovskite. *Radiation Measurements, 29*(3-4), 337-340, 10.1016/s1350-4487(98)00054-7.

Gobrecht, H., and Hofmann, D., 1966. Spectroscopy of traps by fractional glow technique. *Journal of Physics and Chemistry of Solids*, *27*(3), 509-522,

Godfrey-Smith, D. I., Huntley, D. J., and Chen, W.-H., 1988. Optical dating studies of quartz and feldspar sediment extracts. *Quaternary Science Reviews, 7*(3-4), 373-380,

Goldstein, J. I., Newbury, D. E., Michael, J. R., Ritchie, N. W., Scott, J. H. J., and Joy, D. C., 2017. *Scanning electron microscopy and X-ray microanalysis*: Springer.

Gomez-Ros, J. M., Furetta, C., and Correcher, V., 2006. Simple methods to analyse thermoluminescence glow curves assuming arbitrary recombination-retrapping rates. *Radiat Prot Dosimetry, 119*(1-4), 339-343, 10.1093/rpd/nci523.

Green, J., 1983. Calcination of precipitated Mg (OH) 2 to active MgO in the production of refractory and chemical grade MgO. *Journal of Materials Science*, *18*(3), 637-651,

Gu, F., Li, C. Z., and Jiang, H. B., 2006. Combustion synthesis and photoluminescence of MgO : Eu3+ nanocrystals with Li+ addition. *Journal of Crystal Growth, 289*(1), 400-404, 10.1016/j.jcrysgro.2005.11.116.

Gu, F., Li, C., Cao, H., Shao, W., Hu, Y., Chen, J., and Chen, A., 2008. Crystallinity of Li-doped MgO: Dy3+ nanocrystals via combustion process and their photoluminescence properties. *Journal of Alloys and Compounds, 453*(1-2), 361-365,

Guckan, V., Altunal, V., Nur, N., Depci, T., Ozdemir, A., Kurt, K., Yu, Y., Yegingil, I., and Yegingil, Z., 2017. Studying CaSO4:Eu as an OSL phosphor. *Nuclear Instruments & Methods in Physics Research Section B-Beam Interactions with Materials and Atoms, 407*, 145-154, 10.1016/j.nimb.2017.06.010.

Guckan, V., Altunal, V., Ozdemir, A., and Yegingil, Z., 2020b. Optically stimulated luminescence of MgO:Na,Li phosphor prepared using solution combustion method. *Journal of Alloys and Compounds, 835*, 155253, 10.1016/j.jallcom.2020.155253.

Guckan, V., Altunal, V., Ozdemir, A., Kurt, K., and Yegingil, Z., 2021a. Cu, Li and K activated MgO: A metal oxide thermoluminescent synthesized using solution combustion technique for dosimetry. *Journal of Luminescence, 230*, 117751, 10.1016/j.jlumin.2020.117751.

Guckan, V., Altunal, V., Ozdemir, A., Kurt, K., and Yegingil, Z., 2021b. Use of infrared light-emitting diodes to determine dosimetric characteristics of MgO:Tb,Gd,Li via the optically stimulated luminescence technique. *Journal of Luminescence, 235*, 118005, ARTN 118005 10.1016/j.jlumin.2021.118005.

Guckan, V., Altunal, V., Ozdemir, A., Tsiumra, V., Zhydachevskyy, Y., and Yegingil, Z., 2020a. Calcination effects on europium doped zinc oxide as a luminescent material synthesized via sol-gel and precipitation methods. *Journal of Alloys and Compounds, 823*, 153878, 10.1016/j.jallcom.2020.153878.

Guckan, V., Ozdemir, A., Altunal, V., Yegingil, I., and Yegingil, Z., 2019. Studies of blue light induced phototransferred thermoluminescence in CaSO4:Mg. *Nuclear Instruments & Methods in Physics Research Section B-Beam Interactions with Materials and Atoms, 448*, 31-38, 10.1016/j.nimb.2019.03.058.

Gugliotti, C., Moriya, K., Tatumi, S., and Mittani, J., 2018. Synthesis and luminescence studies of Tb-doped MgO-MgAl2O4-Mg2SiO4 ceramic for use in radiation dosimetry. *Applied Radiation and Isotopes, 135*, 219-223,

Gupta, S. K., Zuniga, J. P., Abdou, M., Ghosh, P., and Mao, Y., 2020. Optical properties of undoped, Eu 3+ doped and Li+ co-doped Y 2 Hf 2 O 7 nanoparticles and polymer nanocomposite films. *Inorganic Chemistry Frontiers*,

Ha, V. T. T., Hai, N. T. Q., and Long, N. N., 2007. Preparation and characteristics of LiF: Mg, Cu, Na, Si thermoluminescent material. *VNU Journal of Science: Mathematics-Physics, 23*(4),

Haskell, E. H., 1993a. Accident Dosimetry Using Environmental Materials - the Role of Thermoluminescence. *Nuclear Tracks and Radiation Measurements, 21*(1), 87-93, Doi 10.1016/1359-0189(93)90050-J.

Haskell, E. H., 1993b. Retrospective Accident Dosimetry Using Environmental Materials. *Radiation Protection Dosimetry, 47*(1-4), 297-303,

Hasnidawani, J., Azlina, H., Norita, H., Bonnia, N., Ratim, S., and Ali, E., 2016. Synthesis of ZnO nanostructures using sol-gel method. *Procedia Chemistry, 19*, 211-216,

He, R., Tang, B., Ton-That, C., Phillips, M., and Tsuzuki, T., 2013. Physical structure and optical properties of Co-doped ZnO nanoparticles prepared by co-precipitation. *Journal of Nanoparticle Research, 15*(11), 2030,

Hirsch, L., and Shankland, T., 1991. Equilibrium point defect concentrations in MgO: Understanding the mechanisms of conduction and diffusion and the role of Fe impurities. *Journal of Geophysical Research: Solid Earth, 96*(B1), 385-403,

Holcomb, D. (1967). KITTEL, C-INTRODUCTION TO SOLID STATE PHYSICS. In: AMER INST PHYSICS CIRCULATION FULFILLMENT DIV, 500 SUNNYSIDE BLVD, WOODBURY ….

Horowitz, Y. S., and Moscovitch, M., 2013. Highlights and pitfalls of 20 years of application of computerised glow curve analysis to thermoluminescence research and dosimetry. *Radiat Prot Dosimetry, 153*(1), 1-22, 10.1093/rpd/ncs242.

Hovington, P., Timoshevskii, V., Burgess, S., Demers, H., Statham, P., Gauvin, R., and Zaghib, K., 2016. Can we detect Li KX-ray in lithium compounds using energy dispersive spectroscopy? *Scanning, 38*(6), 571-578,

Hu, W., Quang, N. D., Majumder, S., Park, E., Kim, D., Choi, H.-S., and Chang, H. S., 2019. Efficient photo charge transfer of Al-doped ZnO inverse opal shells in SnS2 photoanodes prepared by atomic layer deposition. *Journal of Alloys and Compounds*, 153349,

Hua, R. N., Jia, Z. H., and Shi, C. S., 2007. Preparation of KMgF3 and Eu-doped KMgF3 nanocrystals in water-in-oil microemulsions. *Materials Research Bulletin, 42*(2), 249-255, 10.1016/j.materresbull.2006.06.004.

Huang, L., Li, D.-Q., Lin, Y.-J., Wei, M., Evans, D. G., and Duan, X., 2005. Controllable preparation of Nano-MgO and investigation of its bactericidal properties. *Journal of inorganic biochemistry, 99*(5), 986-993,

Huang, X. J., 2008. *Nanotechnology research: new nanostructures, nanotubes and nanofibers*: Nova Publishers.

Huang, X., and Zhang, Q., 2010. Near-infrared quantum cutting via cooperative energy transfer in Gd 2 O 3: Bi 3+, Yb 3+ phosphors. *Journal of Applied Physics, 107*(6), 063505,

Huang, Y., Zhang, S., Kim, S. I., Yu, Y. M., and Seo, H. J., 2011. Multisite Structure and Luminescence Spectra from 4f65d1→ 4(8S7/2) and 4(6P7/2) → 4(8S7/2) Transitions in Eu2+-Doped NaMgPO4. *Journal of The Electrochemical Society*, *159*(2), J23-J28, 10.1149/2.013202jes.

Huntley, D., Godfrey-Smith, D., and Thewalt, M., 1985. 1985: Optical dating of sediments. Nature 313, 105–107.

Husain, S., Alkhtaby, L. A., Giorgetti, E., Zoppi, A., and Miranda, M. M., 2014. Study of cobalt doping on structural and luminescence properties of nanocrystalline ZnO. *Journal of Luminescence*, *154*, 430-436,

Hutt, G., 1989. Infrared stimulated photoluminescence dating of sediment. *Ancient TL*, *7*, 48,

Hütt, G., Jaek, I., and Tchonka, J., 1988. Optical dating: K-feldspars optical response stimulation spectra. *Quaternary Science Reviews*, *7*(3-4), 381-385, 10.1016/0277-3791(88)90033-9.

Jeevanandam, P., and Klabunde, K., 2002. A study on adsorption of surfactant molecules on magnesium oxide nanocrystals prepared by an aerogel route. *Langmuir*, *18*(13), 5309-5313,

JM Le Masson, N., JJ Box, A., WE Van Eijk, C., Furetta, C., and P. Chaminade, J., 2002. Optically and thermally stimulated luminescence of KMgF3: Ce3+ and NaMgF3: Ce3+. *Radiation Protection Dosimetry*, *100*(1-4), 229-234,

Joseph, D. P., Renugambal, P., Saravanan, M., Raja, S. P., and Venkateswaran, C., 2009. Effect of Li doping on the structural, optical and electrical properties of spray deposited SnO2 thin films. *Thin Solid Films*, *517*(21), 6129-6136, 10.1016/j.tsf.2009.04.047.

Kadri, G. B., Das, D., Gupta, S. K., and Sudarshan, K., 2020. Influence of Li+ co-doping on the luminescence of MgO:Eu3+ nanocrystals: Probing asymmetry, energy transfer and defects. *Solid State Sciences*, *105*, 106286, 10.1016/j.solidstatesciences.2020.106286.

Kakkar, R., Kapoor, P. N., and Klabunde, K. J., 2004. Theoretical study of the adsorption of formaldehyde on magnesium oxide nanosurfaces: size effects and the role of low-coordinated and defect sites. *The Journal of Physical Chemistry B, 108*(47), 18140-18148,

Kalita, J. M., Kaya-Keles, S., Cakal, G. O., Meric, N., and Polymeris, G. S., 2021. Thermoluminescence and optically stimulated luminescence properties of ulexite mineral. *Journal of Luminescence, 230*, 117759, ARTN 117759 10.1016/j.jlumin.2020.117759.

Kalita, J., and Chithambo, M., 2017. Thermoluminescence of α-Al2O3: C, Mg: kinetic analysis of the main glow peak. *Journal of Luminescence, 182*, 177-182,

Kang, M., Yan, W., Liu, J., Liu, J., and Sun, R., 2010a. Combustion synthesis and luminescent properties of CaO: Eu3+, M+ (M=Li, Na, K) phosphor. *Journal of Wuhan University of Technology-Mater. Sci. Ed., 25*(2), 179-183, 10.1007/s11595-010-2179-0.

Kang, M., Yan, W., Liu, J., Liu, J., and Sun, R., 2010b. Combustion synthesis and luminescent properties of CaO: Eu 3+, M+(M= Li, Na, K) phosphor. *Journal of Wuhan University of Technology-Mater. Sci. Ed., 25*(2), 179-183,

Kang, S.-g., Kim, Y., Kim, S. E., and Kim, S., 2013. The effects of heat treatment on room temperature ferromagnetism in a digitally Co doped ZnO thin film. *Electronic Materials Letters, 9*(1), 7-11,

Karmakar, M., Bhattacharyya, S., Sarkar, A., Mazumdar, P. S., and Singh, S. D., 2017. Analysis of Thermoluminescence Glow Curves Using Derivatives of Different Orders. *Radiation Protection Dosimetry, 175*(4), 493-502, 10.1093/rpd/ncw378.

Kato, T., Okada, G., and Yanagida, T., 2016. Optical, scintillation and dosimeter properties of MgO transparent ceramic and single crystal. *Ceramics International, 42*(5), 5617-5622, 10.1016/j.ceramint.2015.12.070.

Kaur, P., Kaur, A., Singh, S., Thakur, S., and Singh, L., 2020. Comprehensive analysis of crystal structure, optical and luminescent behavior of Fe doped MgO nanophosphors. *Optik*, *219*, 164742, https://doi.org/10.1016/j.ijleo.2020.164742.

Kawano, N., Kato, T., Okada, G., Kawaguchi, N., and Yanagida, T., 2017a. Optical, scintillation and dosimeter properties of MgO: Tb translucent ceramics synthesized by the SPS method. *Optical Materials*, *73*, 364-370,

Kawano, N., Kato, T., Okada, G., Kawaguchi, N., and Yanagida, T., 2017b. Optical, scintillation and dosimeter properties of MgO:Tb translucent ceramics synthesized by the SPS method. *Optical Materials*, *73*, 364-370, 10.1016/j.optmat.2017.08.025.

Kazakis, N. A., Tsetine, A. T., Kitis, G., and Tsirliganis, N. C., 2016. Insect wings as retrospective/accidental/forensic dosimeters: An optically stimulated luminescence investigation. *Radiation Measurements*, *89*, 74-81, 10.1016/j.radmeas.2016.03.004.

Kingsley, J., Manickam, N., and Patil, K., 1990. Combustion synthesis and properties of fine particle fluorescent aluminous oxides. *Bulletin of Materials Science*, *13*(3), 179-189,

Kirsh, Y., 1992. Kinetic-Analysis of Thermoluminescence - Theoretical and Practical Aspects. *Physica Status Solidi a-Applied Research*, *129*(1), 15-48, DOI 10.1002/pssa.2211290102.

Kitis, G., and Vlachos, N. D., 2013. General semi-analytical expressions for TL, OSL and other luminescence stimulation modes derived from the OTOR model using the Lambert W-function. *Radiation Measurements*, *48*, 47-54, 10.1016/j.radmeas.2012.09.006.

Kitis, G., Furetta, C., Prokic, M., and Prokic, V., 2000. Kinetic parameters of some tissue equivalent thermoluminescence materials. *Journal of Physics D-Applied Physics*, *33*(11), 1252-1262, Doi 10.1088/0022-3727/33/11/302.

Kitis, G., Furetta, C., Sanipoli, C., and Scacco, A., 1999a. KMgF3: Ce, An Ultra-High Sensitivity Thermoluminescent Material-(Letter to the Editor). *Radiation Protection Dosimetry, 82*(2), 151-152,

Kitis, G., Furetta, C., Sanipoli, C., and Scacco, A., 1999b. KMgF3:Ce, An Ultra-High Sensitivity Thermoluminescent Material - (Letter to the Editor). *Radiation Protection Dosimetry, 82*(2), 151-152, 10.1093/oxfordjournals.rpd.a032617.

Kitis, G., Gomez-Ros, J. M., and Tuyn, J. W. N., 1998. Thermoluminescence glow-curve deconvolution functions for first, second and general orders of kinetics. *Journal of Physics D-Applied Physics, 31*(19), 2636-2641, Doi 10.1088/0022-3727/31/19/037.

Kitis, G., Polymeris, G. S., Sahiner, E., Meric, N., and Pagonis, V., 2016. Influence of the infrared stimulation on the optically stimulated luminescence in four K-feldspar samples. *Journal of Luminescence, 176*, 32-39, 10.1016/j.jlumin.2016.02.023.

Kołodziejczak-Radzimska, A., and Jesionowski, T., 2014. Zinc oxide—from synthesis to application: a review. *Materials, 7*(4), 2833-2881,

Kortov, V., Milman, I., Monakhov, A., and Slesarev, A., 1993. Combined TSL-ESR MgO detectors for ionising and UV radiations. *Radiation Protection Dosimetry, 47*(1-4), 273-276,

Kron, T., 1999. Applications of thermoluminescence dosimetry in medicine. *Radiation Protection Dosimetry, 85*(1-4), 333-340, DOI 10.1093/oxfordjournals.rpd.a032865.

Kroon, R. E., 2013. Nanoscience and the Scherrer equation versus the 'Scherrer-Gottingen equation'. *South African Journal of Science, 109*(5-6), 01-02, ARTN a0019 10.1590/sajs.2013/a0019.

Kück, S., and Sokólska, I., 2006. Spectroscopic investigation of Mn2+, Pr3+codoped KMgF3under vacuum-ultraviolet excitation. *Journal of Physics: Condensed Matter, 18*(23), 5447-5457, 10.1088/0953-8984/18/23/016.

Kumar, P. M., Borse, P., Rohatgi, V., Bhoraskar, S., Singh, P., and Sastry, M., 1994. Synthesis and structural characterization of nanocrystalline aluminium oxide. *Materials chemistry and Physics, 36*(3-4), 354-358,

Kunkel, N., Meijerink, A., Springborg, M., and Kohlmann, H., 2014. Eu(ii) luminescence in the perovskite host lattices KMgH3, NaMgH3 and mixed crystals LiBaxSr1−xH3. *Journal of Materials Chemistry C, 2*(24), 4799-4804, 10.1039/C4TC00644E.

Lacis, I., and Valbis, J., 1979. Vacuum-ultraviolet luminescence of Be-Doped MgO epitaxial layers. *physica status solidi (b), 95*(1), K21-K26,

Las, W., and Stoebe, T., 1984. TL mechanisms and luminescence characteristics in MgO. *Radiation Protection Dosimetry, 8*(1-2), 45-67,

Li, J., Wang, Y. H., and Liu, B. T., 2010. Influence of alkali metal ions doping content on photoluminescence of (Y, Gd) BO3:Eu red phosphors under VUV excitation. *Journal of Luminescence, 130*(6), 981-985, 10.1016/j.jlumin.2010.01.009.

Li, Y., Wang, J., Zhou, W. L., Zhang, G. G., Chen, Y., and Su, Q., 2013. Ultraviolet-Visible-Near-Infrared Luminescence Properties and Energy Transfer Mechanism of a Novel 5d Broadband Sensitized Sr3SiO5:Ce3+,Yb3+ Suitable for Solar Spectral Converter. *Applied Physics Express, 6*(8), 082301, Artn 082301 10.7567/Apex.6.082301.

Lide, D. R., 2004. *CRC handbook of chemistry and physics* (Vol. 85): CRC press.

Lim, C. S., Aleksandrovsky, A., Molokeev, M., Oreshonkov, A., and Atuchin, V., 2015. Microwave sol-gel synthesis and upconversion photoluminescence properties of CaGd2(WO4)(4):Er3+/Yb3+ phosphors with incommensurately modulated structure. *Journal of Solid State Chemistry, 228*, 160-166, 10.1016/j.jssc.2015.04.032.

Lines, M. E., and Glass, A. M., 2001. *Principles and applications of ferroelectrics and related materials*: Oxford university press.

Lorbeer, C., Behrends, F., Cybinska, J., Eckert, H., and Mudring, A. V., 2014. Charge compensation in RE3+ (RE = Eu, Gd) and M+ (M = Li, Na, K) co-doped alkaline earth nanofluorides obtained by microwave reaction with reactive ionic liquids leading to improved optical properties. *J. Mater. Chem. C, 2*(44), 9439-9450, 10.1039/c4tc01214c.

Maliyekkal, S. M., Antony, K., and Pradeep, T., 2010. High yield combustion synthesis of nanomagnesia and its application for fluoride removal. *Science of the total environment, 408*(10), 2273-2282,

Marcazzó, J., Santiago, M., D'Angelo, C., Furetta, C., and Caselli, E., 2010. Study of the luminescent properties of KMgF3: Sm. *Nuclear Instruments and Methods in Physics Research Section B: Beam Interactions with Materials and Atoms, 268*(2), 183-186,

Mazhdi, M., Saydi, J., Karimi, M., Seidi, J., and Mazhdi, F., 2013. A study on optical, photoluminescence and thermoluminescence properties of ZnO and Mn doped-ZnO nanocrystalline particles. *Optik-International Journal for Light and Electron Optics, 124*(20), 4128-4133,

McKeever, S. W., 1988. *Thermoluminescence of solids* (Vol. 3): Cambridge University Press.

McKeever, S. W., Moscovitch, M., and Townsend, P. D., 1995. Thermoluminescence dosimetry materials: properties and uses.

McKeever, S. W., Rhodes, J. F., Mathur, V. K., Chen, R., Brown, M. D., and Bull, R. K., 1985. Numerical solutions to the rate equations governing the simultaneous release of electrons and holes during thermoluminescence and isothermal decay. *Phys Rev B Condens Matter, 32*(6), 3835-3843, 10.1103/physrevb.32.3835.

McKeever, S., 1950. S 1985 Thermoluminescence of Solids. *Cambridge, Cambridge UniversityPress*,

Mejdahl, V., 1969. Thermoluminescent dating of ancient Danish ceramics. *Archaeometry, 11*, 99-104,

Mesterházy, D., Osvay, M., Kovács, A., and Kelemen, A., 2012. Accidental and retrospective dosimetry using TL method. *Radiation Physics and Chemistry, 81*(9), 1525-1527,

Mitchell, R. H., Cranswick, L. M. D., and Swainson, I., 2006. Neutron diffraction determination of the cell dimensions and thermal expansion of the fluoroperovskite KMgF3 from 293 to 3.6 K. *Physics and Chemistry of Minerals, 33*(8), 587-591, 10.1007/s00269-006-0106-x.

Morris, M. F., and Mckeever, S. W. S., 1993. Further Developments of a Model for Describing the Optical Bleaching of Thermoluminescence from Quartz as Applied to Sediment Dating. *Radiation Protection Dosimetry, 47*(1-4), 637-641,

Nagpal, J. S., Kathuria, V. K., and Bapat, V. N., 1981. Some Studies of Thermoluminescent Mgf2 Phosphors. *International Journal of Applied Radiation and Isotopes, 32*(3), 147-151, Doi 10.1016/0020-708x(81)90105-8.

Naik, R., Prashantha, S. C., Nagabhushana, H., Sharma, S. C., Nagaswarupa, H. P., and Girish, K. M., 2016. Effect of fuel on auto ignition route, photoluminescence and photometric studies of tunable red emitting Mg2SiO4:Cr3+ nanophosphors for solid state lighting applications. *Journal of Alloys and Compounds, 682*, 815-824, 10.1016/j.jallcom.2016.05.037.

Nakate, U., Bulakhe, R., Lokhande, C., and Kale, S., 2016. Au sensitized ZnO nanorods for enhanced liquefied petroleum gas sensing properties. *Applied Surface Science, 371*, 224-230,

Nassar, E. J., Ciuffi, K. J., Calefi, P. S., Avila, L., Bandeira, L. C., Cestari, A., de Faria, E. H., Marçal, A. L., and Matos III, M., 2010. *Europium III: Different Emission Spectra in Different Matrices, the Same Element*: Nova Science Publishers.

Ntwaeaborwa, O. M., Mofokeng, S. J., Kumar, V., and Kroon, R. E., 2017. Structural, optical and photoluminescence properties of Eu(3+) doped ZnO nanoparticles. *Spectrochim Acta A Mol Biomol Spectrosc, 182*, 42-49, 10.1016/j.saa.2017.03.067.

Oliveira, L. C., Doull, B. A., and Yukihara, E. G., 2013c. Investigations of MgO:Li,Gd thermally and optically stimulated luminescence. *Journal of Luminescence, 137*, 282-289, 10.1016/j.jlumin.2013.01.018.

Oliveira, L. C., Milliken, E. D., and Yukihara, E. G., 2013d. Development and characterization of MgO:Nd,Li synthesized by solution combustion synthesis for 2D optically stimulated luminescence dosimetry. *Journal of Luminescence, 133*, 211-216, 10.1016/j.jlumin.2011.10.032.

Oliveira, L. C., Yukihara, E. G., and Baffa, O., 2016. MgO:Li,Ce,Sm as a high-sensitivity material for Optically Stimulated Luminescence dosimetry. *Scientific Reports, 6*, 24348, ARTN 24348 10.1038/srep24348.

Oliveira, L. C., Yukihara, E. G., and Baffa, O., 2019. Lanthanide-doped MgO: A case study on how to design new phosphors for dosimetry with tailored luminescent properties. *Journal of Luminescence, 209*, 21-30, 10.1016/j.jlumin.2019.01.015.

Oliveira, L., Doull, B., and Yukihara, E., 2013a. Investigations of MgO: Li, Gd thermally and optically stimulated luminescence. *Journal of Luminescence, 137*, 282-289,

Oliveira, L., Milliken, E., and Yukihara, E., 2013b. Development and characterization of MgO: Nd, Li synthesized by solution combustion synthesis for 2D optically stimulated luminescence dosimetry. *Journal of Luminescence, 133*, 211-216,

Orante-Barrón, V., Escobar-Ochoa, F., Cruz-Vázquez, C., and Bernal, R., 2015. Thermoluminescence of novel zinc oxide nanophosphors obtained by glycine-based solution combustion synthesis. *Journal of Nanomaterials, 16*(1), 17,

Orante-Barrón, V., Oliveira, L., Kelly, J., Milliken, E., Denis, G., Jacobsohn, L., Puckette, J., and Yukihara, E., 2011. Luminescence properties of MgO produced by solution combustion synthesis and doped with lanthanides and Li. *Journal of Luminescence, 131*(5), 1058-1065,

Otmar, M., Hintzen, H. T., Dorenbos, P., and van der Kolk, E., 2011. Yb 3+ doped LaSi 3 N 5 and YSi 3 N 5 with low energy charge transfer for near-infrared light-emitting diode and solar cell application. *Journal of Materials Chemistry, 21*(45), 18289-18294,

Ozdemir, A., Altunal, V., Guckan, V., Can, N., Kurt, K., Yegingil, I., and Yegingil, Z., 2018. Characterization and some fundamental features of Optically Stimulated Luminescence measurements of silver activated lithium tetraborate. *Journal of Luminescence, 202*, 136-146, 10.1016/j.jlumin.2018.05.054.

Ozdemir, A., Guckan, V., Altunal, V., Kurt, K., and Yegingil, Z., 2021. Thermoluminescence in MgB4O7:Pr,Dy dosimetry powder synthesized by solution combustion synthesis method. *Journal of Luminescence, 230*, 117761, 10.1016/j.jlumin.2020.117761.

Ozdemir, A., Yegingil, Z., Nur, N., Kurt, K., Tuken, T., Depci, T., Tansug, G., Altunal, V., Guckan, V., Sigircik, G., Yu, Y., Karatasli, M., and Dolek, Y., 2016. Thermoluminescence study of Mn doped lithium tetraborate powder and pellet samples synthesized by solution combustion synthesis. *Journal of Luminescence, 173*, 149-158, 10.1016/j.jlumin.2016.01.013.

Özgür, Ü., Alivov, Y. I., Liu, C., Teke, A., Reshchikov, M., Doğan, S., Avrutin, V., Cho, S.-J., and Morkoç, H., 2005. A comprehensive review of ZnO materials and devices. *Journal of Applied Physics, 98*(4), 11,

Pacchioni, G. (2001). In The Chemical Physics of Solid Surfaces Vol. 9 (ed DP, Woodruff) 94–135. In: Elsevier.

Pagonis, V., Kitis, G., and Furetta, C., 2006. *Numerical and practical exercises in thermoluminescence*: Springer Science & Business Media.

Pal, P. P., and Manam, J., 2013a. Photoluminescence and thermoluminescence studies of Tb3+ doped ZnO nanorods. *Materials Science and Engineering: B, 178*(7), 400-408,

Pal, P. P., and Manam, J., 2013b. Photoluminescence and thermoluminescence studies of Tb3+ doped ZnO nanorods. *Materials Science and Engineering B-Advanced Functional Solid-State Materials, 178*(7), 400-408, 10.1016/j.mseb.2013.01.006.

Pal, P. P., and Manam, J., 2013c. Structural and photoluminescence studies of Eu3+ doped zinc oxide nanorods prepared by precipitation method. *Journal of Rare Earths, 31*(1), 37-43,

Panda, N., Acharya, B., Singh, T. B., and Gartia, R., 2013. Thermoluminescence and decay studies on cerium doped ZnO nanopowders. *Materials Letters, 95*, 205-208,

Pathak, N., Mukherjee, S., Das, D., Dutta, D., Dash, S., and Kadam, R. M., 2020. Evolution of different defect clusters in Eu 3+ doped KMgF 3 and Eu 3+, Li+ co-doped KMgF 3 compounds and the immediate impact on the phosphor characteristics. *Journal of Materials Chemistry C, 8*(21), 7149-7161,

Patil, R. R., Muthal, P. L., Dhopte, S. M., Kondawar, V. K., and Moharil, S. V., 2007. Synthesis and properties of submicron range CaSO4 : Eu particles. *Journal of Luminescence, 126*(2), 571-574, 10.1016/j.jlumin.2006.10.022.

Peng, Z., Dai, G., Chen, P., Zhang, Q., Wan, Q., and Zou, B., 2010. Synthesis, characterization and optical properties of star-like ZnO nanostructures. *Materials Letters, 64*(8), 898-900,

Perez C, L., Cruz Z, E., Marcazzo, J., Hernandez A, J., and Murrieta S, H., 2015. Synthesis and luminescence properties of KMgF 3: Tm 3+ fluoro perovskite.

Pierson, J., Forman, S. L., Lepper, K., and Conley, G., 1994. A Variable Narrow Bandpass Optically Stimulated Luminescence System for Quaternary Geochronology. *Radiation Measurements, 23*(2-3), 533-535, Doi 10.1016/1350-4487(94)90094-9.

Pietkun, A., Polakiewicz, L., and Oczkowski, H. L., 1992. Measurement System for Fractional Glow Technique. *Acta Physica Polonica A, 81*(6), 687-691, DOI 10.12693/APhysPolA.81.687.

Pushpa, N., and Kokila, M. K., 2017b. Effect of cobalt doping on structural, thermo and photoluminescent properties of ZnO nanopowders. *Journal of Luminescence, 190*, 100-107, 10.1016/j.jlumin.2017.05.032.

Pushpa, N., and Kokila, M., 2017a. Effect of cobalt doping on structural, thermo and photoluminescent properties of ZnO nanopowders. *Journal of Luminescence, 190*, 100-107,

Pushpa, N., Kokila, M., and Nagabhushana, K., 2016. Thermoluminescence studies of γ-irradiated ZnO: Mg2+ nanoparticles. *Nuclear Instruments and Methods in Physics Research Section B: Beam Interactions with Materials and Atoms, 379*, 62-68,

Qiu, Y., and Yang, S., 2007. ZnO Nanotetrapods: Controlled Vapor-Phase Synthesis and Application for Humidity Sensing. *Advanced Functional Materials, 17*(8), 1345-1352,

Ramirez-Romero, M. I., Garcia-Salinas, L., Villicana-Mendez, M., Huirache-Acuna, R., Apolinar-Cortes, J., and Gonzalez, P. R., 2018. Dosimetric properties of KMgF3:Tb+PTFE. *Appl Radiat Isot, 141*, 203-205, 10.1016/j.apradiso.2018.04.014.

Randall, J. T., and Wilkins, M. H. F., 1945. The phosphorescence of various solids. *Proceedings of the Royal Society of London. Series A. Mathematical and Physical Sciences, 184*(999), 347-364,

Rao, R. P., 1986. The preparation and thermoluminescence of alkaline earth sulphide phosphors. *Journal of Materials Science, 21*(10), 3357-3386,

Raoufi, D., 2013. Synthesis and photoluminescence characterization of ZnO nanoparticles. *Journal of Luminescence, 134*, 213-219,

Ravichandrika, K., Kiranmayi, P., and Ravikumar, R., 2012. Synthesis, characterization and antibacterial activity of ZnO nanoparticles. *Int. J. Pharm. Pharm. Sci, 4*(4), 0975-1491,

Rawat, N., Dhabekar, B., Kulkarni, M., Muthe, K., Mishra, D., Soni, A., Gupta, S., and Babu, D., 2014. Optimization of CW-OSL parameters for improved dose detection threshold in Al 2 O 3: C. *Radiation Measurements, 71*, 212-216,

Reddy, A. J., Kokila, M., Nagabhushana, H., Rao, J., Shivakumara, C., Nagabhushana, B., and Chakradhar, R., 2011. EPR, thermo and photoluminescence properties of ZnO nanopowders. *Spectrochimica Acta Part A: Molecular and Biomolecular Spectroscopy, 81*(1), 59-63,

Reddy, A. J., Kokila, M., Nagabhushana, H., Sharma, S., Rao, J., Shivakumara, C., Nagabhushana, B., and Chakradhar, R., 2012. Structural, EPR, photo and thermoluminescence properties of ZnO: Fe nanoparticles. *Materials chemistry and Physics, 133*(2-3), 876-883,

Reddy, A. J., Kokila, M., Nagabhushana, H., Shivakumara, C., Chakradhar, R., Nagabhushana, B., and Krishna, R. H., 2014. Luminescence studies and EPR investigation of solution combustion derived Eu doped ZnO. *Spectrochimica Acta Part A: Molecular and Biomolecular Spectroscopy, 132*, 305-312,

Reddy, A. J., Krishna, R. H., Nagabhushana, B., Kokila, M., Nagabhushana, H., Shivakumara, C., and Chakradhar, R., 2015. Synthesis, luminescence properties and EPR investigation of hydrothermally derived uniform ZnO hexagonal rods. *Spectrochimica Acta Part A: Molecular and Biomolecular Spectroscopy*, *139*, 262-270,

Reddy, S. S., Nagabhushana, K. R., and Singh, F., 2017. Mechanism of thermoluminescence in high energy carbon ion irradiated Tb3+doped Al2O3phosphor for carbon ion beam dosimetry. *Materials Research Express*, *4*(9), 095023, 10.1088/2053-1591/aa8928.

Riley, C., and Sibley, W., 1970. Color Centers in KMg F 3. *Physical Review B*, *1*(6), 2789,

Rivera, T., Roman, J., Azorin, J., Sosa, R., Guzman, J., Serrano, A. K., Garcia, M., and Alarcon, G., 2010. Preparation of CaSO4:Dy by precipitation method to gamma radiation dosimetry. *Appl Radiat Isot*, *68*(4-5), 623-625, 10.1016/j.apradiso.2009.09.033.

Rodriguez-Lazcano, Y., Correcher, V., and Garcia-Guinea, J., 2012. Luminescence emission of natural NaCl. *Radiation Physics and Chemistry*, *81*(2), 126-130, 10.1016/j.radphyschem.2011.07.012.

Roman, J., Rivera, T., and Azorin, J., 2009. Thermoluminescent properties of CaSO 4: Dy prepared by precipitation method.

Sadek, A. M., 2013. Test of the accuracy of the computerized glow curve deconvolution algorithm for the analysis of thermoluminescence glow curves. *Nuclear Instruments & Methods in Physics Research Section a-Accelerators Spectrometers Detectors and Associated Equipment*, *712*, 56-61, 10.1016/j.nima.2013.02.011.

Saha, S., Das, S., Ghorai, U. K., Mazumder, N., Gupta, B. K., and Chattopadhyay, K. K., 2013. Charge compensation assisted enhanced photoluminescence derived from Li-codoped MgAl 2 O 4: Eu 3+ nanophosphors for solid state lighting applications. *Dalton Transactions*, *42*(36), 12965-12974,

Sahu, D., Acharya, B., Bag, B., Singh, T. B., and Gartia, R., 2010. Probing the surface states in nano ZnO powder synthesized by sonication method: Photo and thermo-luminescence studies. *Journal of Luminescence, 130*(8), 1371-1378,

Sathyamoorthy, A., and Luthra, J., 1978. Mechanism of thermoluminescence in magnesium oxide. *Journal of Materials Science, 13*(12), 2637-2644,

Sawai, J., Kojima, H., Igarashi, H., Hashimoto, A., Shoji, S., Sawaki, T., Hakoda, A., Kawada, E., Kokugan, T., and Shimizu, M., 2000. Antibacterial characteristics of magnesium oxide powder. *World Journal of Microbiology and Biotechnology, 16*(2), 187-194,

Schmidt-Mende, L., and MacManus-Driscoll, J. L., 2007. ZnO–nanostructures, defects, and devices. *Materials today, 10*(5), 40-48,

Schuyt, J. J., and Williams, G. V. M., 2018. Photoluminescence, radioluminescence and optically stimulated luminescence in nanoparticle and bulk KMgF3(Eu). *Journal of Luminescence, 204*, 472-479, 10.1016/j.jlumin.2018.08.056.

Schuyt, J. J., and Williams, G. V. M., 2019. Development of a 2D dosimeter using the optically stimulated luminescence of NaMgF3:Eu with CCD camera readout. *Radiation Measurements, 121*, 99-102, 10.1016/j.radmeas.2018.12.012.

Scott, J. F., 2007. Applications of modern ferroelectrics. *Science, 315*(5814), 954-959, 10.1126/science.1129564.

Secu, C., and Sima, M., 2009. Photoluminescence and thermoluminescence of ZnO nano-needle arrays and films. *Optical Materials, 31*(6), 876-880,

Sengar, B. S., Garg, V., Kumar, A., Awasthi, V., Kumar, S., Atuchin, V. V., and Mukherjee, S., 2018. Band alignment of Cd-free (Zn, Mg) O layer with Cu2ZnSn (S, Se) 4 and its effect on the photovoltaic properties. *Optical Materials, 84*, 748-756,

Seo, H. J., Tsuboi, T., and Jang, K., 2004. Eu3+luminescence in Eu-dopedKMgF3crystals investigated by site-selective laser-excitation spectroscopy. *Physical Review B, 70*(20), 205113, 10.1103/PhysRevB.70.205113.

Shakti, N., Devi, C., Patra, A. K., Gupta, P. S., and Kumar, S., 2018. Lithium doping and photoluminescence properties of ZnO nanorods. *AIP Advances, 8*(1), 015306, Artn 015306 10.1063/1.5008863.

Sharma, P. K., Pandey, A. C., Zolnierkiewicz, G., Guskos, N., and Rudowicz, C., 2009. Relationship between oxygen defects and the photoluminescence property of ZnO nanoparticles: A spectroscopic view. *Journal of Applied Physics, 106*(9), 094314, Artn 094314 10.1063/1.3256000.

Sharma, V., Pilania, G., Rossetti Jr, G., Slenes, K., and Ramprasad, R., 2013. Comprehensive examination of dopants and defects in BaTiO 3 from first principles. *Physical Review B, 87*(13), 134109,

Shi, S., Gao, J., and Zhou, J., 2008. Effects of charge compensation on the luminescence behavior of Eu3+ activated CaWO4 phosphor. *Optical Materials, 30*(10), 1616-1620, 10.1016/j.optmat.2007.10.007.

Shinde, K. P., Pawar, R. C., Sinha, B. B., Kim, H. S., Oh, S. S., and Chung, K. C., 2014b. Study of effect of planetary ball milling on ZnO nanopowder synthesized by co-precipitation. *Journal of Alloys and Compounds, 617*, 404-407, 10.1016/j.jallcom.2014.08.030.

Shinde, K., Pawar, R., Sinha, B., Kim, H., Oh, S., and Chung, K., 2014a. Study of effect of planetary ball milling on ZnO nanopowder synthesized by co-precipitation. *Journal of Alloys and Compounds, 617*, 404-407,

Shivaramu, N. J., Lakshminarasappa, B. N., Coetsee, E., and Swart, H. C., 2021. Thermoluminescence behavior of gamma irradiated Y2O3: Sm3+ nanophosphor. *Journal of Luminescence, 232*, 117855, ARTN 117855 10.1016/j.jlumin.2020.117855.

Silva, I. M. P., Byzynski, G., Ribeiro, C., and Longo, E., 2016. Different dye degradation mechanisms for ZnO and ZnO doped with N (ZnO: N). *Journal of Molecular Catalysis A: Chemical*, *417*, 89-100,

Smith, B. W., Rhodes, E. J., Stokes, S., Spooner, N. A., and Aitken, M. J., 1990. Optical Dating of Sediments - Initial Quartz Results from Oxford. *Archaeometry, 32*(1), 19-31, DOI 10.1111/j.1475-4754.1990.tb01078.x.

Soares, A. F., Tatumi, S. H., Mazzo, T. M., Rocca, R. R., and Courrol, L. C., 2017b. Study of morphological and luminescent properties (TL and OSL) of ZnO nanocrystals synthetized by coprecipitation method. *Journal of Luminescence, 186*, 135-143, 10.1016/j.jlumin.2017.02.028.

Soares, A., Tatumi, S., Mazzo, T., Rocca, R., and Courrol, L., 2017a. Study of morphological and luminescent properties (TL and OSL) of ZnO nanocrystals synthetized by coprecipitation method. *Journal of Luminescence, 186*, 135-143,

Sokólska, I., and Kück, S., 2001. Observation of photon cascade emission in the Pr3+-doped perovskite KMgF3. *Chemical Physics, 270*(2), 355-362, 10.1016/s0301-0104(01)00408-6.

Spooner, N. A., Aitken, M. J., Smith, B. W., Franks, M., and Mcelroy, C., 1990. Archaeological Dating by Infrared-Stimulated Luminescence Using a Diode-Array. *Radiation Protection Dosimetry, 34*(1-4), 83-86,

Spooner, N., and Questiaux, D. (1989). Optical dating-Achenheim beyond the Eemian using green and infrared stimulation. In *Long and Short Range Limits in Luminescence Dating* (Vol. 9, pp. 97-103): Research Laboratory for Archaeology and the History of Art Oxford.

Strickertsson, K., 1985. The thermoluminescence of potassium feldspars—glow curve characteristics and initial rise measurements. *Nuclear Tracks and Radiation Measurements (1982), 10*(4-6), 613-617,

Sun, L. N., Mai, W. P., Dang, S., Qiu, Y. N., Deng, W., Shi, L. Y., Yan, W., and Zhang, H. J., 2012. Near-infrared luminescence of periodic mesoporous organosilicas grafted with lanthanide complexes based on visible-light sensitization. *Journal of Materials Chemistry*, *22*(11), 5121-5127, 10.1039/c2jm15158h.

Tamboli, S. H., Patil, R. B., Kamat, S. V., Puri, V., and Puri, R. K., 2009. Modification of optical properties of MgO thin films by vapour chopping. *Journal of Alloys and Compounds*, *477*(1-2), 855-859, 10.1016/j.jallcom.2008.11.011.

Tanimizu, S., Shionoya, S., Yen, W., and Yamamoto, H., 1999. *Principal phosphor materials and their optical properties*: Boca Raton, FL: CRC Press.

Tardío, M., Ramírez, R., González, R., and Chen, Y., 2002. p-type semiconducting properties in lithium-doped MgO single crystals. *Physical Review B*, *66*(13), 134202,

Tardıo, M., Ramırez, R., Gonzalez, R., Chen, Y., and Alves, E., 2002. Electrical conductivity of MgO crystals implanted with lithium ions. *Nuclear Instruments and Methods in Physics Research Section B: Beam Interactions with Materials and Atoms*, *191*(1-4), 191-195,

Taunk, P., Das, R., Bisen, D., and Tamrakar, R. K., 2015. Structural characterization and photoluminescence properties of zinc oxide nano particles synthesized by chemical route method. *Journal of Radiation Research and Applied Sciences*, *8*(3), 433-438,

Taurian, O. E., Springborg, M., and Christensen, N. E., 1985. Self-consistent electronic structures of MgO and SrO. *Solid state communications*, *55*(4), 351-355, https://doi.org/10.1016/0038-1098(85)90622-2.

Taylor, G., and Lilley, E., 1978. The analysis of thermoluminescent glow peaks in LiF (TLD-100). *Journal of Physics D: Applied Physics*, *11*(4), 567,

Tereshchenko, A., Bechelany, M., Viter, R., Khranovskyy, V., Smyntyna, V., Starodub, N., and Yakimova, R., 2016. Optical biosensors based on ZnO nanostructures: advantages and perspectives. A review. *Sensors and Actuators B: Chemical, 229*, 664-677,

Thomas, B., and Houston, E., 1964. Correlation of optical absorption and thermoluminescence curves for single crystals of magnesium oxide. *British Journal of Applied Physics, 15*(8), 953,

Timmer, G., and Borstel, G., 1991. Electronic structure of nickel, iron, and cobalt impurities in magnesium oxide. *Physical Review B, 43*(6), 5098,

Tiwari, G., Brahme, N., Sharma, R., Bisen, D. P., Sao, S. K., and Khare, A., 2017. Fracto- mechanoluminescence and thermoluminescence properties of orange-red emitting Eu3+ doped Ca2Al2SiO7 phosphors. *Journal of Luminescence, 183*, 89-96, 10.1016/j.jlumin.2016.11.012.

Ton-That, C., Foley, M., Phillips, M. R., Tsuzuki, T., and Smith, Z., 2012. Correlation between the structural and optical properties of Mn-doped ZnO nanoparticles. *Journal of Alloys and Compounds, 522*, 114-117,

Udayakumar, S., Renuka, V., and Kavitha, K., 2012. Structural, optical and thermal studies of cobalt doped hexagonal ZnO by simple chemical precipitation method. *J. Chem. Pharm. Res, 4*(2), 1271-1280,

Uthirakumar, P., and Hong, C. H., 2009b. Effect of annealing temperature and pH on morphology and optical property of highly dispersible ZnO nanoparticles. *Materials Characterization, 60*(11), 1305-1310, 10.1016/j.matchar.2009.06.002.

Uthirakumar, P., and Hong, C.-H., 2009a. Effect of annealing temperature and pH on morphology and optical property of highly dispersible ZnO nanoparticles. *Materials Characterization, 60*(11), 1305-1310,

Van Uitert, L., 1984. An empirical relation fitting the position in energy of the lower d-band edge for Eu2+ or Ce3+ in various compounds. *Journal of Luminescence, 29*(1), 1-9,

Veronese, I., Galli, A., Cantone, M. C., Martini, M., Vernizzi, F., and Guzzi, G., 2010. Study of TSL and OSL properties of dental ceramics for accidental dosimetry applications. *Radiation Measurements, 45*(1), 35-41, 10.1016/j.radmeas.2009.11.005.

Vorokh, A. S., 2018. Scherrer formula: estimation of error in determining small nanoparticle size. *Nanosystems-Physics Chemistry Mathematics, 9*(3), 364-369, 10.17586/2220-8054-2018-9-3-364-369.

Wang, F., Deng, R., Wang, J., Wang, Q., Han, Y., Zhu, H., Chen, X., and Liu, X., 2011a. Tuning upconversion through energy migration in core–shell nanoparticles. *Nature materials, 10*(12), 968-973,

Wang, X. F., Wang, R. C., Peng, C. G., Li, T. T., and Liu, B., 2011b. Growth of BeO Nanograins Synthesized by Polyacrylamide Gel Route. *Journal of Materials Science & Technology, 27*(2), 147-152, Doi 10.1016/S1005-0302(11)60040-6.

Wei, X., Huang, S., Chen, Y., Guo, C., Yin, M., and Xu, W., 2010. Energy transfer mechanisms in Yb 3+ doped YVO 4 near-infrared downconversion phosphor. *Journal of Applied Physics, 107*(10), 103107,

Wintle, A., and Huntley, D., 1980. Thermoluminescence dating of ocean sediments. *Canadian Journal of Earth Sciences, 17*(3), 348-360,

Wood, I. G., Knight, K. S., Price, G. D., and Stuart, J. A., 2002. Thermal expansion and atomic displacement parameters of cubic KMgF3 perovskite determined by high-resolution neutron powder diffraction. *Journal of Applied Crystallography, 35*(3), 291-295, 10.1107/S0021889802002273.

Wu, J., and Xue, D., 2011. Progress of science and technology of ZnO as advanced material. *Science of Advanced Materials, 3*(2), 127-149,

Wu, M., Song, E. H., Chen, Z. T., Ding, S., Ye, S., Zhou, J. J., Xu, S. Q., and Zhang, Q. Y., 2016b. Single-band red upconversion luminescence of Yb3+-Er3+ via nonequivalent substitution in perovskite KMgF3 nanocrystals. *Journal of Materials Chemistry C, 4*(8), 1675-1684, 10.1039/c5tc03600c.

Wu, M., Song, E., Chen, Z., Ding, S., Ye, S., Zhou, J., Xu, S., and Zhang, Q., 2016a. Single-band red upconversion luminescence of Yb 3+–Er 3+ via nonequivalent substitution in perovskite KMgF 3 nanocrystals. *Journal of Materials Chemistry C, 4*(8), 1675-1684,

Xie, A., Yuan, X. M., Wang, F. X., Shi, Y., and Mu, Z. F., 2010. Enhanced red emission in ZnMoO4:Eu3+ by charge compensation. *Journal of Physics D-Applied Physics, 43*(5), 055101, Artn 055101 10.1088/0022-3727/43/5/055101.

Xie, S., Han, X., Kuang, Q., Zhao, Y., Xie, Z., and Zheng, L., 2011. Intense and wavelength-tunable photoluminescence from surface functionalized MgO nanocrystal clusters. *Journal of Materials Chemistry, 21*(20), 7263-7268,

Xu, J., Wang, N. T., and Wang, W. Q., 2011. Synthesis and photoluminescence properties of self-assembled Eu-doped ZnO hollow microspheres. *Physica Status Solidi a-Applications and Materials Science, 208*(12), 2833-2838, 10.1002/pssa.201127290.

Yang, L., Jiang, Z. C., Dong, J. Z., Pan, A. L., and Zhuang, X. J., 2014. The study on crystal defects-involved energy transfer process of Eu3+ doped ZnO lattice. *Materials Letters, 129*, 65-67, 10.1016/j.matlet.2014.04.191.

Yukihara, E. G., and McKeever, S. W., 2011. *Optically stimulated luminescence: fundamentals and applications*: John Wiley & Sons.

Yukihara, E. G., Doull, B. A., Gustafson, T., Oliveira, L. C., Kurt, K., and Milliken, E. D., 2017. Optically stimulated luminescence of MgB4O7:Ce, Li for gamma and neutron dosimetry. *Journal of Luminescence, 183*, 525-532, 10.1016/j.jlumin.2016.12.001.

Yukihara, E. G., McKeever, S. W., and Akselrod, M. S., 2014a. State of art: Optically stimulated luminescence dosimetry–Frontiers of future research. *Radiation Measurements, 71*, 15-24,

Yukihara, E. G., Milliken, E. D., and Doull, B. A., 2014b. Thermally stimulated and recombination processes in MgB4O7 investigated by systematic lanthanide doping. *Journal of Luminescence, 154*, 251-259, 10.1016/j.jlumin.2014.04.038.

Yukihara, E. G., Milliken, E. D., Oliveira, L. C., Orante-Barron, V. R., Jacobsohn, L. G., and Blair, M. W., 2013b. Systematic development of new thermoluminescence and optically stimulated luminescence materials. *Journal of Luminescence, 133*, 203-210, 10.1016/j.jlumin.2011.12.018.

Yukihara, E., Milliken, E., Oliveira, L., Orante-Barrón, V., Jacobsohn, L. G., and Blair, M., 2013a. Systematic development of new thermoluminescence and optically stimulated luminescence materials. *Journal of Luminescence, 133*, 203-210,

Zhang, G., Liu, C., Wang, J., Kuang, X., and Su, Q., 2011. An intense charge transfer broadband sensitized near-infrared emitting CaLaGa 3 S 6 O: Yb 3+ phosphor suitable for solar spectral convertor. *Optics express, 19*(24), 24314-24319,

Zhang, S., Hao, Z., Zhang, L., Pan, G.-H., Wu, H., Zhang, X., Luo, Y., Zhang, L., Zhao, H., and Zhang, J., 2018. Efficient Blue-emitting Phosphor SrLu2O4:Ce3+ with High Thermal Stability for Near Ultraviolet (~400 nm) LED-Chip based White LEDs. *Scientific Reports, 8*(1), 10463, 10.1038/s41598-018-28834-8.

CURRICULUM VITAE

Veysi GÜÇKAN, Completed his primary, secondary and high school education in Nicosia, North Cyprus. He received his B.S. degree in the Physics Department at the Faculty of Arts and Sciences from Cukurova University in 2014. He graduated from MSc in the Physics Department from the Cukurova University in 2017. After his MSc graduation, he started to PhD education in the Physics Department in Cukurova University in 2017. He has worked in several research projects supported by Scientific and Technological Council of Turkey (TUBİTAK) and Scientific Research Project Unit of Cukurova University during PhD. He also worked as a researcher in two international projects supported by NATO during his MSc and PhD. His research areas are radiation dosimetry, thermoluminescence, optically stimulated luminescence, photoluminescence, radioluminescence, dosimeters, material synthesis.